

Particle image velocimetry of the undercarriage flow
of downscaled train models in a water-towing tank
for the assessment of ballast flight

Vom Promotionsausschuss der
Technischen Universität Hamburg-Harburg
zur Erlangung des akademischen Grades
Doktor-Ingenieur (Dr.-Ing.)
genehmigte Dissertation

von

Per Mattias Jönsson

aus

Rebberberga, Schweden

2016

Vorsitzender des Promotionsverfahrens:

Prof. Dr.-Ing. Gerhard Schmitz (TUHH)

Gutachter der Dissertation:

1. Gutachter: Prof. Dr.-Ing. Thomas Rung (TUHH)

2. Gutachter: Prof. Dr.-Ing. Markus Raffel (DLR und Leibniz Universität Hannover)

Zusätzliche Gutachter:

Prof. Dr.-Ing. Heinz Herwig (TUHH)

Prof. Dr.-Ing. Gerhard Schmitz (TUHH)

Tag der mündlichen Prüfung:

Montag, 20. Juni 2016

Abstract

In this thesis the issue of ballast flight beneath high-speed trains is closely examined using (a) two-component high-speed particle image velocimetry of the undercarriage flow beneath downscaled high-speed train models in a water-towing tank and (b) simplified momentum calculations regarding the dislodgement, transport and flight of trackbed ballast particles.

The horizontal and vertical velocity components in the vertical plane extending between the trackbed and the train undercarriage in the trackbed line of symmetry were measured for three different 1:50 high-speed train models and for three different trackbeds.

With the aid of a moving-model rig each of the three different 1:50 high-speed train model configurations was hauled over (1) a smooth trackbed, (2) a rough trackbed and (3) one with sleepers. The attained speed of 4 m/s corresponds to a Reynolds number of $Re = 0.25 \cdot 10^6$ based on the reference length of the model (0.06 m), the rig speed and the kinematic viscosity of water. The scale-model configurations were all realised by modifying the undercarriage roughness of a four-unit generic high-speed train model consisting of two end-cars and two mid-cars. The reference train model reflects a conventional non-articulated high-speed train with inter-car gaps and two bogies per car. To create a completely smooth undercarriage on the smooth train model all bogies were removed and any open gaps covered. On the rough train model all gaps were left open but the bogies were removed.

The results of the undercarriage flow for the reference train model on the smooth ground obtained in the water-towing tank were compared to full-scale measurements on high-speed trains in commercial operation. The comparisons revealed that the main characteristics of the undercarriage flow were reproduced, implying that the scale train model experiments in the water-towing tank are suitable for studying the main properties of undercarriage flows of high-speed trains. Furthermore, the undercarriage flow field obtained for the three train configurations showed that undercarriage irregularities like bogies, bogie housings, inter-car gaps, cavities or protruding obstacles increase the local and overall flow speeds, velocity fluctuations and velocity gradients at the ground, thus increasing both the aerodynamic forces on the trackbed and the risk of ballast flight.

The undercarriage flow fields of all measured configurations were applied to an exposed, simplified and virtual ballast particle in the trackbed to simulate its dislodgement, its transport over the trackbed and its flight after upward deflection from the

trackbed. Calculations of the ballast flight problem indicated that the most susceptible train configuration to ballast flight incidents is the rough train model. These results lead to the conclusions that bogies, bogie housings, cavities or any other undercarriage irregularities inducing strong local flow accelerations similar to those of the open bogie housings of the rough train model should be avoided to contain the risk of ballast flight. The benefits of a smooth undercarriage were, furthermore, highlighted by the drastic reduction in ballast flight risk achieved by covering all cavities and gaps as well as by aligning all protrusions or features of the undercarriage. Finally, ballast trackbeds without cross-going sleepers are more conducive to ballast flight than trackbeds with cross-going sleepers and lowered ballast levels, even if ballast particles initially lie on top of sleepers.

Acknowledgements

I would like to express my gratitude to Prof. Dr.-Ing. Claus Wagner, Prof. Dr.-Ing. Markus Raffel and Dipl.-Phys. Sigfried Loose for supporting and providing the possibility to do my PhD at the German Aerospace Center. I am also grateful that Dr.-Ing. Alexander Orellano and Dr.-Ing. Martin Schober from Bombardier Transportation introduced and initiated the possibility for me to work at the German Aerospace Center, which lead to my PhD.

I sincerely thank Prof. Dr.-Ing. Thomas Rung for accepting me as an external PhD student at the Technical University of Hamburg-Harburg and for all the support and efforts he invested in and around my PhD.

I would also like to acknowledge the efforts of the reviewers Prof. Dr.-Ing. Thomas Rung and Prof. Dr.-Ing. Markus Raffel as well as the additional reviewers Prof. Dr.-Ing. Gerhard Schmitz and Prof. Dr.-Ing. Heinz Herwig but also Prof. Dr.-Ing. Gerhard Schmitz for organising and chairing this examination board.

Special thanks to Dr.-Ing. Hugues Richard for the comprehensive support and help with the particle image velocimetry measurement technique, my office colleague Johannes Haff for all the useful discussions and the effortless support and motivation of Prof. Dr.-Ing. Claus Wagner.

Last but not least, I am deeply thankful for the support and encouragement from my family but of course also my colleagues and friends to keep on working on my thesis during all these years.

December 7th, 2016

Mattias Jönsson

Contents

List of figures	ix
List of tables	xxiii
Nomenclature	xxvii
1 Introduction	1
1.1 High-speed train aerodynamics	1
1.2 The ballast flight problem	3
1.3 Previous work: Ballast flight and undercarriage aerodynamics	7
1.4 Motivation and objectives	24
2 Particle image velocimetry	29
2.1 The principles of particle image velocimetry	29
2.2 Particle image velocimetry equipment and apparatus	30
2.3 Particle image velocimetry analysis	34
2.4 Advantages and disadvantages of particle image velocimetry	36
3 Measurement facility	39
3.1 Water-towing tank	39
3.2 Particle image velocimetry set-up in the water-towing tank	40
4 Measured configurations	43
4.1 High-speed train model	43
4.2 High-speed train model configurations	44
4.3 Ground configurations	45
4.4 Overview of the measured configurations	46
5 Post-processing of the particle image velocimetry data	49
5.1 Evaluation of the particle image velocimetry raw data	49
5.2 Particle image velocimetry error estimation	50
5.3 Velocity data post-processing	54
5.4 Definition of coordinate system and velocity components	56
6 Particle image velocimetry results	57
6.1 Undercarriage flow field in the water-towing tank	57

6.2	Reynolds number dependency in the water-towing tank	63
6.3	Comparison of the train configurations	67
6.3.1	The statistically averaged undercarriage flow field	67
6.3.2	Instantaneous undercarriage flow field	76
6.3.3	Horizontal velocity profiles	84
6.3.4	Vertical velocity profiles	92
6.4	Ground roughness effects	95
6.4.1	Flow field over the rough ground	96
6.4.2	Flow field over the sleepers	98
6.4.3	Equivalent roughnesses of the different ground configurations . .	103
6.4.4	Ground roughness effects on the undercarriage flow for the con- sidered train models	108
6.5	Overall comparison of the measured train and ground configurations . .	111
7	Full-scale measurements	117
7.1	Full-scale measurements on a high-speed train	117
7.2	Comparison of the downscaled water-towing tank experiments to full- scale measurements	125
8	Evaluation of ballast flight	133
8.1	Particle dislodgement	133
8.2	Ballast particle initiation	137
8.2.1	Physical approach for the ballast particle initiation	137
8.2.2	Ballast particle initiation calculations: Influencing parameters . .	140
8.2.3	Ballast particle initiation calculations: Critical train speeds	143
8.3	Ballast particle transport over the trackbed	164
8.3.1	Physical approach for the ballast particle transport over the trackbed	164
8.3.2	Ballast particle transport calculations	169
8.4	Ballast particle flight	175
8.4.1	Physical approach to the ballast particle flight phase	175
8.4.2	Ballast flight calculations for the rough ground	176
8.4.3	Ballast flight calculations for the ground with sleepers	186
8.5	Overall comparison of the risk of ballast flight incidents	198
9	Conclusions and outlook	203
9.1	Conclusions	203

9.2 Outlook	208
References	211
Appendix	225
Appendix A: The reference train model	225
Appendix B: Spatial horizontal averages of the undercarriage flow field	227
Appendix C: Convergence of the calculated mean velocity values and their standard deviations for the undercarriage flow field	235
Appendix D: Influence of the ground proximity on the lift coefficient for the simplified ballast particle	239
Appendix E: Magnus effect for the simplified ballast particle	240
Appendix F: Vertically spatially-averaged U velocity along the train for the height of the exposed simplified ballast particle	241
Appendix G: Critical train speeds of ballast flight incidents for the rough ground condition	245
Appendix H: Critical train speeds for the simplified ballast particle to be transported past the consecutive sleeper	247

List of figures

Figure 1:	The ballast flight problem.	3
Figure 2:	The principle of particle image velocimetry (PIV).	29
Figure 3:	The water-towing tank at DLR in Göttingen (left), the moving-model rig with train model and ground plate (middle) and a close-up view of the train model (right).	39
Figure 4:	The moving-model rig speed (left) and acceleration during a single run in the water-towing tank. Vertical lines indicate where the train model reaches and leaves the ground plate (dotted vertical lines) and the field of view or measurement field of the PIV cameras (solid vertical lines).	40
Figure 5:	The 2C-PIV set-up in the water-towing tank.	41
Figure 6:	The 1:50 high-speed train model.	43
Figure 7:	The 1:50 high-speed train model: Head of the train model (left), the inter-car region (middle) and the simplified bogie (right). . .	43
Figure 8:	The three considered train configurations: The reference train model (upper, T.C. 1), the smooth train model (middle, T.C. 2) and the rough train model (lower, T.C. 3).	44
Figure 9:	The trailer bogie for the Siemens high-speed train Velaro CRH3.	45
Figure 10:	The three considered ground configurations: Smooth ground (G.C. A), rough ground (G.C. B) and ground with protruding sleepers (G.C. C).	45
Figure 11:	Magnification and perspective error due to the laser light sheet thickness.	51
Figure 12:	Definition of the coordinate system and velocity components. . .	56
Figure 13:	Normalised mean velocity component in the travelling direction U and in the vertical direction W along the normalised length for the reference train model (T.C. 1) on the smooth ground condition (G.C. A) at the height of the top of the rail ($TOR = Z / H_{GAP} = 0.476$). The vertical lines indicate the positions of the train axles. $U_{TRAIN} = 4$ m/s.	57

-
- Figure 14: Normalised vertical profiles of the mean velocity component in the travelling direction U over the undercarriage gap (ground and the train undercarriage) for the reference train model (T.C. 1) on the smooth ground (G.C. A). The horizontal line indicates the height of the top of the rail ($TOR = Z / H_{GAP} = 0.476$). $U_{TRAIN} = 4$ m/s. 59
- Figure 15: Normalised horizontal profiles of the mean velocity component in the travelling direction U at different heights over the trackbed for the reference train model (T.C. 1) on the smooth ground (G.C. A). The vertical lines indicate the positions of the train axles. $U_{TRAIN} = 4$ m/s. 60
- Figure 16: Normalised horizontal profiles of the mean velocity component in the vertical direction W at different heights over the trackbed for the reference train model (T.C. 1) on the smooth ground (G.C. A). The vertical lines indicate the positions of the train axles. $U_{TRAIN} = 4$ m/s. 61
- Figure 17: Normalised mean (red line) velocity component in the travelling direction U (left) and in the vertical direction W (right) with the corresponding 22 single runs (blue lines) at the height of $TOR \times 0.75$ ($Z / H_{GAP} = 0.357$) for the reference train model (T.C. 1) on the smooth ground (G.C. A). The vertical black lines indicate the positions of the train axles. $U_{TRAIN} = 4$ m/s. 61
- Figure 18: Histograms (blue) and the corresponding probability density functions (red) of the u (left) and w (right) velocities at the height $TOR \times 0.75$ at the middle of the trailing end-car for the reference train model (T.C. 1) on the smooth ground (G.C. A). $U_{TRAIN} = 4$ m/s. 63
- Figure 19: Horizontal profiles of the normalised ensemble average velocity component in the travelling direction U (upper) and its standard deviation U_{SD} (lower) for the reference train model (T.C. 1) on the smooth ground (G.C. A) at the height of $Z / H_{GAP} = 0.238$ ($TOR \times 0.5$) for different train model speeds. The vertical black lines indicate the positions of the train axles. 64
-

-
- Figure 20: Vertical profiles of the normalised ensemble average velocity component in the travelling direction U (two upper rows) and its standard deviation U_{SD} (two lower rows) at the centre of each train car for the reference train model (T.C. 1) on the smooth ground (G.C. A) for different train model speeds. The horizontal black line indicates the height of the top of the rail ($Z / H_{GAP} = 0.476$). 66
- Figure 21: Normalised mean velocity field of the velocity component in the travelling direction U for the leading end-car of the reference train model (T.C. 1) (upper plot), the rough train model (T.C. 3) (middle plot) and the smooth train model (T.C. 2) (lower plot) on the smooth ground condition (G.C. A). $U_{TRAIN} = 4$ m/s. . . . 67
- Figure 22: Normalised mean velocity field of the velocity component in the travelling direction U for the first mid-car of the reference train model (T.C. 1) (upper plot), the rough train model (T.C. 3) (middle plot) and the smooth train model (T.C. 2) (lower plot) on the smooth ground condition (G.C. A). $U_{TRAIN} = 4$ m/s. 68
- Figure 23: Normalised mean velocity field of the velocity component in the travelling direction U for the second mid-car of the reference train model (T.C. 1) (upper plot), the rough train model (T.C. 3) (middle plot) and the smooth train model (T.C. 2) (lower plot) on the smooth ground condition (G.C. A). $U_{TRAIN} = 4$ m/s. . . . 69
- Figure 24: Normalised mean velocity field of the velocity component in the travelling direction U for the trailing end-car of the reference train model (T.C. 1) (upper plot), the rough train model (T.C. 3) (middle plot) and the smooth train model (T.C. 2) (lower plot) on the smooth ground condition (G.C. A). $U_{TRAIN} = 4$ m/s. . . . 69
- Figure 25: Normalised mean velocity field of the velocity component in the vertical direction W for the leading end-car of the reference train model (T.C. 1) (upper plot), the rough train model (T.C. 3) (middle plot) and the smooth train model (T.C. 2) (lower plot) on the smooth ground condition (G.C. A). $U_{TRAIN} = 4$ m/s. 70
-

-
- Figure 26: Normalised mean velocity field of the velocity component in the vertical direction W for the first mid-car of the reference train model (T.C. 1) (upper plot), the rough train model (T.C. 3) (middle plot) and the smooth train model (T.C. 2) (lower plot) on the smooth ground condition (G.C. A). $U_{TRAIN} = 4$ m/s. 71
- Figure 27: Normalised mean velocity field of the velocity component in the vertical direction W for the second mid-car of the reference train model (T.C. 1) (upper plot), the rough train model (T.C. 3) (middle plot) and the smooth train model (T.C. 2) (lower plot) on the smooth ground condition (G.C. A). $U_{TRAIN} = 4$ m/s. 71
- Figure 28: Normalised mean velocity field of the velocity component in the vertical direction W for the trailing end-car of the reference train model (T.C. 1) (upper plot), the rough train model (T.C. 3) (middle plot) and the smooth train model (T.C. 2) (lower plot) on the smooth ground condition (G.C. A). $U_{TRAIN} = 4$ m/s. 72
- Figure 29: Turbulence intensity field for the leading end-car for the reference train model (T.C. 1) (upper plot), the rough train model (T.C. 3) (middle plot) and the smooth train model (T.C. 2) (lower plot) on the smooth ground condition (G.C. A). $U_{TRAIN} = 4$ m/s. 74
- Figure 30: Turbulence intensity field for the first mid-car for the reference train model (T.C. 1) (upper plot), the rough train model (T.C. 3) (middle plot) and the smooth train model (T.C. 2) (lower plot) on the smooth ground condition (G.C. A). $U_{TRAIN} = 4$ m/s. . . . 74
- Figure 31: Turbulence intensity field for the second mid-car for the reference train model (T.C. 1) (upper plot), the rough train model (T.C. 3) (middle plot) and the smooth train model (T.C. 2) (lower plot) on the smooth ground condition (G.C. A). $U_{TRAIN} = 4$ m/s. 75
- Figure 32: Turbulence intensity field for the trailing end-car for the reference train model (T.C. 1) (upper plot), the rough train model (T.C. 3) (middle plot) and the smooth train model (T.C. 2) (lower plot) on the smooth ground condition (G.C. A). $U_{TRAIN} = 4$ m/s. 75
-

-
- Figure 33: Close-up view of the sixth bogie region showing a snapshot of the normalised instantaneous velocity component in the travelling direction u as contour superimposed with in-plane velocity vectors for the reference train model (T.C. 1) (upper row), the smooth train model (T.C. 2) (middle row) and the rough train model (T.C. 3) (lower row) on the smooth ground (G.C. A). $U_{TRAIN} = 4$ m/s. 78
- Figure 34: Close-up view of the seventh bogie region showing a snapshot of the normalised instantaneous velocity component in the travelling direction u as contour superimposed with in-plane velocity vectors for the reference train model (T.C. 1) (upper row), the smooth train model (T.C. 2) (middle row) and the rough train model (T.C. 3) (lower row) on the smooth ground (G.C. A). $U_{TRAIN} = 4$ m/s. 79
- Figure 35: Close-up view of the sixth bogie region showing contours of the normalised ensemble average flow field for U with in-plane velocity vectors (left column) and the standard deviation fields U_{SD} (right column) for the reference train model (T.C. 1) (upper row), the smooth train model (T.C. 2) (middle row) and the rough train model (T.C. 3) (lower row) on the smooth ground (G.C. A). $U_{TRAIN} = 4$ m/s. 81
- Figure 36: Close-up view of the seventh bogie region showing contours of the normalised ensemble average flow field for U with in-plane velocity vectors (left column) and the standard deviation fields U_{SD} (right column) for the reference train model (T.C. 1) (upper row), the smooth train model (T.C. 2) (middle row) and the rough train model (T.C. 3) (lower row) on the smooth ground (G.C. A). $U_{TRAIN} = 4$ m/s. 82
- Figure 37: Normalised mean velocity component in the travelling direction U along the normalised train length at the height of the top of the rail ($Z / H_{GAP} = 0.476$) for the three considered train configurations on the smooth ground (G.C. A), the rough ground (G.C. B) and the ground with sleepers (G.C. C). The vertical lines indicate the positions of the train axles. $U_{TRAIN} = 4$ m/s. 85
-

-
- Figure 38: Normalised mean velocity component in the vertical direction W along the normalised train length at the height of the top of the rail ($Z / H_{GAP} = 0.476$) for the three considered train configurations on the smooth ground (G.C. A), the rough ground (G.C. B) and the ground with sleepers (G.C. C). The vertical lines indicate the positions of the train axles. $U_{TRAIN} = 4$ m/s. 87
- Figure 39: Normalised standard deviation of the velocity component in the travelling direction U_{SD} along the normalised train length at the height of the top of the rail ($Z / H_{GAP} = 0.476$) for the three considered train configurations on the smooth ground (G.C. A), the rough ground (G.C. B) and the ground with sleepers (G.C. C). The vertical lines indicate the positions of the train axles. $U_{TRAIN} = 4$ m/s. 88
- Figure 40: Normalised standard deviation of the velocity component in the vertical direction W_{SD} along the normalised train length at the height of the top of the rail ($Z / H_{GAP} = 0.476$) for the three considered train configurations on the smooth ground (G.C. A), the rough ground (G.C. B) and the ground with sleepers (G.C. C). The vertical lines indicate the positions of the train axles. $U_{TRAIN} = 4$ m/s. 89
- Figure 41: Normalised vertical profiles of the velocity component in the travelling direction U over the undercarriage gap for the three considered train configuration on the smooth ground (G.C. A), the rough ground (G.C. B) and the ground with sleepers (G.C. C). The horizontal black line indicates the height of the top of the rail. $U_{TRAIN} = 4$ m/s. 93
- Figure 42: Normalised vertical profiles of the standard deviation of the velocity component in the travelling direction (U_{SD}) over the undercarriage gap for the three considered train configuration on the smooth ground (G.C. A), the rough ground (G.C. B) and the ground with sleepers (G.C. C). The horizontal black line indicates the height of the top of the rail. $U_{TRAIN} = 4$ m/s. 94
-

-
- Figure 43: Vertical profiles of the mean U velocity at the middle of the trailing end-car for the reference train model (T.C. 1) at different downstream positions from the rough-to-smooth ground roughness transition (G.C. B). The horizontal black line indicates the height of the top of the rail. $U_{TRAIN} = 4$ m/s. 97
- Figure 44: Vertical profiles of the standard deviation U_{SD} at the middle of the trailing end-car for the reference train model (T.C. 1) at different distances from the rough-to-smooth ground roughness transition (G.C. B). The horizontal black line indicates the height of the top of the rail. $U_{TRAIN} = 4$ m/s. 97
- Figure 45: Normalised mean U (upper) and W (lower) velocity field over the sleepers at the middle of the trailing end-car for the reference train model (T.C. 1) for $U_{TRAIN} = 4$ m/s. 99
- Figure 46: Normalised vertical profiles of the mean U velocity (upper row) and the corresponding U_{SD} (lower row) in the inter-sleeper region at different downstream positions from the sleeper and at the middle of the trailing end-car for the reference train model (T.C. 1). The horizontal black line indicates the height of the top of the rail. $U_{TRAIN} = 4$ m/s. 100
- Figure 47: Normalised vertical velocity profiles of the mean U velocity (upper row) and the corresponding U_{SD} (lower row) above a sleeper at different distances from the upstream sleeper edge for the undercarriage flow at the middle of the trailing end-car for the reference train model (T.C. 1). The horizontal black line indicates the height of the top of the rail. $U_{TRAIN} = 4$ m/s. 101
- Figure 48: Comparison between the vertical profiles of the normalised mean U velocity (left) and its corresponding standard deviation U_{SD} above a sleeper (middle) and in the inter-sleeper region ($\Delta X = 8$ mm) for the undercarriage flow at the middle of the trailing end-car for the reference train model (T.C. 1) for $U_{TRAIN} = 4$ m/s. 102
-

-
- Figure 49: Mean velocity profiles using inner variables for the undercarriage flow at the middle of the trailing end-car for the reference train model (T.C. 1) on the smooth ground (G.C. A), rough ground (G.C. B) and the ground with sleepers (G.C. C), together with the law of the wall for a smooth wall using the Clauser chart method (CCM) and the standard slope method (SSM) for the determination of the friction velocity. $U_{TRAIN} = 4$ m/s. 106
- Figure 50: Vertical profiles of the normalised mean U velocity, demonstrating the ground roughness effects for each of the three considered train configurations for the smooth ground (blue line), the rough ground (red line), the inter-sleeper region (green line) and above a sleeper (black line). The black horizontal line indicates the height of the top of the rail. $U_{TRAIN} = 4$ m/s. 109
- Figure 51: Vertical profiles of the normalised standard deviation U_{SD} showing the ground roughness effects for each of the three considered train configurations for the smooth ground (blue line), the rough ground (red line), in the inter-sleeper region (green line) and above a sleeper (black line). The black horizontal line indicates the height of the top of the rail. $U_{TRAIN} = 4$ m/s. 110
- Figure 52: Overall comparison of the vertical profiles of the normalised mean U velocity for the considered train configurations on all ground conditions at the end of the seventh bogie (position 1) and in the middle of the trailing end-car (position 2). $U_{TRAIN} = 4$ m/s. 112
- Figure 53: Overall comparison of the vertical profiles of the normalised standard deviation U_{SD} for the considered train configurations on all ground conditions at the end of the seventh bogie (position 1) and in the middle of the trailing end-car (position 2). $U_{TRAIN} = 4$ m/s. 114
- Figure 54: Normalised mean U velocity values with error bars equal to $2 \cdot U_{SD}$ at the height of $Z / H_{GAP} = 0.1$ at the trailing axle of the seventh bogie (left) and at the middle of the trailing end-car (right) for all measured train and ground configurations. $U_{TRAIN} = 4$ m/s. 115
-

-
- Figure 55: Full-scale measurement set-up: vertical rakes of Pitot-probes together with a light gate for the determination of the air velocity and train speed, respectively (left), and a static surface pressure plate with distributed pressure taps (right). 117
- Figure 56: Ensemble average of the normalised U velocity (upper graphic) and its standard deviation U_{SD} (lower graphic) for the four Pitot-probes in the trackbed line of symmetry ($Y = 0$ mm). The vertical black lines indicate the positions of the train axles. The red frames indicate the flow disturbances from cooling air outlets and/or protruding auxiliary undercarriage equipment. 119
- Figure 57: Vertical dependency of the mean U velocity (left) and the stream-wise velocity fluctuations U_{SD} (right) calculated between the fifth and the last bogie of the train. 120
- Figure 58: Lateral dependency of the mean U velocity (left) and the stream-wise velocity fluctuations U_{SD} (right) calculated between the fifth bogie of the second mid-car and the last bogie of the trailing end-car. 121
- Figure 59: Ensemble average (upper plot) and the standard deviation (lower plot) of the static surface pressure coefficient C_P on the trackbed plate for pressure taps: P1($X = 500$ mm, $Y = 0$ mm) (blue), P2(1000 mm, 550 mm) (red), P3(1000 mm, 250 mm) (green), P4(1000 mm, 0 mm) (black), P5(1000 mm, -250 mm) (magenta), P6(1000 mm, -550 mm) (cyan) and P7(1500 mm, 0 mm) (yellow). The vertical black lines indicate the positions of the train axles. The red frames indicate the flow disturbances from cooling air outlets and/or protruding auxiliary undercarriage equipment. 122
- Figure 60: Lateral dependency of the mean static surface pressure coefficient C_P (left) and its corresponding standard deviation (right) for every pressure tap at $\Delta X = 1000$ mm calculated between the fifth bogie of the second mid-car and the last bogie of the trailing end-car. 123
-

-
- Figure 61: Close-up view of the normalised mean U velocity for the fully developed undercarriage flow between the fourth and the last bogie for the four Pitot-probes installed in the trackbed at the trackbed line of symmetry (upper plot) and the mean static surface pressure coefficient C_p on the trackbed plate for the pressure taps: P1($X = 500$ mm, $Y = 0$ mm) (blue), P2(1000 mm, 550 mm) (red), P3(1000 mm, 250 mm) (green), P4(1000 mm, 0 mm) (black), P5(1000 mm, -250 mm) (magenta), P6(1000 mm, -550 mm) (cyan) and P7(1500 mm, 0 mm) (yellow). The vertical black lines indicate the positions of the train axles. 124
- Figure 62: Comparison of the vertical profiles of the normalised mean U velocity (upper row) and of the velocity fluctuations U_{SD} (lower row) at the middle of the train cars for the 1:50 reference train model (T.C. 1) on the smooth ground (G.C. A) in the water-towing tank (blue lines) with vertical rake of Pitot-probes in the trackbed line of symmetry for the presented full-scale measurements (red lines). 126
- Figure 63: Comparison of the normalised mean U velocity at $Z / H_{GAP} = 0.3289$ of the 1:50 reference train model (T.C. 1) on the smooth ground (G.C. A) in the water-towing tank with the conducted full-scale measurements on the ICE3 high-speed train on a concrete slab track. The first axles of the trains are aligned in the upper plot and the last axles of the trains are aligned in the lower plot. 127
- Figure 64: Comparison of the normalised streamwise turbulence (U_{SD}) at $Z / H_{GAP} = 0.3289$ of the 1:50 reference train model (T.C. 1) on the smooth ground (G.C. A) in the water-towing tank with the conducted full-scale measurements on the ICE3 high-speed train on a concrete slab track. The first axles of the trains are aligned in the upper plot and the last axles of the trains are aligned in the lower plot. 127
-

-
- Figure 65: Comparison of the normalised mean U velocity for the reference train model (T.C. 1) on the smooth ground (G.C. A) in the water-towing tank with that of the full-scale measurements for the ETR 500 [47] at the height of the top of the rail ($Z / H_{GAP} = 0.476$). The first axles of the trains are aligned in the upper plot and the last axles of the trains are aligned in the lower plot. 129
- Figure 66: Comparison of the normalised standard deviation U_{SD} for the reference train model (T.C. 1) on the smooth ground (G.C. A) in the water-towing tank with that of the full-scale measurements on the ETR 500 [47] at the height of the top of the rail ($Z / H_{GAP} = 0.476$). The first axles of the trains are aligned in the upper plot and the last axles of the trains are aligned in the lower plot. . . . 130
- Figure 67: Governing forces for an exposed ballast particle in the evaluation for the initial particle movement scenarios denoted as ballast particle slide and ballast particle direct take-off. 138
- Figure 68: Governing forces and moments around the downstream edge, A, of an exposed ballast particle for the evaluation of the ballast particle rolling as the initial particle movement scenario. 140
- Figure 69: Critical air velocities as a function of the edge length of the simplified exposed cubical ballast particle for the three considered initiation scenarios. 141
- Figure 70: Critical air velocities as a function of the edge length for the simplified exposed ballast particle for the three considered ballast particle initiation scenarios under the influence of trackbed vibration in a trackbed ($a_z = 3 \text{ m/s}^2$) and on top of a sleeper ($a_z = 7 \text{ m/s}^2$). 143
- Figure 71: The actual flow field (black) and the mean flow field (red) over the ballast particle height. 144
- Figure 72: Critical train speeds for the initiation of ballast particle movement as a function of the edge length of the simplified exposed ballast particle for the three train models and the considered ballast particle trackbed positions using the mean U velocity flow field data. 145
-

-
- Figure 73: Critical train speeds for the initiation of ballast particle movement as a function of the edge length of the simplified exposed ballast particle for the three train models and the considered ballast particle trackbed positions using the mean U velocity + U_{SD} flow field data. 148
- Figure 74: Critical train speeds for the initiation of ballast particle movement as a function of the edge length of the simplified exposed ballast particle for the three train models and the considered ballast particle trackbed positions using the mean U velocity + $2 \cdot U_{SD}$ data flow field data. 149
- Figure 75: The mean static pressure coefficient C_P (blue line) and its corresponding standard deviation (red line) for the static pressure probe installed in the trackbed line of symmetry ($Y = 0$ mm) at a height 250 mm above the concrete slab track ($Z / H_{GAP} = 0.447$) of the conducted full-scale measurements. The black vertical lines indicate the train axle positions. 154
- Figure 76: Governing forces on an exposed simplified ballast particle regarding the initial particle movement through ballast particle slide for the train-induced static pressure gradient. 154
- Figure 77: Governing forces on an exposed simplified ballast particle regarding the initial particle movement through ballast particle rolling for the train-induced static pressure gradient. 156
- Figure 78: Comparison of the mean static pressure coefficient around the head of the train for the static pressure probe installed in the trackbed line of symmetry for the full-scale measurements in section 7 (red) with the calculated mean static pressure coefficient from the flow field data of the reference train model (T.C. 1) on the smooth ground (G.C. A) (blue). 159
- Figure 79: The normalised mean U velocity and its corresponding mean static pressure coefficient around the head of the train for the reference train model (T.C. 1) on the smooth ground (G.C. A) at the height $Z / H_{GAP} = 0.091$ 161
-

-
- Figure 80: Pressure force (F_P) fraction of the maximum total force (F_{tot}) on a simplified ballast particle (cube) with an edge length of $a = 0.02 - 0.06$ m, induced by the mean (full lines) and the mean + $2 \cdot \sigma$ (dashed lines) flow and static pressure around the head of the reference train model (T.C. 1) for the considered ground configurations. 162
- Figure 81: Ballast particle rolling over the trackbed. 167
- Figure 82: Velocity (left) and displacement (right) of the simplified ballast particle on top of a sleeper (initially the central position) with an edge length of 28 mm exposed to the expected maximum aerodynamic forces (mean + $2 \cdot SD \cdot \text{sign}(\text{mean})$) around the head of the reference train model (T.C. 1) for different train speeds. . . . 169
- Figure 83: Velocity (left) and displacement (right) for the simplified ballast particle on top of a sleeper (initially the central position) with an edge length of 28 mm exposed to the expected maximum aerodynamic forces (mean + $2 \cdot SD \cdot \text{sign}(\text{mean})$) around the head for the reference (T.C. 1), smooth (T.C. 2) and the rough (T.C. 3) train models for a train speed of 400 km/h. 171
- Figure 84: The normalised mean U velocity (upper) and its corresponding velocity fluctuations U_{SD} (lower) spatially-averaged over the vertical height of a simplified ballast particle with an edge length of $a = 40$ mm on the smooth ground (G.C. A) for the three considered train configurations. 172
- Figure 85: Comparison of the ballast particle velocity along the train length for the three considered train configurations on the smooth ground (sliding motion) for a simplified ballast particle with an edge length of 40 mm and a train speed of 350 km/h using the mean (upper), mean + SD (middle) and mean + $2 \cdot SD$ U velocity and C_P data taking the direction of the induced aerodynamic force into account, mean + $SD \cdot \text{sign}(\text{mean})$ 173
-

-
- Figure 86: The normalised extrapolated mean U velocity (upper) and its corresponding velocity fluctuations U_{SD} (lower), spatially-averaged over the vertical height of the exposed simplified ballast particle with an edge length of $a = 40$ mm on the rough ground (G.C. B) for the reference train model (blue), rough train model (red) and smooth train model (green) as 8-unit train sets. 178
- Figure 87: Critical train speeds for the ballast particle impact with the train undercarriage for the three considered train configurations on the rough ground (G.C. B) using the mean (dotted lines), mean + SD (dashed lines) and mean + 2·SD (full lines) U and W velocity and C_p data, taking the direction of the flow and pressure gradient into account (mean + SD·sign(mean)). 179
- Figure 88: The considered initial positions for the calculation of the critical train speed needed for the simplified exposed ballast particle in the inter-sleeper region to be transported over the first downstream sleeper. 187
- Figure 89: The two considered trajectories over the downstream sleeper for the simplified ballast particle with an initial position on top of a sleeper. 194
- Figure 90: Three considered initial positions for the simplified ballast particle: downstream (d), middle (m) and upstream (u) at the corresponding distances of 125, 75 and 25 mm (1:1) from the upstream edge of the sleeper. 195
- Figure 91: Comparison of the lowest critical train speeds for ballast pitting (smooth and rough grounds) and for a ballast particle to be transported over the downstream sleeper with an initial position on top of a sleeper and in an inter-sleeper region for the considered train configurations and sizes of the simplified exposed ballast particle using the mean + 2·SD·sign(mean) data of the U and W velocity and C_p field. 200
-

List of tables

Table 1:	Overview of the test conditions for the measured configurations in the water-towing tank.	46
Table 2:	Data sample sizes for the measured configurations in the water-towing tank.	55
Table 3:	The different heights over the trackbed for the presented horizontal velocity profiles.	60
Table 4:	Spatial averages between the first and last train axles of the normalised ensemble average U velocity, W velocity and their corresponding velocity fluctuations U_{SD} and W_{SD} at the height of the top of the rail ($Z / H_{GAP} = 0.476$) for all considered configurations.	91
Table 5:	The estimated friction velocity according to the standard slope method, the roughness function extracted from Figure 49, the roughness Reynolds number and the equivalent sand grain roughness using Equation (13) for the reference train model (T.C. 1) on the considered ground conditions.	107
Table 6:	Critical train speeds according to the friction velocity threshold proposed by Bagnold in Equation (16) for the measured train and ground configurations in the water-towing tank for the ballast particle sizes of $d_B = 28, 40$ and 50 mm. The two characteristic flow regions are included, i.e. above and in the middle of a sleeper (C2) and $\Delta X = 8$ mm downstream of a sleeper in the inter-sleeper region (C1).	135
Table 7:	Applied boundary conditions for the considered ballast particle trackbed positions.	144
Table 8:	Critical train speeds for the initiation of motion for the exposed simplified ballast particle with an edge length of $a = 28, 40$ and 50 mm for the reference (T.C. 1), smooth (T.C. 2) and rough (T.C. 3) train models on the smooth ground (G.C. A), rough ground (G.C. B) and the two considered positions of the ground with sleepers, i.e. in a inter sleeper region (G.C. C1) and on top of a sleeper (G.C. C2).	150

Table 9:	Critical train speeds for the initiation of motion for the simplified exposed ballast particle with edge lengths of $a = 28, 40$ and 50 mm for the flow field around the head of the reference train model (T.C. 1) on the considered ground configurations.	152
Table 10:	Critical train speeds in for the initiation of sliding motion for the simplified ballast particle on the smooth ground (G.C. A) using the static pressure coefficient, mean, mean + SD and mean + 2·SD data from the conducted full-scale measurements in section 7. . .	157
Table 11:	Critical train speeds for the initiation of ballast particle slide (smooth ground and above sleeper) and rolling (rough ground and between sleepers) for simplified exposed ballast particles with edge lengths of $a = 28, 40$ and 50 mm using the calculated mean, mean + SD and mean + 2·SD static pressure gradient data, taking positive and negative pressure gradients into account (mean + SD·sign(mean)) around the head for the reference train model (T.C. 1).	160
Table 12:	Critical train speeds for initiation of ballast particle sliding (smooth ground and above sleeper) and rolling (rough ground and between sleepers) for simplified exposed ballast particles using the mean, mean + SD and mean + 2·SD of the calculated static pressure gradients together with the flow field data around the head of the reference train model.	162
Table 13:	Critical train speeds for ballast pitting (left, $Z_B = 235$ mm (1:1)) and ballast impact with the train undercarriage (right, $Z_B = 500$ mm (1:1)) for the reference (T.C. 1), the smooth (T.C. 2) and the rough train model (T.C. 3) on the rough ground (G.C. B) using the mean + 2·SD·sign(mean) data of the U and W velocity and C_p field for different sizes of the exposed simplified ballast particle. .	182
Table 14:	Critical train speeds for ballast pitting ($Z = 235$ mm (1:1)) and impact with the train undercarriage ($Z = 500$ mm (1:1)) for the three considered train configurations on the rough ground (G.C. B) using the mean + 2·SD·sign(mean) data of the U and W velocity and C_p field for the exposed simplified ballast particle with an edge length of $a = 28$ mm and a restitution coefficient of $e = 0.75$ and $e = 0.5$ (in brackets).	184

-
- Table 15: Critical train speeds for the ballast particle impact with the train undercarriage ($Z = 500$ mm (1:1)) for different train lengths of the three considered train configurations on the rough ground (G.C. B) using the mean + 2·SD·sign(mean) data of the U and W velocity and C_P field for the exposed simplified ballast particle with an edge length of $a = 28$ mm. Two values of the restitution coefficient were considered, $e = 0.5$ and $e = 0.75$ (brackets), representing the upward deflection off the other ballast in the trackbed and a sleeper. 185
- Table 16: Critical train speed to pass the downstream sleeper for simplified ballast particles of different sizes and for different inter-sleeper positions for the reference train model (T.C. 1) using the mean + 2·SD·sign(mean) data of the U and W velocity and C_P field. 188
- Table 17: Lowest critical train speed necessary for the simplified exposed ballast particle of different sizes in the inter-sleeper region to pass the downstream sleeper for the three considered train configurations using the mean + 2·SD·sign(mean) data of the U and W velocity and C_P field. The bracketed upper case numbers indicate the initial inter-sleeper positions of the ballast particles. 191
- Table 18: Lowest critical train speed necessary for the simplified exposed ballast particle of different sizes in the inter-sleeper region to pass the downstream sleeper for the three considered train configurations using the mean + 2·SD·sign(mean) data of the U and W velocity and C_P field. The bracketed upper case numbers indicate the initial inter-sleeper positions of the ballast particles. 195
-

Nomenclature

Latin letters

Scalars

a_x acceleration in the X direction

a, b, c height (vertical), length (along-track) and width (across track) of a ballast particle

a_z vertical acceleration of a ballast due to the trackbed vibration

A empirical threshold value for particle dislodgement

A_B aerodynamic reference area of a ballast particle

A_{ref} aerodynamic reference area

B log-law empirical constant for the wall roughness

C_A empirical constant for the acceleration force in a viscous fluid

C_D aerodynamic drag coefficient

C_f skin-friction coefficient $C_f = 2 \cdot \left(\frac{U_\tau}{U_\infty} \right)^2$

C_L aerodynamic lift coefficient

C_{M_y} aerodynamic moment coefficient around the Y-axis

C_P static pressure coefficient

d_B ballast particle diameter

d_p particle diameter

D spherical particle diameter

d_{tp} tracer particle diameter

e restitution coefficient

F_A acceleration force

F_D aerodynamic drag

F_{fr} friction force

F_G force due to gravity

F_L aerodynamic lift

F_P pressure force

F_X horizontal force on a ballast particle along the direction of the track

F_Z vertical force on a ballast particle caused by trackbed accelerations

f_{loss} ballast particle momentum-loss for repetitive contacts with the trackbed

f_s sampling frequency

g gravitational acceleration $g = 9.82 \text{ m/s}^2$

H_{GAP} ground clearance height (trackbed to train undercarriage) $H_{GAP} = 9.88 \text{ mm}$

I light intensity

k roughness element height

k_S equivalent sand grain roughness

k_S^+, k^+ roughness parameter or roughness Reynolds number

L_{TRAIN} train model length = 2.142 m

m_B ballast particle mass

M_Y aerodynamic moment around the Y-axis

N sample size

P pressure

P_{total} total pressure

$P_{dynamic}$ dynamic pressure

P_{static} static pressure

r_B ballast particle radius

R_{II} discrete cross-correlation function of the light intensity distribution of two PIV images

Re Reynolds number

Re_τ particle friction Reynolds number

t time

TI turbulence intensity

u, v, w instantaneous flow velocity components

u', v', w' fluctuating part of the flow velocity components

U, V, W average flow velocity components

U_B, V_B, W_B ballast particle horizontal, lateral and vertical velocity components

$U_{crit-ballast-slide}$ critical flow velocity for ballast particle slide

$U_{crit-ballast-slide-vibration}$ critical flow velocity for ballast particle slide with trackbed vibration

$U_{crit-ballast-take-off}$ critical flow velocity for ballast particle direct take-off

$U_{crit-ballast-take-off-vibration}$ critical flow velocity for ballast particle direct take-off with trackbed vibration

$U_{crit-ballast-rolling}$ critical flow velocity for ballast particle rolling

$U_{crit-ballast-rolling-vibration}$ critical flow velocity for ballast particle rolling with trackbed vibration

U_f flow velocity of the surrounding fluid

U_{SD}, V_{SD}, W_{SD} standard deviation of the flow velocity

U_{tp} tracer particle velocity

$U_{train-crit-slide-vibration}$ critical train speed for ballast particle slide with trackbed vibration

$U_{train-crit-rolling-vibration}$ critical train speed for ballast particle rolling with trackbed vibration

U_{TRAIN} train model speed

U_{τ} friction velocity $U_{\tau} = \sqrt{\frac{\tau_w}{\rho_f}}$

$U_{\tau_{critical}}$ critical threshold friction velocity for particle dislodgement

U_{∞} free flow velocity

U^+ dimensionless flow velocity in wall units $U^+ = \frac{U}{U_{\tau}}$

ΔU^+ roughness function

V_{air} Pitot-probe air velocity

V_B ballast particle volume

V_{min} wind tunnel speed initiating ballast particle motion

V_{max} wind tunnel speed initiating motion of all tested ballast particles

V_{ref} aerodynamic reference volume

X, Y, Z along-track, across track and vertical coordinates

X_B, Y_B, Z_B ballast particle displacement in the along track, across track and vertical coordinates

Z^+ dimensionless wall normal distance in wall units $Z^+ = \frac{Z \cdot U_{\tau}}{\nu}$

Vectors

\bar{V} velocity vector

Greek letters

Scalars

Δt temporal increment

$\Delta X, \Delta Y, \Delta Z$ spatial increment in the Cartesian coordinate system

ε_{max} maximum measurement error

ε_{rms} random measurement error

κ von Karman constant = 0.41

μ_f dynamic viscosity of the surrounding fluid

μ_{static} static friction coefficient

$\mu_{dynamic}$ dynamic friction coefficient

μ_t turbulent viscosity or eddie viscosity

ν kinematic viscosity

ρ_B ballast particle density

ρ_f fluid density

ρ_p particle density

ρ_{tp} tracer particle density

σ standard deviation of a Gaussian distribution

τ_w wall shear stress

ω_B ballast particle rotational speed

Indices and other symbols

Subscript

$(\cdot)_i$ vector coordinate component

$(\cdot)_{ij}$ tensor coordinate component

Other symbols

$|\cdot|$ absolute value

$\hat{\cdot}$ normalised value

Abbreviations

1-D, 2-D, 3-D one, two or three-dimensional

2C-PIV two-component or planar Particle Image Velocimetry

3C-PIV stereoscopic Particle Image Velocimetry

ADIF Administrador de Infraestructuras Ferroviarias

AOA Aerodynamics in Open Air

BFPF Ballast Flying Probability Factor

CCD Charge-Coupled Device

CCM Clauser Chart Method

CFD Computational Fluid Dynamics

CMOS Complementary Metal Oxide Semiconductor

COM Centre Of Mass

DES Detached Eddy Simulations

DLR Deutsches Zentrum für Luft- und Raumfahrt

EN Europäischen Normen

EMU Electrical Multiple Unit

ETR Elettro Treno Rapido

FFT Fast Fourier Transform

FT Fourier Transform

G.C. Ground Configuration

ICE Inter City Express (German high-speed train)

KTX Korea Train eXpress

LDA Laser-Doppler-Anemometry

LED Light Emitting Diodes

LES Large Eddy Simulation

MEMS Micro Electro Mechanical Systems

NACA National Advisory Committee for Aeronautics

Nd:YAG Neodymium doped Yttrium Aluminium Garnet laser

Nd:YLF Neodymium doped Yttrium Lithium Fluoride laser

PCI Peripheral Component Interconnect

PDF Probability Density Function

PIV Particle Image Velocimetry

RANS Reynolds Averaged Navier-Stokes

rms root-mean-square

RTRI Railway Technical Research Institute

SD Standard Deviation

SSIA Stress-Strength Interference Analysis

SSM Standard Slope Method

T.C. Train Configuration

TGV Train á Grande Vitesse

TOR Top Of the Rail

TOS Top Of the Sleeper

TSI Technical Specification for Interoperability

URANS Unsteady Reynolds Averaged Navier-Stokes

1 Introduction

1.1 High-speed train aerodynamics

The interest in high-speed train aerodynamics has grown over the past 30 years due to the increasing speeds in today's high-speed rail travel and the desire to further increase speeds in the future [1]. Aside from lowering ticket prices, reducing travel time is the best way to attract passengers. Increasing the cruising speed of a given train, however, results in an increase to the total train resistance and a higher energy consumption rate. In order to make attractive ticket prices possible, the train resistance, which is directly proportional to the energy consumption of the train, must be reduced. Reducing energy consumption is also important with regard to pollution and the conservation of limited resources. According to the Davis equation [2], the main contributor to the total train resistance at higher speeds is aerodynamic drag because it increases quadratically in relation to train speed. Besides reducing drag by streamlining the shape of the train, other strategies for reducing energy consumption include weight optimisation [3, 4, 5, 6], new or improved energy effective traction concepts [7, 8, 9] and recycling energy (e.g. regenerative braking) [8, 10, 11].

Reducing drag is only one of many aerodynamic challenges. Another is the vital safety issue of cross-wind stability [12, 13, 14, 15]. In general, cross-winds increase the aerodynamic forces on trains. The roll-moment around the leeward rail that results from the lateral force, the lift force and the roll moment caused by cross-winds are crucial. If the roll-moment around the leeward rail (a shape function of train speed, wind strength and angle) exceeds the counter-moment provided by a train's own weight, there is a risk that the train can derail or even tip over on its side. The aforementioned strategy of reducing energy consumption through weight reduction is, however, problematical because it reduces the cross-wind stability.

Similarly, drag optimisation and cross-wind stability are aerodynamic challenges for most other types of vehicles as well. There are additionally aerodynamic challenges specific to trains. These result from a train's much greater length-to-diameter ratio, higher cruising speeds and passing of trains in close proximity to one another and to trackside objects and people. The aerodynamic forces caused by the induced flow of passing trains are commonly divided into two well-known effects or problem areas. These are the head pressure pulse [16, 17] and the slipstream [18, 19, 20]. The first is associated with the aerodynamic forces caused by the strong and rapid pressure

changes around the head and the tail of the train. The slipstream concerns the aerodynamic forces caused by the complex wake flow behind the train. The aerodynamic forces of the head pressure pulse and the slipstream can damage trackside infrastructure as well as cause injury to trackside workers or passengers on platforms (Endoh et al. [21]). The strong pressure gradients around the head of trains can additionally cause seriously dynamic instabilities when trains pass, severely disturbing passenger comfort or, in the worst-case, causing derailment. The head pressure pulse and the slipstream induced aerodynamic forces are primarily influenced by the train's speed, cross-sectional area, train surface roughness (for the slipstream) and the shape of its head and tail.

A complicated and specific railroad problem results from the aerodynamic effects that occur as trains enter and travel through tunnels. These effects are especially problematic for high-speed trains passing through narrow tunnels. When a train enters a tunnel, a pressure wave (compression wave) develops ahead of the train propagates at nearly the speed of sound towards the tunnel exit. There a part of the compression wave produces an impulse noise; the major part of the initial compression wave is reflected back towards the train as an expansion wave. When the expansion wave arrives at the tunnel entrance, part of it is again reflected back as a compression wave. When the tail of the train enters the tunnel, it also produces an expansion wave. The successive reflections and interaction of both pressure waves result in large pressure transients that impact the train. Moreover, the wave fractions are also partially reflected when meeting the train in the tunnel. These pressure transients cause dynamic instabilities for the train, as well as imposing strong loads on the tunnel infrastructure and the train structure itself; moreover, they present a problem with respect to passenger comfort. The confined space between the tunnel wall and train surface also increases the skin friction drag of the train. This is especially apparent in longer tunnels. For further and more detailed information about the compression wave propagation and interaction in tunnels see [3, 22, 23, 24].

The noise produced on both the inside and outside of trains is an important environmental topic with respect to the attractiveness and public acceptance of rail transport. Typical sound sources of trains are engines, cooler fans, brakes, wheel-rail interaction and aero-acoustic effects. Aerodynamic noise is especially worthy of consideration with respect to high-speed trains, since it increases to approximately the sixth power of the train speed. According to Loose et al. [25], aerodynamic noise becomes the significant noise source for trains exceeding 200 km/h. Aerodynamic noise is also pro-

duced at tunnel entrances, or when trains pass trackside structures and at bogies and bogie housings [25, 26], inter-car gaps, pantographs or any other object protruding the streamlined shape of a high-speed train. Measures such as bogie skirts or trackside noise barriers help prevent aerodynamic noise escaping to the surroundings from the lower part of the train (i.e. from the bogie regions and wheel-rail interaction). This leaves the pantograph as the main noise source according to Sueki et al. [27]. In Japan aero-acoustic improvements made to the pantograph of the Shinkansen high-speed train reduced both its noise levels and aerodynamic drag [22, 27, 28].

When one takes all the aerodynamic challenges thus far considered into account, it becomes clear how difficult it is to develop new high-speed trains. What complicates matters even further is the fact that the aerodynamic design of trains must allow for their bidirectional travel.

1.2 The ballast flight problem

A relative new problem referred to as ballast flight (or alternatively as ballast projection or ballast pick-up) arose at the beginning of the 21st century for high-speed trains travelling near 300 km/h [29]. The aerodynamically triggered ballast flight problem consists of several different physical sub-processes, as shown in Figure 1, with similarities to the better-known problem of wind erosion as described by Bagnold [30]. The

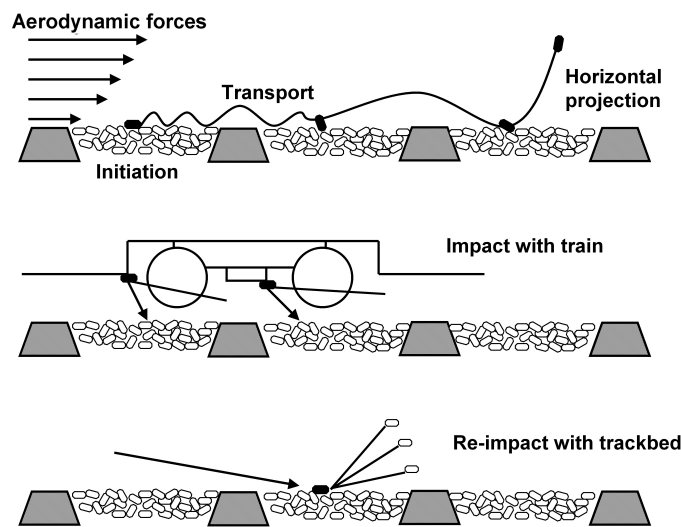


Figure 1: The ballast flight problem.

aerodynamic forces on a trackbed as induced by a train are strong enough to dislodge

gravel stones (ballast particles), according to Kwon and Park [29]. The dislodged ballast particle is then set into motion and given momentum by the flow underneath the train, sending it rolling and jumping over the trackbed [29, 31]. If the moving ballast particle gains sufficient momentum it can be deflected sufficiently upward by the trackbed to reach vertical heights where the undercarriage air velocities are sufficient to initiate ballast flight, see Quinn et al. [32]. Depending on the initial vertical velocity of the ballast particle, the ballast particle flight path can either end in an impact with the train undercarriage or a return downward to further transportation over the trackbed and subsequent flight paths [31]. After an impact with the train undercarriage, the ballast particle may return to the trackbed with greater momentum, dislodging new ballast particles that can possibly initiate flight and impact the train. According to Schroeder-Bodenstein [33], ballast flight incidents with very high rates of train-ballast particle impacts sounding like machine-gun fire have occurred.

Ballast flight incidents have been reported for various high-speed trains in Europe [32, 33, 34, 35] and Asia [29, 36] resulting in damage to both trains and infrastructure. The summary of ballast flight incidents and damage reports, by Claus [37] within the AOA-project (Aerodynamics in Open Air), concluded that the ballast particle impacts caused severe damage to the undercarriage equipment, affecting the performance of the train. Damage to the wheel-rail running surface caused by ballast particles crushed between the wheel and the rail (ballast pitting) on the Channel Tunnel Rail Link was also reported by Quinn et al. [32]. A damaged running surface of the wheel and rail results in poor travel comfort and the formation of hollow areas in the ballast between sleepers (track voids [32]), affecting the track stability. Damage to acoustic screens and broken windows at rail stations from deflected ballast particles, as reported by Kwon and Park [29], highlight the danger posed to trackside workers and passengers on platforms. The ballast flight problem generally prevents high-speed trains from operating at their designed maximum speed. In summary, ballast flight is an economic, an operational and a safety issue.

The ballast flight problem is complex and influenced by a large number of parameters. Weise [38] suggested dividing these into rolling stock- and trackbed-dependent parameters in order to simplify the analysis. The most important rolling stock parameters regarding ballast flight are:

- Train speed
 - Train length
-

-
- Undercarriage geometry (bogies, bogie housings, inter-car gaps, protruding objects)
 - Ground clearance
 - Undercarriage air outlets
 - Train dynamics

In general, the risk of ballast flight increases with higher train cruising speeds, longer train lengths and decreased ground clearance. The risk of ballast flight is very dependent on the undercarriage flow momentum transfer to the moving ballast particle(s). This is basically dependent on the magnitude of the train-induced aerodynamic forces and the exposure time (i.e. the train length). The aerodynamic forces on the trackbed are primarily defined by the train speed, the undercarriage geometry and roughness and the ground clearance. Ventilation airflows towards the trackbed have however also been proved to have a significant influence on the aerodynamic force on trackbeds [39, 40]. The dynamically induced vibration of the trackbed by a train reduces the weight of the ballast particles and thereby its static friction as it begins to "swim", further increasing the risk of ballast flight incidents. The trackbed vibration is also influenced by the trackbed stiffness. Despite the fact that the rolling stock influence is crucial, it is only partially responsible for the risk of ballast flight incidents. The strength of the trackbed or the capacity to prevent ballast particle motion strongly determines the risk of ballast flight incidents. The most important trackbed parameters regarding ballast flight are:

- Trackbed type (concrete slab track, ballast trackbed with monoblock or bi-block sleepers)
- Trackbed design (ballast level, sleeper spacing and shape)
- Ballast particle properties (size, shape, density, position)
- Trackbed stiffness (response/damping of the train-induced dynamics)
- Trackbed quality
- Trackbed history

The trackbed strength is primarily influenced by the trackbed type (monoblock or bi-block sleepers) and design. The wind tunnel experiments within the AOA-project [41] revealed that the dislodged ballast particle rate for a monoblock sleeper trackbed with a lowered ballast level (4 cm below the upper surface of the sleepers) was much

lower in comparison to a trackbed with a flushed ballast level (0 cm) or a bi-block (no cross-going sleepers) sleeper trackbed. The protruding sleepers of the trackbed with a lowered ballast level shielded the ballast from the flow and thus reduced the aerodynamic forces on them. New or remodelled ballast trackbeds are more susceptible to ballast flight due to the presence of small ballast particles in exposed or unstable positions, e.g. on top of sleepers or exposed on top of the trackbed. Based on full-scale field observations, Schroeder-Bodenstein [33] reported that the ballast flight impact rate decreased with the number of train passages due to the exposed ballast particles being blown away or settled into stable positions. This underlines not only the strong influence of the trackbed history, but also the importance of the trackbed quality. The trackbed quality can be maintained by removing ballast particles from the sleepers and through "solidification" by dynamic vibration with a track stabiliser vehicle (Rießberger [42]). The ageing of the trackbed should however also be kept in mind, since the high mechanical loads transferred from the train into the trackbed can crush ballast particles, producing new, lighter ballast particles that are more susceptible to ballast flight [43]. The ballast particle properties are nevertheless of course also amongst the most influential trackbed properties. The ballast particle properties, especially the size and shape, influence every aspect of the ballast flight problem. The size and the shape define the aerodynamic forces acting on the ballast particle (drag, lift, Magnus effect) as the mass is crucial for the friction force (dislodgement and transport) and the gravitational force during the flight phase. The variety of the ballast particle properties (e.g. shape and size) makes them the most challenging parameters to determine and clearly reveal the stochastic nature of the ballast flight problem. Further stochastic influences linked to the ballast particle properties are the momentum loss from the repetitive contact with the trackbed and the characteristics of the upward deflection (e.g. vertical initial velocity and angle), which is strongly influenced by the impacting side of the rotating ballast particle and the impact area in the trackbed. The ballast particle impact with the train is analogous to the upward deflection defined by the impacting surface of the ballast particle and the train. Finally, the motion of the primary ballast particle and, more importantly, the number of new dislodged ballast particles after the re-impact with the trackbed, is apart from the kinetic energy and impact angle strongly influenced of the impact area in the trackbed. Ballast flight incidents related to the precipitation and accretion of snow and ice have been noted in Japan for the Shinkansen high-speed train since the late 1960's [44] and since the beginning of the 1980's in Germany [45]. In Germany and Sweden,

the issue of ice dropping for trackbeds with monoblock sleepers was minimised by lowering the ballast level to 4-6 cm below the upper surface of the sleepers, see Felsing [45]. Theoretical calculations validated by experiments showed that falling ice impacts with the protruding sleepers instead of the ballast for train speeds over 160 km/h [45]. However, for trackbeds with bi-block sleepers (no cross-going sleepers), the measure of lowering the ballast level is redundant and ballast flight triggered by frozen precipitation is still considered to be a problem, according to Schroeder-Bodenstein [33].

In Germany, ballastless trackbed designs (concrete slab tracks) are used for new high-speed lines eliminating the issue of ballast flight, whereas in other countries (France, Spain and Korea [42]), relatively new high-speed rail lines were built using ballast trackbed designs. The fact that new high-speed lines continue to be built using ballast trackbed designs makes ballast flight a persisting issue for high-speed rail.

1.3 Previous work: Ballast flight and undercarriage aerodynamics

In the published work regarding ballast flight, full-scale measurements, model-scale measurements, wind tunnel experiments and numerical simulations have been conducted to obtain data related to undercarriage flow and to understanding the physics of ballast flight. Besides the individual work of train manufactures, railway operators and research institutes, two larger projects have been organized by the European railway community.

Between 2005 and 2008 the physics of ballast flight was intensively studied in a DeuFrako-project (German-French research cooperation) named Aerodynamics in Open Air (AOA). Within the AOA-project, full-scale measurements, computational fluid dynamics (CFD) calculations and wind tunnel measurements were conducted in order to characterise and understand the flow underneath high-speed trains. Numerical simulations and experiments have additionally been undertaken to study and extract the governing parameters of the ballast flight problem. The initiation of the ballast flight problem or particle dislodgement has been investigated in wind tunnels for different trackbed designs, with and without trackbed vibration and for various incoming flow properties. Numerical calculations of the ballast particle re-impact with the trackbed, as shown in Figure 1, have also been performed and validated with ballast gun experiments. The new information obtained from these studies together with the experience of the participants was used to develop a stochastic model to assess the importance

and interdependencies of the sub-processes of the ballast flight problem. A summary of the work, some results and the main outcomes of the AOA-project were presented by Kaltenbach et al. [41]. Despite the new and comprehensive knowledge, the AOA-project revealed the need for further work for a complete understanding of the entire ballast flight process. Furthermore, regarding the risk of ballast flight, a practical and common threshold criterion was needed for the homologation of new high-speed trains or existing high-speed trains in new regions. This motivated the initiation of the second, larger research project dubbed the AeroTRAIN project. This project was together with DynoTRAIN and PantoTRAIN a part of the TrioTRAIN project supported by the European commission's 7th framework programme. The general objective of the TrioTRAIN project was to provide input and/or improve the existing and future Technical Specification for Interoperability (TSI). The AeroTRAIN project concerned various train aerodynamic topics, presented in [46] and including ballast flight. The general objective of the AeroTRAIN project regarding ballast flight was to define a common, robust measurement and post-processing procedure for full-scale measurements using standard measurement techniques. The measurement set-up should capture the necessary parameters for the assessment of the ballast flight problem concerning the approval of trains. Additionally, a threshold criterion for the TSI should be formulated as this was an open problem.

For the general overview of the previous efforts regarding ballast flight, the works of others have been divided into different subgroups. The different approaches or techniques will be briefly discussed along with the outcomes of each study in comparison to the others.

Full-scale measurements of the undercarriage flow:

In the previous work regarding ballast flight, full-scale measurements were the most common and accepted method for gathering undercarriage flow field data. Full-scale measurements have been performed on high-speed trains in Asia [29, 36] and in Europe [31, 32, 46, 47, 48, 49] using various measurement techniques at different vertical, lateral and axial positions in the trackbed. Trackbed-installed measurements are however confined to regions below the height of the top of the rail for the safety of the rolling stock and of course the equipment itself. The most common techniques used for full-scale measurements have been pressure-based. Other measurement techniques have however also been applied, e.g. hot-film or hot-wire anemometry, like in the work of Ido et al. [36], Deeg et al. [47] and Lazaro et al. [31] or ultra-sonic

anemometers [46, 47]. Nevertheless, the most common technique relied on vertical and lateral rakes of several one-dimensional pressure probes, such as Pitot-probes [49, 50], Prandtl-probes [47] or Kiel-probes [29], applied for the measurement of the air velocity in the rail direction. The justification for using one-dimensional pressure probes is that the streamwise velocity in the travelling direction of the train is of much greater magnitude than the velocities in the lateral and vertical directions. This was measured by Quinn et al. [32] for the Eurostar train using a Cobra-probe to gather data for the three velocity components on the Channel Tunnel Rail Link. Additionally, measurements of the ETR 500 (Elettro Treno Rapido) in Italy with 2-D ultrasonic anemometers [47] showed the horizontal velocity to be much larger than the lateral component. Nevertheless, independent of the measurement technique, the results of the full-scale air velocity measurements revealed highly turbulent undercarriage flow for high-speed trains with a dominant air velocity component in the travelling direction of the train. The undercarriage flow developed quickly to a fully developed flow between the second or third car [29, 31, 32, 36] depending on the undercarriage roughness of the train. The change of undercarriage roughness and ground clearance along the train length induced a repetitive flow pattern (or a wavy pattern in the case of the ETR 500 [47]) for the fully developed undercarriage flow. The flow accelerated near the inter-car regions by the bogies and the inter-car gap and it decelerated along the smooth undercarriages of the train cars between the inter-car regions. The local maximum flow velocity values in the undercarriage flow were therefore found around the inter-car regions. The measurements with probe arrays indicated a weak dependence of the velocity component in the travelling direction U on the lateral position between the rails, with the largest values at the centre [29, 32, 47]. The vertical velocity profile measured below the rail height demonstrated a decreasing U velocity, almost linear, towards the trackbed. Typical measured values of the normalised mean U velocity at the top of the rail ($Z / H_{GAP} \sim 0.5$) were around half of the train speed ($U / U_{TRAIN} = 0.4 - 0.55$) [29, 31, 47], with velocity fluctuations around $U_{SD} / U_{TRAIN} = 0.1$ [31, 47]. Regarding the velocity fluctuations or the turbulence in the undercarriage flow, Deeg et al. [47] measured a degree of anisotropy between the horizontal and the lateral velocity fluctuations, with the largest values for the horizontal component. Furthermore, the probability density functions of the instantaneous velocity of the horizontal and lateral velocity component from the measurements within the AOA-project [51] demonstrated distributions similar to a Gaussian or normal distribution for both velocity components.

Full-scale measurements conducted on different trackbed designs revealed that the ground roughness has an influence on the undercarriage flow. This was addressed in Deeg et al. [47], who compared results obtained with Pitot-probes installed in the concrete slab track with those installed in the opposite trackbed (double-track) shortly after the transition from ballast (with bi-block sleepers) to concrete trackbed. The upstream roughness lowered the mean U velocity value in comparison to those obtained for the concrete slab track. This is consistent with the measurements by Jacobs [52] and the theory of flows over rough surfaces. Additionally, the velocity fluctuation values were higher for the Pitot-probes installed after the transition from a ballast trackbed [51]. The effect of protruding monoblock sleepers was shown by Kwon and Park [29] who measured a sudden drop of the velocity component in the travelling direction of the train between positions 20 mm above and 20 mm below the upper surface of the sleeper. The sleepers shield the inter-sleeper regions from the undercarriage flow, diminishing the aerodynamic forces on the ballast particles and reducing the risk of ballast flight. If ballast particles lie on top of a sleeper, the chance of ballast flight would increase dramatically due both to the exposed position of the ballast particles and the flow acceleration over the sleeper [31]. The drag of cross-going protruding sleepers is higher than the drag alone from the surface roughness of the ballast. This was concluded by Gautier et al. [35] who obtained lower U velocity values from measurements on a trackbed with a ballast level lowered below that of a trackbed with the ballast level at the same height as the upper surface of the sleepers. The static pressure measurements by Quinn et al. and Deeg et al. [32, 47] revealed small fluctuating values around zero for the static pressure in the undercarriage flow. Moreover, the mean static pressure coefficient did not surpass values larger than $C_p = 0.05$ for the fully developed undercarriage flow. It was only around the head of the train where the static pressure reached values that would actually contribute to ballast particle movement. It was therefore concluded that the main contribution of the aerodynamic forces on the ballast could be assigned to the air velocities.

In the previously mentioned AeroTRAIN project, recommendations and experiences from the AOA-project were used to develop and improve the full-scale measurement set-up of the AeroTRAIN test campaign. An overview of the conducted work was presented by Sima et al. [46]. For the first time a common measurement procedure was used for different high-speed trains, while applying different measurement techniques. 2-D ultrasonic anemometers, Pitot-probes, Prandtl probes and hot-film sensors were installed for the flow measurements and Preston probes for the shear forces

at various vertical, lateral and axial positions in the trackbed. A high-speed camera was also installed to observe marked ballast particles of different sizes and cubic test particles with equal mean ballast particle size but with differing densities. The ballast and cubic test particles were all initially positioned on the top of a sleeper. Additionally, the ground condition was changed by different trackbed preparations, realising ballast levels flush with and below the upper surface of the sleepers and by installing cover plates in the trackbed for a smooth ground condition. The results and the experience from the full-scale measurements were used to propose a common robust full-scale measurement and post-processing procedure capturing the relevant parameters of ballast flight suitable for the authorisation of high-speed trains. The proposal from AeroTRAIN presented by Weise [53] was based on air speed measurements using Pitot-, Prandtl-probes or 1, 2 and 3-D ultrasonic anemometers. The applied probes should be positioned 25 mm below the height of the top of the rail at the three lateral positions 0 mm and ± 200 mm away from the track centreline. The ground condition was defined 175 mm below the top of the rail as a flat and smooth ground with a given roughness. The flat and smooth ground must therefore be realised using cover plates installed in the trackbed with minimum requirements of coverage between the tracks as well as in the up- and downstream of the probes. Test requirements and conditions such as for the infrastructure (no tunnels, bridges etc.), wind and weather conditions, vehicle specifications, measurement parameters (e.g. sampling frequency, signal to noise ratio etc.) and the post-processing of the measured data were defined. The proposed set-up and requirements should guarantee that comparisons of different measurement campaigns at different locations remain valid. This would aid train manufactures as well as train operators in the assessment of ballast flight for the authorisation of high-speed trains.

Nevertheless, full-scale measurements are not an option in the development of new high-speed trains with new undercarriage designs. The undercarriage flow properties must be estimated before the train production if not before the bid phase. Other methods are therefore applied to investigate the undercarriage flow, including numerical simulations (most commonly CFD), or downscaled train models in wind tunnels with moving belts or in moving-model facilities. A further motivation for CFD or experiments with downscaled models is the possibility to gather data over the entire gap between the trackbed and the train as this is not possible for full-scale measurements.

Downscaled measurements of the undercarriage flow:

Scale model experiments of the undercarriage flow of trains are difficult because the relative motion between the vehicle and ground must be simulated in a realistic way. The vehicle-ground relation is realised either by moving the train model or by the ground in a wind tunnel. Furthermore, the total length of the downscaled train set is often limited by the test facility (e.g. the length of the moving belt), not allowing measurements along entire train sets. Applying yet smaller scale train models allows for the possibility of using longer train sets, but this option is not always beneficial due to the loss of train details and the decreased Reynolds number. The Reynolds number for scale model experiments is nevertheless generally always lower than for full-scale studies. Some of the experiments on scale models have been published, e.g. work of Ido et al., using the large-scale, low noise wind tunnel with a moving belt [36, 54] at the Railway Technical Research Institute (RTRI) in Japan and in the towing wind tunnel facility [36, 55] of Tohoku University. The wind tunnel tests with moving belt for a 1:7 train model of a leading end-car, a mid-car and a trailing end-car were performed at a wind tunnel speed of 50 m/s, corresponding to a Reynolds number of $2 \cdot 10^6$ with the train width as the reference length. The mid-car was centred over the moving belt since the length of the train set was longer than the moving belt. The undercarriage flow field below the mid-car at the track centreline was measured with a traversable rake of hot-wire anemometers installed attached to the train car [36]. The results revealed a Couette-like undercarriage flow [56] with air velocity values in the same range as the full-scale measurements despite the one order of magnitude lower Reynolds number. Furthermore, the addition of bogie fairings, but most of all the complete removal of bogies and the closing of all gaps, realising a completely smooth undercarriage, reduced the undercarriage flow velocities as well as the chance of ballast flight. A similar set-up (three unit train set) in the same wind tunnel and for the same Reynolds number was used to measure the drag on the mid-car with load cells and the surface pressure in the inter-car gap and in the bogie housings for different underframe configurations [54]. The results indicated that drag optimisation of the undercarriage also reduced the risk of ballast flight, since the smoother undercarriage decreased the undercarriage flow velocities. This was also confirmed in the thesis work of Schitthelm [57] for the undercarriage optimisations that were done on the 1:7 generic train undercarriage representing the inter-car region of an ICE3 (German high-speed train: Inter City Express 3). The generic train undercarriage with two realistic bogies and an inter-car gap in a duct flow with a stationary ground achieving a

Reynolds number of $1 \cdot 10^5$ was developed during the AOA-project for the validation of CFD [58].

The first measurements in the towing wind tunnel facility of Tohoku University were presented by Ido et al. [36]. They used a 1:8.4 three unit train model with a ground-attached hot-wire anemometer for measuring the undercarriage flow outside the track at the height of the top of the rail. The further development of the facility together with a more detailed study of the undercarriage flow were presented by Ido and Yoshioka [55]. The undercarriage flow of the five unit train set (leading end-car, three mid-cars and trailing end-car at 1:8.4 scale) was measured with a ground-attached hot-wire anemometer at the track centreline and rail surface height. Additionally, measurements were also undertaken with vertical rakes of Pitot-probes installed between both bogies on one of the three mid-cars. The five vertical rakes covered the distance between the trackbed and the train undercarriage and were installed at different lateral positions. At the maximum speed of the moving train model a Reynolds number of $5 \cdot 10^4$ was achieved based on the ground clearance (ground to train undercarriage) as reference length. The time series of the ground-fixed hot-wire anemometer from both measurement campaigns confirmed the full-scale measurements with a normalised mean flow speed of about half of the train speed ($u / U_{TRAIN} = 0.5$). The results from the Pitot rakes installed on all three mid-cars indicated that fully developed undercarriage flow was achieved by the middle of the second mid-car, in accordance with full-scale measurements [29, 31, 32, 36]. Additionally, the U velocity profile in the vertical direction was similar to that of the Couette-like flow found in the moving-belt wind tunnel tests by Ido et al. [36]. The lateral dependence of the U velocity however contradicted that from full-scale measurements, with increasing U velocity values for lateral positions away from the track centreline.

The results from moving-model experiments and wind tunnel measurements with moving belts demonstrated that scale model experiments were feasible for the study of the undercarriage flow since they qualitatively agreed with the undercarriage flow found from full-scale measurements. The results for the scale model experiments at lower Reynolds numbers should however be considered with caution.

Numerical simulations of the undercarriage flow:

The undercarriage flow is characterised by flow separations and unsteadiness behind the bluff body geometries of the train undercarriage. The realistic prediction of these flow effects are challenging for numerical simulations. The previously mentioned

wind tunnel experiments for the generic train undercarriage of an ICE3 [58] were therefore used to validate commercially available numerical approaches within the AOA-project. In the work of Sima et al. [59] different CFD approaches were applied for the 1:7 generic train undercarriage and compared to the LDA measurements by Kaltenbach et al. [58]. CFD simulations were performed with different commercial codes (Star-CD, Fluent and CFX), computational meshes, CFD approaches, turbulence models (RANS, URANS, LES and DES) and numerical schemes to find the most suitable numerical set-up for the simulation of the undercarriage flow. The applied CFD approaches captured the main characteristics of the undercarriage flow but they all failed to correctly predict the highly turbulent separated flow at the end of the bogies. The most appropriate numerical set-up for this flow region proved to be the DES approach. However, the choice of turbulence model and numerical schemes affected the accuracy of the DES dramatically, highlighting the necessity for further study.

Another challenge for numerical simulations and of importance for the assessment of ballast flight is the influence and simulation of the trackbed ground roughness. This was also studied within the AOA-project by Garcia et al. [60] with the purpose to find by numerical simulation the equivalent roughness of different ballast trackbed designs with monoblock sleepers. The equivalent roughness was numerically calculated with the help of 2-D RANS simulations for a moving upper wall and a lower wall with three sleepers. The ballast particles in the inter-sleeper regions were simulated by defining a surface roughness. At the inlet and outlet of the computational domain, periodic boundary conditions were applied to realise a fully developed Couette-flow. The spatial averaged velocity profile in the streamwise direction was used together with the law of the wall to calculate the equivalent roughness for trackbeds with different sleeper spacing and dimensions (height and width). The results indicated that the calculated equivalent roughness depended on the turbulence models used for the RANS simulations. Additionally, applying the calculated equivalent roughness for numerical simulations revealed that the choice of the near wall mesh resolution affected the result over the entire gap.

Despite the presented issues, the most appropriate numerical set-up for RANS simulations were used to simulate the undercarriage flow of full-scale high-speed trains at realistic speeds. A method referred to as the "marching technique" was applied in the RANS simulations of the flow around highly detailed geometries of the German high-speed train ICE3 [39, 40] and the Italian ETR 500 [61] in the AOA-project. Masson et al. [62] also applied this method to the French high-speed train TGV (Train à Grande

Vitesse) and in the Master thesis of Jönsson [63] for the ICE3. With the marching technique, the entire train length is divided into overlapping sub-domains with a length of a train car. The sub-domain cut is in the middle of the train car due to the simple train geometry but also to avoid a cut in the more complex flow around the bogie regions. The flow field just before the outlet of preceding sub-domain is used as an inlet for the subsequent sub-domain to calculate the entire length of the high-speed train. The results of the numerical simulations on the different high-speed trains were compared to full-scale measurements confirming the problem with the correct prediction of the undercarriage flow. Nevertheless, the numerical simulations by Jönsson [63] confirmed the conclusions of the downscaled experiments [54, 57], that the reduced drag of a smoother undercarriage also decreased the flow speeds of the undercarriage flow and thus reduced the risk of ballast flight. The relevance of smoothing of the underframe was also stated by Masson et al. [62] since 41% of the total drag of a TGV was contributed to the bogies themselves. It was also estimated that the drag of the bogies could be reduced by 20% by installing deflectors, bogie skirts, undercarriage fairings over the bogies and the realisation of non-protruding bogies. Moreover, the high velocities and shear forces associated with the protruding bogie dampers, found just outside the track for the ICE3 [63], indicate the potential of bogie skirts for reducing both the drag and the risk of ballast flight. Finally yet importantly, the CFD simulations in the AOA-project for the ICE3 proved that the undercarriage ventilation airflows towards the trackbed should be considered, since they had a significant influence on the aerodynamic forces on the trackbed [39, 40].

With increasing computational power, the potential of numerical simulations increases as well. This will allow for highly detailed simulations of high-speed trains, perhaps of entire train sets, using transient methods requiring high computational power, like LES and DES. Significant work and research must however be done to find the best practice approach for the numerical set-ups necessary in order to reliably predict the undercarriage flow.

Ballast flight experiments:

In order to realistically assess the risk of ballast flight incidents, the most crucial parameters for the entire problem must be identified. The best way to avoid ballast flight incidents is however of course to prevent ballast particle dislodgement. This is also reflected by the majority of the conducted works that have focused on identifying the crucial parameters of the initiation of ballast particle movement. A simple

approach was applied by Kwon and Park [29], who gathered ballast particles from a trackbed, put them on the wind tunnel floor and slowly increased the wind velocity to observe ballast particle movement. The gathered ballast particles were divided into three groups based on their shape. 16% were characterised as flat, 44% as hemispherical and 40% as spherical. The masses of the gathered ballast particles were found to be between 17 g and 200 g, with most being between 50 g and 120 g. The wind tunnel tests revealed that spherical ballast particles weighing below 50 g were the most susceptible to movement at a wind tunnel speed of 20 m/s. Additionally, for more realistic simulations of the ballast particle movement, a trackbed with simplified monoblock sleepers and a flushed ballast level was installed in the wind tunnel with ballast particles positioned on the top of a sleeper. The ballast particles on top of a sleeper initiated movement at 20 m/s, analogously to those directly on the wind tunnel floor. However, the first movement of ballast particles between the sleepers began at greater wind tunnel speeds of 33 m/s.

In the AOA-project two experimental studies were conducted with a focus on the ballast particle initiation, including wind tunnel measurements with a full-scale trackbed and monoblock sleepers [64] and wind tunnel experiments using different trackbed designs of scale 1:10 [65]. In [64], a full-scale trackbed with rails was installed at an elevated position (avoiding the ground boundary layer) above the wind tunnel floor, with a wall installed over the trackbed to simulate a simplified undercarriage of a high-speed train. Wind gusts were simulated with a shutter and the train-induced vibration of the sleeper by a vibrating pot in a dummy sleeper. Video recordings of the ballast particles positioned on top of the sleeper indicated that ballast particle displacement and take-off increased with increasing air speed. Furthermore, the sleeper vibration increased the rate of initiated ballast particles due to the vertical accelerations giving the ballast particles an initial velocity for the take-off or lowering the ballast particle weight, i.e. lowering the friction force keeping the ballast particles from sliding on the sleeper. The second experimental study within the AOA-project [65] investigated whether the ballast particle initiation was comparable to the geophysical erosion processes also known as wind erosion or aeolian processes. Three different ballast trackbed configurations, a trackbed with monoblock sleepers with lowered (4 cm below the upper surface of the sleeper in full-scale) and flushed (at the same level as the sleeper, 0 cm) ballast levels and a trackbed with bi-block sleepers (no cross-going sleeper), were exposed to different wind velocities and the number of dislodged ballast particles were counted. The ballast particles were dislodged from the

trackbed for friction velocities of about twice the value of the classical threshold value found by the empirical work of Bagnold [30] and Kind [66]. The large deviation was related to the uncertainties in the measurements of the friction velocity as well as to the pre-measurement treatment of the trackbed. The trackbed was placed on a shaker to simulate the settlement of the ballast due to train-induced vibration. The trackbed configuration had an immense influence on the ballast particle dislodgement rate, with the highest rate for the bi-block sleeper trackbed. For the ballast trackbed with monoblock sleepers and a lowered ballast level, no ballast particles were dislodged from the trackbed, demonstrating the beneficial effect the protruding sleepers have in shielding the ballast from incoming air flow.

Wind tunnel experiments on the ballast particle initiation were also conducted by Sanz-Andrés and Navarro-Medina [67] with a hemispherical ballast particle on a wind tunnel floor exposed to wind gusts at different frequencies. The wind tunnel tests were undertaken to validate the theoretical model they developed to predict ballast particle initiation from the rotation around the downstream edge of a particle. The main outcome of the work is presented in the next section, since its focus was on the development of the theoretical model.

If a ballast particle is set into motion and gains sufficient momentum during its advection over the trackbed to initiate flight, the continuation of the ballast flight problem depends on the physical properties of the ballast particle impact back with the trackbed. Dependent on the flight path, the ballast particle may return with an increased momentum after the impact with the train or from the undercarriage flow itself. To determine the necessary physical properties of the ballast particle impact with the trackbed, experiments [68] and numerical simulations [69] of a single ballast particle impact with the trackbed were undertaken in the AOA-project. Similar studies were done by Felsing [45], Shinojima [44] and Kawashima [70] but for the ballast particle dynamics after the impact of falling ice blocks. In the AOA-project, a ballast gun or catapult was built to accelerate single ballast particles into a box filled with ballast. The impacts were recorded by a high-speed camera and the images were evaluated to extract the velocity and the height of the impacting ballast particle and the newly ejected ballast particles following the impact. The mass, velocity and impact angle of the accelerated ballast particles were varied in the study. The ballast gun experiments revealed that the number of ejected stones from the trackbed was primarily dependent on the kinetic energy (mass and velocity) and the impact angle of the primary ballast particle. Generally, larger values of the kinetic energy and

impacting angles increased the number of ejected ballast particles from the trackbed. However, impact velocities exceeding 150 km/h and angles steeper than 40° degrees lead to total destruction of the primary stone. Furthermore, the local friction coefficient and the restitution coefficient of the ballast particles were determined to be 0.7 and 0.4, respectively.

Ballast flight simulations and calculations:

Besides experimental work, numerical simulations and theoretical calculations have also been conducted to determine and study the crucial parameters of the ballast flight problem.

The ballast particle initiating motion through rotation around its rear-facing edge was studied by Sanz-Andrés and Navarro-Medina [67, 71]. They presented a nonlinear mathematical model for the rotation dynamics of a body around its rear-facing supporting point under in a time-dependent flow (i.e. wind gusts). The nonlinear problem required solving by numerical integration. However, a linear approximation was presented to extract helpful information about the conditions initiating the rotating motion turning over the body. The linear approximation allowed the definition of gust duration necessary to the rotation of the body. The gust duration range consisted of two limits, one for long- and one for short-duration gusts. The limit for the short duration gusts was fixed whereas the limit of the long duration gust was dependent on the amplitude of the gust. Gust durations longer than the upper limit could be treated assuming a quasi-steady flow, whereas short gust durations (i.e. below the lower limit) were filtered away by the inertia of the body. In [67], the two gust limits were calculated for a hemispherical body and validated in wind tunnel experiments with satisfactory agreement. The theoretical and experimental results revealed that a flow with gusts lowered the critical overall mean air velocity needed to initiate the rotating motion of a hemispheric body in comparison to the value for a steady flow. A similar theoretical approach for the ballast particle initiation, also assuming ballast particle rotation, was presented by Sorribes et al. [48]. The input data for the aerodynamic forces applied for the theoretical model were obtained from full-scale pressure tap measurements on a two-dimensional reference body (a semi-cylindrical and a rectangular body) installed between two sleepers. The obtained pressure distribution on the test body was used to calculate the angular impulses on the test body from the undercarriage flow of a passing train. Considering the principle of the conservation of mechanical energy, the critical angular impulse needed to change the angle

of attack for the reference body from 0° (at rest) to 45° could be determined. At 45° , the moment of the body's own weight becomes zero, which was the crucial condition for the rolling of the test body. The method proved to be effective for evaluating the susceptibility to ballast flight for different high-speed trains.

In the work of Quinn et al. [32], supplementary theoretical calculations were conducted in addition to the full-scale measurements in order to evaluate the relevant parameters causing ballast pitting. Potential ballast flight paths were modelled with the debris flight equations [72, 73]. Spherical particles of different diameters represented ballast particles exposed to a mean flow field defined from full-scale measurements of an undercarriage flow. The calculations presented two possible scenarios for a successful flight over the rail. The first was without an in-flight lift and a large initial vertical velocity of the ballast particle ($W_B = 1\text{-}3\text{ m/s}$, $D = 10\text{-}30\text{ mm}$) and the second one had a small initial vertical velocity of $W_B = 0.02\text{ m/s}$ (from the trackbed vibration) together with a large in-flight lift ($W = 14\text{ m/s}$, $D = 10\text{ mm}$). However, the flight path calculations did not take the pressure difference caused by the train, the vertical component of the air velocity, or the highly turbulent nature of the undercarriage flow into account. These flow quantities are considered to contribute to a successful flight above the rail.

The ballast gun experiments within the AOA-project were conducted together with numerical simulations of the ballast particle impact with the trackbed [69]. Discrete element simulations were performed to study the impact process of single ballast particle with a 3-D trackbed using digitised model particles and the local friction and restitution coefficients found in the ballast gun experiments. The velocities (100-350 km/h), impacting angles ($10\text{-}80^\circ$) and impact locations of the primary ballast particle were varied in the simulations of the impact. The numerical simulations were in reasonable agreement with the ballast gun experiments, confirming that the number of ejected ballast particles from the trackbed was primarily influenced by the kinetic energy and the impacting angle of the incoming ballast particle. A linear relation between the initial kinetic energy and the number of ejected ballast particles was found. The slope of the linear fit was however dependent on the impacting angle. The restitution coefficient was found for each calculated impact angle and divided into a normal and a tangential restitution coefficient.

The theoretical work thus far has focused on a single ballast particle to establish whether the aerodynamic forces are sufficient to turn over ballast particles and to evaluate the possible ballast flight paths and the effects of ballast particle impact with

the trackbed. The first numerical simulations coupling the ballast particle dynamics in the trackbed and the undercarriage flow interaction were conducted by Saussine et al. [49, 50]. The 3-D numerical simulations were conducted on a portion of a ballast trackbed with bi-block sleepers and rails with rigid irregular polyhedral particles as ballast. Digitalisation of realistic railway ballast was used to define the size and shape of the discrete ballast used in the simulations. The friction coefficient and the restitution coefficient of the ballast were set to 1 and 0.4, respectively. The undercarriage flow field was extracted from full-scale measurements with five vertical rakes of four Pitot-probes per rake (in total 20 Pitot-probes) installed at different lateral positions. The aerodynamic force on the trackbed was applied as a body force (like gravity) using a 3-D matrix with velocity vectors interpolated from the results of the full-scale measurements. To simulate the undercarriage flow of a passing train, the 3-D matrix with velocity vectors was displaced with the train speed. The forces on and the dynamics of the ballast particles were solved by a non-smooth contact dynamics approach [50]. The discrete numerical approach was validated using the previously presented ballast flight experiments on a full-scale trackbed in a wind tunnel [64], with good agreement for the ballast particle motion. With the help of the full-scale measurements and the results from the numerical simulations, a relevant parameter was identified that described the relation between ballast particle motion and the flow field characteristics. The relevant parameter was the sum of the signal power ($V_{air}(t)^2$) of all Pitot-probes installed in the trackbed. The sum of the signal power of the air velocity in the travelling direction of the train had a linear relation to the percentage of ballast particles with a displacement larger than 10 cm. Additionally, a relation between the number of ejected ballast particles in relation to the fraction of displaced ballast particles was found and was considered to be around 2%.

Assessment of ballast flight:

It has long been of great interest to the railway community to be able to assess the risk of ballast flight. Besides guaranteeing the safety for passengers and trackside workers, its assessment would also aid estimation of the necessary cost and intervals for maintenance work to the rolling stock due to ballast particle impacts and to the infrastructure due to ballast pitting [74]. It would also be useful for train manufacturers to guarantee the promised performance of new high-speed trains or the performance of existing high-speed trains for new regions with other trackbed designs, as well as quality standards, without risking the severe consequences of ballast

flight incidents. Since the first ballast flight incidents, different theoretical models and approaches have been developed to assess the risk of ballast flight. All known or published methods applied the results from full-scale measurements to define the aerodynamic forces on the trackbed.

One of the first published methods to estimate the probability of ballast flight was presented by Kwon and Park [29], based on their full-scale measurements and wind tunnel experiments on the ballast particle initiation. Two critical air velocity limits were found in the wind tunnel for the gathered ballast particles. The lower limit was determined from the movement of the first ballast particle (V_{min}) and the upper limit from the initiated motion of all ballast particles (V_{max}). The wind tunnel results were used together with full-scale measurements of the mean air velocity value in the train travelling direction for the fully developed undercarriage flow (V_{track}) to calculate the qualitative probability of ballast flight according to Equation (1).

$$BFPF = \int_{m_{B1}}^{m_{B2}} \left[\frac{V_{track} - V_{min}}{V_{max} - V_{min}} \right] \frac{dm_B}{m_{B2} - m_{B1}} \quad (1)$$

$$i) V_{track} < V_{min}, BFPF = 0 \quad ii) V_{track} > V_{max}, BFPF = 1$$

The Ballast Flying Probability Factor (BFPF) reflected that small ballast particles ($m_B = 0-50$ g) were the most susceptible to ballast flight.

The information obtained from the full-scale measurements, CFD-calculations, experiments and numerical simulations of the undercarriage flow and the ballast flight physics in the AOA-project were incorporated in a global model [41, 75] for the simulation of ballast flight. The developed global model was the first model to include all sub-processes of the ballast flight problem and was used to analyse the dependencies and importance of the different sub-processes. The global model included various definitions of the ballast particle initiation, the modelling of the ballast particle motion over the trackbed including secondary stone initiation, ballast particle absorption and drop out as well as the ballast particle impact with the train and the re-impact with the trackbed. Simplifications of the detailed work and calculations of the different sub-processes as well as assumptions of unavailable information were however necessary to set up the global model. Nevertheless, the global model provided an improved knowledge of the underlying mechanisms of the ballast flight problem, although it was far from being complete, since it was based on assumptions

requiring validation. After the AOA-project, work on the development of practical and simple yet but still appropriate tools for the assessment of ballast flight has continued. Different approaches and considerations were presented in the published work of Schroeder-Bodenstein [33], Saussine et al. [49, 50] and Lazaro et al. [31]. Schroeder-Bodenstein presented equations for the ballast particle transport over the trackbed (momentum equation in the train travelling direction) and addressed some of the challenges for the assessment of the risk of ballast flight based on full-scale observations of high-speed trains. An interesting full-scale observation greatly relevant to the assessment of ballast flight were the increased rates of ballast particle impacts for new or remodelled ballast tracks. The reason for the higher ballast particle impact rates was the existence of small and susceptible ballast particles in unstable and/or unfavourable positions. Schroeder-Bodenstein [33] therefore recommended that the ballast size distribution should be modelled as a Gaussian distribution to represent the case for new or remodelled tracks. The smaller and susceptible ballast particles should be removed from the size distribution as they are blown away with each train passage, captured in undercarriage cavities or settled in stable positions. This would account for the effect observed for new or remodelled tracks. Nevertheless, the predictions of the presented transport equations indicated a higher rate of ballast flight than actually found for the full-scale observations. The ballast particle motion over the trackbed was modelled by applying only the transport equations without a ballast particle initiation threshold. All ballast particles were thus considered to be initiated when the train passed. The exaggerated ballast flight impact rate clearly highlights the importance of considering ballast particle initiation.

In the AeroTRAIN project three different assessment quantities or risk parameters of various complexity regarding the risk of ballast flight were proposed [53]. The proposed models were developed based on the AeroTRAIN project, the AOA-project, the individual work of train manufactures and operators and published work. The first proposed assessment quantity was based on the previously presented work of Saussine et al. [49, 50] (see ballast flight simulations and calculations). The risk or probability of ballast flight was determined using the method referred to as Stress-Strength Interference Analysis (SSIA). This method is based on the calculation of the probabilistic interaction between two independent probability density functions (PDFs) also known as the failure probability between the two PDFs. The aerodynamic forces (i.e. the stress distribution) were obtained by calculating the sum of the power signal from full-scale air velocity measurements ($V_{air}(t)^2$) over a number of train pas-

sages. The trackbed resistance or capacity to limit ballast particle motion (trackbed strength) was defined by determining the allowed fraction of displaced [50] or the maximum number of ejected ballast particles [49]. With the defined trackbed threshold, the strength distribution in the global signal power values could be extracted from the results of the numerical simulations, coupling the ballast particle motion to the aerodynamic forces. Thereafter, the ballast flight probability was calculated from the two independent PDFs (stress and strength) representing the aerodynamic force and the trackbed strength using the SSIA method. The second assessment quantity proposed in the AeroTRAIN project was a simple particle motion approach for a virtual ballast particle, developed from observations during the full-scale measurements in the Aurigidas project [31] and the simulation results of the global model developed in the AOA-project [75]. The particle motion or dislodgement from the trackbed was delayed by the initiation thresholds derived with the assumption of a successful rotation of a ballast particle exposed to an unsteady or gusty flow. After the particle motion was initiated through rotation the transport phase over the trackbed began where the particle gained speed from the undercarriage flow. The particle speed was determined by numerical integration of a simple momentum equation in the travelling direction of the train, which balanced the aerodynamic forces with the particle inertia and those from the repetitive contacts with the trackbed. The integrated kinetic energy of the particle along the train length averaged over the different particle classes was used as the indicating parameter for the risk of ballast flight. Last but not least, was the more complex and stochastic particle method developed by Prof. Benigno Lazaro at the Polytechnic University of Madrid together with ADIF within the Aurigidas project. This method incorporated the first three sub-processes shown in Figure 1, the initiation of ballast particle motion, the ballast particle transport over the trackbed and finally the ballast particle flight, deriving the number of impacts with the rolling stock. The trackbed ballast size distribution (e.g. Gaussian distribution) was divided into (N) different size classes. The average number of ballast particle impacts for all ballast particle size classes as well as the average number of impacts weighted with the kinetic energy of the impacting ballast particle were used as risk parameters for the assessment of ballast flight. The following simplified physical thresholds defined the ballast particle motion over the trackbed. The initiation of motion of the ballast particle occurred as the aerodynamic force overcame the gravitationally driven equilibrium (gravity and friction forces) for a minimum time interval. The ballast particle motion over the trackbed was described by the integration of the momentum equa-

tion in the train travel direction. The aerodynamic force was modelled under the assumption that the ballast particle velocity was much smaller than the air velocity of the undercarriage flow and did not account for the ballast particle inertia. The influence or resistance of the trackbed was however realised with a momentum loss term representing the ballast particle and trackbed contacts. The ballast particle flight phase was first initiated when the ballast particle surpassed the momentum threshold and maintained this value for a minimum longitudinal distance needed to realise an upward deflection initiating ballast particle flight. The total flight phase of the ballast particle was described as a sequence of consecutive parabolic flight trajectories, observed during full-scale measurements [31]. These were all time dependent and solved by temporal integration with momentum losses at every trackbed contact. The number of impacts with the rolling stock was calculated by evaluating each consecutive parabolic flight trajectory.

1.4 Motivation and objectives

The main research aim of this thesis is to study in detail the characteristics of the undercarriage flow and the effect of the train undercarriage and trackbed roughnesses in order to be able to reduce or prevent ballast flight incidents. In the following the motivation and the objectives for the methods of this thesis, including high-speed particle image velocimetry (PIV) of the undercarriage flow in a water-towing tank for downscaled train models and corresponding simplified momentum calculations of the ballast flight problem are discussed.

The discussion of the previous work revealed that full-scale measurements have been the most common way for obtaining undercarriage flow data for the risk assessment of ballast flight. Water-towing tank experiments with scale train models are motivated by the following points:

- Arranging full-scale measurements is difficult and not always possible within given time frames due to the extensive organisational effort, lack of a suitable measurement locations (e.g. tunnels, bridges, curves, track accessibility etc.) or regulations.
 - Water-towing tank experiments make it possible to control boundary conditions and obtain data throughout the entire undercarriage flow.
 - Numerical simulations (CFD) have not been successful in modelling trackbed
-

roughness or correctly predicting the undercarriage flow.

- According to Papenfuss and Kronast [76], a moving-model facility is more effective than a wind tunnel with a moving belt with respect to measuring the undercarriage flow along an entire train.
- A 4-unit train configuration (1:50) is possible assuring that the fully developed undercarriage flow necessary to the study to ballast flight may be realised [29, 31, 32, 36].

The aim of this thesis is the velocity measurements, since the main contribution of the train-induced aerodynamic forces on the trackbed is the one from the velocity component in the travelling direction of the train [32, 47]. The motivation for applying high-speed PIV in water-towing tank experiments relates to the following points:

- The much higher spatial resolution of the measured flow field in comparison to more classical techniques with rakes of pressure probes or hot-wire anemometers.
- The temporal and spatial resolution of the entire undercarriage flow field between the trackbed and the train undercarriage, including the velocity gradients at the ground and the train undercarriage. The undercarriage flow field closest to the trackbed is of particular interest since it is responsible for the flow-induced loads on the ballast and is crucial for the risk assessment of ballast flight. Understanding the entire ballast flight problem, the flight phase should be considered, requiring the entire undercarriage flow field between the trackbed and the train undercarriage to be measured.
- PIV is a convenient, non-intrusive optical technique that may be installed outside the water-towing tank, resulting in no flow disturbances like from a rake or the placement of pressure probes or hot-wire anemometers.

The objectives and scope of the high-speed PIV study of the undercarriage flow in a water-towing tank using 1:50 scale train models and ground configurations with different roughness are presented below.

- To establish whether it is possible to capture the realistic undercarriage flow along the entire train length in the water-towing tank by applying the PIV technique.
 - To assess the advantages and disadvantages of applying the PIV technique in a
-

water-towing tank facility for the study of high-speed train undercarriage aerodynamics.

- To use different train models to establish the local and overall influence of bogies, bogie housings, cavities and inter-car gaps on undercarriage flows. The thesis however places emphasis on the study of velocity magnitudes, velocity gradients, instantaneous flow effects and turbulence close to the trackbed.
- A train model with a completely smooth undercarriage shall be used to reflect the undercarriage flow of the aerodynamically perfect high-speed train to set the limit for the lowest achievable values of the train-induced aerodynamic forces on the trackbed.
- The different ground configurations shall reveal if the ground roughness of the most common trackbed designs influences the entire undercarriage flow, or only the flow near the trackbed.
- The ground configurations shall also unveil in detail why the trackbed design without cross-going sleepers is more susceptible to ballast flight incidents than a trackbed design with cross-going sleepers and a lowered ballast level [41].
- The train configurations shall be measured on the different ground conditions in order to examine any interference effects on the undercarriage flow between the train undercarriage and the ground roughness. The results shall indicate if it is possible to treat the rolling stock and the trackbed properties separately or if the interference effects must be considered.

The undercarriage flow field data for the considered train models and trackbed designs shall be used together with simplified physical approaches to simulate the ballast particle initiation, transport over the trackbed and flight of a virtual ballast particle. The objectives of the simplified ballast flight simulations are

- to realistically and accurately identify the most susceptible train model or undercarriage detail, trackbed design and train-trackbed combination regarding the risk of ballast flight incidents.
 - to verify if ballast particles on top of sleepers are the worst-case scenario for ballast flight incidents.
 - to evaluate the influence of important parameters regarding ballast flight, such as trackbed vibration, ballast particle size, train length, head pressure pulse and trackbed restitution coefficient.
-

- to evaluate the most likely ballast particle initiation scenario (slide, direct take-off or roll-over), dependent on the trackbed position.
 - to provide the critical train speed for ballast pitting and ballast flight impact for the considered train and ground configurations.
-

2 Particle image velocimetry

2.1 The principles of particle image velocimetry

The principles of PIV are found in a wide range literature [77, 78, 79] and in detail in Raffel et al. [80]. The physics, equipment and apparatus, post-processing and advantages and disadvantages of PIV will be briefly explained in the following sections to give an overview of the measurement technique.

PIV is an optical, non-intrusive (besides added tracers in the flow) and indirect velocity measurement technique used in the area of fluid dynamics to obtain instantaneous velocity fields within fluid flows. The measurement technique uses a light source to illuminate tracer particles in the flow (seeding particles, droplets or bubbles) and subsequently takes two pictures of them in rapid succession in a plane of the flow. The recorded movement of the tracers within the small and defined time separation between the two illuminations is then used to calculate the velocity vectors of the flow field. A typical PIV set-up is shown in Figure 2 and consists of several sub-systems working together. The tracer particles are illuminated in a plane of the flow using a

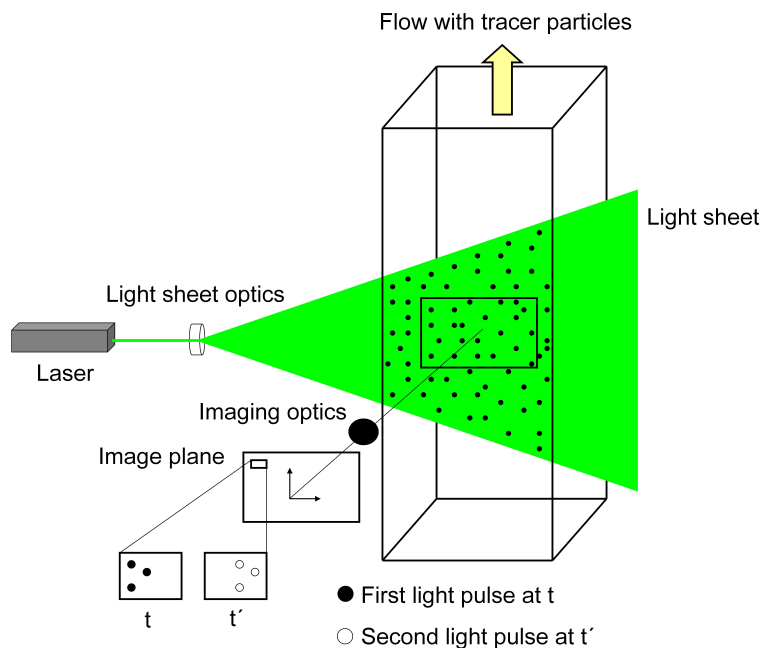


Figure 2: The principle of particle image velocimetry (PIV).

light sheet typically from a double-pulsed laser. The reason for using a double pulsed laser is the possibility to generate two laser pulses with a time delay in the range of

microseconds and a short pulse duration around 5-15 nanoseconds [78]. The velocity field is "frozen" and does not change over a matter of microseconds and the short pulses prevent blurred images for faster flow speeds. The laser light is focused into a thin light sheet using the optics so that only particles in the measurement field needed for the PIV technique are illuminated. The scattered light from the particles must be recorded and saved for both pulses within a very short time and this is achieved with modern digital cameras (CCD (charge-coupled device) or CMOS (complementary metal oxide semiconductor) cameras). The timing of the laser and the camera must be synchronised, which is done, by a computer using highly accurate electronics.

The standard or classical PIV set-up is the two-component PIV set-up (2C-PIV) with a planar illumination and the digital cameras installed perpendicular to the light sheet (measurement field). With the 2C-PIV set-up, only two (in-plane) components of the velocity vector can be determined. By adding an additional camera to the 2C-PIV set-up with a different viewing angle, the third velocity component can be reconstructed with the perspective distortion of the particle displacement of the two cameras [81] and is denoted as stereoscopic PIV or 3C-PIV. An expansion of the stereoscopic PIV is the dual-plane PIV [82] using two light sheets with a small offset and two pairs of cameras in a stereoscopic arrangement focused on one of the two light sheets and measuring simultaneously. The above described PIV techniques are all based on planar illumination of the flow field. However, more complex PIV techniques have also been developed, such as the holographic PIV [83] and the tomographic PIV [84] using the illumination of a complete volume of the flow for the fully three-dimensional determination of the velocity field. PIV techniques have also been developed for special applications such as Micro-PIV [85] for the analysis of microstructures, MEMS and biomedical flows and Endoscopic-PIV [86] for internal combustion engines, turbomachinery or pumps with minimal optical access.

2.2 Particle image velocimetry equipment and apparatus

Tracers:

Tracers or seeding particles added to the flow are an essential part of the PIV technique. The tracer particles must meet two requirements to be suitable as tracer, follow the flow without any excessive slip velocity and being efficient scatterers of the illuminating laser light. To follow the flow with an acceptable flow-particle response

time and without buoyancy effects, the particle density should be similar to the surrounding medium. A particle density equal to the medium is of course optimum and a response time smaller than the smallest time scales of the flow is critical. If the particle density does not match that of the medium, the particle size and thus inertia must be small enough for a low response time. The particles must also be smaller than the smallest structures in the flow so that they do not have an effect on the structure of the flow. Since the scattered light from the particles is a function of the ratio of the particle refractive index to the surrounding medium's, the particle size, shape and orientation (in addition to the polarization and observation angle) [80], larger particles are desirable to scatter a sufficient amount of light for the PIV images. This means that in most cases a compromise between tracer qualities (small particles) and light-scattering qualities (large particles) must be made when selecting suitable seeding particles. Applying Stokes drag under the assumption of low particle Reynolds number to determine the settling velocity of the particles, according to Equation (2), is a simple method to evaluate if the particles follow the flow. If the settling velocity is negligible to the flow velocities, the particles are suitable as tracers according to Prasad [87].

$$U_{tp} = \frac{g \cdot d_{tp}^2 \cdot (\rho_{tp} - \rho_f)}{18 \cdot \mu_f} \quad (2)$$

Other parameters influencing the choice of seeding particles are the cost, manufacturing difficulty or accessibility, environmental aspects, hazard to the users, cleaning effort and compatibility with the test facility. Typical seeding materials and particle sizes for liquid flows and gas flows can be found in the tables in [80]. The particle size of tracers are normally in the range of 0.1 to 1000 μm .

Generating and adding seeding particles to a flow is an additional challenge, especially for gaseous flows where mostly droplets but also solid particles are used as seeding particles. The seeding particles must be added to the flow shortly before the measurement and close to the measurement volume since the droplets tend to either evaporate quickly or settling away. For the case of solid particles, it is difficult to seed them so that they are not clumped together. A number of methods to generate and seed particles to flows have been developed using air jets, fluidized beds, condensation generators and atomizers. Some of these techniques are described by Melling [88]. PIV in wind tunnels often utilises atomizers with a Laskin nozzle generator and oil to produce seeding particles (for details see [89]). Adding seeding particles to liq-

uid flows is in most cases easier than for gaseous flows. The solid seeding particles have little density difference to the fluid and may be suspended in the fluid so that they may mix and become evenly distributed.

Light source and light sheet optics:

The PIV technique requires a light source with a high intensity to be able to scatter detectable light from the particles under a short duration of time to freeze the particles and avoid particle streaking (blurred images). The illuminating light must be suitable to the formation of a thin light sheet defining the particle positions. Lasers are appropriate light sources for the PIV technique with monochromatic and collimated light and a large coherence length that can easily be used to form a thin light sheet. Lasers are also able to produce a high-power light with short pulse duration. The typical modern PIV lasers are frequency doubled pulsed Nd:YAG lasers consisting of two separate co-axial lasers emitting light independently, allowing an optimal time separation of the two laser pulses. The time delay between the two pulses must be large enough to determine the displacement without losing track of the particles or allowing the velocity field to change. The only limitations of Nd:YAG lasers are that the double pulse repetition rate of 10-50 Hz restricts the usage of Nd:YAG lasers for time-resolved flow field measurements. However, the development of solid-state lasers during the last decade has improved the performance of diode-pumped Nd:YLF lasers that produce high-energy pulses at repetition rates up to 10 kHz. During the last years, high power light emitting diodes (LED) have been used as light sources for PIV, see Willert et al. [90] and Estevadeordal and Goss [91]. Using LEDs as light sources over conventional lasers has advantages, such as low cost, ease of handling due to their small size and weight, low energy consumption, availability in different wavelengths, adjustable pulse and repetition rate and suitability to forming light sheets with a slit diaphragm. However, some of the disadvantages should also be mentioned, namely the lower light intensity of LEDs, their broad wavelength spectrum and spatial radiation pattern.

The formation of two-dimensional thin laser light sheets with nearly constant thickness (at least for the measurement location) and high intensity using Nd:YAG and Nd:YLF lasers are achieved using combinations of spherical and cylindrical lenses. Three different combinations used for PIV measurements are presented by Raffel et al. [80]. In practice mirrors are often used to guide the laser beam to the light sheet optics or to direct the light sheet itself, increasing the accessibility of the PIV tech-

nique.

Recording device:

Originally, photography was used to capture the illuminated particles from the two exposures on the same frame. After digitalization of the photo, the velocity field could be evaluated by means of auto-correlation techniques. The fact that both exposures were captured on one frame made it impossible to separate the particles from the first exposure from those of the second and therefore the direction of the flow could not be determined. Today, the use of electronic imaging using digital cameras with CCD (charge-coupled device) or CMOS (complementary metal oxide semiconductor) sensors allow capturing the illuminated tracer particles from the two exposures on separate frames. This allows the determination of the velocity and the direction of the flow field using cross-correlation techniques. Additionally, electronic imaging is much more convenient than photography due to the instant availability of the images with the possibility to check the results in matter of seconds. Furthermore, the electronic control of the camera simplifies the synchronisation with the laser for large sequences of images. The higher light sensitivity of CCD- and CMOS-cameras enables the usage of less powerful light sources (mostly lasers) or the possibility of measurements with larger fields of view, though with a lower resolution than for the high-resolution photographic films. The classical approach of choosing PIV cameras with CCD- or CMOS-sensors is based on the priority of spatial or temporal resolution. CCD-cameras with large pixel arrays, small pixels and low signal-to-noise ratios are the most widely used PIV cameras for reasons of spatial resolution, whereas the faster CMOS-cameras are used for temporal resolution with a higher signal-to-noise ratios and larger pixels. The latest development in digital cameras for PIV, however, have realised CMOS-cameras with a significantly improved image quality and these are now considered the most suitable cameras for high-speed PIV. Detailed information about the physical and technical properties of CCD- and CMOS-cameras is found in [80] and a performance comparison is presented by Hain et al. [92].

Synchroniser:

Modern PIV systems all consist of digital sub-systems controlled by a computer with accurate electronics (PCI-card), also referred to as the synchronisation unit or sequencer. The sequencer coordinates the timing of the camera(s) with the firing of the laser(s) to realise the recording of the illuminated particles during the two, short and

consecutive pulses from the laser. Additionally, the digital PIV system controlled by the sequencer can also conveniently be synchronised with other measurement techniques e.g. force and pressure measurements or transient flow conditions.

2.3 Particle image velocimetry analysis

The general steps of the modern digital PIV evaluation of double image and single-exposure recordings obtained by a PIV set-up as the one presented in Figure 2 are discussed below. The PIV evaluation can generally be divided into the four steps, the image windowing, cross-correlation analysis, sub-pixel interpolation and data scaling.

1. Image windowing:

The obtained double image of the two exposures for one PIV-recording are both divided into smaller sub-windows also known as interrogation windows. The tracer particles in the individual interrogation windows of both exposures are used to calculate the mean tracer particle displacement for the local region. Thus, a local spatial averaged tracer particle displacement is calculated.

2. Cross-correlation analysis:

The mean tracer particle displacement between both exposures is statistically evaluated with the cross-correlation function for every individual interrogation window. The discrete cross-correlation function of both exposures is presented in Equation (3) [80]. I and I' are the light intensity distribution for the interrogation windows of the first laser pulse (t) and the second laser pulse ($t + \Delta t$), respectively.

$$R_{II}(X, Z) = \sum_{i=-K}^K \sum_{j=-L}^L [I(i, j)][I'(i + X, j + Z)] \quad (3)$$

The discrete cross-correlation plane can be calculated direct from Equation (3) by shifting the template I over the larger template I' pixel by pixel and calculating the sum of the products of all overlapping pixels for every shift. The sum of the products for the correct shift (the images of the tracer particles are best aligned) is greater than for all other values and thus yields the peak value in the cross-correlation plane. However, performing the necessary multiplications to find the cross-correlation peak for every interrogation window of the

entire image and for a series of PIV-recordings requires a large computational effort. Modern PIV evaluation methods use the correlation theorem i.e. the cross-correlation of two functions is equivalent to the complex conjugate multiplication of their Fourier transforms (FT). In practice, the well-known fast Fourier transform (FFT) is however implemented to further reduce the required computation time [80]. The general process of modern PIV evaluation uses FFT to transform the interrogation window of both exposures from real to complex, multiplies complex conjugates for the interrogation windows and performs the inverse FFT transform from complex back to real results, yielding a discrete cross-correlation plane with a correlation peak. The correlation peak position relative to the cross-correlation plane origin describes the mean pixel displacement of the tracer particles within the interrogation window.

3. Interpolation of the correlation peak:

The pixel position of the correlation peak relative to the origin found in the discrete cross-correlation plane has only pixel integer accuracy. The more accurate position (sub-pixel accuracy) of the correlation peak is estimated using various approaches. Commonly, the correlation peak is fitted to a function, e.g. a Gaussian peak fit.

4. Data scaling:

The local mean pixel displacement evaluated for every interrogation window is divided by the defined pulse delay between the two exposures and the magnification factor from the PIV camera calibration to extract the velocity value.

Different advanced digital interrogation techniques are used to increase the accuracy of digital PIV evaluation. Two regularly implemented techniques are the window-shifting and window-deformation schemes used in multiple-pass interrogation processes, also applied for the PIV data evaluation in this thesis. The multi-pass interrogation process is an iterative procedure using the mean pixel displacement of the previous interrogation pass to apply a new window-offset. The interrogation passes are performed until the adjusted window-offset converges. According to Raffel et al. [80], three passes are required. The window-shifting technique improves the signal-to-noise ratio by increasing the fraction of tracer particle pairs between both exposures. Furthermore, for small displacements below half a pixel, the window-shifting improves the accuracy of the velocity estimation by simplifying the detection of the tracer particle displacement. However, for flows with large velocity gradients the

window-shifting, which is linear, does not provide satisfactory coverage of the tracer particle pairs. The introduction of window-deformation schemes of second order reveals a more robust and accurate technique in comparison to window-shifting for boundary layers, shear flows, vortices and for turbulent flows in general. Nonetheless, multi-pass interrogation applied together with an interrogation-window size refinement with window-shifting or window deformation allows for the usage of smaller window sizes, improving the spatial resolution of the calculated velocity vectors.

2.4 Advantages and disadvantages of particle image velocimetry

Every measurement technique has advantages and disadvantages and should therefore be carefully chosen considering the measurement requirements or aims, the effort of applying the technique and any necessary cost or investment. The pros and cons of applying particle image velocimetry are discussed below.

Advantages:

The optical and non-intrusive PIV technique is applicable to measuring velocities without disturbing the flow, e.g. in high-speed flows with shocks, boundary layers close to walls or in micro-fluidics. This contrasts more classical measurement techniques using mountings to hold pressure probes or hot-wire anemometers. Additionally, PIV is able to simultaneously measure the velocity at various positions with two in-plane velocity components (2C-PIV) or all three velocity components (3C-PIV), for an entire velocity field at one instant in time. This significant feature is not possible with single-point measurement techniques like pressure probes or hot-wire anemometers, nor for other optical measurement technique such as the laser-doppler-anemometry (LDA). The classical PIV set-up with CCD-cameras and an Nd:YAG laser offered high spatial resolution, but a lower temporal resolution in contrast to the above mentioned classical measurement techniques. However, the development during the last decade of CMOS-cameras and diode-pumped lasers (Nd:YLF) has evolved PIV into a time-resolved measurement technique with a high spatial resolution able to generate large sets of data within short periods of time. The spatial and temporal resolution of the data acquired from PIV are the most adequate data for the validation of numerical calculations. Furthermore, the indirect velocity measurement can be beneficial for two-phase flows with a dispersed-phase of larger particles by

measuring the velocities of the larger particles, but also of the flow around them from added smaller tracer particles.

Disadvantages:

The optical access required for the camera(s) and the laser(s) but also the fluid (gas or liquid), which need to be transparent, is crucial for the PIV technique and is the most common limiting parameter. The indirect measurement technique using tracer particles to measure the flow velocity requires tracer particles that follows the flow with negligible velocity lag and buoyancy (small particles) and at the same time scatter enough light to be detected by the PIV camera (large particles). This entails a compromise between the particle flow tracking and scattering properties. Moreover, it is also a challenge to obtain a homogeneous tracer particle distribution for the flow region of interest without disturbing the flow. The particle distribution has a direct influence on the spatial resolution due to the minimum number of tracer particles per interrogation-window statistically required for PIV evaluation of the velocity vectors. The calculated velocity field from PIV is the spatial averaged representation of the actual flow. This highlights the importance of the spatial resolution to reflect velocity gradients and vortices in an accurate way. The goal of maintaining a high spatial resolution, i.e. small interrogation-window, in combination with a dynamic velocity range (e.g. instantaneous flow effects), can result in the loss of tracer particle pairs (in-plane loss) and more noise in the discrete cross-correlation plane. The loss of particle-pairs is also a problem for PIV in flow fields with strong cross-flows (i.e. out-of-plane loss). The practical handling of a PIV set-up, guiding the laser beam (typically re-directed by mirrors before the light sheet optics) to and through the light sheet optics and illuminating the measurement plane is more complicated, frail and dangerous than the use of, e.g., pressure probes. Nonetheless, PIV systems are relatively expensive.

3 Measurement facility

3.1 Water-towing tank

The presented measurements of the undercarriage flow using the PIV technique were all conducted in the water-towing tank located at DLR in Göttingen and shown in Figure 3. General information about and properties of a water-towing tank facility can be found in the work of Gad-el-Hak [93]. The water-towing tank at DLR in Göttingen is an 18 m long open surface steel tank with a cross-section of 1.1 m x 1.1 m (W x H). Windows are installed on both sidewalls and at the bottom of the tank, facilitating optical measurement techniques and flow visualisations. The moving-model rig is hauled through the tank with the help of a steel cable and an electric motor (7 kW) guided on two rails installed on top of the sidewalls. The moving-model rig speed can be varied to any desired value between 0 and 4 m/s. For the presented PIV experiments, a rig speed of 4 m/s was used, corresponding to Reynolds number of $2.5 \cdot 10^5$ based on the rig speed, the reference length of 0.06 m (the usual reference length for train aerodynamics is 3 m in full-scale [94]) and the kinematic viscosity of water. Additionally, measurements with lower rig speeds ($U_{RIG} = 1, 2$ and 3 m/s) were undertaken for the reference train model on the smooth ground to investigate the Reynolds number dependency of the undercarriage flow. The 1:50 train model

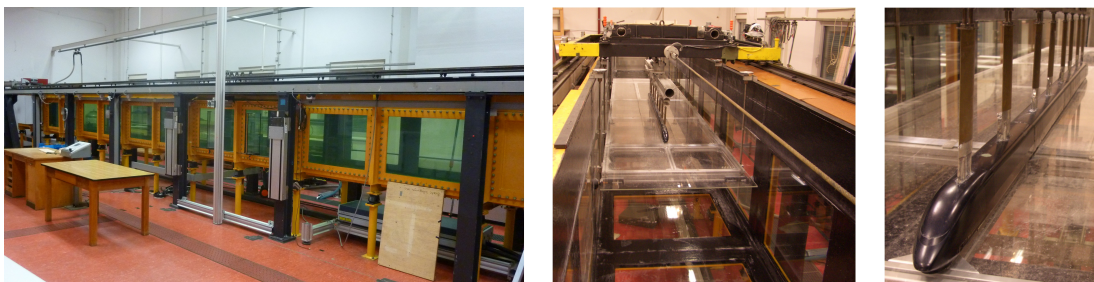


Figure 3: The water-towing tank at DLR in Göttingen (left), the moving-model rig with train model and ground plate (middle) and a close-up view of the train model (right).

was mounted on the moving-model rig with the help of two NACA 0030 profiles per car. The NACA profiles were mounted on the roof of the train to minimise any influence on the undercarriage flow, as shown in the photo to the right in Figure 3. In total eight NACA profiles for the entire train set, which guide the train model through the water. For the realistic simulation of the movement of the ground relative to the train (fixed ground and moving train), a ground plate was installed in the tank.

The 4.6 m x 0.9 m (L x W) ground plate consisted of three plexiglass plates mounted on an aluminium frame held by eight threaded rods. The threaded rods allow to adjust the ground clearance to any desired value. For the presented measurements, a ground clearance of 9.88 mm corresponding to 0.494 m in full-scale was used, which according to the TSI [94] is the ground clearance used for wind tunnel cross-wind measurements without trackbed simulation.

The moving-model rig velocity and acceleration over a run in the water-towing tank are plotted in Figure 4. The PIV set-up was positioned close to the end of the ground plate (second dotted line in Figure 4) in order to achieve a stable undercarriage flow without disturbances from the leading edge of the ground plate. It was also desirable to measure the undercarriage flow for a constant train model velocity. Within the measurement field of the PIV, a train model speed repeatability of $\pm 2\%$ was achieved.

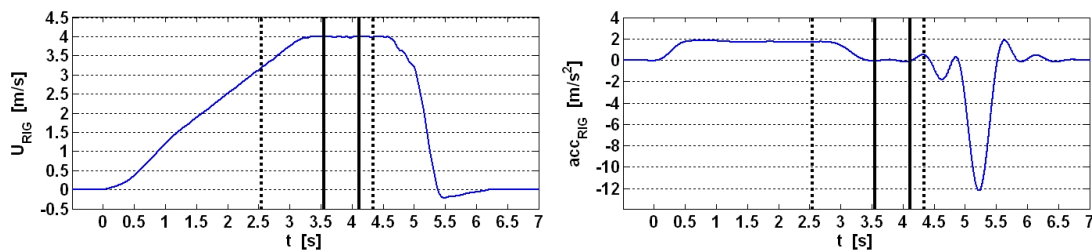


Figure 4: The moving-model rig speed (left) and acceleration during a single run in the water-towing tank. Vertical lines indicate where the train model reaches and leaves the ground plate (dotted vertical lines) and the field of view or measurement field of the PIV cameras (solid vertical lines).

3.2 Particle image velocimetry set-up in the water-towing tank

The two-component PIV set-up used in the water-towing tank and sketched in Figure 5, was arranged in such a way that the vertical plane XZ, with X in the trackbed line of symmetry and Z stretching vertically from the ground to the train undercarriage, could be measured. The XZ-plane in the trackbed line of symmetry was chosen to capture the dominant velocity component of the undercarriage flow, the velocity component (u) in the travelling direction of the train. Furthermore, full-scale air velocity measurements for different lateral positions (Y direction) disclosed that the largest mean U velocity values exist along the trackbed line of symmetry [29, 32, 47]. This

plane was also favourable since both rails were removed to provide the necessary optical access for PIV and the influence of the removed rails is least consequential for the flow field in this plane. The laser, laser light sheet optics, mirror and PIV cameras were all installed outside of the tank, as sketched in Figure 5. The laser, light

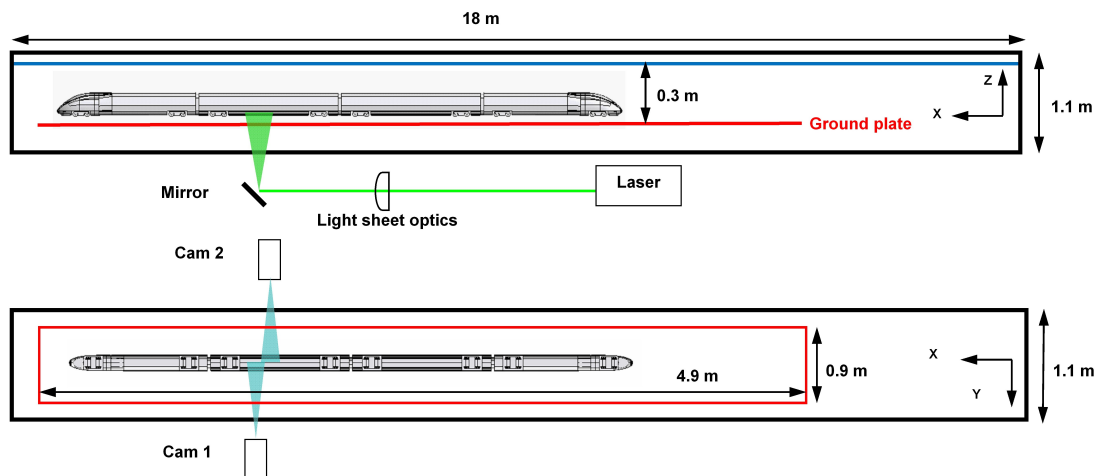


Figure 5: The 2C-PIV set-up in the water-towing tank.

sheet optics and the mirror were placed underneath the tank, where the laser beam was guided through a set of optics to form the light sheet (-150 mm spherical lens, +300 mm spherical lens and +80 mm cylindrical lens). The mirror redirected the laser light sheet through the bottom glass window and the ground plate (plexiglass plate) before illuminating the $20\ \mu\text{m}$ polymer particles (added to the water) in the vertical (XZ) measurement plane. The laser light sheet was about 0.4 m wide in the X direction for the measurement region with a thickness of 2 mm (Y direction) in the centre (X direction) of the light sheet. Two PIV cameras were positioned at both sides of the water-towing tank, as sketched in Figure 5. The physical size of the PIV cameras was too large for them to be placed on the same side of the tank and at the same time create an overlap between the two field of views of both PIV cameras.

For the undercarriage flow measurements two different types of PIV (hardware) systems were used, one with a 10 Hz acquisition rate and a high-speed PIV system with acquisition rates between 0.1 to 10 kHz. The measurements with the 10 Hz PIV system were conducted as a precursor to the comprehensive high-speed PIV test campaign. The 10 Hz PIV system was used to test and evaluate whether the PIV technique was suitable for undercarriage flow measurements in the water-towing tank. Thereafter, different train configurations and ground conditions were tested and the experience

were used for adjustments prior to the comprehensive high-speed PIV test campaign. The results using the 10 Hz PIV system were published in [95] and the high-speed PIV results are presented in this thesis as well as in [96].

For the 10 Hz PIV system, two PCO 1600 cooled digital 14-bit CCD cameras with 1600 x 1200 pixel resolution and a frame rate of 30 frames per second were used. The field of view of both cameras together was 0.065 m x 0.025 m (W x H). The acquisition rate limitation was the doubled pulsed Nd:YAG 150 mJ laser from Lumonics, which had maximum double pulse rate of 10 Hz. The combination of an acquisition rate of 10 Hz, the small field of view and the train model speed of 4 m/s did not allow for the recording of the entire flow field beneath the train for every run. The challenges of recording the entire flow field underneath the train and of gathering more data for increased statistics were solved by the high-speed PIV system. The high-energy, 60 mJ diode pumped Nd:YLF laser from Quantronix was able to generate double laser pulses in the frequency range of 0.1 to 10 kHz. The double laser pulses were recorded by two PCO dimax 12-bit high-speed CMOS cameras with resolutions of 2016 x 2016 pixels and a full frame rate of 1279 frames per second. The field of view of both cameras together spanned an area of 0.082 m x 0.033 m (WxH).

4 Measured configurations

4.1 High-speed train model

The 1:50 scale train model shown in Figure 6 was the reference train model used for the water-towing tank measurements. The reference train model represents a conventional non-articulated high-speed train with inter-car gaps and two bogies per car. For the model-scale experiments in the water-towing tank, the maximum possible length of a 1:50 model was used. This allowed a four-unit train set consisting of two end-cars and two mid-cars with a total model length of 2.14 m. The geometry for the reference



Figure 6: The 1:50 high-speed train model.

train model is a combination of the German high-speed train ICE3 and the geometry of an ICE2. The head and the tail of the train model reflects an ICE3. Shortly after the first bogie, the cross-section smoothly changes to that of an ICE2 mid-car. This transition is depicted by the left image of Figure 7. The two mid-cars have the cross-section

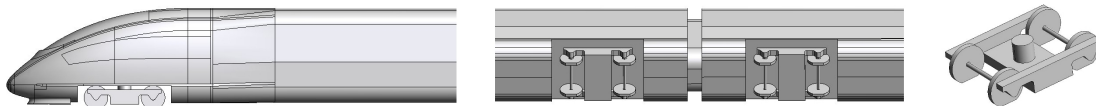


Figure 7: The 1:50 high-speed train model: Head of the train model (left), the inter-car region (middle) and the simplified bogie (right).

of an ICE2. The most obvious difference between the two cross-sections relates to the roof radius, whereas a difference is difficult to detect for the undercarriage. It is therefore concluded that the change in the undercarriage cross-section is irrelevant when considering the undercarriage flow. It is difficult for downscaled models to resolve all details of the full-scale trains, since simplifications in their geometry must be introduced for their manufacturing. These simplifications are most obvious for the bogies, since the full-scale bogie geometry is complex and full of details, such as gearboxes, electrical motors, brakes, dampers etc. for motorised bogies, which cannot be realised for the downscaled models. The simplified bogie used for the downscaled train model is shown in Figure 7. The bogie wheels did not rotate for the presented measurements. The influence of rotating wheels on the undercarriage flow is however

confined to a small region around the wheel [97], it can therefore be neglected for the flow field analysis in the trackbed symmetry plane. Further details and dimensions of the used reference train model are found in Appendix A.

4.2 High-speed train model configurations

The three different train configurations employed in this study are presented in Figure 8. The undercarriage for the reference train model (T.C. 1 in Figure 8) was modified to realise the two additional train configurations. For the train configuration denoted

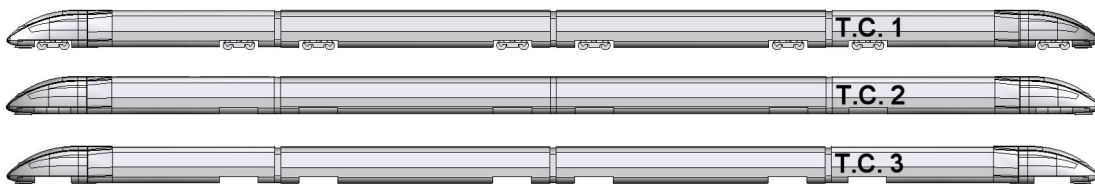


Figure 8: The three considered train configurations: The reference train model (upper, T.C. 1), the smooth train model (middle, T.C. 2) and the rough train model (lower, T.C. 3).

as the rough train model (T.C. 3 in Figure 8), the bogies were removed from the reference train model and the bogie housings were left open. Moreover, all bogies were removed and the bogie housings and inter-car gaps were covered to achieve a completely smooth underbelly. This is therefore referred to as the smooth train model (T.C. 2 in Figure 8). The smooth train model should represent the aerodynamically perfect high-speed train with the lowest possible velocities in the undercarriage flow. The motivation for the rough train model stemmed from the results obtained for the reference train model. The comparison of the reference train model to full-scale measurements indicated lower undercarriage U velocity values for the measurements in the water-towing tank. The lower undercarriage flow velocities were partially attributed to the simplified bogies, which are smoother than the complex bogies of a full-scale train, as shown in Figure 9. The smooth and ground-parallel lower surface of the simplified bogies was deemed as aerodynamically beneficial in comparison to full-scale bogies featuring a significant roughness. The effect of the greater permeability of realistic bogies was simulated in an extreme but simple way by removing the bogies completely and leaving the bogie housing open to generate an extreme rough undercarriage.

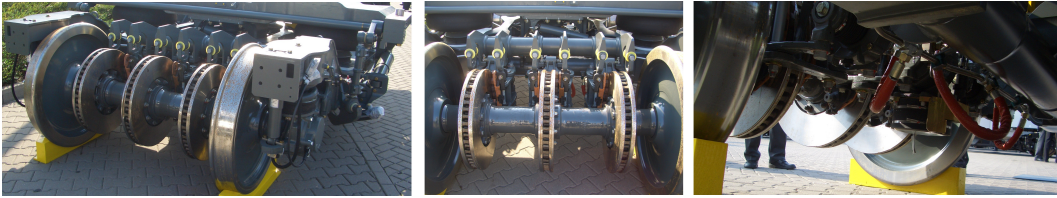


Figure 9: The trailer bogie for the Siemens high-speed train Velaro CRH3.

4.3 Ground configurations

The three considered train configurations were all measured on a smooth ground, a rough ground and a ground with sleepers, each shown in Figure 10. The smooth

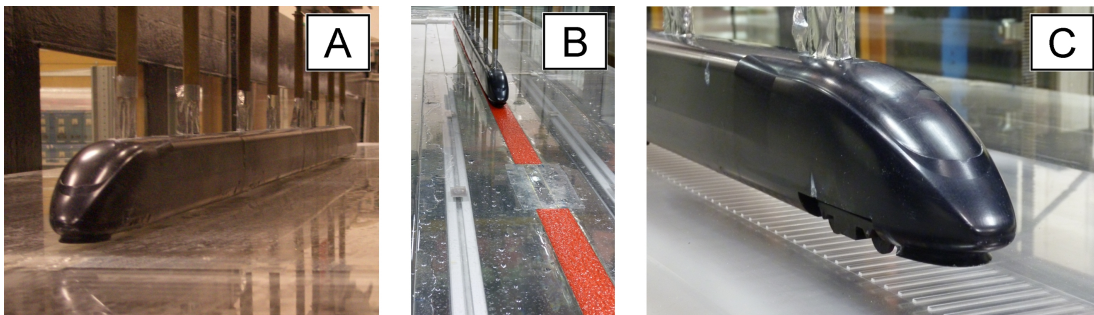


Figure 10: The three considered ground configurations: Smooth ground (G.C. A), rough ground (G.C. B) and ground with protruding sleepers (G.C. C).

ground was realised with the ground plate itself (a smooth plexiglass plate). For the rough ground configuration, two additional plexiglass plates of 1000 mm x 400 mm (L x W) were mounted on the ground plate and a grinding belt was glued on top of them. The grinding belt was chosen such that its grain size corresponded to 1:50 ballast particle. The ballast for European trackbeds are defined according to the EN-13450 [98], where sieves with a mesh width between 22.4 mm and 63 mm defines the size range of the ballast. This technique realises a ballast particle size distribution mainly between 31.5 mm and 50 mm, or 31.6 mm and 63 mm in full-scale. The selected water- and oil-proof grinding belt had a grain size of less than 0.764 mm (38.2 mm in full-scale). For the necessary optical accessibility of the laser light sheet, a small part (200 mm) of the grinding belt was removed (see the middle image in Figure 10). For the ground configuration with sleepers, the upper surface of two additional plexiglass plates (also two 1000 mm x 400 mm) were milled down to create the protruding sleepers as indicated in the right image of Figure 10. The sleeper geometry

corresponds to a simplified B70 concrete sleeper from ThyssenKrupp, with a width of 3 mm (X direction or direction of travel) and a length of 52 mm (across rail direction). The height of the sleeper was assigned to 1 mm, corresponding to a trackbed with a lowered ballast level of 5 cm below the upper surface of the sleeper in full-scale. The sleeper spacing was set to 12 mm, or 0.6 m in full-scale, according to Knothe and Stichel [99].

4.4 Overview of the measured configurations

Table 1 presents an overview of each measured configuration, including the applied PIV acquisition rate, the number of PIV cameras, the moving-model rig speed, the conducted number of runs and the Reynolds number. The test conditions have a

T.C.	G.C.	Rig speed	PIV cameras	PIV freq.	Runs	Re
1	A	1 m/s	2	125 Hz	10	$0.625 \cdot 10^5$
1	A	2 m/s	2	250 Hz	15	$1.25 \cdot 10^5$
1	A	3 m/s	2	500 Hz	15	$1.875 \cdot 10^5$
1, 2, 3	A	4 m/s	2	500 Hz	30	$2.5 \cdot 10^5$
1, 2, 3	B	4 m/s	1	1000 Hz	80	$2.5 \cdot 10^5$
1, 2, 3	C	4 m/s	2	750 Hz	30	$2.5 \cdot 10^5$

Table 1: Overview of the test conditions for the measured configurations in the water-towing tank.

lower Reynolds number than full-scale high-speed trains under realistic conditions ($Re \sim 1.2 \cdot 10^7$), as is common for most scale model experiments. Scale model measurements are therefore often executed at the highest achievable Reynolds number of the test facility. Consistent with this, most runs in this work were conducted at the maximum possible moving-model rig speed of $U_{TRAIN} = 4$ m/s. Nevertheless, measurements were also conducted for lower Reynolds number ($U_{TRAIN} = 1, 2$ and 3 m/s) for the reference train model on the smooth ground in order to evaluate the Reynolds numbers dependency of the undercarriage flow.

The PIV acquisition rate was set to 500 Hz for the train configurations on the smooth ground, enabling the two PIV cameras ($\Delta X = 0.082$ m) to capture 10 samples of the instantaneous flow field for each train position and each run with a train model speed of 4 m/s. These 10 samples per run together with the 30 conducted runs of the smooth ground condition (sample size of ~ 300) were estimated to be sufficient for the reliable calculation of statistical quantities. Furthermore, considering the full-scale data

treatment by Deeg et al. [47] and the recommendations from the AeroTRAIN consortium [53], using a 75 Hz low-pass filter and still reflecting the important flow features regarding ballast flight, implies that the PIV sampling frequencies of 500 Hz should be sufficient according to the Nyquist-Shannon sampling theorem. The runs for the lower Reynolds numbers were conducted only after the other measurements, since the primary interest was in the effect on the undercarriage flow at the larger Reynolds numbers and not lower. A reduced number of runs were therefore measured with a reduced PIV acquisition rate at the lower Reynolds numbers ($U_{TRAIN} = 1$ and 2 m/s) to avoid excessively large data sets.

The rough ground and the ground with sleepers introduced local ground effects generated by the rough-to-smooth ground transition and the protruding sleepers, respectively (shown in Figure 10). Accounting for the local ground effects as well as the train position reduced the effective measurement field. The equidistant spacing of identical sleepers justified the usage of two PIV cameras to measure the passing train over seven sleepers and six inter-sleeper regions. An acquisition rate of 750 Hz was used to compensate for the data loss, given the relative position of the train and the sleepers. The rough-to-smooth ground roughness transition for the rough ground reduced the measurement field of interest to the small region closest to the transition. This motivated the usage of only one PIV camera. The PIV acquisition rate as well as the number of conducted runs were increased to guarantee a sample size sufficient for the reliable calculation of statistically quantities for the undercarriage flow field.

5 Post-processing of the particle image velocimetry data

5.1 Evaluation of the particle image velocimetry raw data

The PIV double image recordings obtained from the model-scale experiments in the water-towing tank were evaluated with the commercial software PIVview from PIVtec. PIVview applies the general steps of modern digital PIV evaluation as presented in section 2.3 with image windowing, cross-correlation analysis, sub-pixel interpolation of the cross-correlation peak and data scaling to extract velocity vectors from tracer particle displacements.

The PIV data were evaluated using a multi-grid interrogation (grid refinement) algorithm starting off with an larger interrogation window size of 64×64 pixels which is refined with each image interrogation pass to a final window size of 24×24 pixels, assuring a minimum of 5 tracer particles per interrogation window. For every image interrogation pass, two cross-correlation planes were calculated with a small spatial separation using a phase-only cross-correlation approach with Nyquist filtering. The two cross-correlation planes were then multiplied to enhance the signal-to-noise ratio of the newly calculated cross-correlation plane. The random noise is cancelled out due to the small spatial separation between the two calculated cross-correlation planes [100]. The correlation peak found in the cross-correlation plane was fitted using the Whittaker reconstruction scheme to estimate the maximum value of the peak, using all horizontal and vertical values in the cross-correlation plane that intersect the correlation peak position. The determined position of the correlation peak, i.e. the local average particle displacement, was checked for validity (for every displacement vector after every interrogation pass) using two outlier detection thresholds. Displacement vectors were considered to be outliers if the displacement magnitude was larger than 12 pixels (average displacement in the core of the undercarriage flow was around 3-4 pixels) and if the difference to the adjacent vectors was larger than 5 pixels for more than four of the eight neighbouring vectors. The displacement vectors labelled as outliers were replaced using the following scheme [100]: (i) using lower order peaks (the three strongest peaks were saved for every cross-correlation plane), (ii) using bi-linear interpolation with the valid and adjacent vectors or with a Gaussian-weighted interpolation if the adjacent vectors were also outliers and (iii) by re-evaluation with a larger interrogation window size. Additionally, for the final

image interrogation pass, a second order sub-pixel image shifting was applied using the displacement from the previous image interrogation pass together with a cubic b-spline interpolation scheme to apply a window deformation. This technique increases the fraction of tracer particle pairs and enhances the signal-to-noise ratio.

The final interrogation window size of 24×24 pixels corresponds to 0.541×0.541 mm. The windows have a 75% overlap, resolving the flow with velocity vectors every $\Delta X = \Delta Z = 0.135$ mm.

5.2 Particle image velocimetry error estimation

The total error estimation of the PIV in the water-towing tank is a challenging task, since it is influenced by a variety of parameters concerning the entire chain from the experimental set-up to the digital PIV image evaluation. Nevertheless, the most influential parameters for the PIV set-up may be controlled, minimised, or determined by following PIV best practice guidelines. The important parameters include the choice of tracer particles, the choice of PIV cameras, the properties of the light sheet, the calibration, the optical aberrations and the acceleration error between the two illuminations.

Not every source of uncertainty was considered for the error estimation of the PIV measurements. The used tracer particles are considered to be suitable according to Prasad [87], since the settling velocity of the tracer particles, defined in Equation (2), is negligible when compared to the flow velocity ($U_{tp} = 0.0000505$ m/s). The tracer particles were therefore assumed to follow the flow perfectly. Furthermore, the noise from the PIV cameras and the acceleration error introduced between the two illuminations were not considered and the laser light sheet was assumed to coincide more or less perfectly with the trackbed line of symmetry (perfectly perpendicular to the PIV cameras). The common uncertainty sources of PIV, such as the magnification error, perspective view error and the error introduced by the determination of the particle displacement using the cross-correlation technique were considered for the PIV error estimation in the water-towing tank. The magnification error results from the thickness of the laser light sheet. The tracer particles are illuminated and recorded in a plane not aligned with the calibration plane. The maximum magnification error is found for the combination of an illuminated tracer particle, e.g. tracer particle 2 in Figure 11 as the calibration grid was position in the XZ-plane of tracer particle 1 in Figure 11. The relative magnification difference between tracer particles 1 and 2 in

Figure 11 directly relates to the velocity error. The magnification error is proportional to the ratio of the laser light sheet thickness and the distance from the PIV camera objective to the laser light sheet ($\Delta Y_0 / Y_0$), according to Adrian and Westerweel [101]. With a laser light sheet thickness of $\Delta Y_0 = 2$ mm and a distance of $Y_0 = 0.62$ m between the PIV camera objective plane to the laser light sheet plane (position 1 in Figure 11), the maximum velocity error caused by the magnification error was calculated to be less than 0.32 %. The error due to the positioning of the calibration perpendicular to the camera and extracting the magnification factor from the PIV evaluation software using best practice guidelines is about 0.04 % according to Harris [102]. Another un-

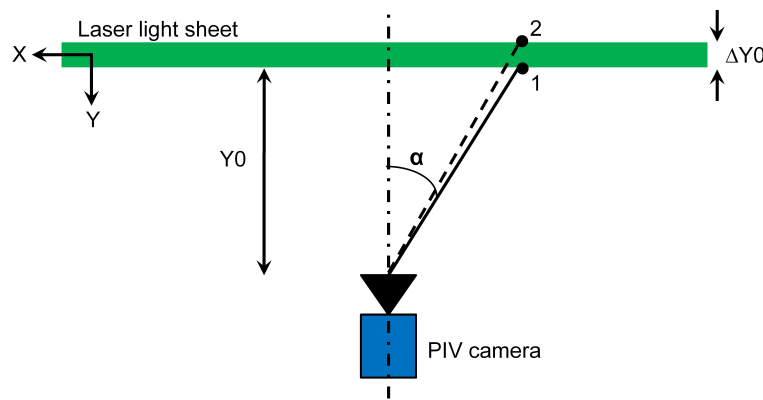


Figure 11: Magnification and perspective error due to the laser light sheet thickness.

certainty source also due to the laser light sheet thickness and the viewing angle of the PIV camera(s) is referred to as the perspective view error. The out-of-plane displacement (Y direction) of the tracer particle (tracer particle displacement between position 1 and 2 in Figure 11) appears as an in-plane displacement for the PIV camera under larger viewing angles. This generates artificially incorrect tracer particle displacements (i.e. velocity vectors). This error is significant for large viewing angles and/or tracer particle displacement normal to the laser light sheet, e.g. measuring the cross-flow components in the flow field with a main flow normal to the measurement field. Due to the small viewing angle in the water-towing tank and the expectation of only small cross-flows on the trackbed line of symmetry, the perspective error could be neglected.

The post-processing of the digital PIV images, i.e. the determination of the tracer particle displacement mostly by applying statistical cross-correlation methods has associated sources of uncertainty. According to Raffel et al. [80] a popular technique for evaluating the uncertainties of the digital PIV evaluation is to apply numerical simu-

lations (Monte Carlo simulations) to artificial particle image recordings with known properties, e.g. tracer particle displacements. In [80], key parameters like the tracer particle image diameter, interrogation window size, tracer particle image displacement, tracer particle density, image quantization and background noise were evaluated. The outcome of the Monte Carlo simulations in [80] demonstrated that the tracer particle image diameter and the tracer particle density strongly influenced the measurement uncertainty. Moreover, the measurement uncertainty was more or less independent of the tracer particle displacement (> 0.5 pixel tracer particle displacement), the background noise ($< 10\%$ of the image dynamic range) and the quantization level (> 6 bit/pixel). The evaluated PIV post-processing uncertainty (ϵ_{rms}) in [80], similar to the evaluation of the water-towing tank PIV images with regard to the tracer particle image diameter (2-3 pixels) and tracer particle density (assuring 5 tracer particles per interrogation window), revealed a measurement uncertainty of $\epsilon_{rms} = 0.035$ pixels. Similar measurement uncertainty was presented by Westerweel et al. [103] based on analytical results and Monte Carlo simulations using a tracer particle image diameter of 2 pixel, but with 10 tracer particles per interrogation window. Additionally, the measurement uncertainty based on the Monte Carlo simulations, as well as the analytical results, was confirmed by PIV measurements in a grid-generated turbulent flow in a closed-loop water channel. Furthermore, Westerweel et al. [103] demonstrated that applying discrete window-shifting to the digital cross-correlation of the PIV images of the turbulent flow in the water channel (as applied for the water-towing tank PIV data), increased the signal-to-noise ratio and thus decreased the measurement uncertainty. The presented noise reduction [103] using discrete window-shifting for the typical turbulence levels found in the undercarriage flow of the water-towing tank suggested that the measurement uncertainty from the Monte Carlo simulations [80] would decrease from $\epsilon_{rms} = 0.035$ pixel to 0.02 pixel. The presented PIV post-processing method by Nobach et al. [104] improved the measurement uncertainty to $\epsilon_{rms} = 0.01$ pixel by applying an iterative, multi-step method with a sub-pixel window-shift and a polynomial interpolation for the cross-correlation peak of the simulated PIV images with photon noise (similar to the water-towing tank PIV data evaluation). Considering the measurement uncertainties of the digital PIV post-processing by Westerweel et al. [103] and Nobach et al. [104], it is reasonable to assume a post-processing uncertainty of $\epsilon_{rms} = 0.01$ -0.02 pixel for the water-towing tank PIV data. Assuming a normal distribution of the random error, the maximum measurement uncertainty with a confidence interval of 95 % is $2 \cdot \epsilon_{rms}$. The

time delay between the two laser pulses was varied for the different train and ground configurations to achieve a tracer particle displacement of about 3-5 pixels over the major part of the undercarriage gap ($Z / H_{GAP} = 0.1-0.9$) for the fully developed undercarriage flow. The tracer particle displacements for the fully developed undercarriage flow were thereby evaluated to within an accuracy of 1.33 %. The development of the undercarriage flow along the first half of the train set as well as in the flow field close to the ground is however associated with lower measurement accuracy due to the smaller tracer particle displacements. Typical tracer particle displacements of 1-2 pixels were found close to the ground, with a corresponding accuracy of 4 %. Moreover, the ground plate and the trackbed in the PIV images were covered by a mask excluding the region from the PIV post-processing. The interrogation windows closest to the ground, covering both the flow field and the disabled masked ground, were however still evaluated if the valid flow field fraction exceeded 50 % of the window. For the borderline interrogation windows, the masked (disabled) pixels of the ground were replaced with the background image of the valid flow field in order to avoid window size discontinuities. The probability of observing the suggested minimum number of tracer particles (i.e. 5) within an interrogation window, as well as the reliability of the resulting velocity vector, decreases for the interrogation windows closest to the ground due to the smaller effective window size. This applies for the velocity field below $Z / H_{GAP} = 0.03$. The vertical profiles of the U velocity presented later revealed a linear U velocity increase starting at the ground ($U = 0$) and ending for the more reliable interrogation windows (i.e. $Z / H_{GAP} > 0.03$). Since the region had a linear increase in U and no discontinuity in the gradient was found, the results are considered to be reliable. Another issue is the spatial averaging that results from using interrogation windows for the calculation of velocity vectors. This especially affects flow regions with large velocity gradients. However, this problem is generally avoided with the use of small interrogation windows together with a grid refinement algorithm for applying window-deformation (see Raffel et al. [80]).

Summarising the sources of uncertainty, which in this case were the considered magnification error ($\epsilon_{max} = 0.0032$) and the error associated with the digital evaluation of the PIV images ($\epsilon_{max} = 0.04$), the velocity vectors in the water-towing tank by means of PIV were determined to within an uncertainty below 4 % ($\sqrt{(0.0032)^2 + (0.04)^2}$).

5.3 Velocity data post-processing

The instantaneous velocity fields obtained from the PIV evaluation were used to calculate statistical quantities of the flow field for the entire measurement plane (XZ contours) or for horizontal (X direction) and vertical (Z direction) profiles. The undercarriage flow is presented and described using the ensemble average of the velocity component in the travelling direction U and in the vertical direction W , calculated according to Equation (4) and the corresponding standard deviation and a 2-D turbulence intensity which are defined in Equations (5) and (6), respectively.

$$C(X_j, Z_k) = \frac{1}{N} \sum_{i=1}^N c_i(X_j, Z_k) \quad (4)$$

$$C_{SD}(X_j, Z_k) = \sqrt{\frac{1}{N-1} \sum_{i=1}^N (c_i(X_j, Z_k) - C(X_j, Z_k))^2} \quad (5)$$

$$TI(X_j, Z_k) = \frac{\sqrt{\frac{1}{2}(U_{SD}(X_j, Z_k)^2 + W_{SD}(X_j, Z_k)^2)}}{U_{TRAIN}} \quad (6)$$

The correct determination of the train position is important for the quality of the aforementioned statistical quantities and is crucial to resolving undercarriage flow effects. This is especially true for strong flow accelerations with large velocity gradients. Nevertheless, the sleepers and the rough-to-smooth ground roughness transition of the rough ground (shown in Figure 10) also influence the undercarriage flow. This highlights the need to account for the local effects of the ground topology as well as for the train position. The different approaches for processing the PIV velocity data for the three ground configurations considered are discussed below.

The train position for every PIV double image was initially estimated with the expected train shift ($\Delta X = U_{TRAIN} / f_s$). However, the inherent small deviations to the velocity (less than $\pm 2\%$) from the mechanical system of the moving-model rig motivated the usage of a more precise method for determining the train position. The undercarriage structures like the edges of the bogie housings or the reference lines painted on the train were used to enhance the accuracy of measuring the train position. The train position could therefore be determined with an accuracy of ± 0.3 mm (about 0.53% of the bogie length). Knowing the train image positions, the presented

statistical quantities could be calculated for the considered train configurations on all ground types. The differences in the evaluation of the velocity data were introduced by the different methods of extracting the data from the instantaneous undercarriage flow field while accounting for the previously mentioned local ground effects. For the smooth ground, the entire instantaneous flow field of both PIV cameras could be used to extract velocity data in the vertical and horizontal directions due to the uniform plexiglass plate simulating the smooth ground. This was not the case for the rough ground and the ground with sleepers, due to the local ground effects. Flow field data had to be extracted in the vertical direction (Z direction) for fixed ground positions (X positions), analogous to how vertical rakes of pressure probes have been installed in trackbeds to measure the flow beneath passing trains. Data for the rough ground were extracted for a small region ($\Delta X = 4$ mm) closest to the rough-to-smooth ground roughness transition shown in Figure 10. Advantage was taken of the identical sleepers with equidistant spacing for extracting undercarriage flow field data. Three positions on top of a sleeper (for the seven sleepers) and nine positions in the region between two sleepers (for the six inter-sleeper regions) were used to extract the data for the ground with sleepers. Additional runs and higher sampling rates were used as an attempt to compensate for the "loss" of data with a smaller effective measurement field (extracting data only at fixed X positions), so that a sample would remain large enough for the reliable calculation of statistical quantities. The sample sizes for every measured configuration are listed in Table 2. The extracted data were

T.C.	G.C.	Rig speed	PIV cameras	PIV freq.	Runs	N horiz.	N vertic.
1	A	1 m/s	2	125 Hz	10	110	110
1	A	2 m/s	2	250 Hz	15	165	165
1	A	3 m/s	2	500 Hz	15	200	200
1, 2, 3	A	4 m/s	2	500 Hz	30	>250	>250
1, 2, 3	B	4 m/s	1	1000 Hz	80	~120	~90
1, 2, 3	C	4 m/s	2	750 Hz	30	~200	~70

Table 2: Data sample sizes for the measured configurations in the water-towing tank.

then shifted to the corresponding train position and interpolated on a global grid for the subsequent calculation of the aforementioned statistical quantities for the entire flow field.

5.4 Definition of coordinate system and velocity components

The definition of the coordinate system and the velocity components are sketched in Figure 12 and are used to present the undercarriage flow velocity field and position. The horizontal origin of the coordinate system is defined at the nose of the train,

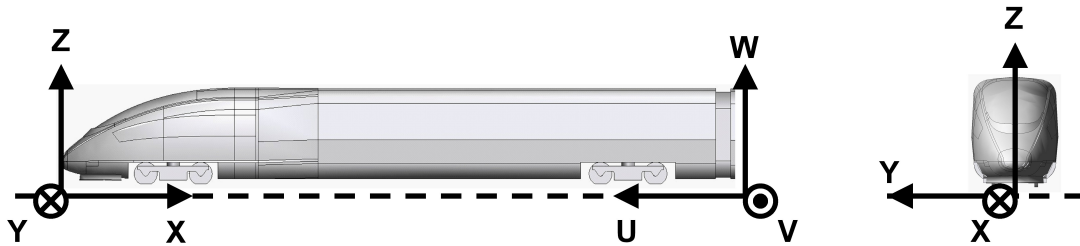


Figure 12: Definition of the coordinate system and velocity components.

with a positive X direction towards the end of the train. The lateral origin is in the trackbed line of symmetry, at the same position as the PIV laser light sheet, with the positive Y direction to the left when facing the train, as in the right sketch in Figure 12. The trackbed surface or ground serves as a vertical origin with a positive Z direction towards the undercarriage of the train. The presented velocity components in this thesis are the two measured u and w velocity in the vertical plane (XZ) between the trackbed and the train undercarriage along the trackbed line of symmetry. The horizontal velocity (u) is defined as positive in the travelling direction of the train and the vertical velocity component (w) points away from the trackbed.

6 Particle image velocimetry results

6.1 Undercarriage flow field in the water-towing tank

To provide better insight into undercarriage flow characteristics, a selection of PIV results obtained in the water-towing tank for the reference train model on the smooth ground condition are presented and discussed. In Figure 13 the normalised ($U_{TRAIN} = 4$ m/s) mean streamwise velocity U and vertical velocity W at the height of the top of the rail ($TOR = Z / H_{GAP} = 0.476$) for the reference train model on the smooth ground are plotted along the length of the train, as normalised by the train length ($L_{TRAIN} = 2.14$ m). The two horizontal velocity profiles clearly reveal that the dominant ve-

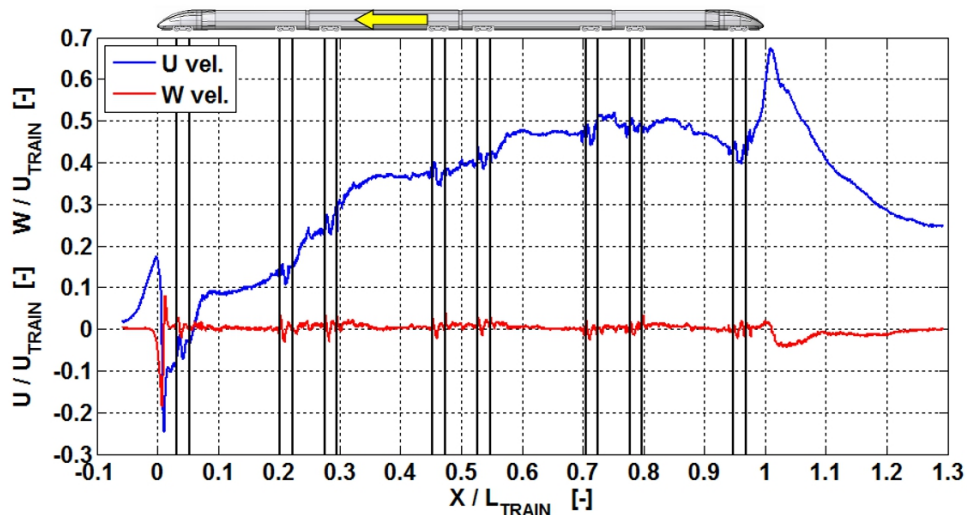


Figure 13: Normalised mean velocity component in the travelling direction U and in the vertical direction W along the normalised length for the reference train model (T.C. 1) on the smooth ground condition (G.C. A) at the height of the top of the rail ($TOR = Z / H_{GAP} = 0.476$). The vertical lines indicate the positions of the train axes. $U_{TRAIN} = 4$ m/s.

locity component in the undercarriage flow is the one in the travelling direction (U) of the train. Since the undercarriage along a high-speed train is more or less a flat and parallel surface to the ground, indicates that there is no direct reason for the flow to be deflected in the vertical direction. The measurements W indicates that the undercarriage flow is only deflected in the vertical direction close to geometric obstacles or irregularities of the undercarriage, such as the head and the tail, the bogie regions, the inter-car gaps or any other geometric obstacles. The results of the full-scale measurements conducted by Quinn et al. [32] and Deeg et al. [47] revealed that

the velocity component in the travelling direction U was clearly the dominant one in comparison to the lateral mean velocity component V . In the same manner as for the vertical velocity component, the flow only turns in the lateral direction where there are geometric obstacles or irregularities. This indicates that the main contribution to the aerodynamic forces on the trackbed during a train passage result from the velocity component in the train travelling direction (U), thus the most interesting component regarding ballast flight. For U in Figure 13, four characteristic flow regions were identified. These are the flow around the head, the Couette-like undercarriage flow (presented in detail in Figure 14), the near-wake flow following the tail and the far wake region further downstream. Considering that the accelerated flow around the head induces aerodynamic forces strong enough to dislodge ballast particles from the trackbed. It is however most likely that the dislodged ballast particles come to rest again due the sudden drop of the mean U velocity found shortly after the train head at $X / L_{TRAIN} = 0$ in Figure 13. Nevertheless, the dislodged ballast particles from the accelerated flow around the head can be transported into unfavourable positions for the subsequent and stronger undercarriage flow. The strongest accelerations for the undercarriage flow, together with the maximum values for U , are found shortly after the tail of the train, in the near-wake region. The dislodged ballast particles in the near-wake flow or the ballast particles already set into motion cannot further damage the train, although they may still damage trackside objects or injure trackside workers and passengers on rail platforms. The near-wake flow can also move ballast particles into exposed or critical positions for the next train's passage, like on top of sleepers. This concludes that the most interesting region regarding ballast flight is the Couette-like undercarriage flow. For more detailed information about Couette flow, the reader is referred to Schlichting [56].

The vertical U -velocity profiles extracted from the centre of each train car in Figure 14, reveal the development of the Couette-like undercarriage flow for the reference train model on the smooth ground. The normalised mean U velocity is plotted as the abscissa and the vertical height normalised by the ground clearance (H_{GAP}) between the ground ($Z / H_{GAP} = 0$) and the undercarriage of the train ($Z / H_{GAP} = 1$) as the ordinate. The four velocity profiles show that U increases towards the end of the train as momentum is increasingly transferred to the flow. The development of the boundary layers starts at the beginning of the leading end-car on the undercarriage of the train. As the train's boundary layer develops and grows, water closer to the ground is set into motion, eventually forming a boundary layer on the ground. The

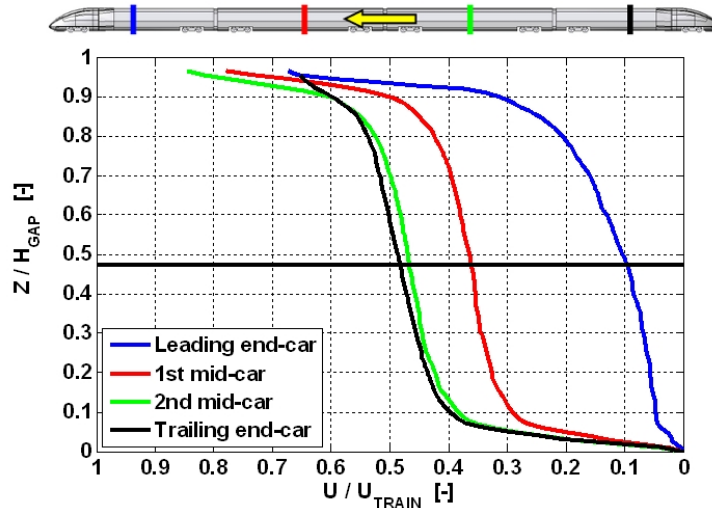


Figure 14: Normalised vertical profiles of the mean velocity component in the travelling direction U over the undercarriage gap (ground and the train undercarriage) for the reference train model (T.C. 1) on the smooth ground (G.C. A). The horizontal line indicates the height of the top of the rail (TOR = $Z / H_{GAP} = 0.476$). $U_{TRAIN} = 4$ m/s.

boundary layers on the train and on the ground develop over the first half of the train length to a nearly fully developed Couette-like flow that persists for the second half of the train length, ending at the tail of the train in the near-wake region. The two velocity profiles for the second half of the train length in the almost fully developed Couette-like flow have a similar shape to those measured by Ido et al. [36] on a down-scaled train model in a wind tunnel with a moving belt. Considering the low mean U velocity values close to the ground and the small vertical velocity gradient at the ground, both related to the aerodynamic forces expected to act on the ballast, little dislodgement of ballast particles for the leading end-car (blue line in Figure 14) is expected. For this reason, ballast flight incidents and damages appear where the flow is close to fully developed. This was also indicated by Sima et al. [46] and Gautier et al. [35]. This also concludes that the development of the undercarriage flow with the length of the train, i.e. the axial gradient of the U -velocity, is of importance regarding ballast flight. Since a steeper axial gradient of the U -velocity (faster undercarriage flow development) increases the risk of ballast flight.

Horizontal mean velocity profiles were extracted at different heights over the trackbed, listed in Table 3, for the reference train model on the smooth ground. These are presented in Figure 15 for U and in Figure 16 for W . The extracted horizontal mean velocity profiles in Figure 15 reflect the vertical gradient found for the vertical velocity distributions in Figure 14. Additionally, the local flow accelerations caused by

Height	Z / H_{GAP} [-]	Z [mm]
TORx0.125	0.059	0.5875
TORx0.25	0.119	1.175
TORx0.5	0.238	2.35
TORx0.75	0.356	3.525
TOR	0.476	4.7
TORx1.25	0.594	5.875
TORx1.5	0.713	7.05

Table 3: The different heights over the trackbed for the presented horizontal velocity profiles.

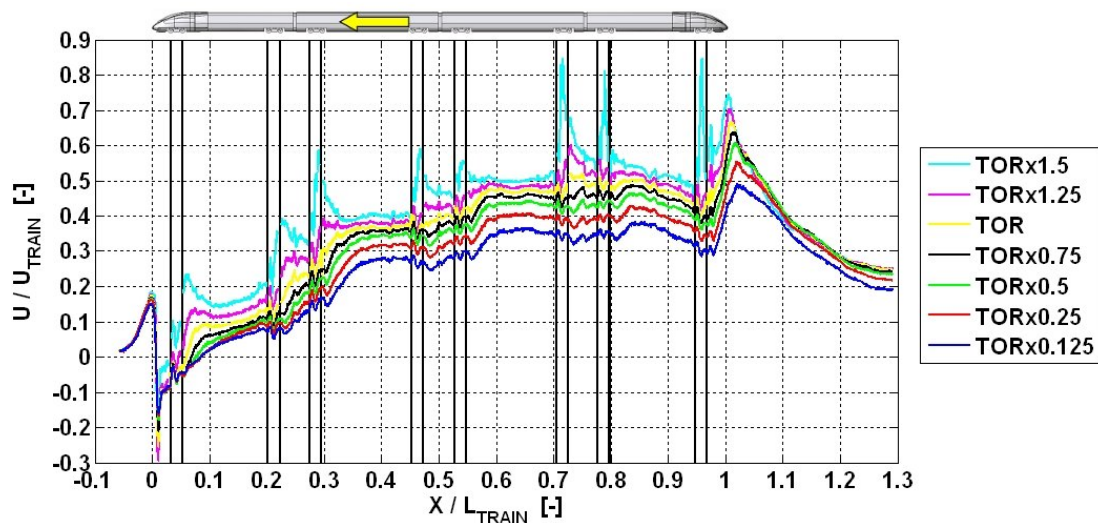


Figure 15: Normalised horizontal profiles of the mean velocity component in the travelling direction U at different heights over the trackbed for the reference train model (T.C. 1) on the smooth ground (G.C. A). The vertical lines indicate the positions of the train axles. $U_{TRAIN} = 4$ m/s.

the increased undercarriage roughness around the inter-car regions are easily identified for the velocity profile closest to the train, the TORx1.5 velocity profile in Figure 15. The local flow accelerations around geometric obstacles (bogies, inter-car gaps, gaps, protruding objects) and the fact that the mean U velocity is strongest close to the train, indicate that a narrow ground clearance increases the aerodynamic forces on the trackbed and thus the risk of ballast flight. The Figure 16 results for the mean vertical velocity W reflect the idea that vertical accelerations of the undercarriage flow are due to geometric features such as bogies, inter-car gaps, bogie housings or other irregularities. All vertical flow accelerations are found near the inter-car regions and near the head and the tail of the train. Along the train car, where the undercarriage is smooth and parallel to the ground, the mean vertical velocity values are around zero.

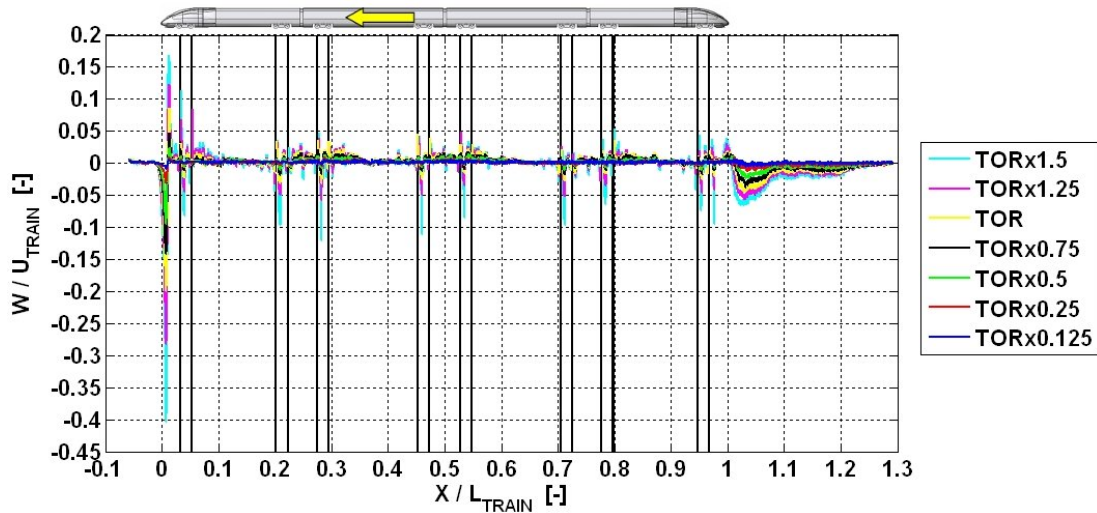


Figure 16: Normalised horizontal profiles of the mean velocity component in the vertical direction W at different heights over the trackbed for the reference train model (T.C. 1) on the smooth ground (G.C. A). The vertical lines indicate the positions of the train axes. $U_{TRAIN} = 4$ m/s.

The measured velocities for the turbulent undercarriage flow are shown in Figure 17, where 22 single runs are presented together with the calculated ensemble average for the normalised velocities at a height of $TORx0.75$ ($Z / H_{GAP} = 0.357$) for the reference train model on the smooth ground. Turbulent flows are described as irregular, chaotic

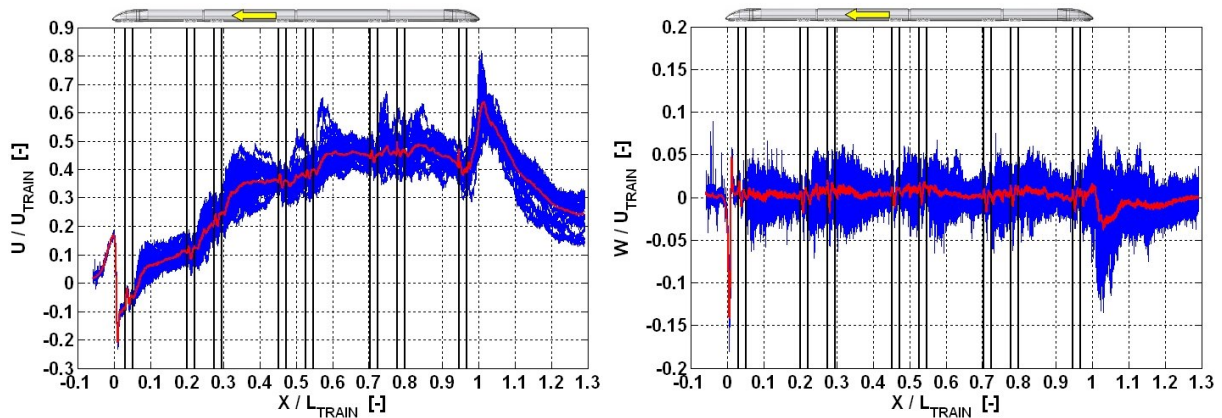


Figure 17: Normalised mean (red line) velocity component in the travelling direction U (left) and in the vertical direction W (right) with the corresponding 22 single runs (blue lines) at the height of $TORx0.75$ ($Z / H_{GAP} = 0.357$) for the reference train model (T.C. 1) on the smooth ground (G.C. A). The vertical black lines indicate the positions of the train axes. $U_{TRAIN} = 4$ m/s.

and unpredictable. This is reflected by the obtained PIV results in Figure 17, where instantaneous velocities vary around calculated ensemble average, highlighting the importance of considering the turbulent nature of the undercarriage flow. Regard-

ing the assessment of ballast flight, the instantaneous data are of great importance since the ballast in the trackbed are exposed to instantaneous aerodynamic forces and not mean forces. To describe turbulent flows, the Reynolds decomposition [105] is used, which for this example separates the instantaneous velocity component in the travelling direction $u(t)$ into a mean (time average) velocity component (U) and a fluctuating velocity component (U_{SD}), as in Equation (7).

$$u(t) = U + U_{SD} \quad (7)$$

The calculated mean velocities and their corresponding standard deviations (velocity fluctuations) are of great use for the comparison of different parameters such as train configurations, ground conditions and Reynolds numbers, but also as input data for theoretical calculations or ballast flight assessment models.

Instantaneous velocity data were extracted between both bogies of the trailing end-car ($X / L_{TRAIN} = 0.841$) at the height of $Z / H_{GAP} = 0.356$ from every single run and are plotted as histograms in Figure 18 together with the normal probability density functions calculated from the corresponding mean ($U / U_{TRAIN} = 0.465$, $W / U_{TRAIN} = 0.009$) and standard deviation ($U_{SD} / U_{TRAIN} = 0.060$, $W_{SD} / U_{TRAIN} = 0.029$) velocity values. The applied normal probability density function is defined according to Equation (8) (for the velocity component in the travelling direction). To simplify the expression of Equation (8) following declinations were used: $\hat{u} = u / U_{TRAIN}$, $\hat{U} = U / U_{TRAIN}$ and $\hat{U}_{SD} = U_{SD} / U_{TRAIN}$ for the velocity component in the travelling direction.

$$PDF(\hat{u}, \hat{U}, \hat{U}_{SD}^2) = \frac{1}{\hat{U}_{SD} \cdot \sqrt{2 \cdot \pi}} \cdot e^{-\frac{1}{2} \cdot \left(\frac{\hat{u} - \hat{U}}{\hat{U}_{SD}}\right)^2} \quad (8)$$

The distribution of the velocity component in the travelling and the vertical direction is similar to a normal or a Gaussian distribution, especially for the velocity component more interesting for ballast flight i.e. the velocity component in the travelling direction. Similar Gaussian distributions were also found for the fully developed undercarriage flow around the inter-car regions. This was also the case for the velocity components in the travelling and the lateral directions for the full-scale measurements of Deeg et al. [51]. Moreover, the distribution of the velocity component in the travelling and the vertical direction in Figure 18 does not perfectly fit the calculated normal probability density functions. The skewness was calculated to be -0.52 for the horizontal respectively 0.67 for the vertical velocity component. These values of the

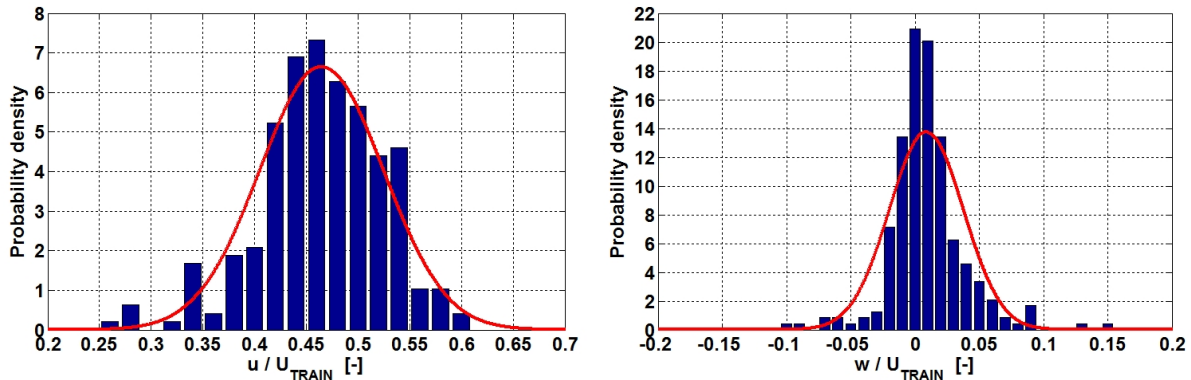


Figure 18: Histograms (blue) and the corresponding probability density functions (red) of the u (left) and w (right) velocities at the height $TOR \times 0.75$ at the middle of the trailing end-car for the reference train model (T.C. 1) on the smooth ground (G.C. A). $U_{TRAIN} = 4$ m/s.

skewness are still in the range that the measured distributions can be treated as fairly symmetrically, which the distributions in Figure 18 confirms. However, the distribution of the horizontal velocity component is slightly to the right (negative skewness) as the vertical velocity component distribution is slightly to the left (positive skewness) in comparison to the calculated normal probability density function. The more obvious difference of the distributions to the calculated normal probability density functions is the fit of the peak, especially for the vertical velocity component. The results in Figure 18 reflect the calculated flatness of the distributions (0.58 for u and 4.59 for v) with longer and fatter tails and higher and sharper peaks, particularly for the vertical velocity component. Despite the deviations it is still considered to be realistic to assume a normal distribution for the velocity components of the undercarriage flow.

6.2 Reynolds number dependency in the water-towing tank

In accordance with most scale model experiments, the water-towing tank tests were conducted with a lower Reynolds number ($0.25 \cdot 10^6$ with the maximum rig speed of $U_{TRAIN} = 4$ m/s) than the values for full-scale high-speed trains cruising at speeds around 300 km/h ($Re \sim 16 \cdot 10^6$). Nevertheless, the Reynolds number dependency of the undercarriage flow in the water-towing tank was analysed by measuring the undercarriage flow for the reference train model on the smooth ground for the possible lower train model speeds of $U_{TRAIN} = 1, 2$ and 3 m/s corresponding to Reynolds

numbers of $0.0625 \cdot 10^6$, $0.125 \cdot 10^6$ and $0.1875 \cdot 10^6$. Although the Reynolds numbers of interest are the larger values, the obtained results from the water-towing tank should help to quantitatively assess the Reynolds number effect of the undercarriage flow. The results reveal that the most interesting Reynolds number effects were found for the velocity component in the travelling direction U . The only Reynolds number effect found for the mean vertical velocity component was lower mean W velocity values for the flow around the head of the train for the lowest Reynolds number ($U_{TRAIN} = 1$ m/s). Additionally, the Reynolds number dependency of the vertical velocity fluctuations (W_{SD}) was very similar to the one in the travelling direction U_{SD} . Therefore, only the ensemble average and the velocity fluctuations of the velocity component in the travelling direction are presented in Figure 19 and Figure 20. The velocity component in the travelling direction and its corresponding velocity fluctuations (U_{SD}) are also the most interesting regarding ballast flight. Comparing the horizontal profiles

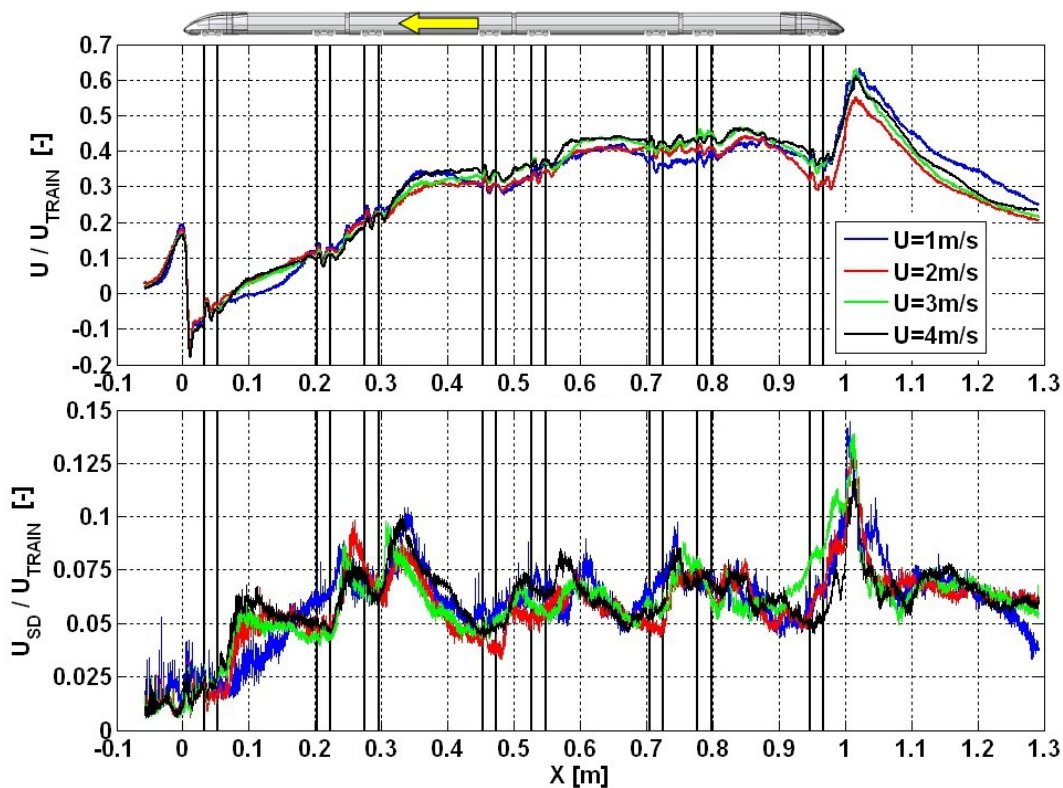


Figure 19: Horizontal profiles of the normalised ensemble average velocity component in the travelling direction U (upper) and its standard deviation U_{SD} (lower) for the reference train model (T.C. 1) on the smooth ground (G.C. A) at the height of $Z / H_{GAP} = 0.238$ (TORx0.5) for different train model speeds. The vertical black lines indicate the positions of the train axes.

of the mean U velocity in the upper graphic of Figure 19 reveal that the most distinc-

tive Reynolds number effects are found for the nearly fully developed Couette-like undercarriage flow for the second half of the train model. The Reynolds number effects found at the second half of the train model indicate lower normalised mean U velocity values with decreasing Reynolds number or train model speed. Additionally, the flow development after the first bogie at the leading end-car is also affected by the Reynolds number, slower undercarriage flow development for the lowest Reynolds number ($U_{TRAIN} = 1$ m/s). The slower flow development along the leading end-car is associated with the lower generation of turbulence found after the first bogie (blue line in the lower graphic in Figure 19). The turbulence is beneficial for the flow development as momentum is mixed between the flow closer to the train and towards the trackbed. In contrast to the mean U velocity, the velocity fluctuations U_{SD} for the more developed undercarriage flow show no significant Reynolds number dependency for the considered train model speeds.

For a more detailed comparison, vertical velocity profiles of the normalised ensemble average U velocity and the corresponding standard deviation U_{SD} at the centre of each train car are presented in Figure 20. The vertical profiles of the mean U velocity in Figure 20 indicate that a decreasing Reynolds number results in lower mean U velocity values over the entire gap as well as decreased velocity gradients at the trackbed for the fully developed flow along the second half of the train model. The vertical profiles confirm that besides the differences in the velocity fluctuations (U_{SD}) for the leading end-car, no significant Reynolds number effects are found for the more developed undercarriage flow. This indicates that the topology of the train's undercarriage dominates the generation of undercarriage turbulence and overrides the influence of the Reynolds number variation. Considering the Reynolds number effects found in the water-towing tank experiments, an additional increase in the normalised mean U velocity over the entire gap as well as larger velocity gradients at the trackbed, are expected for the undercarriage flow of a full-scale high-speed train alone from the Reynolds number difference. Regarding ballast flight, the Reynolds number effect of larger normalised mean U velocity values and velocity gradients at the trackbed increases the aerodynamic forces on the trackbed and thus the chance of ballast flight. Nevertheless, the effects of the Reynolds number are still relatively small, indicating that the undercarriage flow is predominantly ruled by geometric objects with sharp edges known to be less sensitive to variations of the Reynolds number.

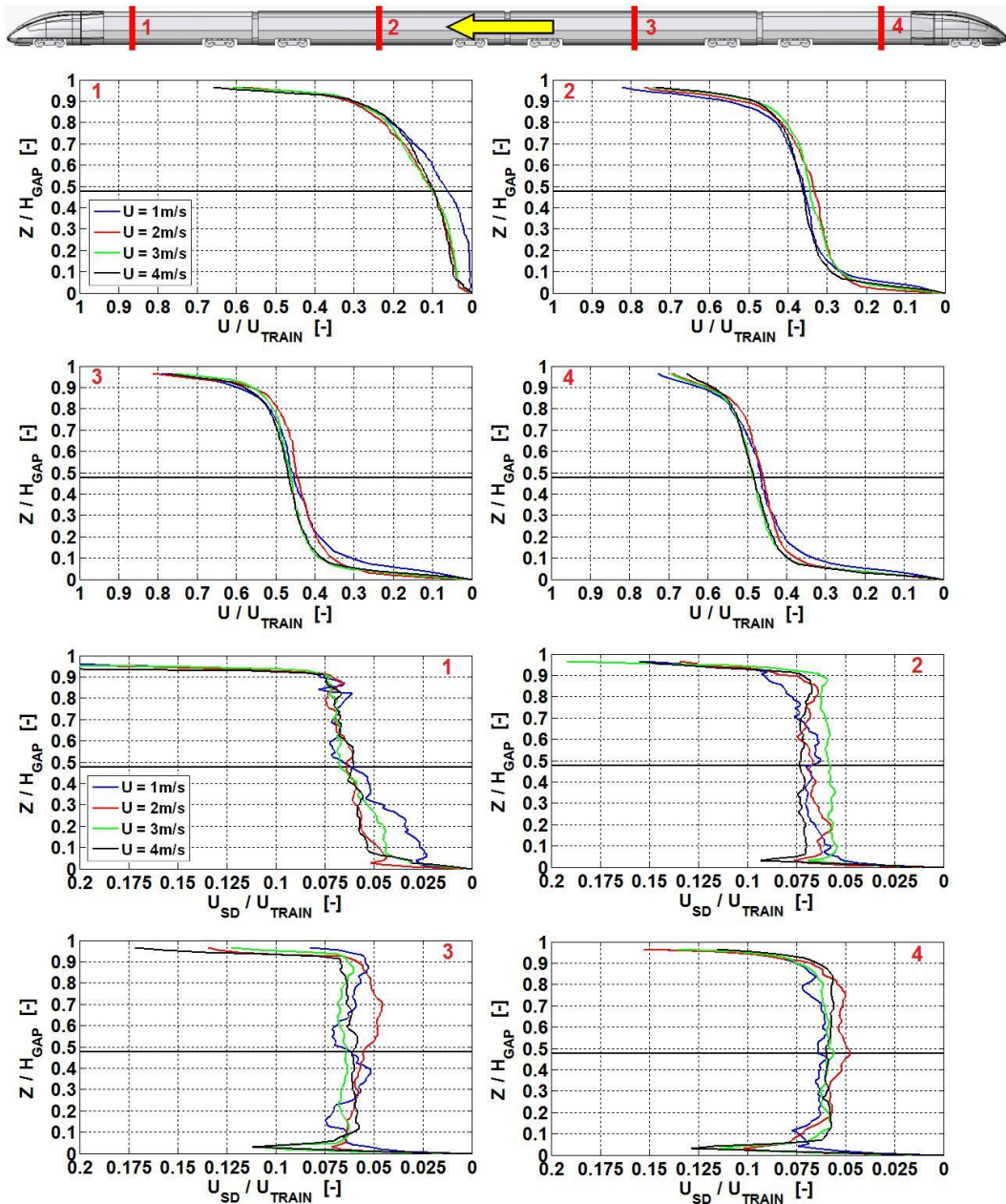


Figure 20: Vertical profiles of the normalised ensemble average velocity component in the travelling direction U (two upper rows) and its standard deviation U_{SD} (two lower rows) at the centre of each train car for the reference train model (T.C. 1) on the smooth ground (G.C. A) for different train model speeds. The horizontal black line indicates the height of the top of the rail ($Z / H_{GAP} = 0.476$).

The water-towing tank experiments are nevertheless also compared to two different full-scale test campaigns for two different high-speed trains in commercial operation in section 7.2.

6.3 Comparison of the train configurations

6.3.1 The statistically averaged undercarriage flow field

The general differences in the undercarriage flow between the three considered train models on the smooth ground will be discussed and presented using the calculated normalised ensemble averages of the U velocity, W velocity and turbulence intensity for the measured vertical plane through the trackbed line of symmetry. The mean U velocity flow field for the leading end-car of the three train configurations in Figure 21, presents the characteristic flow around the head and the beginning of boundary layer growth on the train undercarriage and trackbed. The flow around the head of

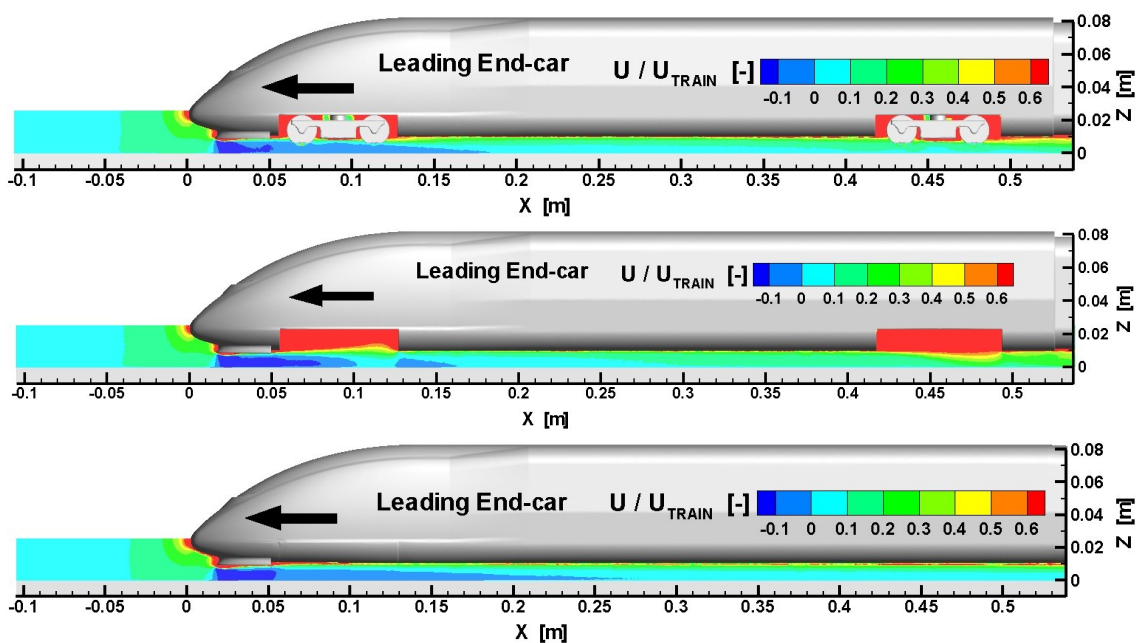


Figure 21: Normalised mean velocity field of the velocity component in the travelling direction U for the leading end-car of the reference train model (T.C. 1) (upper plot), the rough train model (T.C. 3) (middle plot) and the smooth train model (T.C. 2) (lower plot) on the smooth ground condition (G.C. A). $U_{TRAIN} = 4$ m/s.

the train is, according to full-scale flow visualisations by Quinn et al. [106] on a high-speed train, displaced in all directions and thus generating a highly three-dimensional flow. This three-dimensional flow is reflected by the water-towing tank results. The flow ahead of the train is displaced in the travelling direction of the train ($X < 0.02$ m in Figure 21) and this is immediately followed by a reverse flow region below the head at $X = 0.02$ m in Figure 21. After the head of the train, the boundary layer grows with the train length, turning the flow back into the direction of travel until the boundary

layer reaches the trackbed, i.e. where the reverse flow region ends. From this point on, the Couette-like undercarriage flow region is initiated as the boundary layer on the ground begins to develop. The results in Figure 21 reveal that the boundary layer develops faster for the train configurations with a rougher undercarriage since the most extended reverse flow region is found for the smooth train model.

Comparing the ensemble averaged U velocity field of the different train models in Figures 22 - 24, the faster boundary layer development for the rougher undercarriage of the reference and the rough train models results in larger mean U velocity values along the entire train length than those for the smooth train model. This indicates that bogies, bogie housings, inter-car gaps, gaps, cavities, or any other geometric obstacle on train's undercarriage increases the overall roughness and enhances the boundary layer development resulting in larger mean U velocity values and thus generally increasing the risk of ballast flight. The ensemble averaged flow fields of the different

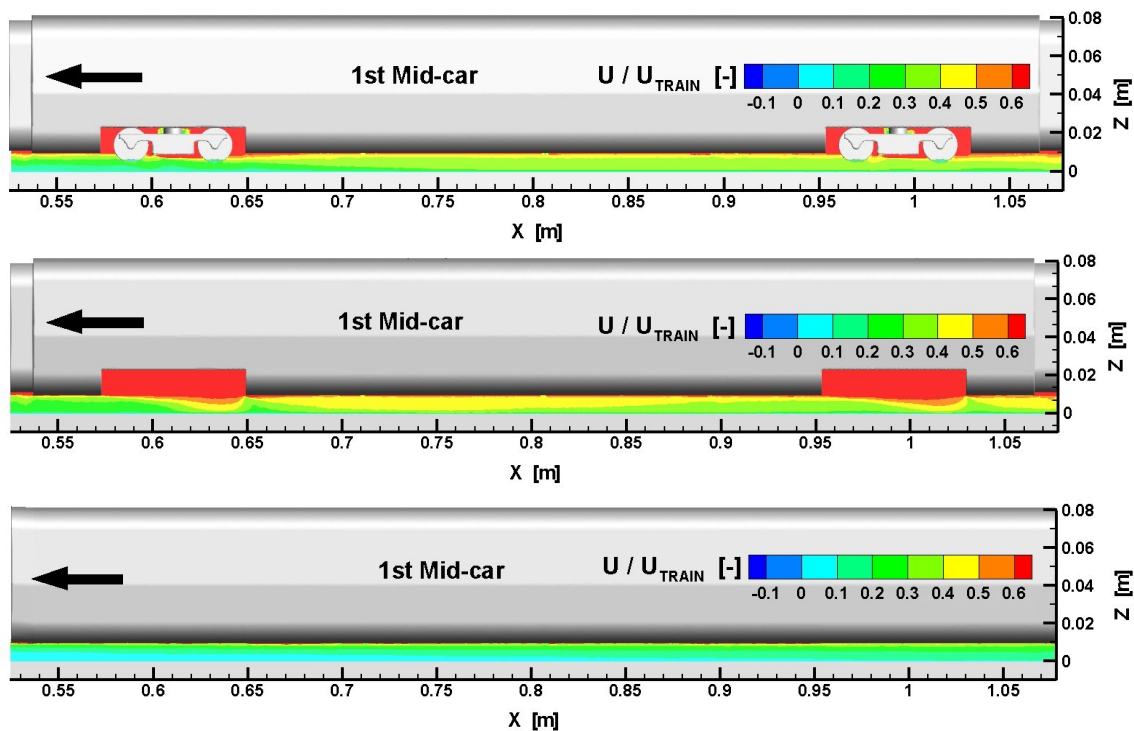


Figure 22: Normalised mean velocity field of the velocity component in the travelling direction U for the first mid-car of the reference train model (T.C. 1) (upper plot), the rough train model (T.C. 3) (middle plot) and the smooth train model (T.C. 2) (lower plot) on the smooth ground condition (G.C. A). $U_{TRAIN} = 4$ m/s.

train models in Figures 22 - 24 also indicate two different undercarriage flow characteristics along the train length. One of them is a steady boundary layer growth

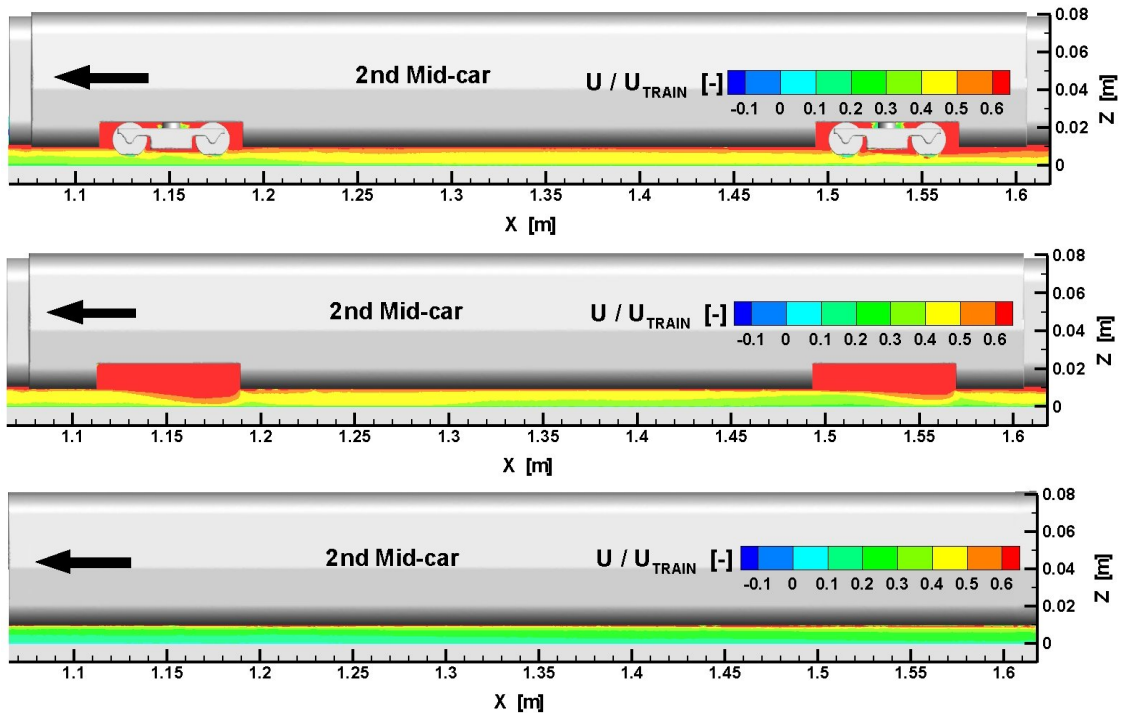


Figure 23: Normalised mean velocity field of the velocity component in the travelling direction U for the second mid-car of the reference train model (T.C. 1) (upper plot), the rough train model (T.C. 3) (middle plot) and the smooth train model (T.C. 2) (lower plot) on the smooth ground condition (G.C. A). $U_{TRAIN} = 4$ m/s.

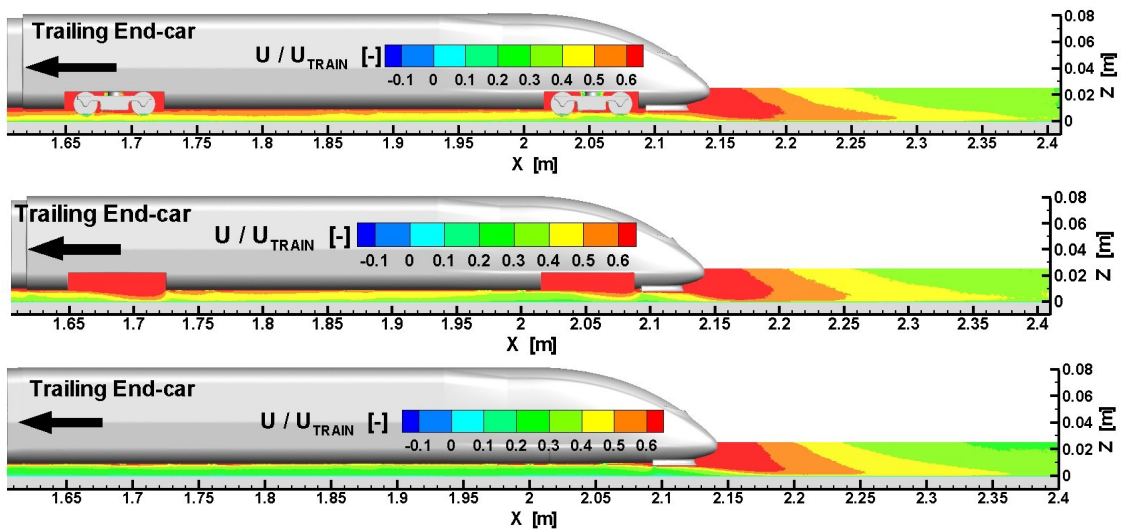


Figure 24: Normalised mean velocity field of the velocity component in the travelling direction U for the trailing end-car of the reference train model (T.C. 1) (upper plot), the rough train model (T.C. 3) (middle plot) and the smooth train model (T.C. 2) (lower plot) on the smooth ground condition (G.C. A). $U_{TRAIN} = 4$ m/s.

along the train length with increasing mean U velocity values, eventually developing to a nearly fully developed undercarriage flow as found for the smooth and the reference train model. The other is a more dynamic undercarriage flow behaviour of the rough train model, dominated by the strong local flow acceleration around every open bogie housing. The strong flow accelerations around the open bogie housings are followed by flow decelerations along the smooth train undercarriages, resulting in a self-similar or wavy flow characteristics.

The normalised ensemble average flow field for the vertical velocity component W is presented for all train models on the smooth ground in Figures 25 - 28. The results for the smooth train model in comparison to the two other train models confirms the statement in section 6.1, that the only reasons for the flow to be directed in the vertical direction are due to undercarriage irregularities or obstacles such as bogies, bogie housings, or inter-car gaps in addition to the head and the tail of the train.

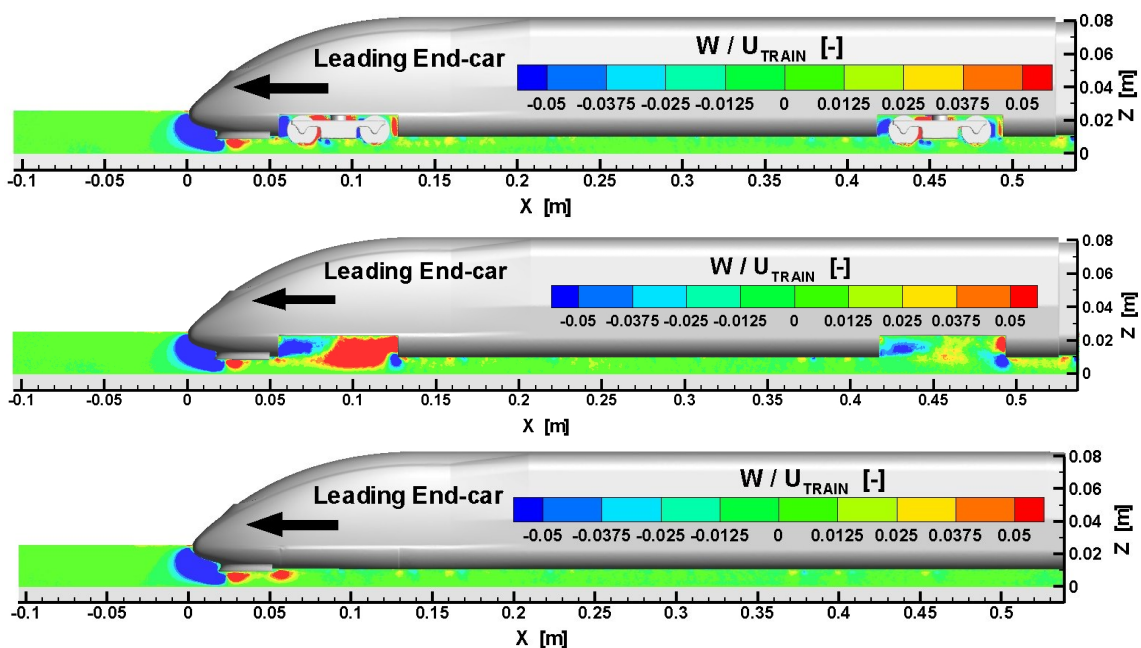


Figure 25: Normalised mean velocity field of the velocity component in the vertical direction W for the leading end-car of the reference train model (T.C. 1) (upper plot), the rough train model (T.C. 3) (middle plot) and the smooth train model (T.C. 2) (lower plot) on the smooth ground condition (G.C. A). $U_{TRAIN} = 4$ m/s.

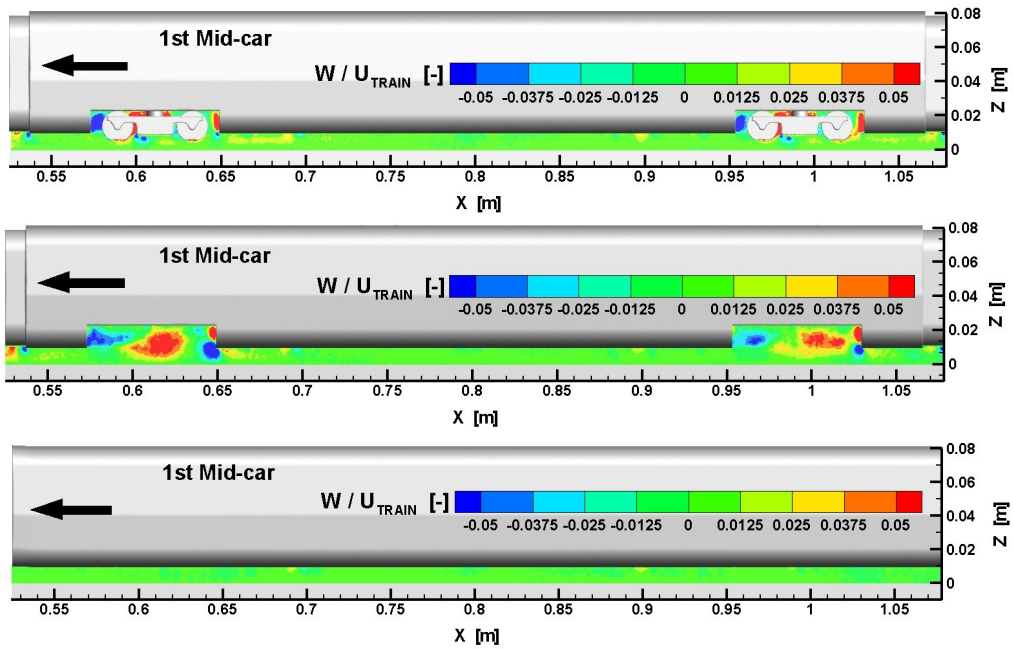


Figure 26: Normalised mean velocity field of the velocity component in the vertical direction W for the first mid-car of the reference train model (T.C. 1) (upper plot), the rough train model (T.C. 3) (middle plot) and the smooth train model (T.C. 2) (lower plot) on the smooth ground condition (G.C. A). $U_{TRAIN} = 4$ m/s.

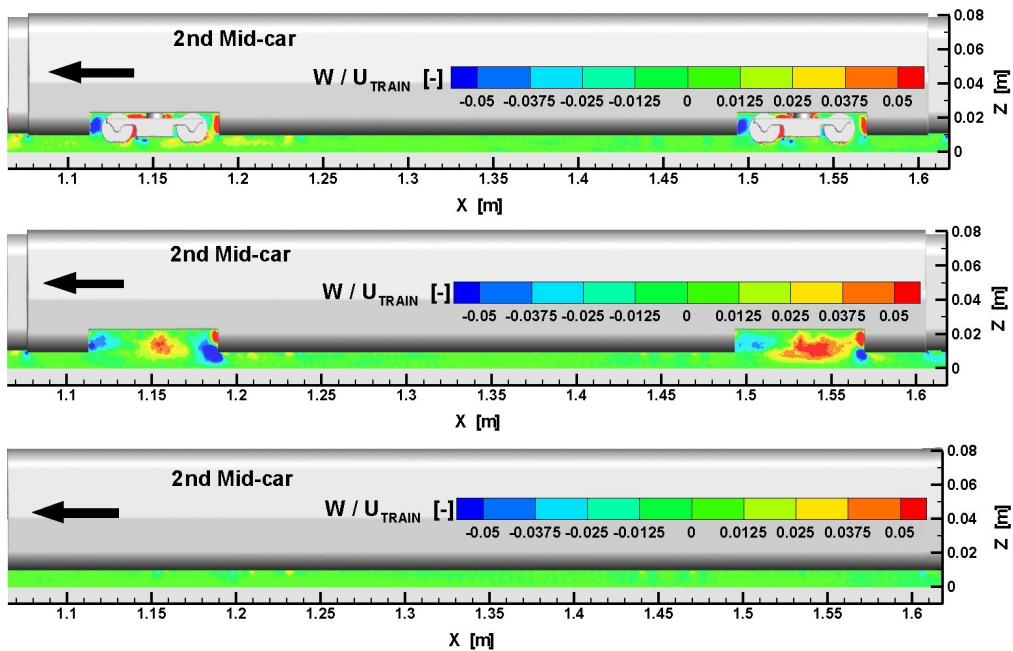


Figure 27: Normalised mean velocity field of the velocity component in the vertical direction W for the second mid-car of the reference train model (T.C. 1) (upper plot), the rough train model (T.C. 3) (middle plot) and the smooth train model (T.C. 2) (lower plot) on the smooth ground condition (G.C. A). $U_{TRAIN} = 4$ m/s.

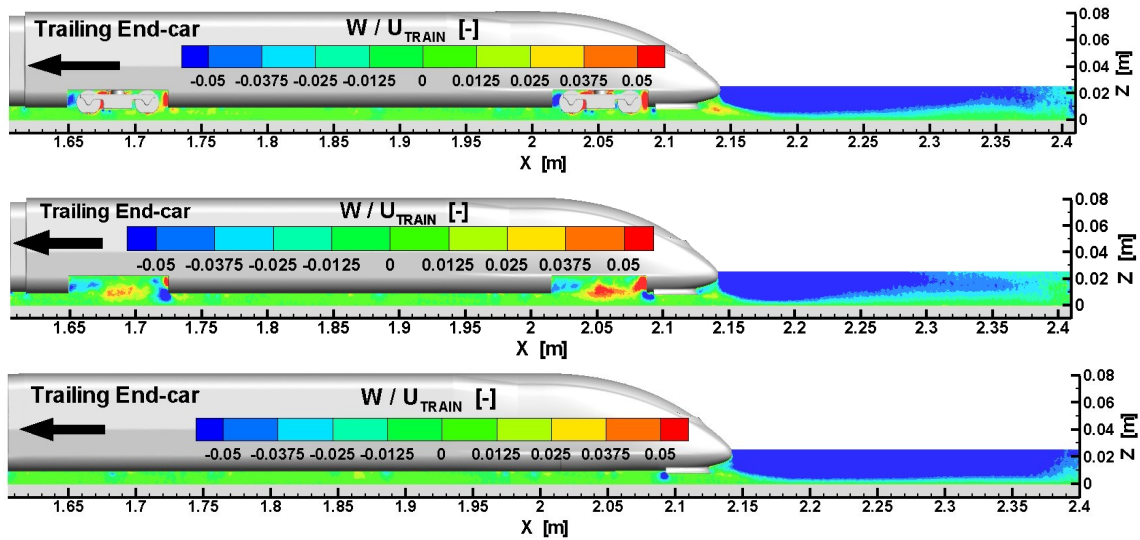


Figure 28: Normalised mean velocity field of the velocity component in the vertical direction W for the trailing end-car of the reference train model (T.C. 1) (upper plot), the rough train model (T.C. 3) (middle plot) and the smooth train model (T.C. 2) (lower plot) on the smooth ground condition (G.C. A). $U_{TRAIN} = 4$ m/s.

The normalised ensemble average velocity field of the U and the W velocity indicates that geometric irregularities/obstacles on a train's undercarriage accelerating the flow in the vertical direction are correlated with the local increase of the velocity values in the horizontal direction (U). Another undercarriage source inducing vertical flows towards the trackbed is cooling air outlets. According to Sima et al. [39], undercarriage cooling air outlet flows towards the trackbed had a significant influence on the undercarriage flow, accelerating the flow in the travelling direction similar to how protruding objects do. The vertical velocity component W reveals disturbing geometric objects or air outlets responsible for larger U velocity values and can therefore be used to streamline or to optimise the undercarriages of high-speed trains. Furthermore, the growing boundary layer along the train undercarriage is beneficial for geometric undercarriage irregularities closer to the end of the train. The boundary layer suppresses the vertical flow acceleration around undercarriage obstacles such as the inter-car gaps and bogie regions for the rough train model and the reference train model in Figure 25 - 28. However, due to the bidirectional travel design requirement, the feature of the growing boundary layer is of little use for the design of high-speed train undercarriages.

The flow in the open bogie housings for the rough train model is comparable to the flow structures, i.e. recirculation zones, found for the classical fluid mechanics prob-

lem of cavity flows (see Gloerfelt [107]). For the presented results, the only indications of a flow recirculation in the bogie housings for the rough train model and the reference train model are found for W. The reason for this is the fixed or Eulerian view of the PIV cameras. The flow trapped in the bogie housings is the superposition of the train speed and the recirculation in the bogie housings. By subtracting the train's speed from the ensemble averaged flow field for U in the travelling direction, thus using a Lagrangian specification of the flow field, the recirculation in the bogie housings was revealed. Additionally, the recirculation and the shear layer interactions with trailing edges of the bogie frame for the reference train model and the trailing edge of the bogie cavity for the rough train model are sources of aero-acoustic noise [107] and increased drag, both of which are undesirable for high-speed trains.

The presented normalised ensemble averaged flow field of the velocity component in the travelling direction U and in the vertical direction W reflects the main undercarriage flow features of the different train models. The results in Figure 17 of the horizontal distributions of the horizontal and vertical velocity components for the individual runs together with the calculated ensemble averages reveal the importance of considering the turbulence of the undercarriage flow. The turbulence intensity field was therefore calculated (according to Equation (6) in section 5.3) and compared for each train car for the three considered train configurations on the smooth ground in Figures 29 - 32. The presented turbulence intensity fields identify regions of high turbulence (i.e. velocity fluctuations) and more importantly, the sources or objects associated with the generation of turbulence. Regions of high turbulence are characterised by instantaneous velocity values that substantially deviate from the average velocity values. Thus, regarding ballast flight, the possibility of considerably increased velocity values compared to the "expected" mean velocity values may appear for regions with high turbulence. The results in Figures 29 - 32 clearly demonstrate that the undercarriage flow for the reference and the rough train models are characterised by regions of strong turbulence intensity produced by the geometric irregularities and/or obstacles around the inter-car regions. The presented results for the reference and the rough train models clearly indicate that the largest instantaneous velocity values in the undercarriage flow are expected to appear around the inter-car regions, which agrees with results of full-scale measurements on high-speed trains.

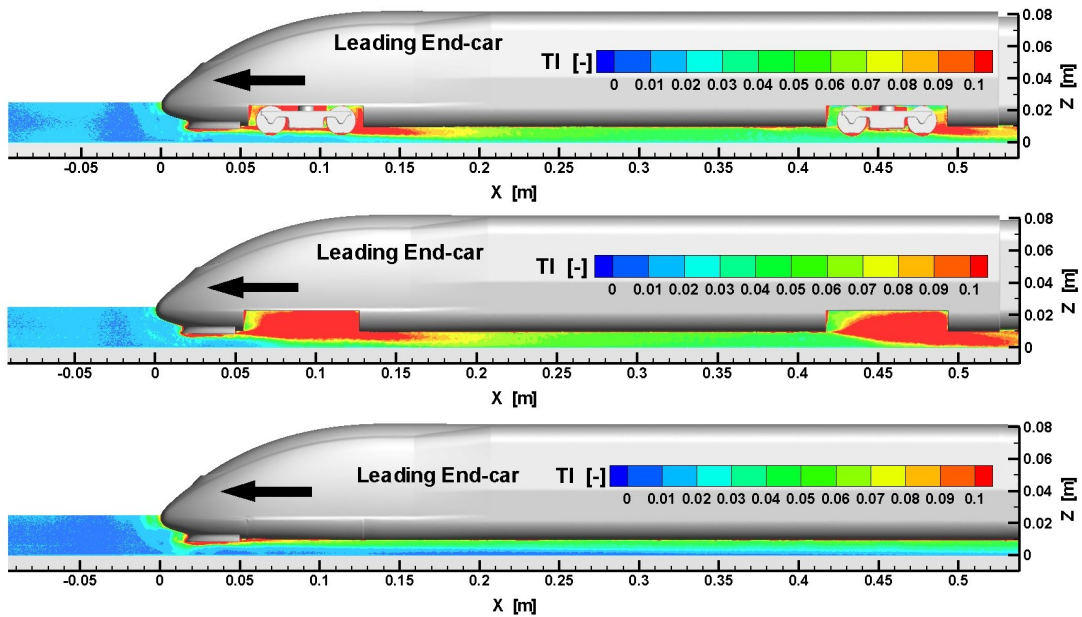


Figure 29: Turbulence intensity field for the leading end-car for the reference train model (T.C. 1) (upper plot), the rough train model (T.C. 3) (middle plot) and the smooth train model (T.C. 2) (lower plot) on the smooth ground condition (G.C. A). $U_{TRAIN} = 4$ m/s.

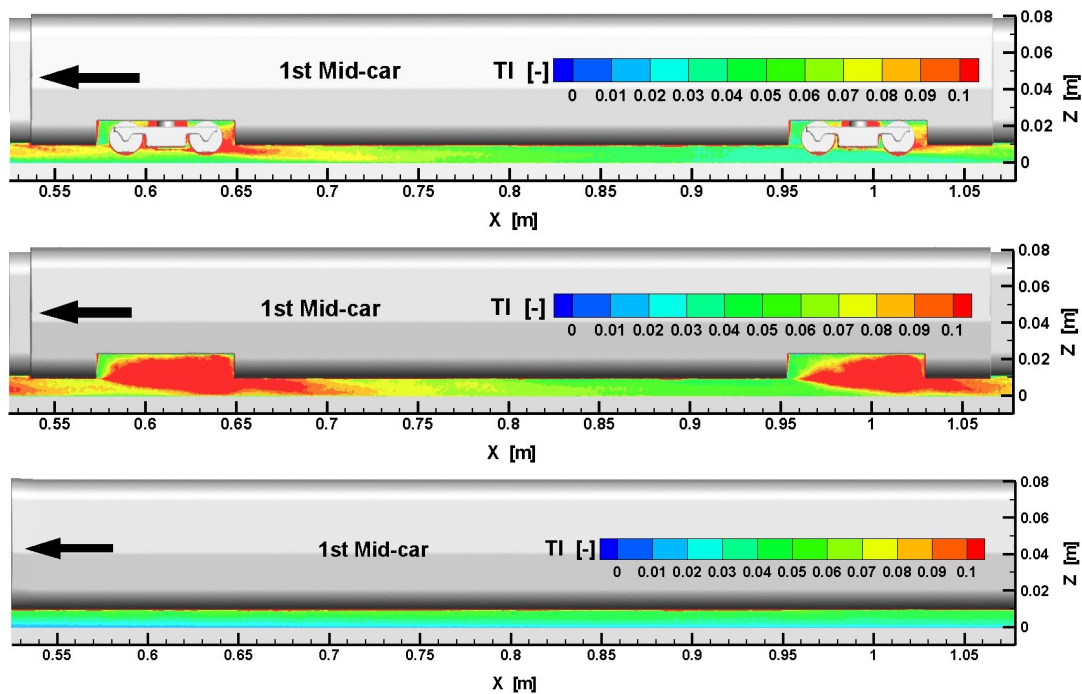


Figure 30: Turbulence intensity field for the first mid-car for the reference train model (T.C. 1) (upper plot), the rough train model (T.C. 3) (middle plot) and the smooth train model (T.C. 2) (lower plot) on the smooth ground condition (G.C. A). $U_{TRAIN} = 4$ m/s.

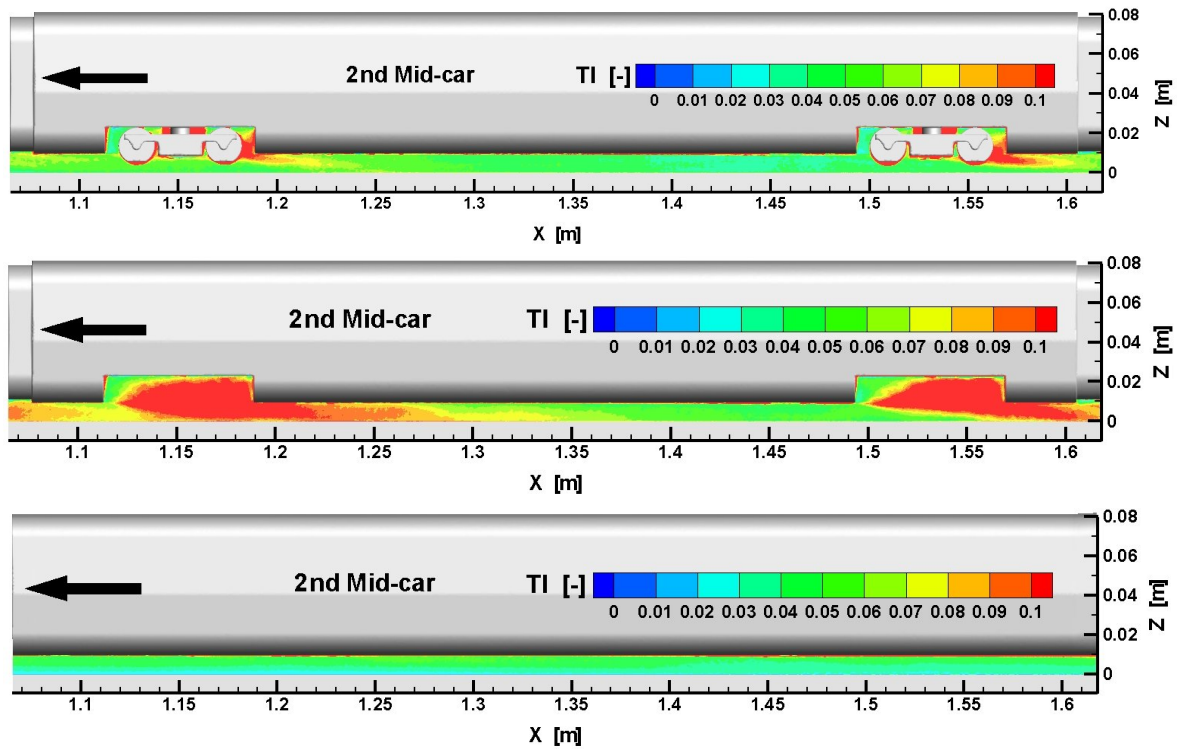


Figure 31: Turbulence intensity field for the second mid-car for the reference train model (T.C. 1) (upper plot), the rough train model (T.C. 3) (middle plot) and the smooth train model (T.C. 2) (lower plot) on the smooth ground condition (G.C. A). $U_{TRAIN} = 4$ m/s.

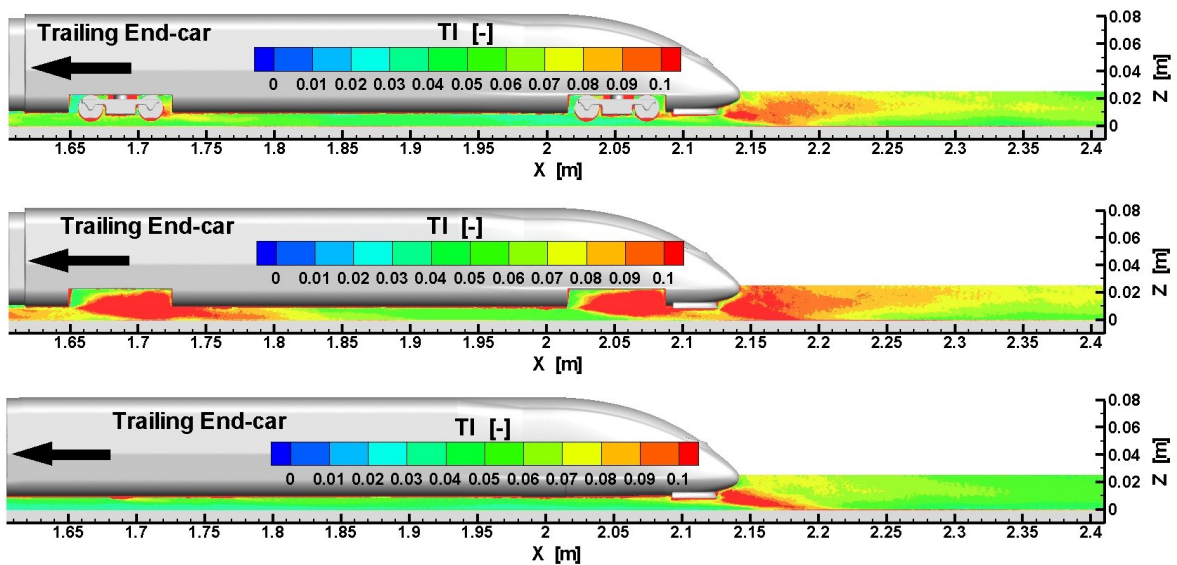


Figure 32: Turbulence intensity field for the trailing end-car for the reference train model (T.C. 1) (upper plot), the rough train model (T.C. 3) (middle plot) and the smooth train model (T.C. 2) (lower plot) on the smooth ground condition (G.C. A). $U_{TRAIN} = 4$ m/s.

The normalised ensemble average flow field (U and W velocities) together with the turbulence intensity field, demonstrate that the undercarriage flow is characterised by the flow effects around the inter-car regions. This means that the inter-car regions are of central interest for the optimisation of the undercarriage flow with regard to ballast flight. The inter-car regions are to a greater or lesser extent the only regions of high-speed trains free for or requiring design improvements.

The presented results of the three different train models proved that it is possible to change the characteristics of the undercarriage flow by altering the inter-car regions of the same train model. The reference train model with the realistic undercarriage realises an undercarriage flow characteristic of a non-articulated high-speed train with velocity values and a turbulence level in a realistic range, whereas the low values of the smooth train model reflect the undercarriage flow of the ideal high-speed train. Leaving the bogie housings open generated an undercarriage flow characteristic with velocity values in the same range as the reference train model but with stronger local flow effects associated with larger local velocity and velocity fluctuation values. The three different undercarriage flows will be used to analyse the influence and significance of the mean velocities, their corresponding velocity fluctuations and local flow accelerations with regard to the risk of ballast flight.

6.3.2 Instantaneous undercarriage flow field

The flow accelerations and velocity fluctuations around the bogie regions for the reference and the rough train models are associated with instantaneous flow effects that might be difficult to identify for the mean velocity and the velocity fluctuation field. The instantaneous flow fields along the entire train model length were analysed, especially around the bogie regions, to determine the variation of the instantaneous flow field and identify instantaneous flow effects of interest concerning ballast flight. Regarding ballast flight, the nearly fully developed undercarriage flow for the second half of the train model is of interest due to its larger aerodynamic forces on the trackbed. The instantaneous flow effects around the sixth and the seventh bogie are therefore presented in Figure 33 and Figure 34, respectively. In Figure 33 and Figure 34 the instantaneous velocity fields (u contour with in-plane velocity vectors) normalised by the train model speed ($U_{TRAIN} = 4 \text{ m/s}$) are presented for the three considered train configurations on the smooth ground. To visualise the variation or dynamics of the undercarriage flow around the sixth and seventh bogies, two instan-

taneous flow fields were chosen from the 30 conducted runs. One with low and one with high velocity values of u . Comparing the two instantaneous velocity fields (high and low u velocity) reveal the dynamic range of flow features within the instantaneous flow field around the two considered bogie regions for the nearly fully developed undercarriage flow. The results for the smooth train model (without bogies and all gaps closed) reflect the turbulent boundary layer growth of the smooth train undercarriage, generating a weakly turbulent flow with low u velocity values. Thus, there is only a small difference between the presented instantaneous flow fields in Figure 33 and Figure 34. The two other train configurations are characterised by cavity-type flow effects around the bogie housings, clearly visible in Figure 33 and Figure 34 for the rough train model with the open bogie housings. Around the trailing edge of the bogie housings, large-scale flow structures emerge and are expelled towards the ground with high momentum, increasing the u velocity values close to the trackbed. The described cavity flow effects are weaker for the reference train model than those found for the rough train model since the bogie and especially its smooth solid lower surface, shields the cavity and therefore restrains the strong flow accelerations. Nevertheless, the bogie underframe misalignment with the train's underbelly also produces instantaneous flow accelerations, increasing the u velocity values near the trackbed, as for the left image in Figure 34. The flow fields obtained for the open bogie housings of the rough train model reveal a highly dynamic instantaneous flow around the open cavities. Regarding the risk of ballast flight, the strong accelerations towards the ground with u velocity values equal to the train speed ($U / U_{TRAIN} = 1$), as in Figure 34 for the seventh bogie, can single-handedly dislodge ballast particles from the trackbed or initiate the flight of ballast particles already in motion. The other obtained instantaneous flow field with low u velocities, however, shows in contrast to the accelerated flow towards the ground, a flow guided into the open bogie housing away from the trackbed. For this precise moment, a moving ballast particle may come to rest again. The duration or frequency of the presented flow effects, e.g. the accelerated flow towards the trackbed for the rough train model, were analysed for each train configuration by evaluating all instantaneous flow fields for the 30 conducted runs capturing the flow around the sixth and the seventh bogie regions. The PIV set-up used for the smooth ground configuration with two PIV cameras (as presented in Figure 5), with a total measurement field of ~ 0.08 m, a PIV acquisition rate of 500 Hz and for a train model speed of 4 m/s, allowed the measurement of 10 instantaneous flow fields of the same train position during a single run. The results of

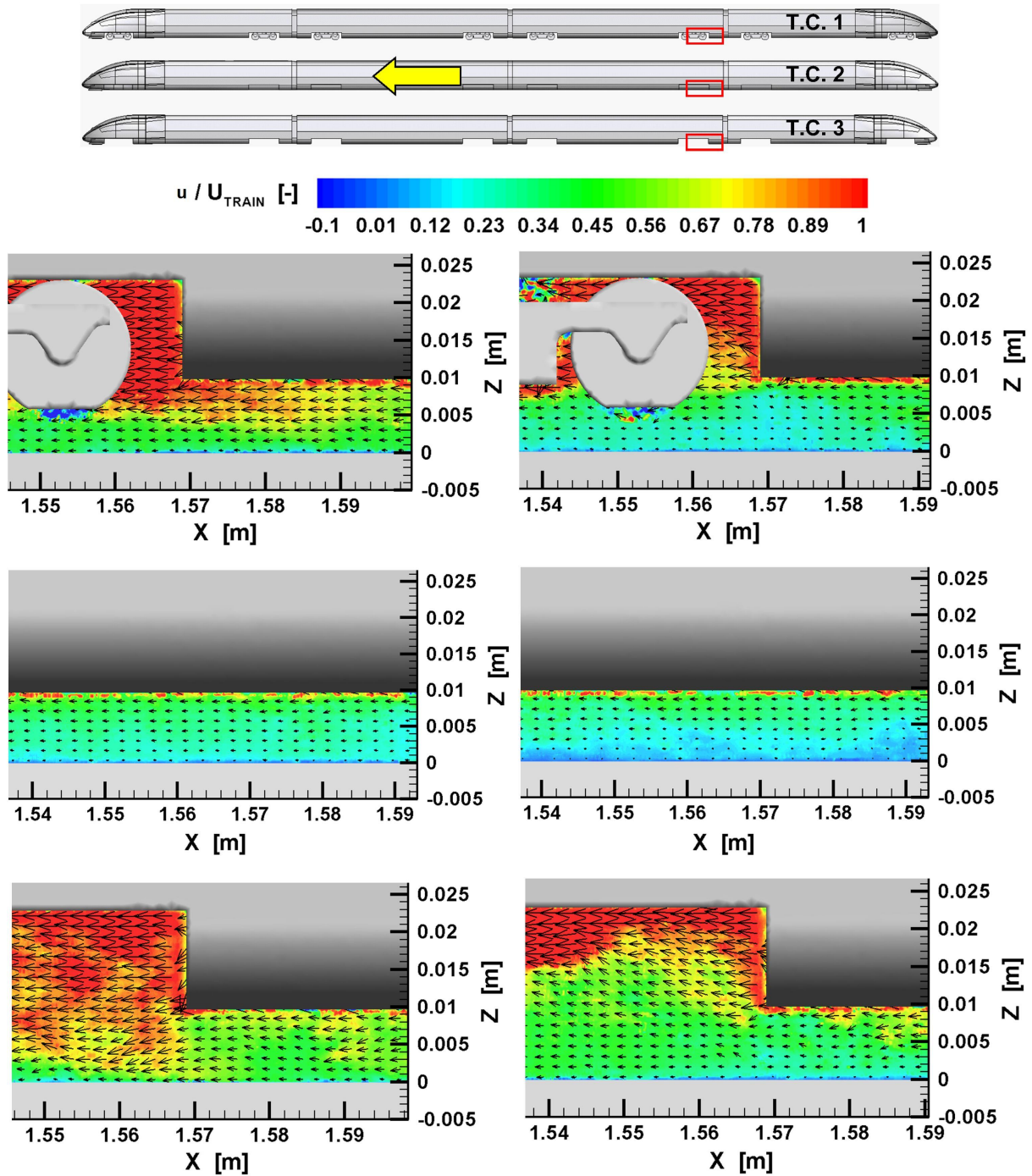


Figure 33: Close-up view of the sixth bogie region showing a snapshot of the normalised instantaneous velocity component in the travelling direction u as contour superimposed with in-plane velocity vectors for the reference train model (T.C. 1) (upper row), the smooth train model (T.C. 2) (middle row) and the rough train model (T.C. 3) (lower row) on the smooth ground (G.C. A). $U_{TRAIN} = 4$ m/s.

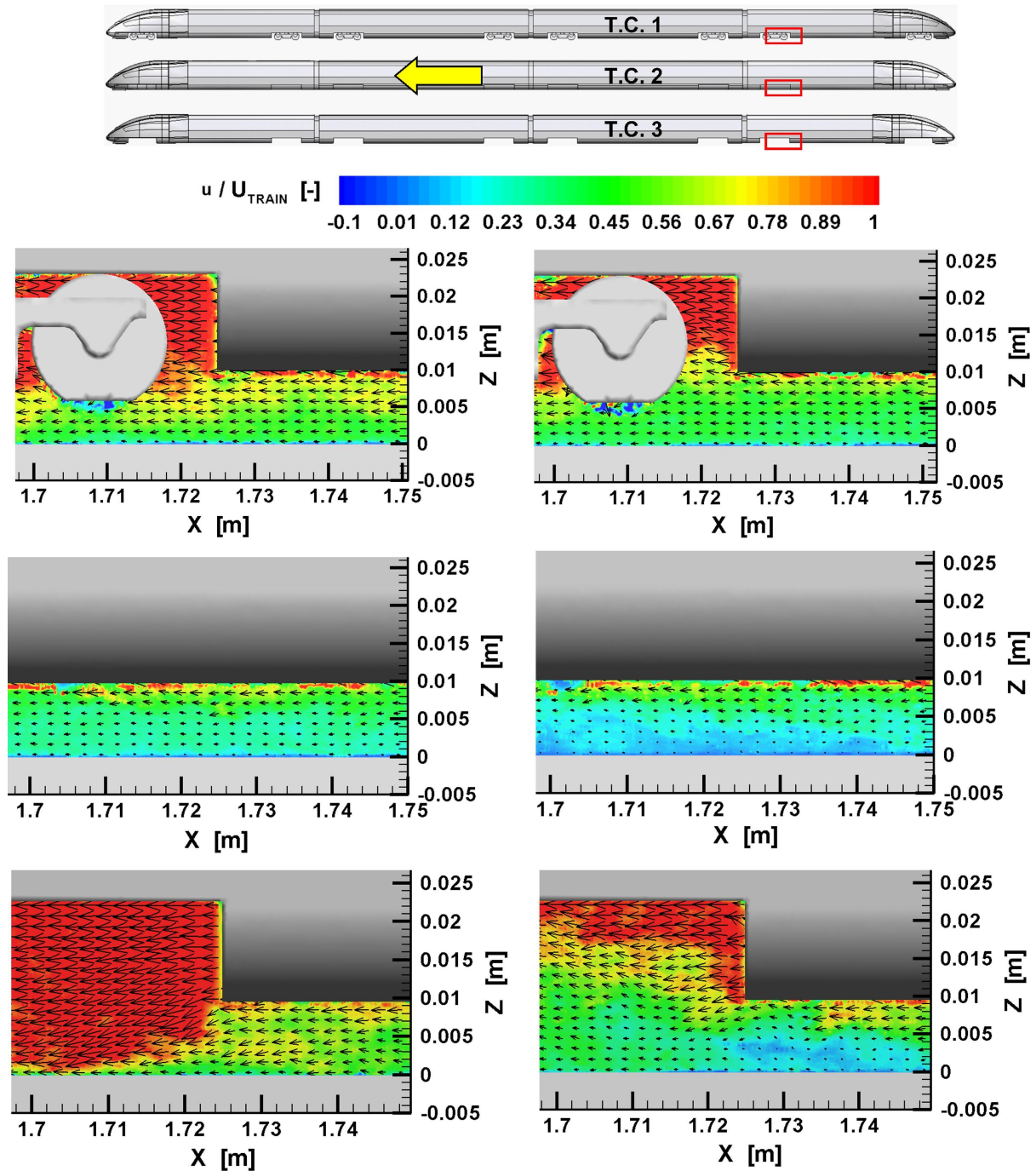


Figure 34: Close-up view of the seventh bogie region showing a snapshot of the normalised instantaneous velocity component in the travelling direction u as contour superimposed with in-plane velocity vectors for the reference train model (T.C. 1) (upper row), the smooth train model (T.C. 2) (middle row) and the rough train model (T.C. 3) (lower row) on the smooth ground (G.C. A). $U_{TRAIN} = 4$ m/s.

the instantaneous flow fields around the sixth and seventh bogies from the conducted runs did not reveal the duration or frequency of the instantaneous flow effects presented in Figure 33 and in Figure 34. The instantaneous results for all runs and for the two considered bogie regions demonstrate that the discussed flow effects are either unchanged, develops and remains or vice versa are present and dissolves for the 10 sequential PIV recordings of a single run. Considering the short total observation time of 0.02 s (PIV measurement field / U_{TRAIN}) together with the flow development during this time interval indicates that the durations of the flow effects are larger than 0.02 s and thus the frequency is below 50 Hz. Nonetheless, the transition from flow accelerating towards the trackbed to being guided away from the trackbed into the bogie housing was found for a single run for both the reference and the rough train models. This highlights the possibility of a flow transition between the two presented instantaneous flow effects but with a frequency lower than 50 Hz. For a thorough investigation of the presented flow effects, the PIV cameras and the laser light sheet must move with the train model to resolve the instantaneous flow for a fixed train position. Such a set-up is however quite complicated to construct for moving-model experiments. The use of a wind tunnel with a moving-belt is more suitable for the study of local flow effects. Nevertheless, the aim of this work remains to study the development of the undercarriage flow along the entire train length, which motivates the use of the water-towing tank with a moving-model rig.

The corresponding normalised ensemble average velocity field U , with in-plane velocity vectors and the standard deviation U_{SD} around the sixth bogie, are presented in Figure 35 and for the seventh bogie in Figure 36 for the considered train configurations on the smooth ground. Comparing the selected instantaneous flow fields in Figure 33 and Figure 34 with their corresponding mean U velocity fields in Figure 35 and in Figure 36 reveals that the presented and discussed instantaneous flow effects around the bogie regions are not reflected in the mean U velocity field for the reference and the rough train models. In contrast, the turbulent boundary layer flow found along the smooth sections of the undercarriage or for the smooth train model is more or less reflected by the ensemble average U velocity field. Considering the velocity fluctuations (U_{SD}), the range of the u velocity values and the location of the instantaneous flow effects can be estimated. The actual instantaneous u velocity distributions and the actually load on the trackbed around the bogie regions are difficult to estimate, even with reliable ensemble average flow fields and velocity fluctuations. It is therefore concluded that the instantaneous flow field should be analysed in addi-

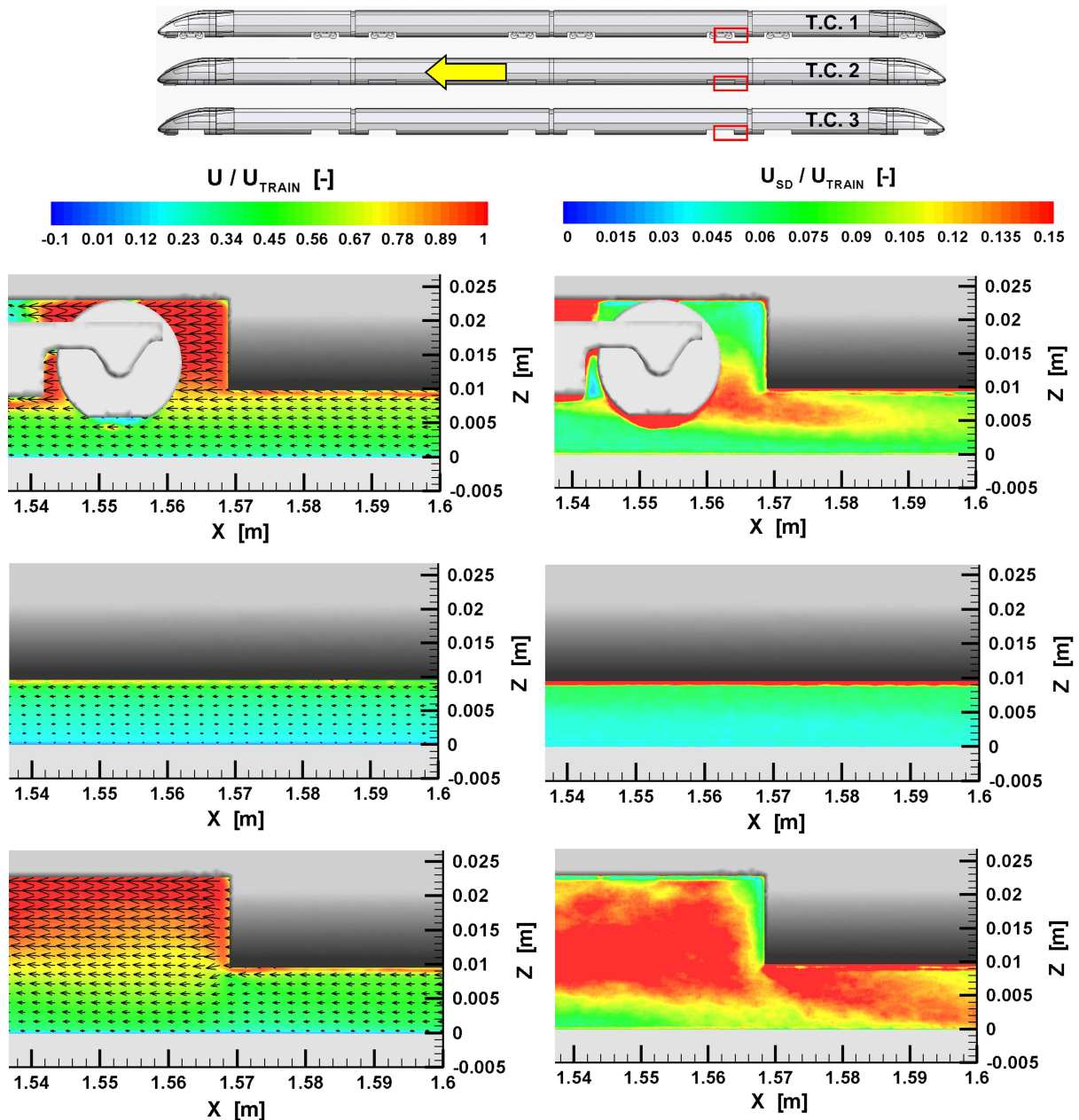


Figure 35: Close-up view of the sixth bogie region showing contours of the normalised ensemble average flow field for U with in-plane velocity vectors (left column) and the standard deviation fields U_{SD} (right column) for the reference train model (T.C. 1) (upper row), the smooth train model (T.C. 2) (middle row) and the rough train model (T.C. 3) (lower row) on the smooth ground (G.C. A). $U_{\text{TRAIN}} = 4 \text{ m/s}$.

tion to the mean velocity field and the velocity fluctuations in order to reveal the true nature of the undercarriage flow. This especially applies for the undercarriage flow regions with larger turbulence intensities, like bogie regions.

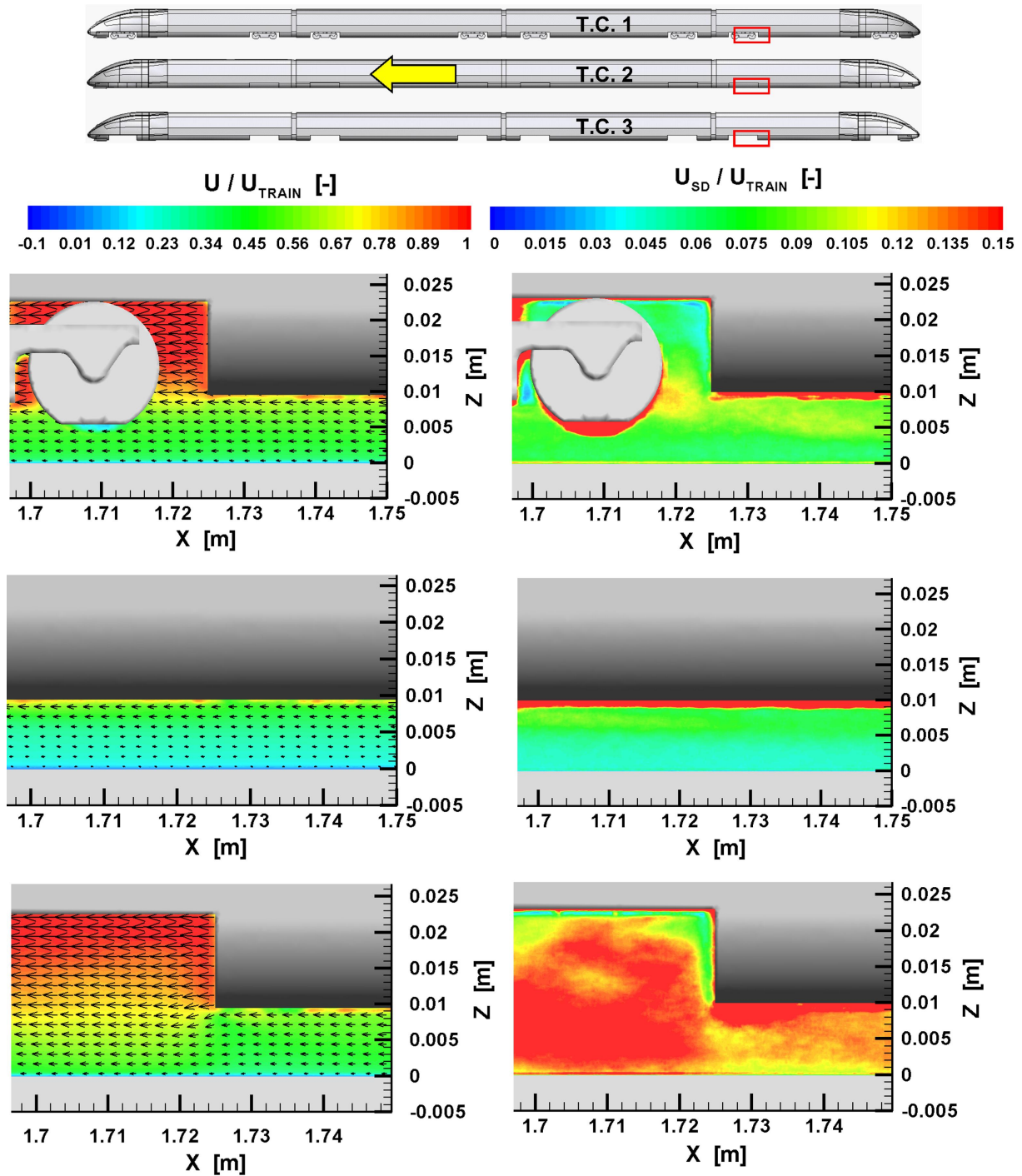


Figure 36: Close-up view of the seventh bogie region showing contours of the normalised ensemble average flow field for U with in-plane velocity vectors (left column) and the standard deviation fields U_{SD} (right column) for the reference train model (T.C. 1) (upper row), the smooth train model (T.C. 2) (middle row) and the rough train model (T.C. 3) (lower row) on the smooth ground (G.C. A). $U_{TRAIN} = 4$ m/s.

The flow characteristics around the bogie regions are influenced by the different incoming flow conditions introduced for non-articulated train sets with two bogie regions per train car, as for the considered high-speed train model used for the water-towing tank experiments. The leading bogie region of every train car is in the wake of the bogie region of the previous train car and the passenger gangway (inter-car gap), with an accelerated incoming flow with strong turbulence intensities. The second and trailing bogie region of the same train car is exposed to the more steady flow with a lower turbulence level that develops along the smooth undercarriage of the train car. The flow fields for the sixth and seventh bogie region, presented in Figure 35 and Figure 36 for the reference and rough train models, show that the only the velocity fluctuations U_{SD} change, whereas the mean U velocity flow fields remain more or less unchanged. The practically identical flow fields (mean U velocity and U_{SD}) for the smooth train model reflect the turbulent boundary layer growth for two smooth surfaces and the short distance between the considered positions. Taking the overall flow fields in section 6.3.1 into account shows that the only periodic flow element around the two bogies at every inter-car gap is the one found for the rough train model. The overall tendency for the reference train model is the decrease in turbulence with the boundary layer growth. Regarding the risk of ballast flight for the rough train model, the bogie region following the inter-car gap (in this case the seventh bogie region in Figure 36) induces larger aerodynamic forces than the preceding (sixth bogie region in Figure 35) bogie region, given that the strong velocity fluctuations are felt by the trackbed. The differences in the U_{SD} distribution around the bogie regions are also reflected in the instantaneous flow fields, for which a much stronger flow acceleration towards the ground exists for the seventh bogie region. Therefore, non-articulated train sets with larger bogie housings or bogie designs causing flow effects similar to the open bogie housing of the rough train model are considered as highly susceptible to ballast flight. It is also considered that articulated train sets sharing the same bogie at the inter-car gaps are less susceptible to ballast flight, avoiding the strong flow accelerations towards the trackbed found for the subsequent bogie of a non-articulated train. Additionally, the overall undercarriage roughness of articulated train set is also lower and thus the aerodynamic forces on the trackbed are lower as well. Independent of whether a high-speed train is articulated or not, large bogie housings or cavities should be avoided or kept as small as possible to avoid instantaneous flow effects associated with high momentum flows towards the trackbed that increase the forces on the trackbed and thus the chance of ballast flight as well. The

results for the reference train model show the positive effect of the smooth ground-parallel lower surface of the bogie in restraining the undercarriage flow from being accelerated by the bogie housing cavity. Therefore, it is recommended to pack bogie equipment closely together and also to use cover plates to shield parts or the entire lower surfaces of bogies. These measures together with a bogie frame aligned with the train undercarriage and tight bogie housing would help to create an undercarriage flow approaching that found for the smooth train model.

Nonetheless, the instantaneous flow effects found around the bogie regions, together with other stochastic parameters influencing the ballast flight problem like ballast particle size, shape and position or vehicle-induced trackbed vibration, reveal the complexity of ballast flight assessment.

6.3.3 Horizontal velocity profiles

Undercarriage flow field data were extracted along the entire train length at the height of the top of the rail ($Z / H_{GAP} = 0.476$) for a more detailed comparison of the three considered train configurations. The horizontal profiles of U normalised with the model rig speed ($U_{TRAIN} = 4$ m/s) for the three considered train configurations on the smooth ground, the rough ground and the ground with sleepers are compared to each other in Figure 37. The presented horizontal profiles for the ground with sleepers were extracted from a single position in the measured flow field, similar to installing a probe in the trackbed. The selected position was the more interesting region regarding ballast flight, that is between two sleepers, where the ballast is located. The data were extracted at a distance of $\Delta X = 8$ mm downstream (in the train travel direction) from the centre of a sleeper (12 mm sleeper spacing), where the maximum U velocity value for the inter-sleeper region appeared. Unless otherwise noted, the inter-sleeper position $\Delta X = 8$ mm downstream from the centre of a sleeper is used to represent the ground with sleepers. The four characteristic flow regions discussed in Figure 13 for the reference train model on the smooth ground, i.e. flow around the head, Couette-like undercarriage flow, near-wake flow and the far-wake flow, are also identified for the rough and the smooth train models on all ground conditions in Figure 37 and in Figure 41. Comparing the results for the three considered train configurations reveal that noticeable differences between the train configurations are found in the Couette-like undercarriage flow between the first and the last bogie, independent on the ground condition. One may thus conclude that the mean flow around the

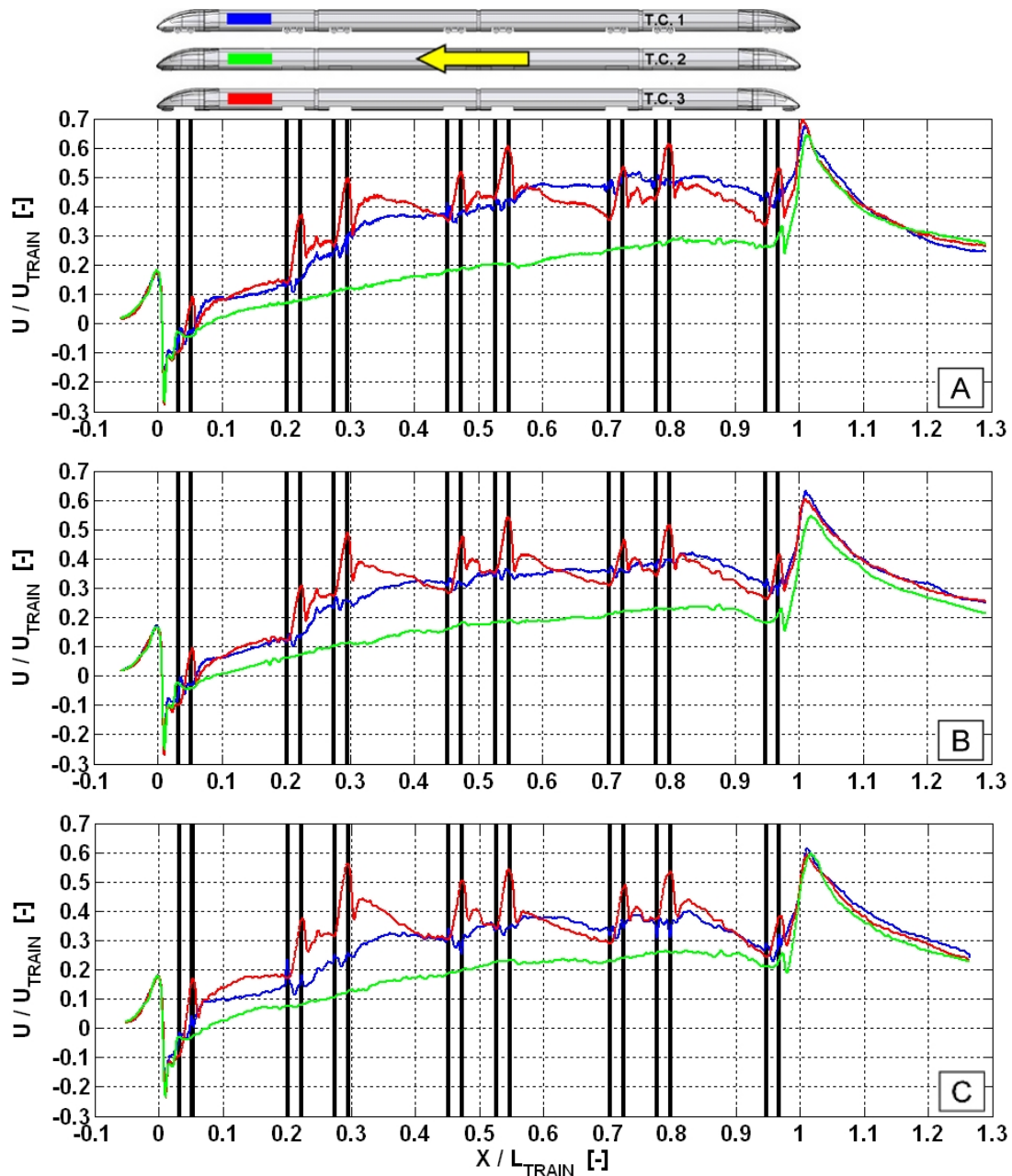


Figure 37: Normalised mean velocity component in the travelling direction U along the normalised train length at the height of the top of the rail ($Z / H_{GAP} = 0.476$) for the three considered train configurations on the smooth ground (G.C. A), the rough ground (G.C. B) and the ground with sleepers (G.C. C). The vertical lines indicate the positions of the train axes. $U_{TRAIN} = 4$ m/s.

head and the tail are dominated by the train geometry, while the undercarriage geometry has no or minimal influence. The horizontal velocity profiles or the variation of U with X in Figure 37 clearly agrees with the result in section 6.3.1, that increasing the undercarriage roughness by adding bogies, bogie housings, cavities, inter-car

gaps or any other geometric obstacle, accelerates the growth of the boundary layer on the train's undercarriage, resulting in a faster undercarriage flow development and higher overall U velocity values. The positive effect of a smooth underbelly is also indicated in Figure 37. The mean U velocity values are almost halved for the nearly fully developed undercarriage flow under the second half of the train.

The motivation for the open bogie housings was to produce an undercarriage flow with higher overall U velocities than for the reference train model as well as to generate the wavy shape of the horizontal U velocity profiles along the train found for full-scale measurements and later in Figure 65 in section 7.2. Higher overall U velocities were not observed for the rough train model. The local flow accelerations around the bogie regions, followed by the flow deceleration along the smooth underbelly of the train car, were however similar to the full-scale measurements. Nevertheless, with the U velocity values in the same range as those obtained for the reference train model, the possibility remains to evaluate the influence of strong local flow accelerations with regards to the risk of ballast flight.

The normalised horizontal velocity profiles of the vertical velocity component W along the height of the top of the rail are compared for the three train configurations in Figure 38 on the smooth ground (G.C. A), rough ground (G.C. B) and the ground with sleepers (G.C. C). The results clearly show that the maximum values of the mean W velocity are found around the head of the train for all ground and train configurations. It is therefore considered that the maximum mean W velocity values exist in general around the head of high-speed trains. Once again, this underlines that the U velocity is the one of interest for the undercarriage flow regarding the aerodynamic forces on the trackbed and the assessment of ballast flight. According to Sima et al. [39], vertical air flows towards the trackbed influence the undercarriage flow like protruding objects and thus accelerate the flow in the travelling direction. The strong local U velocity maximum at the open bogie housings, (see the red line in Figure 37), are therefore linked to the strong vertical flows in Figure 38. This implies that cooling air outlet flows towards the trackbed can generate similar local flow accelerations in the travelling direction as the open bogie housings of the rough train model. Geometric obstacles as well as cooling air outlets inducing strong vertical flows toward the trackbed, accelerating the flow in the travelling direction, have a significant impact on the aerodynamic forces on the trackbed [39] and should therefore be avoided to prevent ballast flight incidents.

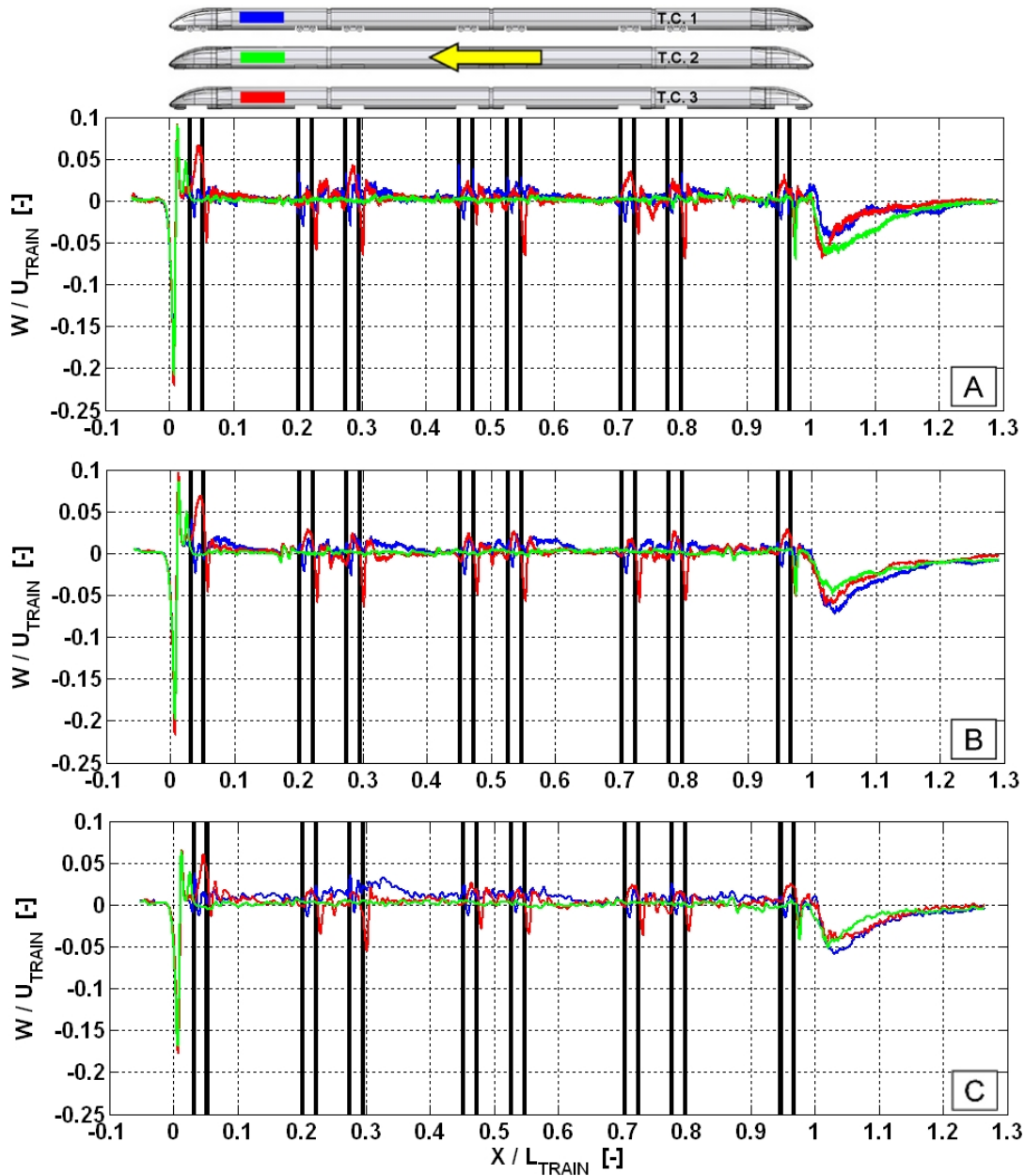


Figure 38: Normalised mean velocity component in the vertical direction W along the normalised train length at the height of the top of the rail ($Z / H_{GAP} = 0.476$) for the three considered train configurations on the smooth ground (G.C. A), the rough ground (G.C. B) and the ground with sleepers (G.C. C). The vertical lines indicate the positions of the train axes. $U_{TRAIN} = 4$ m/s.

In Figure 39 and 40, the corresponding horizontal profiles of the standard deviation of the velocity component in the travelling direction (U_{SD}) and in the vertical direction (W_{SD}) are presented at the height of the top of the rail for the considered train configurations on the three ground conditions. The spatial variation of the horizon-

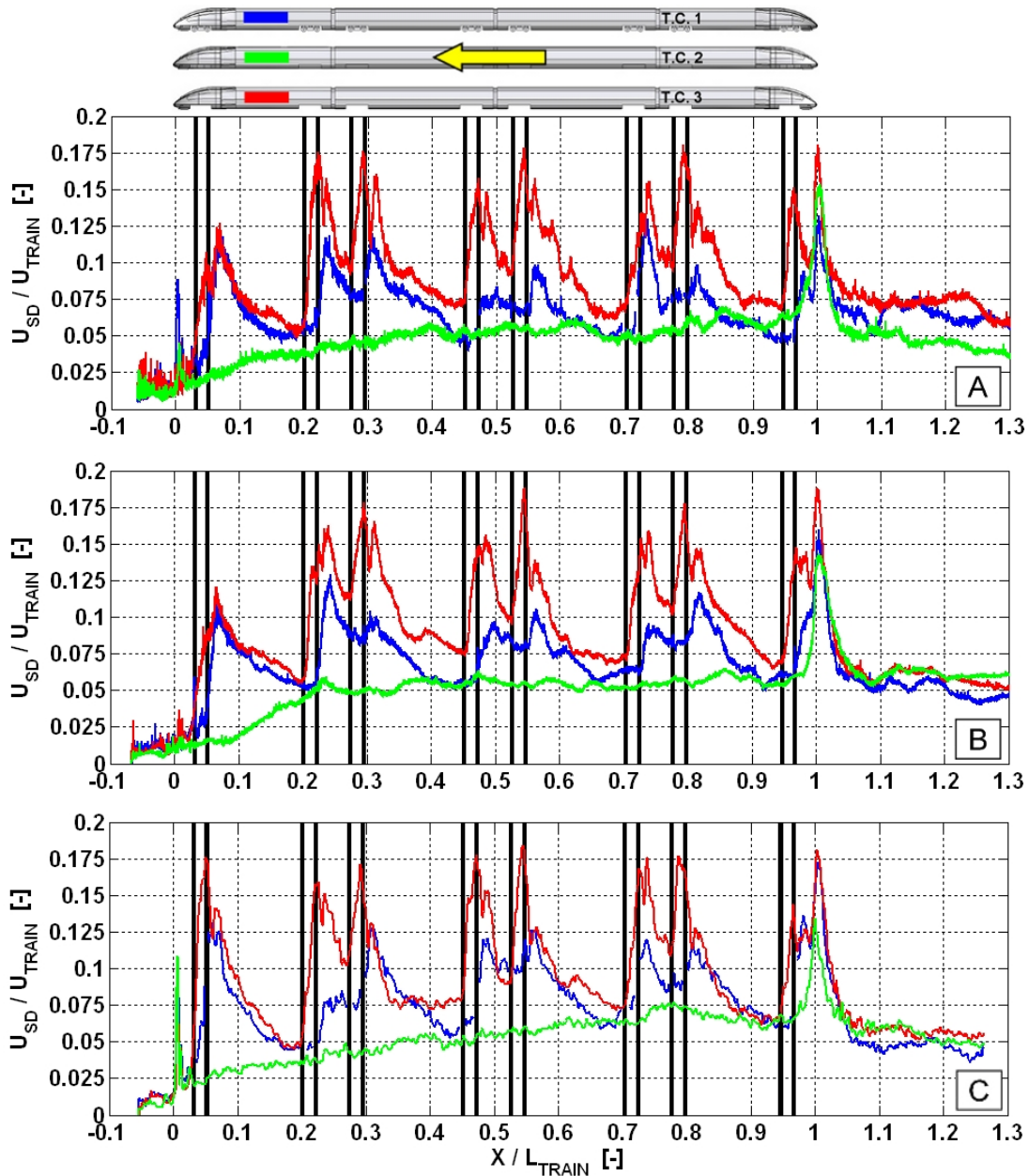


Figure 39: Normalised standard deviation of the velocity component in the travelling direction U_{SD} along the normalised train length at the height of the top of the rail ($Z / H_{GAP} = 0.476$) for the three considered train configurations on the smooth ground (G.C. A), the rough ground (G.C. B) and the ground with sleepers (G.C. C). The vertical lines indicate the positions of the train axes. $U_{TRAIN} = 4$ m/s.

tal profiles of the velocity fluctuations (U_{SD} and W_{SD}) reveal large values around the inter-car regions that decay quickly along the smooth undercarriage of the train car. This confirms (see section 6.3.1) that the generation of turbulence in the undercarriage flow is characterised by the inter-car regions. Additionally, the open bogie housings

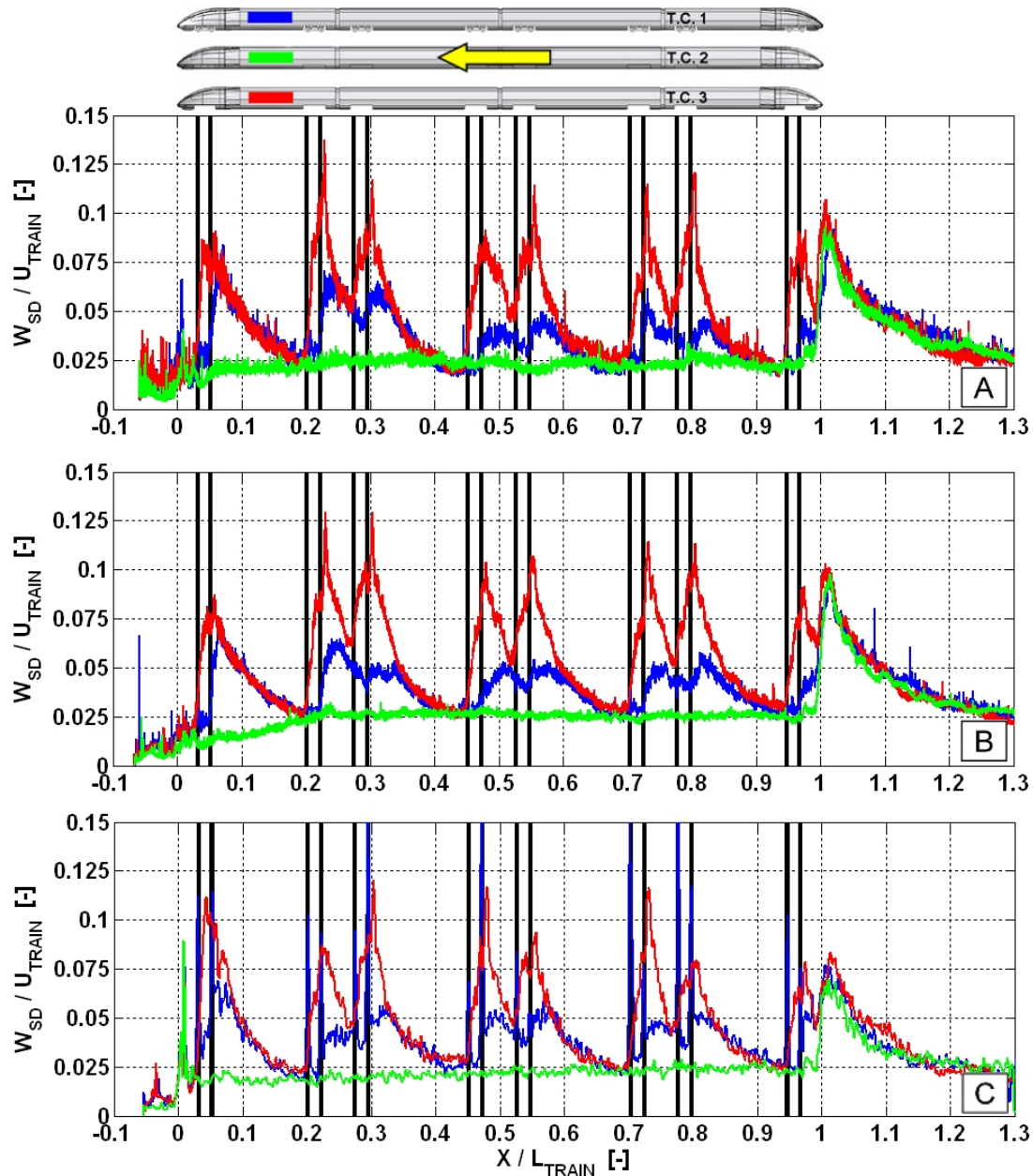


Figure 40: Normalised standard deviation of the velocity component in the vertical direction W_{SD} along the normalised train length at the height of the top of the rail ($Z / H_{GAP} = 0.476$) for the three considered train configurations on the smooth ground (G.C. A), the rough ground (G.C. B) and the ground with sleepers (G.C. C). The vertical lines indicate the positions of the train axes. $U_{TRAIN} = 4$ m/s.

of the rough train model (red lines in Figure 39 and 40) did not only have the strongest local effects but also increased the overall velocity fluctuations in the travelling direction (U_{SD}) along the entire train length. The characteristic production of turbulence in the undercarriage flow for the three considered train models on all ground conditions

quickly develops into a self-similar or repetitive pattern already after the second bogie of the train. Comparing the velocity fluctuations in the travelling direction (U_{SD}) with those in the vertical direction (W_{SD}) reveal that the turbulence in the undercarriage flow is anisotropic since the U_{SD} values are almost a factor of two larger than those of the W_{SD} . This was also found for full-scale measurements in the AOA-project [51], where the U_{SD} values were clearly larger than those in the lateral direction (V_{SD}). Like the mean undercarriage flow, the dominant component for the velocity fluctuations is the one in the travelling direction of the train. In the following sections of this work, the focus will therefore concentrate on the velocity component in the travelling direction. The importance of considering the velocity fluctuations in the risk assessment of ballast flight was already highlighted in section 6.1 and further accentuated by the instantaneous flow effects around the inter-car regions presented in section 6.3.2. In section 6.1, it was found that the histograms of the instantaneous velocity component in the travelling and the vertical directions were similar to Gaussian distributions. The Gaussian velocity distribution can be used to estimate the expected minimum and maximum instantaneous velocities with help of the empirical rule or 2σ -rule according to Vännman [109]. 95.45% of all values belonging to the Gaussian distribution are all within 2σ (2 standard deviations) of the mean value. The results in Figure 39 demonstrate that it is not only important to consider the velocity fluctuations for the reference and the rough train models but also for the smooth train model, since the u velocity values for the smooth train model can increase by as much as 10% (mean U velocity + $2 \cdot U_{SD}$). The velocity fluctuations should thus be included in the risk assessment of ballast flight for all high-speed trains, although they are highly optimised, to account for the effect of the turbulence in the undercarriage flow. The presented results thus far reveal that an increased undercarriage roughness from bogies, bogie housings, gaps, cavities, inter-car gaps, protruding objects or any geometric obstacle in general increases the expected maximum u velocity values and thus increase the chance of ballast flight. Furthermore, the results for the rough train model clearly demonstrate the increased susceptibility to ballast flight for trains with more airy bogie regions, with which the undercarriage flow develops more quickly, increasing the local and overall turbulence and inducing strong flow accelerations towards the trackbed. Last but not least, the general undercarriage flow characteristics of the considered train configurations remain unaffected by the different ground roughnesses of the three different trackbeds.

Spatial averages were calculated between the first and last train axle for the presented

normalised horizontal profiles of the mean U and W velocity and their standard deviations (U_{SD} and W_{SD}) at the height of the top of the rail to provide a simple overall overview of the flow effects found for the considered train and ground configurations. The calculated spatial averages of the considered configurations in the water-towing tank are listed in Table 4. The calculated spatial averages in Table 4 confirm the pre-

T.C.	G.C.	U / U_{TRAIN}	W / U_{TRAIN}	U_{SD} / U_{TRAIN}	W_{SD} / U_{TRAIN}
1	A	0.34390	0.00466	0.06932	0.03576
2	A	0.17268	0.00179	0.04890	0.02276
3	A	0.35493	0.00360	0.09947	0.05074
1	B	0.27909	0.00614	0.07361	0.03909
2	B	0.14644	0.00149	0.04916	0.02407
3	B	0.30124	0.00259	0.10226	0.05619
1	C	0.27911	0.00996	0.08147	0.03738
2	C	0.17082	0.00127	0.05273	0.02145
3	C	0.32461	0.00481	0.10212	0.05042

Table 4: Spatial averages between the first and last train axles of the normalised ensemble average U velocity, W velocity and their corresponding velocity fluctuations U_{SD} and W_{SD} at the height of the top of the rail ($Z / H_{GAP} = 0.476$) for all considered configurations.

vious statements that adding bogies, inter-car gaps, cavities or any other geometric obstacle increase the mean U velocities as well as the turbulence (U_{SD} and W_{SD}) in the undercarriage flow. Additionally, the averages also reveal, in accordance with the presented horizontal velocity profiles, that the dominating velocity component is the one in the travelling direction. The calculated averages over the train length, however, do not reflect the undercarriage flow characteristics. This is the case for the reference and the rough train models on the smooth ground, with distinctively different flow characteristics but almost the same calculated spatial average of the mean U velocity. The calculated spatial averages can therefore be used to identify general trends, but are considered to be less suitable for the risk assessment of ballast flight. The flow characteristics and most of all the local flow effects associated with large velocity and velocity fluctuation values drastically increase the load on the trackbed and are crucial to ballast flight. Nevertheless, the increased drag of the ground roughness (rough ground and the sleepers) lowered the mean U velocity values as the velocity fluctuations in the travelling direction increased (U_{SD}) for the three considered train configurations. This agrees with the theory of flows over rough surfaces and the full-scale measurements by Deeg et al. [51]. The ground roughness undercarriage flow effects are however analysed in detail in section 6.4. Calculated spatial averages of the

normalised horizontal profiles of the mean U and W velocities are found in Appendix B, along with their standard deviations (U_{SD} and W_{SD}) at different vertical heights between the first and last axle of the train as well as for the nearly fully developed undercarriage flow for the second half of the train.

6.3.4 Vertical velocity profiles

Regarding ballast flight, the undercarriage flow characteristics close to the ground are decisive for the ballast particle initiation and the ballast particle transport over the trackbed. Undercarriage flow field data were therefore extracted over the entire undercarriage gap at different positions along the train length. The vertical velocity profiles of the normalised mean U velocity over the normalised undercarriage gap at the middle of each train car are considered in Figure 41 for the three train configurations on the smooth ground (G.C. A), the rough ground (G.C. B) and the ground with sleepers (G.C. C). The vertical velocity profiles for the three considered train models on the different ground conditions reflect the results in Figure 37 in section 6.3.3 and confirm that a rougher train undercarriage (adding bogies, bogie housings, cavities, inter-car gaps or any other geometric obstacle) increases the mean U velocity values. The undercarriage flow field closest to the trackbed is responsible for the aerodynamic forces on the trackbed causing ballast particle dislodgement. The aerodynamic forces on the ballast are composed of both shear forces (proportional to the near-wall velocity gradient ($\partial U / \partial Z$) and the surface area exposed to the fluid, i.e., the "wetted surface") and pressure forces (proportional to the shape and cross-sectional surface of the exposed ballast particle), with both increasing quadratically with the flow velocity (U). The proportion of the aerodynamic forces (shear forces and pressure forces) is highly dependent on the position of the ballast particle. If the critical ballast particle is buried in the trackbed, the shear forces dominate, while the pressure forces dominate for the ballast particle exposed on the surface of the trackbed. The CFD simulations conducted by Garcia et al. [60] of a Couette-like flow over a ballast trackbed showed that over 90 % of the aerodynamic force on protruding sleepers (using different trackbed designs) consisted of pressure forces. Based on this, it is concluded that the forces acting on the exposed ballast particles in the trackbed are essentially pressure forces. This also agrees with the theory of bluff body aerodynamics [110]. Besides the dislodgement of ballast particles from the trackbed, the undercarriage flow close to the ground determines the momentum transfer to the dislodged ballast

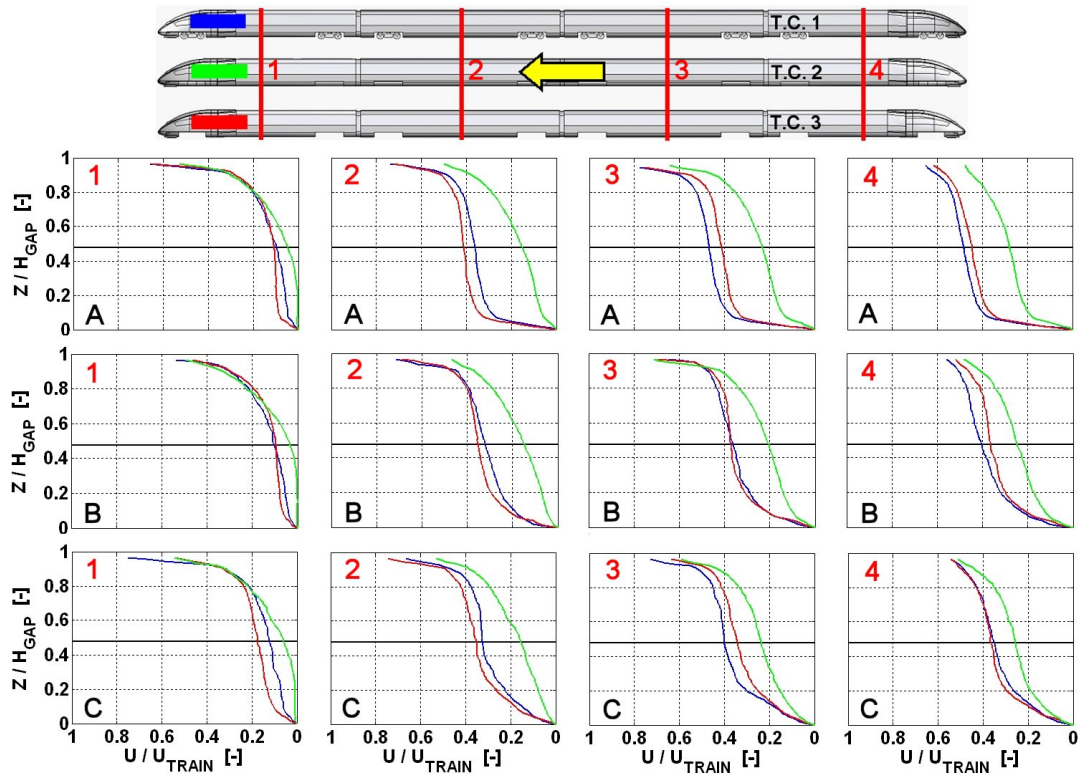


Figure 41: Normalised vertical profiles of the velocity component in the travelling direction U over the undercarriage gap for the three considered train configuration on the smooth ground (G.C. A), the rough ground (G.C. B) and the ground with sleepers (G.C. C). The horizontal black line indicates the height of the top of the rail. $U_{TRAIN} = 4$ m/s.

particles and is therefore crucial for the vertical heights that are reached by upward deflection from the trackbed that might result in ballast flight. Considering the lower velocity gradients ($\partial U/\partial Z$) and mean U velocity values in the vicinity of the trackbed (i.e. aerodynamic forces) for the smooth train model in comparison to the two other train models demonstrates the effectiveness of smoothing the train undercarriage. This indicates that bogies, bogie housings, inter-car gaps, cavities, gaps or other geometric obstacles increase the velocity gradients and the velocity magnitudes close to the trackbed and therefore increase the aerodynamic forces on the trackbed and the risk of ballast flight.

In Figure 42, vertical U_{SD} profiles in the middle of each train car are presented for the three different train models on all ground conditions. The results in Figure 42 also reflect the presented horizontal U_{SD} distributions in Figure 39 and reveal that the undercarriage roughness increases the turbulence level in general over the entire undercarriage gap, independent of the considered ground configuration. The nearly

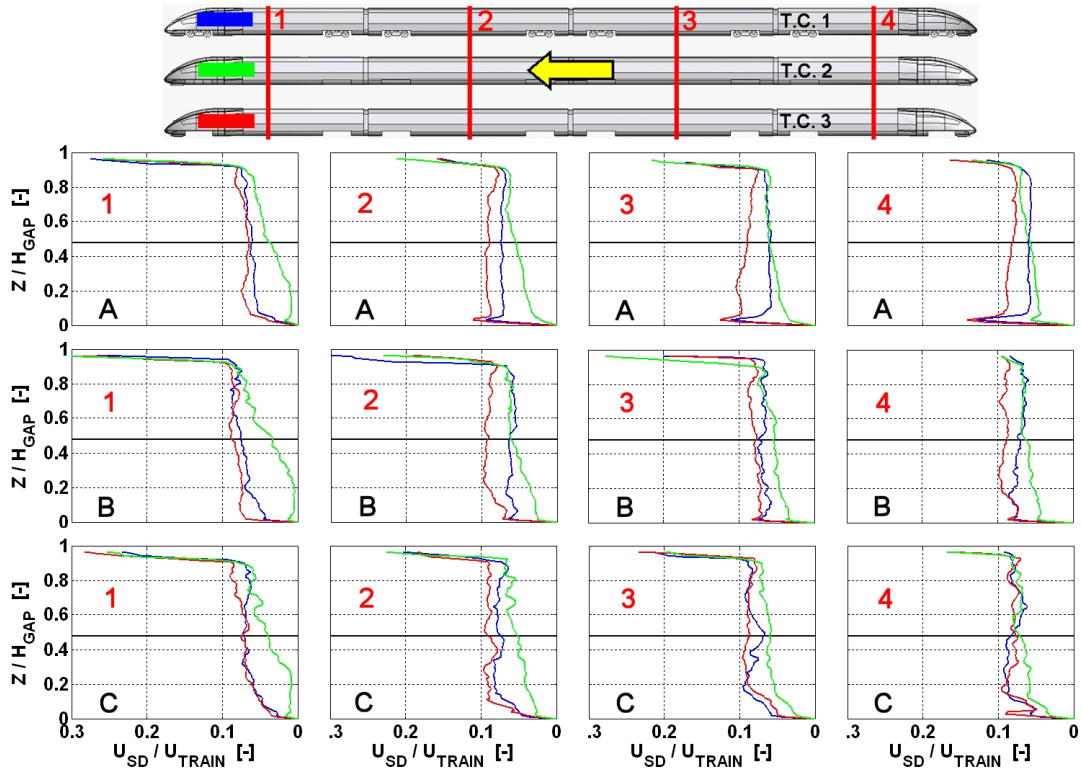


Figure 42: Normalised vertical profiles of the standard deviation of the velocity component in the travelling direction (U_{SD}) over the undercarriage gap for the three considered train configuration on the smooth ground (G.C. A), the rough ground (G.C. B) and the ground with sleepers (G.C. C). The horizontal black line indicates the height of the top of the rail. $U_{TRAIN} = 4$ m/s.

constant turbulence level over the undercarriage gap in the trackbed line of symmetry away from the bogie regions is in keeping with the Couette-flow [56]. The importance of considering the turbulence in the undercarriage flow regarding the expected maximum u velocity affecting ballast flight was stated before. The turbulence in the undercarriage flow also increases the shear stress on the trackbed ballast. According to the Boussinesq approximation, used in numerical simulations like RANS and LES, the momentum transfer in turbulent flows caused by the turbulent eddies is modelled with an additional turbulent viscosity (μ_t) (also known as the eddy viscosity), analogously to the transfer of momentum by the molecular motion in a gas ([108]). Highly turbulent flows are characterised by large turbulent viscosity values increasing the wall shear stress according to Equation (9).

$$\tau_w = (\mu_f + \mu_t) \frac{\partial U}{\partial Z} \quad (9)$$

Nevertheless, using Boussinesq approximation to model the turbulence with an additional turbulent viscosity (μ_t) indicates that turbulence in the undercarriage flow also increases the drag of the train. Smoothing of the undercarriage therefore decreases the drag of the train as well as the chance of ballast flight by lowering the shear stresses on the trackbed ballast and the expected maximum velocity values close to the trackbed.

The presented horizontal and vertical mean U velocity and U_{SD} profiles reveal critical undercarriage structures that increase the susceptibility to ballast flight. Primarily, the presented results show that undercarriage cavities should be avoided or minimised including with the use of tight bogie housings. Furthermore, it is recommended to smoothen the undercarriage of the train by using closed and flushed inter-car gaps, bogies with smooth lower surfaces that are aligned with the train undercarriage and of course with the removal of all protruding objects from the undercarriage. Cooling air outlets towards the trackbed influence the undercarriage flow similarly to protruding objects [39] and should of course be avoided. Striving for the undercarriage flow characteristics of the smooth train model by realising the proposed measures would decrease the aerodynamic forces on the trackbed by lowering the mean U velocity values, velocity gradients and the turbulence levels, thereby reducing the occurrence of ballast flight.

6.4 Ground roughness effects

The behaviour of flows over rough surfaces is a topic of interest for many technical applications as well as for the undercarriage flow of high-speed trains. Regarding ballast flight, the undercarriage flow characteristics close to the trackbed and the influence by its roughness are important for the accurate evaluation of the risk of ballast flight. The fact that different trackbed designs are used for high-speed lines makes it extremely challenging to define a global trackbed roughness representative of the various existing trackbeds. Modern trackbeds can be divided into three major groups, i.e. ballastless concrete trackbeds (slab tracks), ballast trackbeds with bi-block sleepers and ballast trackbeds with monoblock sleepers. Within every trackbed subgroup differences in design exist that alter the global roughness of the trackbed. This is especially the case for the ballast trackbed with monoblock sleepers with different sleeper spacing, sleeper width (X direction) and ballast level (height relative to the upper surface of the sleepers). For all ballast trackbeds, the ballast properties such as

the size, the shape and the degradation of the ballast with time influence the global roughness of the trackbed. The detailed influence of the smooth ground, the rough ground and the ground with sleepers on the undercarriage flow field in the trackbed line of symmetry are presented and discussed in the following sections.

6.4.1 Flow field over the rough ground

The rough ground condition, shown in Figure 10 in section 4.3, was realised by adhering a grinding belt on plexiglass plates mounted on and additional to the original ground plate. The necessary optical access for PIV, in this case for the laser light sheet, was assured by removing 200 mm of the applied grinding belt. The flow effects induced by the rough-to-smooth transition are presented in Figure 43 for the normalised ensemble average U velocity and in Figure 44 for its corresponding standard deviation U_{SD} . The presented vertical velocity profiles in Figure 43 and Figure 44 were all extracted for the fully developed flow at the middle of the trailing end-car of the reference train model at different downstream positions from the rough-to-smooth ground roughness transition. Assuring statistically converged results of the ground roughness effect, all PIV double-image recordings (~ 450 instantaneous flow fields) capturing the middle of the trailing end-car (one PIV camera with a field of view of 40 mm x 27 mm ($W \times H$)) were used to extract flow field data for the fixed ground positions presented in Figure 43 and in Figure 44. The influence on the flow field of the slightly shifted or "wrong" train position (< 30 mm) used for the calculation of the mean U velocity and for U_{SD} diminishes for the fully developed flow along the smooth undercarriage in the middle of the trailing end-car. Comparing the results in Figure 43, in accordance to the measured vertical velocity profiles for a rough-to-smooth surface roughness transition in a wind tunnel by Jacobs [52], there is a progressively steeper velocity gradient close to the ground ($Z / H_{GAP} < 0.25$) with increasing distance to the rough-to-smooth ground roughness transition. The U velocity values away from the ground ($Z / H_{GAP} > 0.25$) for the measured region are not influenced by the ground roughness transition. Nevertheless, with an increasing distance to the ground roughness transition it is presumed that the vertical velocity distribution gradually approaches the velocity values found for the vertical velocity distribution on the smooth ground (i.e. an overall increase of the U velocity values). This is indicated by the vertical profiles of the velocity fluctuations U_{SD} in Figure 44, where the two downstream (20 and 30 mm) vertical profiles approach the charac-

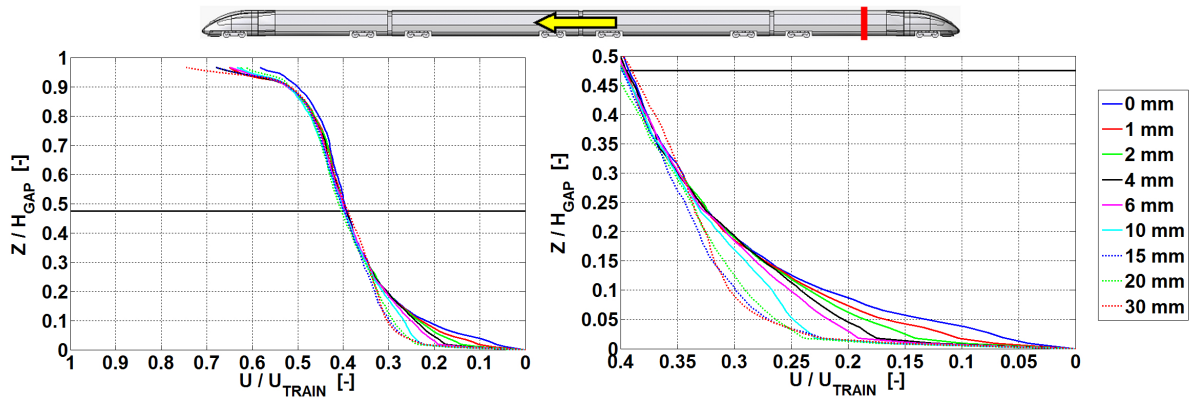


Figure 43: Vertical profiles of the mean U velocity at the middle of the trailing end-car for the reference train model (T.C. 1) at different downstream positions from the rough-to-smooth ground roughness transition (G.C. B). The horizontal black line indicates the height of the top of the rail. $U_{TRAIN} = 4$ m/s.

teristic shape found for the velocity fluctuations on the smooth ground in Figure 42 in section 6.3.4. Furthermore, the results for the standard deviation U_{SD} in Figure 44 show analogously to the mean U velocity that the ground roughness change primarily influence the velocity fluctuations closest to the ground ($Z / H_{GAP} < 0.2$). The velocity fluctuation values (U_{SD}) gradually increase with an increasing distance to the ground roughness transition.

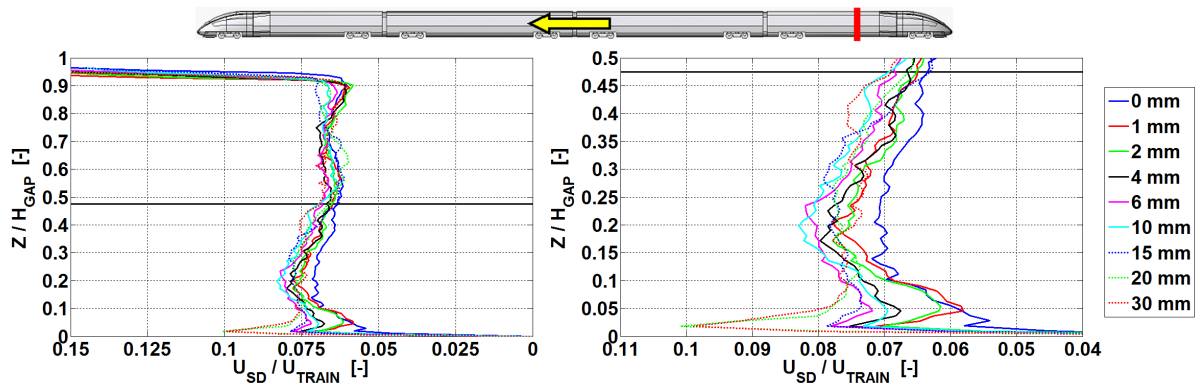


Figure 44: Vertical profiles of the standard deviation U_{SD} at the middle of the trailing end-car for the reference train model (T.C. 1) at different distances from the rough-to-smooth ground roughness transition (G.C. B). The horizontal black line indicates the height of the top of the rail. $U_{TRAIN} = 4$ m/s.

To realise statistically reliable quantities for the presented vertical velocity profiles in section 6.3.4, a compromise between the sample size and the presented ground effects was required. The satisfactory sample size (~ 90) for a fixed train position was

obtained by extracting flow field data from the region 0-4 mm downstream from the rough-to-smooth ground roughness transition. Nevertheless, for the mean U velocity the effect of the rough-to-smooth ground roughness transition was still noticeable for the extracted data. The velocity profiles of the mean U velocity extracted 0-4 mm downstream from the ground roughness transition with a fixed train position were compared to those with a fixed ground position of 1 mm downstream from the ground roughness transition using all PIV recordings at the corresponding train position. The comparison demonstrated a nearly constant offset for the core of the undercarriage flow ($Z / H_{GAP} = 0.2 - 0.95$), which increased towards the ground ($Z / H_{GAP} < 0.2$). The small offset in the core of the undercarriage flow between the vertical distributions is considered to be dominated by the train position, whereas the larger difference closer to the ground is mainly influenced by the distance to the rough-to-smooth ground roughness transition. The presented vertical velocity profiles in section 6.3.4 were therefore all corrected for the region closer to the ground ($Z / H_{GAP} < 0.2$) by calculating the difference between the two aforementioned vertical velocity profiles. The mean difference found for the core of the undercarriage flow ($Z / H_{GAP} = 0.2 - 0.95$) was however first subtracted from the calculated difference and thus only the region closest to the ground was corrected. Additionally, no systematic significant difference was found for the results of the standard deviation U_{SD} , as for the mean U velocity, at the position closest to the ground roughness transition and a data correction was therefore considered to be redundant.

6.4.2 Flow field over the sleepers

The development of the undercarriage flow over the sleepers in the water-towing is described and discussed below using the ensemble average of the U and W velocity together with the standard deviation U_{SD} . Like for the rough ground, all instantaneous flow fields for the middle of the trailing end-car for the reference train model were used to calculate the statistical quantities, thus neglecting the train shift. A sample size of ~ 430 instantaneous flow fields, was used to calculate the statistical quantities. Figure 45 presents the general flow field over the sleepers around the middle of the trailing end-car with the ensemble average velocities U and W . The mean U velocity (upper graphic in Figure 45) reveals a periodic flow pattern with flow accelerations over every sleeper caused by the undercarriage gap contraction of $\sim 10\%$. At the downstream edge of every sleeper a flow separation is identified, causing a

recirculation zone covering nearly 30-40% of the inter-sleeper region before the flow reattaches again. Regarding ballast flight, the inter-sleeper region is of interest since this is the location of the ballast. The separated flow region downstream of a sleeper is therefore considered to be beneficial to reducing the risk of ballast flight since this region is associated with low velocity values close to the ground and small wall-shear stresses. The mean vertical velocity component W (lower plot in Figure 45) clearly shows the strong influence of the protruding sleepers on the flow field in the vicinity of the ground. Nevertheless, it also confirms the wavy flow behaviour obtained for the mean U velocity field, with flow accelerations over the sleepers, flow separations at the downstream sleeper edges and reattachment of the flow in the inter-sleeper regions.

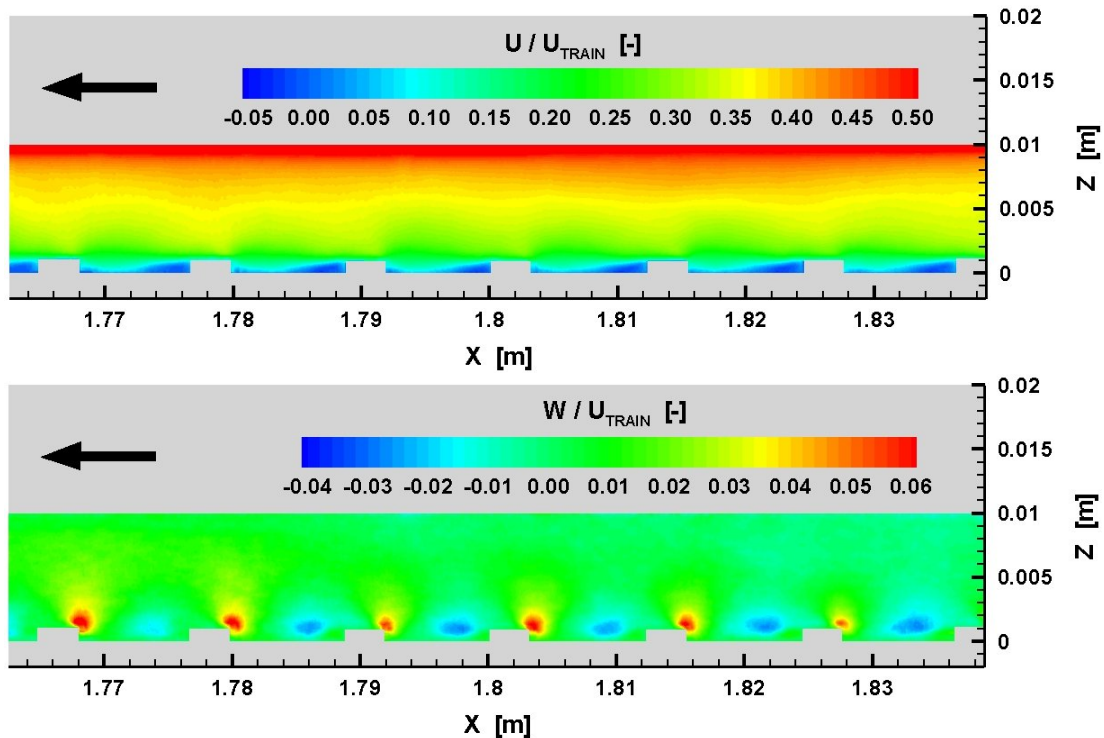


Figure 45: Normalised mean U (upper) and W (lower) velocity field over the sleepers at the middle of the trailing end-car for the reference train model (T.C. 1) for $U_{TRAIN} = 4$ m/s.

The more detailed presentation of the undercarriage flow characteristics over the ground with sleepers are shown in Figures 46 - 48 for the fully developed flow around the middle of the trailing end-car for the reference train model. The extracted vertical profiles of the mean U velocity in the inter-sleeper region at different locations from the downstream edge of a sleeper (upper row in Figure 46) reveal that the no-

table differences are all found below the height of the top of the rail. Additionally, the results in Figure 46 reflect the earlier identified flow regions found for the mean U velocity flow field in Figure 45. The vertical profiles closest to the sleeper (i.e. 0.5

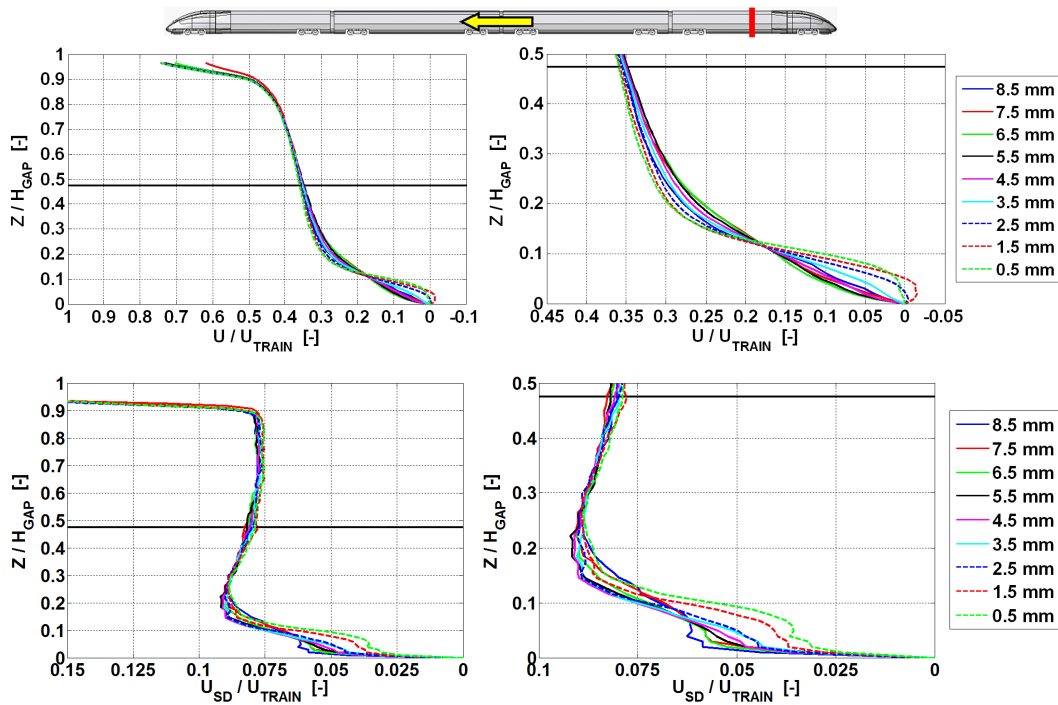


Figure 46: Normalised vertical profiles of the mean U velocity (upper row) and the corresponding U_{SD} (lower row) in the inter-sleeper region at different downstream positions from the sleeper and at the middle of the trailing end-car for the reference train model (T.C. 1). The horizontal black line indicates the height of the top of the rail. $U_{TRAIN} = 4$ m/s.

mm, 1.5 mm and 2.5 mm) in the right graphic in Figure 46 reflect the accelerated flow over the sleeper responsible for the largest mean U velocities just above the height of the sleeper ($Z / H_{GAP} = 0.1$). The flow separation and the recirculation zone immediately downstream of the sleeper are identified for the region close to the ground ($Z / H_{GAP} < 0.1$) for the very same velocity profiles. With an increasing distance to the downstream edge of the sleeper the flow reattaches ($\Delta X \sim 3$ mm) and the ground boundary layer develops until the next sleeper. The maximum mean U velocity value close to the ground for the reattached flow in the inter-sleeper region is found at a distance of 6.5 mm from the downstream edge of the sleeper (corresponding to a distance of 8 mm from the centre of the sleeper). This position was used in the previous graphics and will be used for the following graphics to represent the most interesting position, in the inter-sleeper region regarding ballast flight. The vertical profiles of the mean U velocity close to the sleeper in Figure 46 confirm the sudden air velocity

drop obtained in the full-scale measurements of the Korean high-speed train KTX by Kwon and Park [29] between Kiel-probes installed 20 mm above and 20 mm below the upper surface of the sleepers. The mean U velocity flow characteristics presented for the inter-sleeper region resemble the corresponding velocity fluctuations in Figure 46 in the sense of the shielding effect of the sleepers resulting in a sudden drop in the velocity fluctuations. Furthermore, the accelerated flow over the sleepers induces increased values of the streamwise turbulence. The shielding effect of the sleepers reduces the aerodynamic forces on the ballast in the inter-sleeper region by decreasing the shear forces (flat velocity gradients and low turbulence levels according to Equation (9)) as well as the pressure forces (decreasing the expected maximum u velocity values), reducing the risk of ballast flight.

The vertical velocity profiles of the mean U velocity and its standard deviation U_{SD} for the accelerated flow over a sleeper are presented in Figure 47 for different stream-wise positions on top of the sleeper. The results of the mean U velocity reveal that

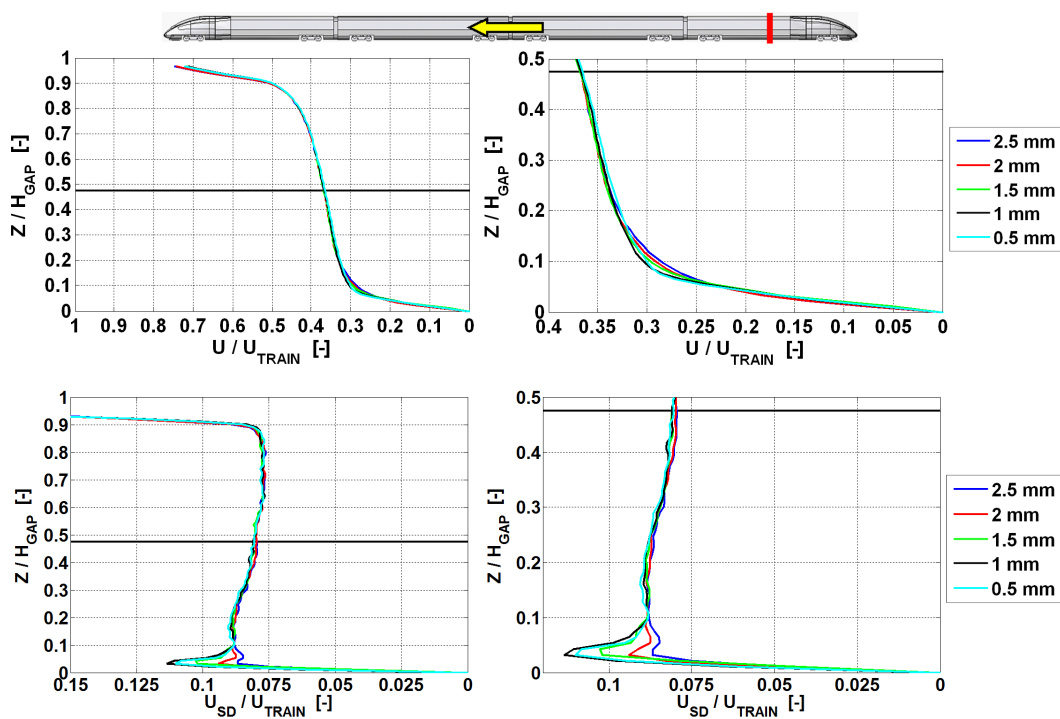


Figure 47: Normalised vertical velocity profiles of the mean U velocity (upper row) and the corresponding U_{SD} (lower row) above a sleeper at different distances from the upstream sleeper edge for the undercarriage flow at the middle of the trailing end-car for the reference train model (T.C. 1). The horizontal black line indicates the height of the top of the rail. $U_{TRAIN} = 4$ m/s.

the accelerated flow is more or less independent of the location on top of the sleeper.

However, for the extracted streamwise velocity fluctuation profiles (U_{SD}), the development of the intense shear layer close to a sleeper's upper surface at the upstream edge clearly separates the profiles from each other. The intense shear layer was also found on top of wall ribs by Cui et al. [111] for LES-simulations of a turbulent channel flow with wall ribs.

The mean U velocity profile and its corresponding standard deviation at the central position above the sleeper are compared to the inter-sleeper position 6.5 mm from the downstream edge of a sleeper (8 mm downstream from the centre of a sleeper) in Figure 48. The comparison in Figure 48 clearly shows the flow speed increase caused by

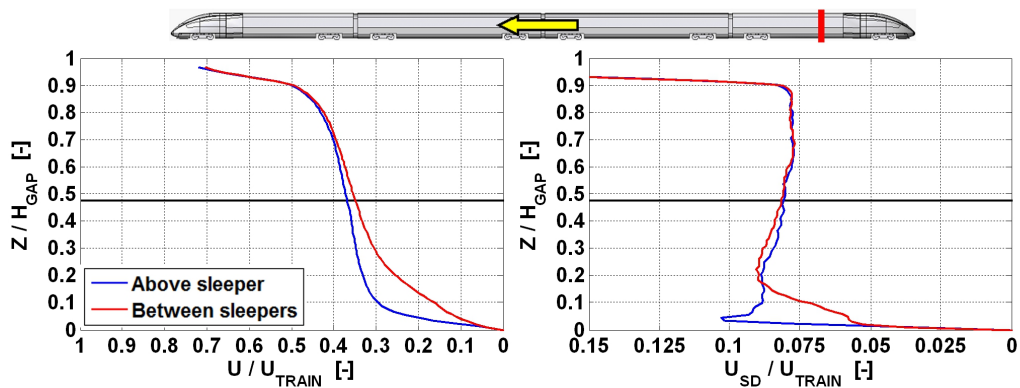


Figure 48: Comparison between the vertical profiles of the normalised mean U velocity (left) and its corresponding standard deviation U_{SD} above a sleeper (middle) and in the inter-sleeper region ($\Delta X = 8$ mm) for the undercarriage flow at the middle of the trailing end-car for the reference train model (T.C. 1) for $U_{TRAIN} = 4$ m/s.

the undercarriage gap contraction of $\sim 10\%$ leading to larger mean U velocity, streamwise velocity fluctuation values close to the ground and steeper velocity gradients at the ground for the flow over a sleeper. The increased flow properties just mentioned relate to an, increased risk of ballast flight if ballast particles for some reason are lying on top of sleepers instead of in the inter-sleeper regions. The results also show that using only one vertical measurement position, e.g. at the height of the top of the rail, might result in misleading assumptions regarding the risk assessment of ballast flight. It is therefore recommended to measure the entire vertical distribution of the flow field below the top of the rail in order to capture ground effects similar to those presented in Figure 48.

6.4.3 Equivalent roughnesses of the different ground configurations

The undercarriage flow over the rough ground and the ground with sleepers agrees well qualitatively with the theory for wall-bounded flows over rough surfaces as well as with the findings from full-scale measurements (see sections 6.4.1 and 6.4.2). Nevertheless, the large Reynolds number difference, $0.25 \cdot 10^6$ in the water-towing tank compared to $16.45 \cdot 10^6$ for a full-scale high-speed train at 300 km/h based on the reference length of 3 m [94] and the train speed, introduces undercarriage flow differences. This especially applies for the boundary layer on the trackbed and for the train undercarriage. Calculations using the $1/7^{\text{th}}$ power law for a fully turbulent boundary layer on a smooth plate was conducted to estimate the boundary layer thickness and the skin-friction coefficient (C_f) in the middle of the fourth train car. The results reveal that the boundary layer thickness and the skin-friction coefficient (C_f) in the water-towing tank experiments should be larger by a factor of ~ 2.3 in comparison to those of a full-scale high-speed train at 300 km/h due to the Reynolds number difference. Since the roughness elements of the rough ground and the ground with sleepers (grain size and sleeper height, respectively) were simply scaled with the model scale (1:50), the relative height of the roughness elements (roughness element height / boundary layer thickness) is changed due to the thicker boundary layer in the water-towing tank. Scaling the roughness elements with the boundary layer thickness instead of the model-scale, the 50 mm sleeper height in full-scale can be considered to be approximately 22 mm, as the grain size of 38 mm in full-scale represents a 17 mm grain for the rough ground. The grain size of 17 mm (scaled with the boundary layer thickness) for the rough ground is outside the ballast size distribution (22.4 mm to 63 mm according to EN-13450 [98]) normally used for the European ballast trackbeds. However, considering ballast fouling and standards of other countries according to Guler and Mert [112], a ballast particle size around 17 mm is still considered as realistic. Throughout Europe, the sleeper height or ballast level for monoblock ballast trackbeds are found to have ballast levels from 60 mm below to flush (0 mm) with the upper surface of the sleepers [31, 35, 45, 60]. The roughness elements applied for the rough ground and the ground with sleepers are therefore considered to be within a realistic range, independent of the Reynolds number dependent scaling methods that are used.

In the theory of turbulent flows over rough surfaces, the roughness parameter also known as the roughness Reynolds number (k_s^+) is commonly used to define the bound-

ary layer characteristics with respect to the surface roughness. The roughness Reynolds number (see Equation (10)) is analogous to the Reynolds number but with the friction velocity (U_τ) and the equivalent sand grain roughness (k_s) in place of the free-stream velocity (U_∞) and a characteristic length.

$$k_s^+ = \frac{k_s \cdot U_\tau}{\nu} \quad (10)$$

The roughness Reynolds number in Equation (10) determines whether the wall can be treated as smooth (hydraulically smooth), transitional or fully rough. Schlichting [56] presented a physical interpretation of the three wall roughness regimes. For a wall to be treated as hydraulically smooth the roughness elements must be completely submerged in the viscous sub-layer, yielding the same wall friction drag as a smooth wall. In the transition regime, the onset of the wall roughness effects increase the wall friction drag since roughness elements are slightly thicker than the viscous sub-layer. If the roughness elements are much larger than the viscous sub-layer is, the viscous sub-layer is destroyed and the wall friction drag becomes dominated by the form drag of the roughness elements in the fully rough regime. In the literature, different limits are found for the wall roughness regimes, e.g. the proposed limit for the fully rough regime is: $k_s^+ = 55$ according to Rotta [113], $k_s^+ = 70$ according to Schlichting [56] and $k_s^+ = 100$ according to Mohrig [114]. This indicates, in agreement with Schultz and Flack [115], that the limits of the roughness regimes are strongly dependent on the roughness type, uniformity and distribution. Therefore, Jiménez [116] recommends to treat every surface individually. Determining the wall roughness regime belonging to the rough ground and the ground with sleepers used in the water-towing tank, the friction velocity (U_τ) must be determined. The friction velocity is also of great interest for the skin-friction coefficient comparison with full-scale measurements. Determining the wall shear stress (τ_w) by the direct evaluation of the velocity gradient ($\tau_w = \mu(\partial U / \partial Z)$) in the viscous sub-layer is known to be a difficult task to measure experimentally. Therefore, indirect methods using wall similarity methods, like the well-known law of the wall, are one of the most commonly applied methods for the estimation of the wall shear stress. Applying the law of the wall requires that the boundary layer is fully developed, in equilibrium conditions, over a smooth and flat wall and with no longitudinal pressure gradient. Fulfilling the mentioned flow requirements, the logarithmic region (log-law) in the boundary layer for the mean velocity distribution can be expressed as a function of the friction velocity,

as in Equation (11).

$$U^+ = \frac{1}{\kappa} \ln(Z^+) + B \quad (11)$$

The dimensionless variables of the log-law for smooth grounds (Equation (11)) are defined as $U^+ = U / U_\tau$ and $Z^+ = (Z \cdot U_\tau) / \nu$, where the ν is the kinematic viscosity of the fluid and U_τ the friction velocity. The smooth-wall log-law intercept $B = 5.0$ and the von Karman constant $\kappa = 0.41$ are two empirical constants. The corresponding log-law for the rough ground is expressed as for the smooth ground in Equation (11). Instead of the viscous length scale (ν / U_τ) the equivalent sand grain roughness (k_s) is used together with a log-law intercept B , assuming different values for the transition regime and 8.5 for the fully rough regime. A simpler technique for the evaluation of the wall roughness effect was presented by Clauser [117] and Hama [118], demonstrating a downshift in the log-law caused by the surface roughness and defined as the roughness function (ΔU^+). The log-law for smooth walls are used together with the roughness function (see Equation (12)) to represent boundary layers for smooth walls ($\Delta U^+ = 0$) as well as for rough walls.

$$U^+ = \frac{1}{\kappa} \ln(Z^+) + B - \Delta U^+ \quad (12)$$

Considering the flow conditions required to apply the law of the wall and the undercarriage flow characteristics of high-speed trains, the law of the wall is most applicable to the fully developed Couette-like and ensemble averaged undercarriage flow in the middle of a train car. In the middle of a train car, the strong flow accelerations and larger pressure gradients around the bogie regions are avoided. The full-scale measurements by Deeg et al. [47] and the full-scale measurements in section 7 however revealed a positive longitudinal pressure gradient within the undercarriage flow along the smooth train car. Despite the longitudinal pressure gradient and the dynamics of the undercarriage flow caused by the bogie regions, the law of the wall was applied for the undercarriage flow at the middle of the trailing end-car for the reference train model on the different ground conditions. According to Baron and Quadrio [119], there are several flows that do not in practice fulfil the requirements for the law of the wall, but for which it still delivers satisfactory results. The smooth ground condition was used as a reference case to confirm that the applied techniques provide reliable values of the friction velocity. The Clauser chart method [78] and the so-called standard slope method [119] were used to determine the friction velocity

under the assumption that the smooth plexiglass plate can be treated as hydraulically smooth. The results for the smooth ground in Figure 49 confirm that the smooth ground can be treated as hydraulically smooth and that the Clauser chart method and the standard slope method provide reliable results, as both results coincide and fit the curve of the law of the wall. The standard slope method was used for the fric-

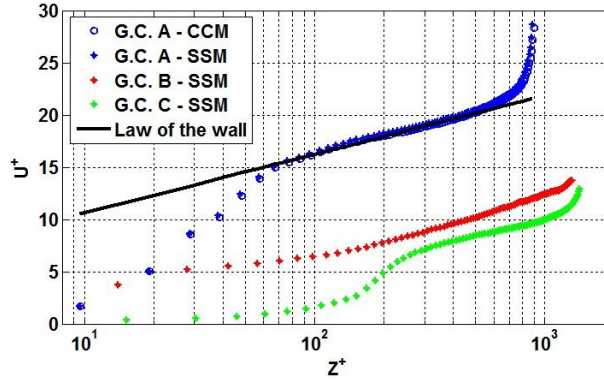


Figure 49: Mean velocity profiles using inner variables for the undercarriage flow at the middle of the trailing end-car for the reference train model (T.C. 1) on the smooth ground (G.C. A), rough ground (G.C. B) and the ground with sleepers (G.C. C), together with the law of the wall for a smooth wall using the Clauser chart method (CCM) and the standard slope method (SSM) for the determination of the friction velocity. $U_{TRAIN} = 4$ m/s.

tion velocity evaluation of the rough ground and the ground with sleepers since the Clauser chart method is only valid for smooth grounds. The friction velocity for the ground with sleepers was calculated analogously to the work by Cui et al. [111] and Garcia et al. [60] from the streamwise-averaged flow over the sleepers. The average flow field over the sleepers was calculated from the vertical velocity profiles of the mean U velocity at nine different positions in the inter-sleeper region and for three locations above the sleeper. The downshift of the mean velocity profiles in Figure 49 highlights the increased drag of the rough ground and the ground with sleepers. The calculated values of the friction velocity and the downshift or roughness function are listed in Table 5. As previously mentioned, the upper critical limit (fully rough) of the roughness Reynolds number is highly dependent on the roughness elements. The roughness Reynolds number was calculated according to Equation (10), but with the physical mean size of the roughness elements (k) instead of the equivalent sand grain roughness. The calculated roughness Reynolds number (k^+) of 107 for the rough ground and 153 for the ground with sleepers, respectively, suggests that both ground conditions are in the fully rough regime (>100 [114]). Furthermore, the different roughness functions presented by Jiménez [116], including the classical

Ground config.	U_τ [m/s]	ΔU^+ [-]	k_s^+ [-]	k_s [m]
Smooth (G.C. A)	0.096052	-	-	-
Rough (G.C. B)	0.141462	10.02	255	0.001818
Sleepers (G.C. C)	0.153696	11.68	504	0.003304

Table 5: The estimated friction velocity according to the standard slope method, the roughness function extracted from Figure 49, the roughness Reynolds number and the equivalent sand grain roughness using Equation (13) for the reference train model (T.C. 1) on the considered ground conditions.

roughness functions of Nikuradse [120] and Colebrook [121], reveal that for ΔU^+ values greater than ~ 7 , all roughness functions collapse on one another and the fully rough regime is reached. Since the roughness function of both ground conditions is larger than 10 and that the calculated roughness Reynolds numbers ($(U_\tau \cdot k) / \nu$) are larger than all the presented critical upper limits for the fully rough regime (>100), the rough ground and the ground with sleepers can be concluded to be in the fully rough regime. The equivalent sand grain roughness (k_s) and the roughness Reynolds number (k_s^+) could therefore be calculated using Equation (13), which is deduced by subtracting the log-law for smooth walls from the log-law for fully rough walls.

$$\Delta U^+ = \frac{1}{\kappa} \ln(k_s^+) - 3.5 \quad (13)$$

The results in Table 5 confirm once again that the rough ground and the ground with sleepers used in the water-towing tank experiments are in the fully rough regime since the roughness Reynolds numbers (k_s^+) are clearly larger than 100. The full-scale measurements of the undercarriage flow by Lazaro et al. [31] also concluded that the ballast trackbed with monoblock sleepers is in the fully rough regime. This was also the case for the numerical simulations by Garcia et al. [60] of a Couette-flow over a trackbed with monoblock sleepers. Besides both the rough ground and the ground with sleepers being in the fully rough regime, the friction velocity and the roughness function indicate that the drag of the ground with sleepers is larger than that for the rough ground. The larger drag resulting from the sleepers is correlated with the larger projected surface perpendicular to the main flow of the sleepers, 1×52 mm (H x W), than the projected surface of the distributed grains with diameters less than 0.764 mm. The equivalent sand grain roughness calculated for the ground with sleepers in the water-towing tank ($k_s = 0.003304$ m) is more or less the same as the value found for the CFD simulations of a Couette-flow over a ballast trackbed with monoblock sleep-

ers [60]. The nearly identical values of the equivalent sand grain roughness imply that the protruding sleepers dominate the wall roughness effect and that the ballast roughness between the sleepers (simulated in the CFD simulations and neglected in the water-towing tank experiments) may not be necessary for the simulation of a ballast trackbed with monoblock sleepers and a lowered ballast level of 5 cm in full-scale. The skin-friction coefficients (C_f) determined in the water-towing tank for the reference train model were compared to the previously mentioned CFD simulations of the simplified Couette-flow by Garcia et al. [60] and to those of Jönsson [63] on a highly detailed ICE3. The CFD simulations were conducted under realistic flow conditions with a Reynolds number of $\sim 15 \cdot 10^6$. The skin-friction coefficient comparisons with the CFD simulations of Couette-flow over a trackbed with sleepers and with the CFD simulations of the ICE3 on a smooth ground reveal that the values obtained in the water-towing tank experiments were larger by a factor of 2.4 and 1.95, respectively. The CFD simulations on the ICE3 by Jönsson [63] were compared to full-scale measurements with Preston-probes installed in a concrete slab track, demonstrating that the skin-friction coefficients estimated by CFD were in a satisfactory range compared to those obtained from full-scale measurements. The skin friction coefficient difference due to the Reynolds number difference between the water-towing tank experiments and a full-scale high-speed train was previously estimated to differ by a factor of ~ 2.3 using the $1/7^{th}$ power law of a fully turbulent boundary layer on a smooth wall. The large C_f differences between the experiments in the water-towing tank with downscaled train models, CFD simulations with realistic flow conditions and full-scale measurements are therefore considered to be essentially a Reynolds number effect.

The analytical solution of a Couette-flow presented by Garcia et al. [60], considering both undercarriage and trackbed as smooth walls, provides skin-friction coefficients that satisfactorily agree with full-scale measurements as well as with the downscaled experiments in the water-towing tank. Therefore, the analytical solution is suitable for estimating the wall shear stress for the fully developed Couette-like mean undercarriage flow.

6.4.4 Ground roughness effects on the undercarriage flow for the considered train models

For the thorough analysis of the ground roughness effect of the three ground condi-

tions used in the water-towing tank experiments, vertical profiles of the mean U velocity and its standard deviation U_{SD} were extracted along the entire train model length. Flow field data of the flow accelerated over the sleeper (centre of the sleeper) and in the inter-sleeper region ($\Delta X = 8$ mm downstream from the centre of the sleeper) were used to represent the undercarriage flow over a trackbed with cross-going (monoblock) sleepers. The ground roughness effect is compared separately for each train configuration. The results for the mean U velocity extracted at the centres of the four train cars and presented in Figure 50 reveal that the ground roughness effect changes with the undercarriage flow characteristics. In general, the increased drag of the rough

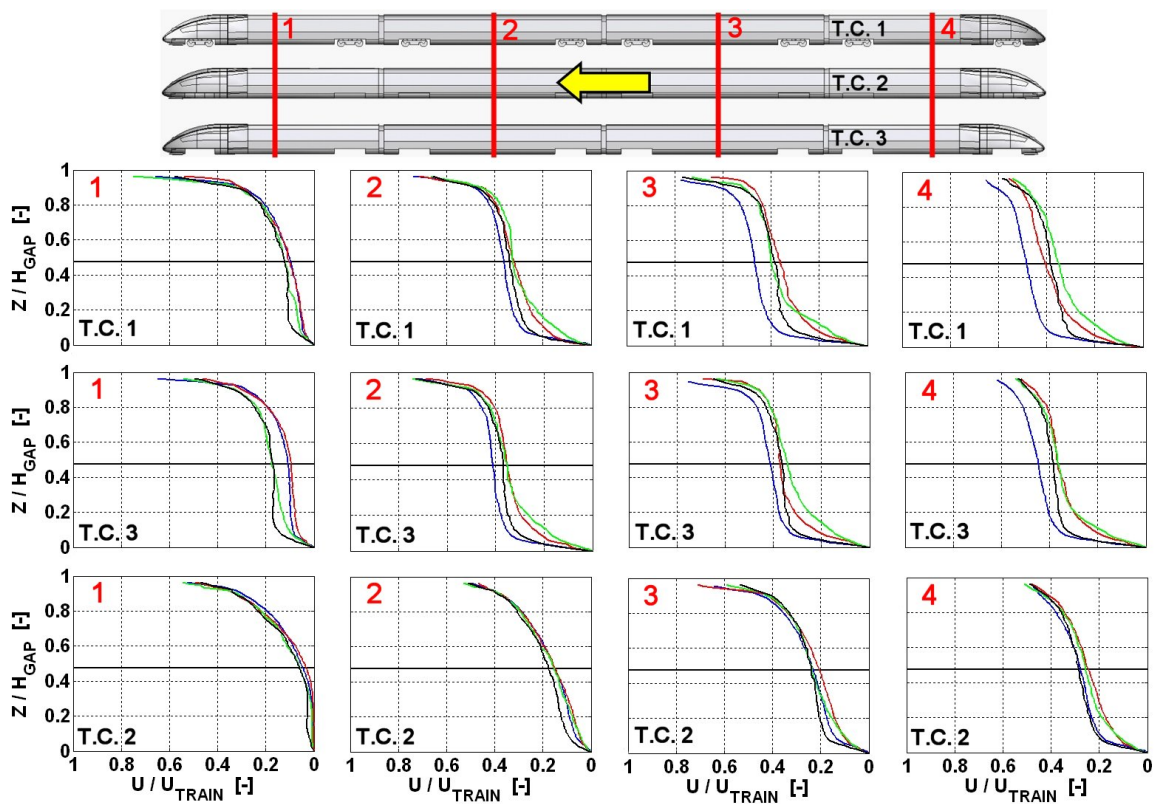


Figure 50: Vertical profiles of the normalised mean U velocity, demonstrating the ground roughness effects for each of the three considered train configurations for the smooth ground (blue line), the rough ground (red line), the inter-sleeper region (green line) and above a sleeper (black line). The black horizontal line indicates the height of the top of the rail. $U_{TRAIN} = 4$ m/s.

ground and the sleepers lowers the volume rate of the undercarriage flow and correspondingly the mean U velocity values. The higher drag of the ground with sleepers, determined in section 6.4.3, is the reason for the lowest mean U velocity values for the nearly fully developed Couette-like undercarriage flow. This was also confirmed by full-scale air velocity measurements on the French high-speed train TGV by Gautier

et al. [35], which conclude that the measured air velocities for a trackbed with lowered ballast level (sleepers exposed to the undercarriage flow) were lower than those measured for a trackbed with a flushed ballast sleeper level. However, for regions with low mean U velocity values, as for the middle of the leading end-car and along the smooth train model, the local flow accelerations over the sleepers caused by the undercarriage gap contraction superimpose the higher drag of the sleepers, leading to overall larger mean U velocity values.

The influence of the ground roughness on the streamwise turbulence in the undercarriage flow at the centres of the four train cars are presented for each train configuration in Figure 51. The results for the different train configurations reveal that the flow

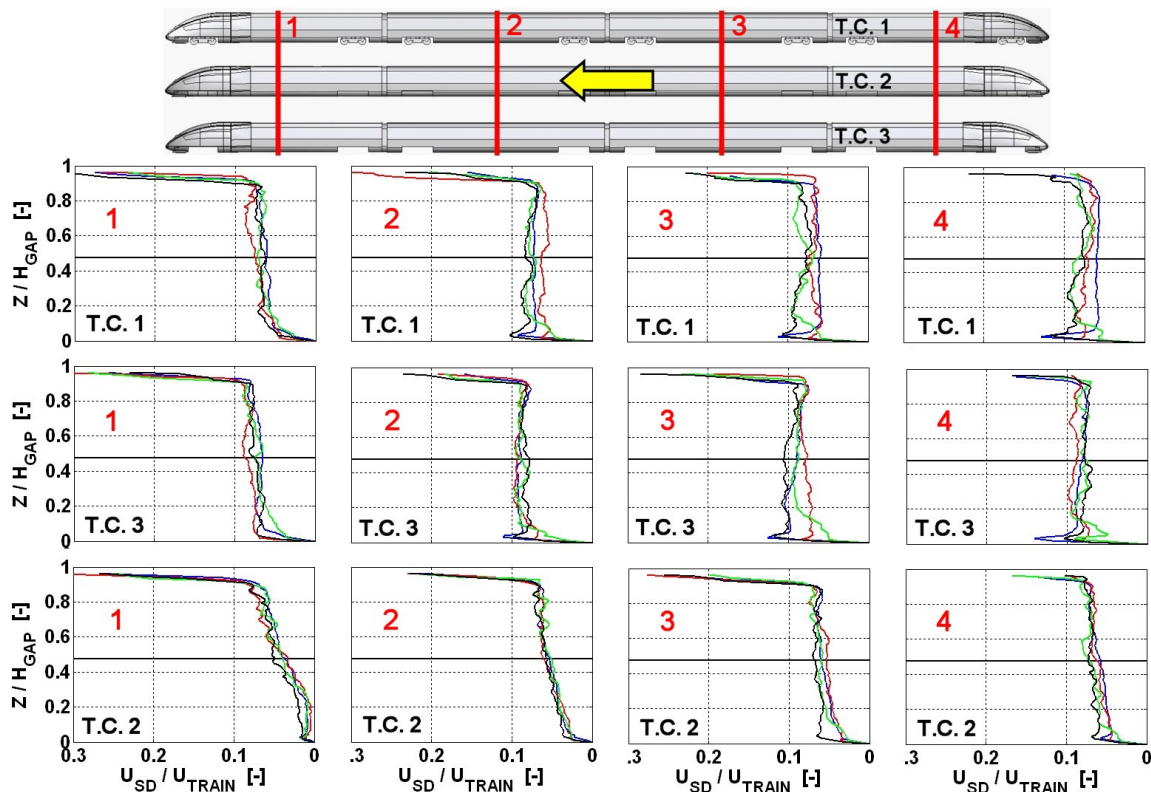


Figure 51: Vertical profiles of the normalised standard deviation U_{SD} showing the ground roughness effects for each of the three considered train configurations for the smooth ground (blue line), the rough ground (red line), in the inter-sleeper region (green line) and above a sleeper (black line). The black horizontal line indicates the height of the top of the rail. $U_{TRAIN} = 4$ m/s.

features resulting from the train undercarriage and from the trackbed roughness interact to determine the characteristic streamwise velocity fluctuations U_{SD} . The most distinctive ground roughness effect for the entire undercarriage flow is found for the reference train model, indicating that the turbulence intensity increases with the drag

or roughness of the trackbed. Increased streamwise velocity fluctuations (U_{SD}) due to the larger trackbed roughness were also obtained by Deeg et al. [51] for full-scale measurements on the Italian ETR 500 high-speed train. Pitot-probes installed shortly after the transition from the slab track to the ballast trackbed measured larger values of U_{SD} than those installed in the opposite slab track. The smooth train model with generally no recognisable ground roughness effect, besides similarities to the reference train model for the trailing end-car, indicates that undercarriage flows with low mean U velocity values and turbulence levels are not significantly influenced by ground roughness effects. This was also the case for the rough train model, though the strong turbulent undercarriage flow generated by the open bogie housings overcomes the effects of the ground roughness. Finally, the two characteristic flow regions for the ground with sleepers previously presented in Figure 48 in section 6.4.2 for the reference train model are also found for the two other train configurations.

Regarding ballast flight, the nearly fully developed Couette-like undercarriage flow underneath the second half of the train model is a priority due to the greater aerodynamic forces on the trackbed. The increased trackbed drag of the rough ground and the sleepers has a positive influence of the risk on ballast flight by reducing the mean U velocity and U_{SD} values as well as lowering the velocity gradient at the trackbed and thus the aerodynamic forces. Comparing the results between the rough ground and the ground with sleepers, indicate that the chance of ballast flight incidents is higher for a trackbed without cross-going sleepers than it is with them. The reason for this is the effect of the protruding sleepers that shield the ballast in the intersleeper region from the undercarriage flow, further decreasing the aerodynamic forces by reducing the values of the mean U velocity and velocity fluctuations close to the trackbed along with the velocity gradients at the trackbed. Once more, the accelerated flow over sleepers accentuates the strongly increased risk of ballast flight for ballast particles lying on top of sleepers.

6.5 Overall comparison of the measured train and ground configurations

The overall comparison of the three considered train models on the smooth ground, rough ground and ground with sleepers are presented for the vertical profiles of the mean U velocity component in Figure 52 and its corresponding standard deviation U_{SD} in Figure 53. The two positions for the nearly fully developed flow at the middle

of the trailing end-car and the end of the seventh bogie housing (local maxima of the mean U velocity for the rough train model) represent the typical undercarriage flow generally described as a Couette-like flow with periodic flow perturbations resulting from the bogie regions. Furthermore, to represent the local flow effects identified for the ground with sleepers, velocity data for the accelerated flow above a sleeper (centre of the sleeper) and in the inter-sleeper position at $\Delta X = 8$ mm downstream of the sleeper centre were presented for all train configurations. In Figure 52 and in Figure 53, the flow within the open bogie housing ($Z / H_{GAP} > 1$) of the rough train model are not plotted to avoid a distortion of the vertical velocity data from the use of different aspect ratios for the graphics. Moreover, considering the ballast flight problem,

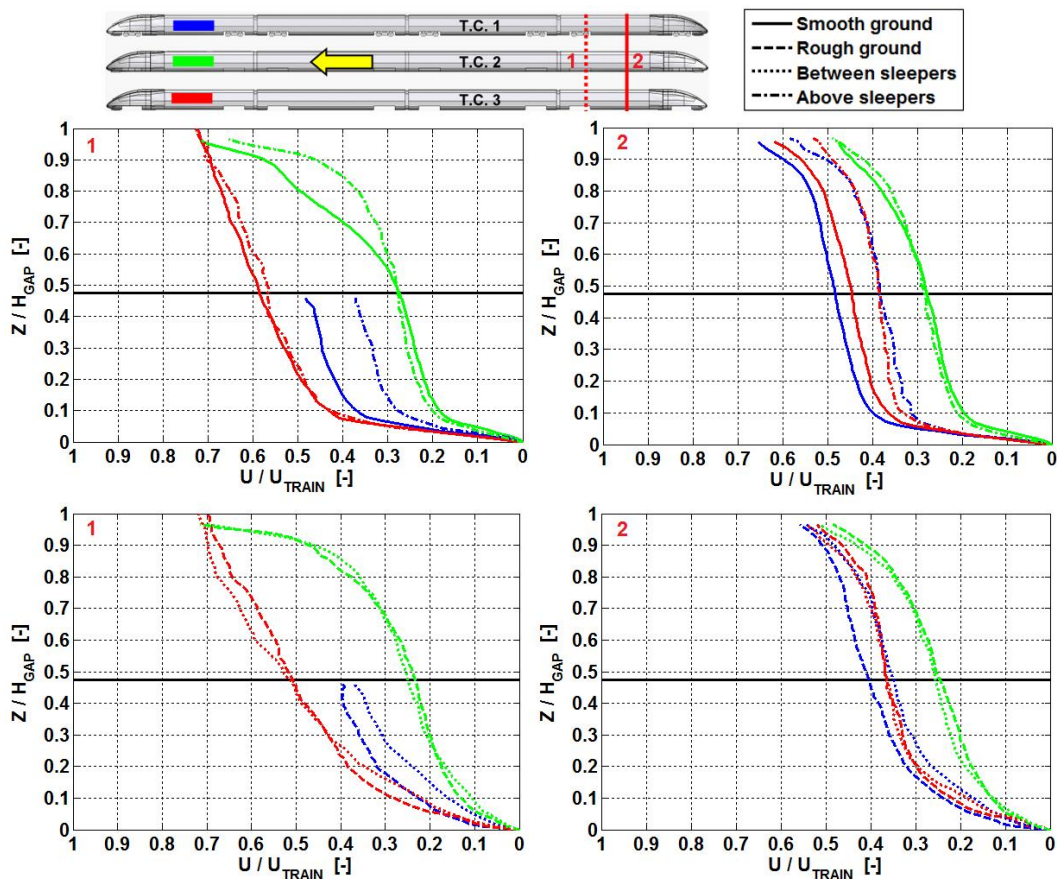


Figure 52: Overall comparison of the vertical profiles of the normalised mean U velocity for the considered train configurations on all ground conditions at the end of the seventh bogie (position 1) and in the middle of the trailing end-car (position 2). $U_{TRAIN} = 4$ m/s.

the flow characteristics close to the ground are of greater interest than the cavity flow inside the bogie housings. The flow within the bogie housing for this position has a constant U velocity gradient ending at a height of $Z / H_{GAP} = 2.3$, with a mean

normalised U velocity of $U / U_{TRAIN} = 1.04$ for all ground conditions. The velocity fluctuation U_{SD} is nearly constant, though with slightly lower values than those for below $Z / H_{GAP} < 1$ in the undercarriage flow. Though the focus remained on the flow characteristics closer to the ground, it was only possible to measure below the height of the top of the rail for the reference train model, since the wheels blocked the view of the PIV cameras. The results in Figure 52 confirm the observed flow characteristics for all train configurations that were found for the horizontal velocity profiles in Figure 37 in section 6.3.3. Comparing the mean U velocity profiles in Figure 52, reflects the almost unchanged mean U velocity values for the fully developed flow for the reference and the smooth train models as well as the more dynamic flow characteristic caused by the open bogie housings of the rough train model. The strong flow acceleration from the open bogie housing creates the largest mean U velocity values close to the ground for all train configurations, independent of the ground type. More interesting is the combination of the strong flow acceleration and undercarriage gap contraction of the sleeper that results in mean U velocity values more or less the same as those found for the smooth ground. The increased mean U velocity values over a sleeper around the bogie regions are not influenced by the higher drag of the sleepers like the mean U velocity values found for the flow away from the bogie regions are, see upper right graphic in Figure 52. Despite the strong flow acceleration around the bogie regions with clearly larger mean U velocity values for the rough train model, the undercarriage flow is strongly decelerated along the smooth undercarriage of the train car, achieving mean U velocity values equal or even lower than those obtained for the reference train model. The strong flow accelerations around the bogie regions for the rough train model generate low-pressure fields that enhance the fluid exchange with the outside flow. The flow exchange or the momentum transfer with the outside flow decreases the mean U velocity values of the undercarriage flow found along the smooth undercarriage of the train car. This was confirmed by the full-scale measurements in section 7.1, where the flow accelerations around the bogie regions were correlated with an underpressure. The flow accelerations around the bogie regions were followed by a deceleration of the undercarriage flow along the smooth undercarriage of the train car, where the static pressure simultaneously increased.

The horizontal distributions of the U_{SD} and the W_{SD} in Figure 39 and Figure 40 in section 6.3.3 revealed that the undercarriage flow is characterised by strong local increases of the turbulence level around the inter-car regions. The exception is of course

the smooth train model with a completely smooth undercarriage. Despite the strong increase of the U_{SD} values at the bogie housing for the rough train model, the U_{SD} values away from the bogies (at the middle of the trailing end-car) are all in the same range ($U_{SD} = 5-10\%$), independent of the train and ground configurations. It is therefore concluded that the streamwise velocity fluctuations for the smooth undercarriage (the case for almost every high-speed train) around the middle of the train car and for the fully developed undercarriage flow will be in the range of 5-10% of the train speed, independent on the trackbed and/or inter-car designs, see Figure 53.

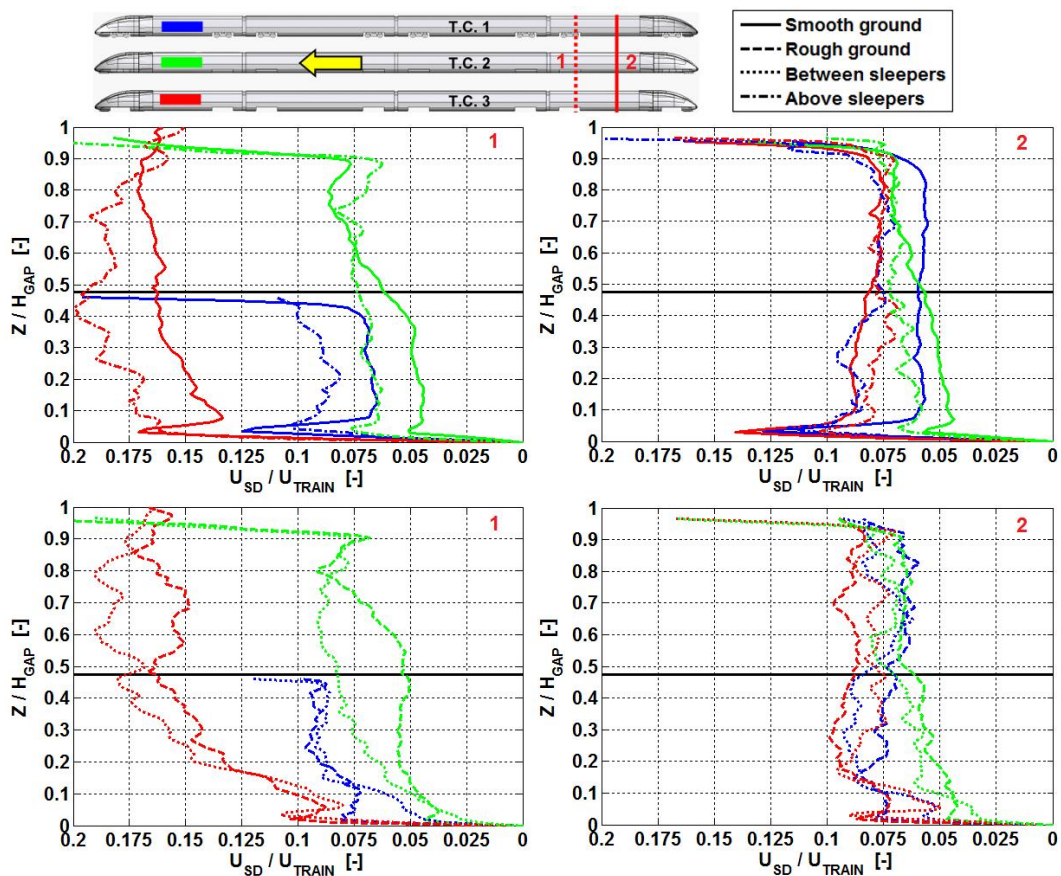


Figure 53: Overall comparison of the vertical profiles of the normalised standard deviation U_{SD} for the considered train configurations on all ground conditions at the end of the seventh bogie (position 1) and in the middle of the trailing end-car (position 2). $U_{TRAIN} = 4$ m/s.

The estimation of the expected maximum u velocity values, assuming a Gaussian distribution of the instantaneous u velocity and applying the 2σ -rule (mean U velocity + $2 \cdot U_{SD}$), is an effective method for the comparison of different high-speed trains regarding the risk of ballast flight. The visualisation of the comparison of the expected maximum u velocity values in the undercarriage flow were simplified for a better

overview by extracting the mean U velocity and U_{SD} values closer to the ground at $Z / H_{GAP} = 0.1$. The mean U velocity values were plotted with $\pm 2 \cdot U_{SD}$ (error bars) in Figure 54 in order to visualise the expected range of the instantaneous u velocity for all measured configurations. The results in Figure 54 reveal that the rough

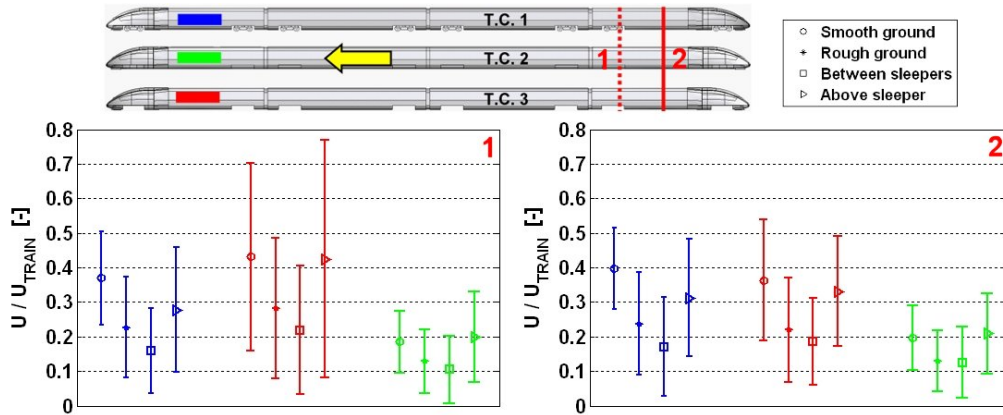


Figure 54: Normalised mean U velocity values with error bars equal to $2 \cdot U_{SD}$ at the height of $Z / H_{GAP} = 0.1$ at the trailing axle of the seventh bogie (left) and at the middle of the trailing end-car (right) for all measured train and ground configurations. $U_{TRAIN} = 4$ m/s.

train model is the train model most conducive to ballast flight, since the values of the expected maximum u velocity, independent of the ground condition, are equal or larger (especially around the bogie regions) than those of the two other train configurations. The accelerated flow at the open bogie housing, with clearly the largest mean U velocity and U_{SD} values, highlight the danger of larger cavities within a train's undercarriage. Furthermore, the small difference between the rough and the reference train models at the middle of the trailing end-car indicates that the local flow effects around the bogie regions are decisive for the occurrence of ballast flight. The importance of considering the velocity fluctuations, as opposed to only the mean U velocity, is also accentuated by the results in Figure 54, where the difference or even the ranking of train models most conducive to ballast flight may change. The previously mentioned positive influence of the rough ground and the ground with sleepers (region between two sleepers) regarding ballast flight via reduction of the mean U velocity values is of course reflected by the expected maximum u velocity values in Figure 54. The results for the ground with sleepers in Figure 54 highlight the preferred trackbed design with cross-going sleepers and with a lowered ballast level, when the ballast particles lie in the inter-sleeper regions. If ballast particles lie on top of sleepers, this is considered to be the most conducive case to ballast flight due to the largest values

of the expected maximum u velocity. This indicates that the risk of ballast flight is not single-handedly caused by the aerodynamic forces induced by the passing trains, but is also dependent on the trackbed design. Furthermore, the importance of the trackbed maintenance or quality is also highlighted by the results for the ground with sleepers, if these help to prevent ballast particles from lying on top of sleepers.

7 Full-scale measurements

7.1 Full-scale measurements on a high-speed train

In the beginning of September 2012, full-scale air velocity and surface pressure measurements were conducted on the German high-speed train ICE3 travelling over a concrete trackbed (slab track) at speeds around 260 km/h ($Re \sim 14 \cdot 10^6$). The measurement set-up, with three vertical rakes of Pitot-probes installed in the trackbed for the measurement of the air velocity and a plate with pressure taps distributed on its upper surface for the measurement of the static surface pressure, is shown in Figure 55.



Figure 55: Full-scale measurement set-up: vertical rakes of Pitot-probes together with a light gate for the determination of the air velocity and train speed, respectively (left), and a static surface pressure plate with distributed pressure taps (right).

The air velocity in the vicinity of the trackbed (all below the height of the top of the rail) was measured by three vertical rakes of Pitot-probes installed in the trackbed at the lateral positions $Y = 0$ mm (trackbed line of symmetry) and $Y = \pm 250$ mm. The two lateral Pitot rakes ($Y = \pm 250$ mm) consisted out of three Pitot-probes ($\Delta Z = 10, 93, 139$ mm below the height of the top of the rail) and a static pressure probe ($\Delta Z = 50$ mm below the height of the top of the rail). The rake in the trackbed line of symmetry was identical but with an additional Pitot-probe located at $\Delta Z = 116$ mm below the height of the top of the rail. For the static surface pressure measurements, a large plate having dimensions of 2000×1300 mm ($L \times W$) was installed in the trackbed, covering the area between both rails with the upper surface located 93 mm below the height of the top of the rail surface. Pressure taps were installed on the upper surface of the plate distributed in the travelling direction on the trackbed line of symmetry ($Y = 0$ mm) for the positions $\Delta X = 500, 1000, 1500$ mm from the upstream edge of the plate. Pressure taps were also distributed for the lateral positions $Y = 0, \pm 250$ and ± 550 mm at the middle of the plate ($\Delta X = 1000$ mm). All pressures (both from Pitot-probes and

pressure taps) were measured with piezoresistive differential pressure transducers (Endevco 8510B-1) with a 1 psi pressure range (~ 6.89 kPa). The air velocity (V_{air}) was determined according to Equation (14), deduced from the Bernoulli equation.

$$V_{air} = \sqrt{\frac{2 \cdot P_{dynamic}}{\rho_f}} \quad (14)$$

The dynamic pressure ($P_{dynamic}$) of the undercarriage flow was extracted by measuring the stagnation pressure (P_{total}) with the Pitot-probes and the static pressure (P_{static}) with the static pressure probe ($P_{dynamic} = P_{total} - P_{static}$). The air density is also necessary for the determination of the air velocity and therefore the air properties such as the atmospheric pressure, air temperature and relative humidity were measured with a thermo-hygrometer sensor (MSR 145) for the determination of the local air density. The static pressure coefficient was calculated according to Equation (15).

$$C_P = \frac{P_{static}}{\frac{1}{2} \cdot \rho_f \cdot U_{TRAIN}^2} \quad (15)$$

The speed and acceleration of the train were determined by two light gates installed with a fixed separation of ~ 20 m. The train speed and acceleration were also used for the accurate determination of the train-probe and train-pressure tap position. The wind direction and wind velocity were also measured to identify and exclude measurements from train passages under stronger cross-winds which affect the calculated ensemble average and standard deviation of the velocity component in the travelling direction U and the static surface pressure coefficient C_P . The raw data signals for every run were first filtered with a two-pass (avoiding data shift), 6-pole Butterworth low-pass filter with a cut-off frequency of 75 Hz, in agreement with the full-scale measurements by Deeg et al. [47] and the recommendations of AeroTRAIN [53]. The ensemble average and the standard deviation were calculated according to Equations (4) and (5) in section 5.3, respectively, using the 41 train passages of the German high-speed train ICE3 in commercial operation at speeds around 260 km/h.

The variation of the normalised horizontal profiles of the ensemble average U velocity and its standard deviation U_{SD} , as measured by the Pitot-probes in the trackbed line of symmetry, are presented in Figure 56. The results in Figure 56 are in agreement with other full-scale measurements of high-speed trains, confirming that the undercarriage flow is a highly turbulent flow characterised by the inter-car regions. Additionally, the flow accelerations at every inter-car region followed by the flow de-

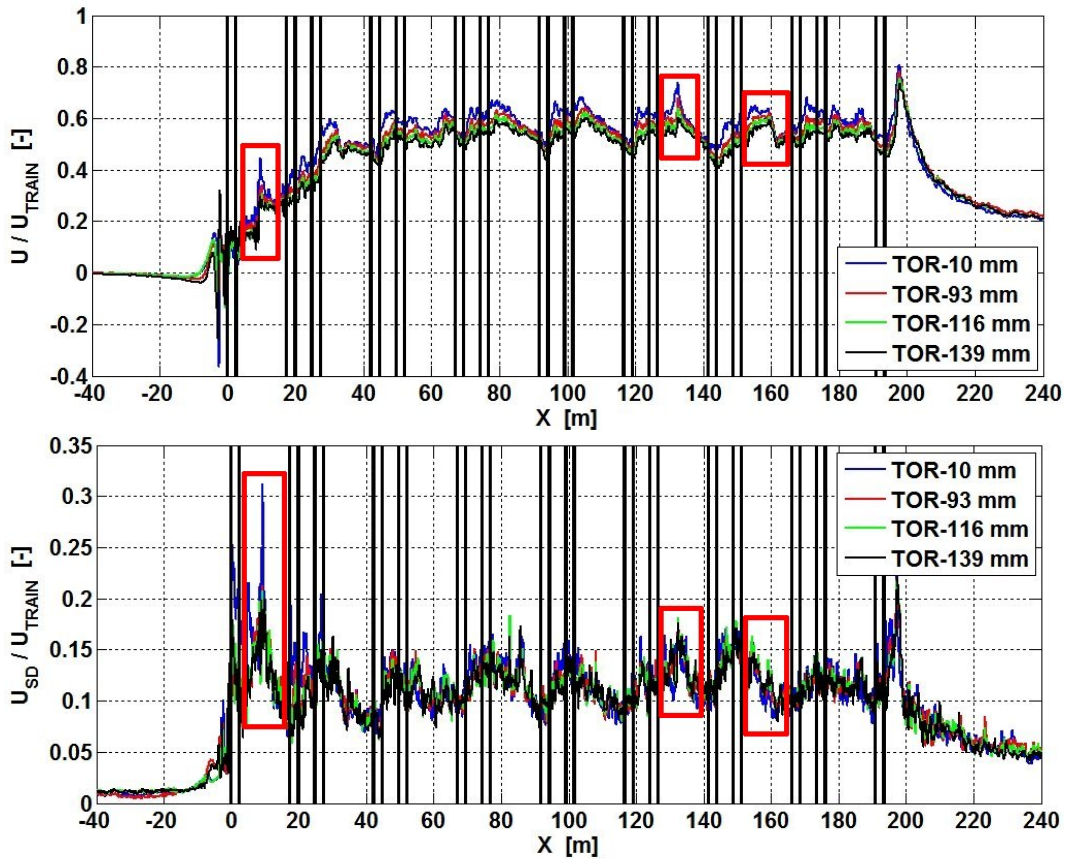


Figure 56: Ensemble average of the normalised U velocity (upper graphic) and its standard deviation U_{SD} (lower graphic) for the four Pitot-probes in the trackbed line of symmetry ($Y = 0$ mm). The vertical black lines indicate the positions of the train axes. The red frames indicate the flow disturbances from cooling air outlets and/or protruding auxiliary undercarriage equipment.

celerations beneath the smooth train cars, result in the periodic nature of the mean U velocity and the turbulence levels (U_{SD}). The undercarriage flow is considered, in agreement with other full-scale measurements [29, 32, 36, 31], to be more or less fully developed after the second train car since the periodic nature of the U velocity repeats itself with similar U velocity values along the remaining length of the train. Disturbances were identified along the "smooth" train car between both bogies that accelerated the undercarriage flow for the leading end-car ($X \sim 10$ m) as well as for the fully developed undercarriage flow at $X \sim 130$ m and $X \sim 160$, framed in Figure 56. These flow accelerations were also found in the full-scale measurements by Lazaro et al. [31] and were associated with auxiliary undercarriage equipment protruding from the smooth undercarriage. According to Sima [39], cooling air outlets can generate similar local flow accelerations in the undercarriage flow as protruding objects

do. The results from the three vertical Pitot rakes in the trackbed revealed that the flow disturbances along the smooth train car were local effects captured by the rake in the trackbed line of symmetry and one of the lateral rakes or only one of the lateral rakes. This indicates that all undercarriage equipment and air-cooling outlets should be considered in the risk assessment of ballast flight. Nevertheless, there are also high-speed trains without or with only negligible auxiliary equipment and air cooling outlets, like for the ETR 500 [47].

The vertical and lateral dependencies of the spatially-averaged mean U velocity and U_{SD} for the fully developed undercarriage flow between the fifth and the last bogie are presented in Figure 57 and in Figure 58. The obtained vertical velocity profiles in Fig-

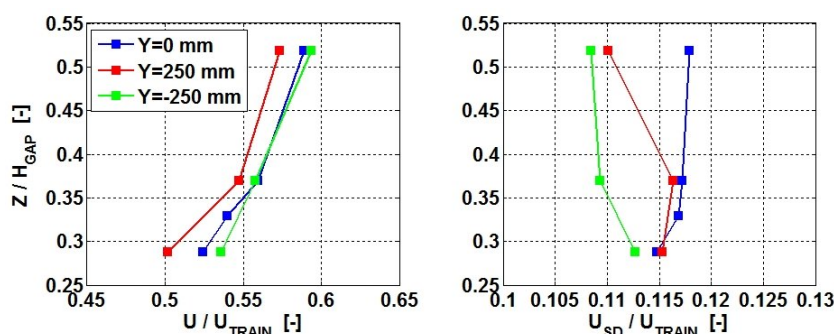


Figure 57: Vertical dependency of the mean U velocity (left) and the streamwise velocity fluctuations U_{SD} (right) calculated between the fifth and the last bogie of the train.

ure 57 confirm the vertical profiles in section 6.3.4 for the fully developed flow at the middle of a train car with a nearly linear mean U velocity gradient and a more or less constant value of the streamwise turbulence (U_{SD}) over the undercarriage gap. Furthermore, the vertical velocity profiles measured by the three Pitot-probe rakes give evidence of a laterally asymmetric flow for the considered high-speed train. Nevertheless, the lateral dependency is still considered as weak, since spatial variation of the mean U velocity and the streamwise velocity fluctuations (U_{SD}) for the two lateral Pitot-probe rakes ($Y = \pm 250$ mm) show almost identical flow characteristics as for the results in the trackbed line of symmetry ($Y = 0$ mm). The most distinguishing differences between the vertical rakes at the different lateral positions in the trackbed was caused by the aforementioned local flow effects linked to the undercarriage auxiliary equipment or cooling vents. The slightly asymmetrical mean U velocity of the undercarriage flow shown in Figure 58 (maximum mean U velocity increase of 2% at $Y = -250$ mm and a decrease of almost 4% at $Y = 250$ mm) is besides the auxiliary equipment and cooling vents, also coupled to the distributed traction concept of the mea-

sured high-speed train, known as electrical multiple unit (EMU). The EMU-technique

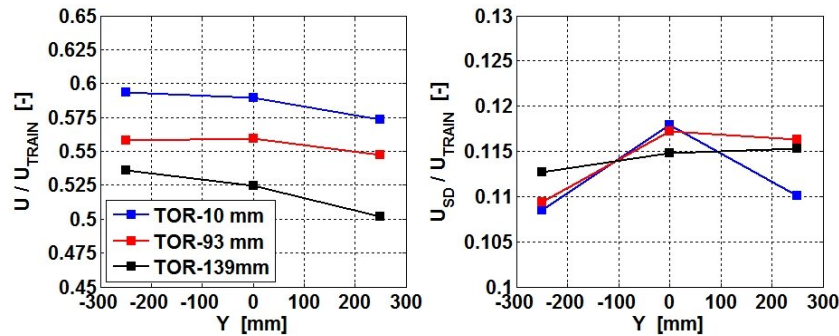


Figure 58: Lateral dependency of the mean U velocity (left) and the streamwise velocity fluctuations U_{SD} (right) calculated between the fifth bogie of the second mid-car and the last bogie of the trailing end-car.

uses traction motors distributed along the entire train length with self-propelled bogies called motor bogies instead of the more classical traction concept with a power-car pushing or pulling the entire train-set. Nevertheless, the two traction motors on the motor bogies (one per train axle) are asymmetrically installed with respect to the trackbed line of symmetry and is therefore considered to be one of the reasons for the asymmetry of the undercarriage flow. The full-scale measurements by Deeg et al. [47] on the ETR 500 using a power-car showed an almost symmetric undercarriage flow with only a weak spatial variation of the mean U velocity with a decrease of -2.5% ($Y = 200$ mm) and -5% ($Y = 400$ mm) for the outer lateral positions. Close to the train, a clear and nearly symmetric lateral dependency of the streamwise turbulence U_{SD} in Figure 58 is measured with the largest values in the trackbed line of symmetry (+8% in comparison to the values at the lateral positions $Y = \pm 250$ mm). The lateral dependency decreases closer to the ground as well as it becomes asymmetric with a U_{SD} difference between the two lateral positions of less than 2%. The presented results clearly reveal that it is meaningful to measure the air velocity at different lateral positions, thereby uncovering possibly asymmetries in the undercarriage flow, including the largest velocity values of the U velocity.

The ensemble average and the fluctuations of the static surface pressure coefficient (C_P) along the entire train length from all pressure taps in the plate installed in the trackbed are presented in Figure 59. The static pressures on the plate clearly reveal that the pressure field around the head, also referred to as the head pressure pulse, clearly dominates the pressure field of the undercarriage flow with the largest positive and negative C_P -values as well as the largest pressure gradients ($\partial C_P / \partial X$). Regarding

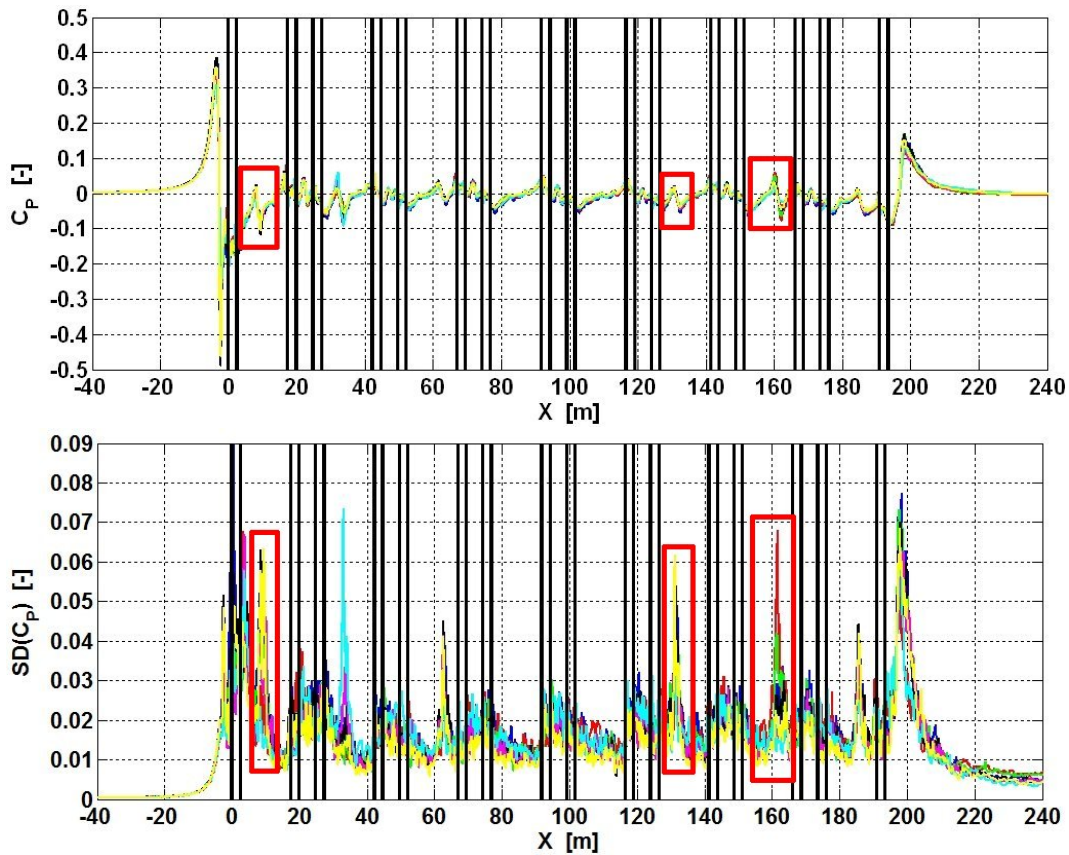


Figure 59: Ensemble average (upper plot) and the standard deviation (lower plot) of the static surface pressure coefficient C_p on the trackbed plate for pressure taps: P1($X = 500$ mm, $Y = 0$ mm) (blue), P2(1000 mm, 550 mm) (red), P3(1000 mm, 250 mm) (green), P4(1000 mm, 0 mm) (black), P5(1000 mm, -250 mm) (magenta), P6(1000 mm, -550 mm) (cyan) and P7(1500 mm, 0 mm) (yellow). The vertical black lines indicate the positions of the train axes. The red frames indicate the flow disturbances from cooling air outlets and/or protruding auxiliary undercarriage equipment.

ballast flight, the pressure field around the head is considered to be the only region of the train's pressure field capable of dislodging ballast particles from the trackbed or at least significantly contributing to the initiation of the ballast particle motion. The pressure field of the Couette-like flow underneath the train thereafter fluctuates around zero until the near-wake flow around the tail of the train. The pressure disturbances linked to the undercarriage ventilation of air and/or from auxiliary equipment have the greatest influence within the undercarriage pressure field, red frames in Figure 59. Furthermore, the pressure fields obtained for the considered high-speed train proved that the fourth and the fifth train car are likely the only train cars with nearly completely smooth train undercarriages between both bogies and without ventilation air outlets. Nevertheless, the ensemble average static pressure and static pressure fluctu-

ation values are much smaller than the mean U velocity and the U_{SD} values, indicating once again that the main contribution of the aerodynamic forces on the trackbed are from the velocity field. The lateral variation (Y direction) of the calculated average of the static pressure and the pressure fluctuations between the fifth and the last bogie of the train are plotted in Figure 60. The lateral variation of the mean pressure and

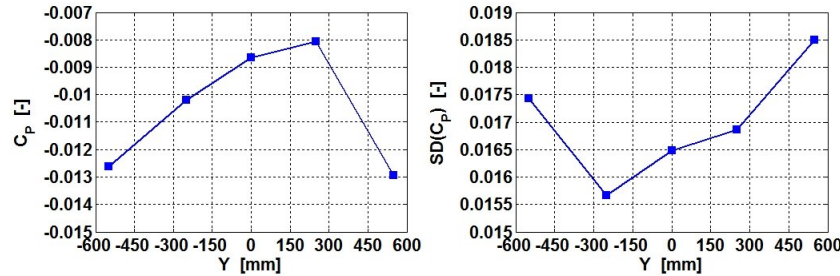


Figure 60: Lateral dependency of the mean static surface pressure coefficient C_p (left) and its corresponding standard deviation (right) for every pressure tap at $\Delta X = 1000$ mm calculated between the fifth bogie of the second mid-car and the last bogie of the trailing end-car.

pressure fluctuation across rail direction reflects the asymmetric undercarriage flow presented in Figure 58. The lower mean U velocity values together with the weaker underpressure at $Y = 250$ mm and the stronger underpressure for $Y = -250$ mm, indicate that the stronger underpressure is correlated with a larger mean U velocity. This entails the possibility that the largest mean U velocity in the undercarriage flow is found near the rail ($Y(\text{rail}) = 717.5$ mm), contradicting the previous observations that the largest mean U velocity exist in the trackbed symmetry plane [29, 32, 47].

In Figure 61, a close-up view of the normalised ensemble average U velocity is presented (upper graphic in Figure 61) along with the mean static surface pressure coefficient (lower graphic in Figure 61) for the fully developed undercarriage flow between the fourth bogie and the last bogie of the train. The results show the mean U velocity characteristics, i.e. the flow accelerations after the bogie regions and the flow disturbances from the undercarriage auxiliary equipment and/or air ventilation outlets, to be well reflected by the mean static surface pressure coefficient C_p . The auxiliary equipment and/or air ventilation outlets are considered to be special features of the measured high-speed train. The fourth and the fifth train cars ($X = 70$ -120 m in Figure 61) of the measured high-speed train therefore more appropriately describe the general undercarriage flow effects of non-articulated high-speed trains. Generally, the undercarriage flow is dominated by the flow effects found around the inter-car regions (bogie - inter-car gap - bogie) like the one between the third and fourth mid-

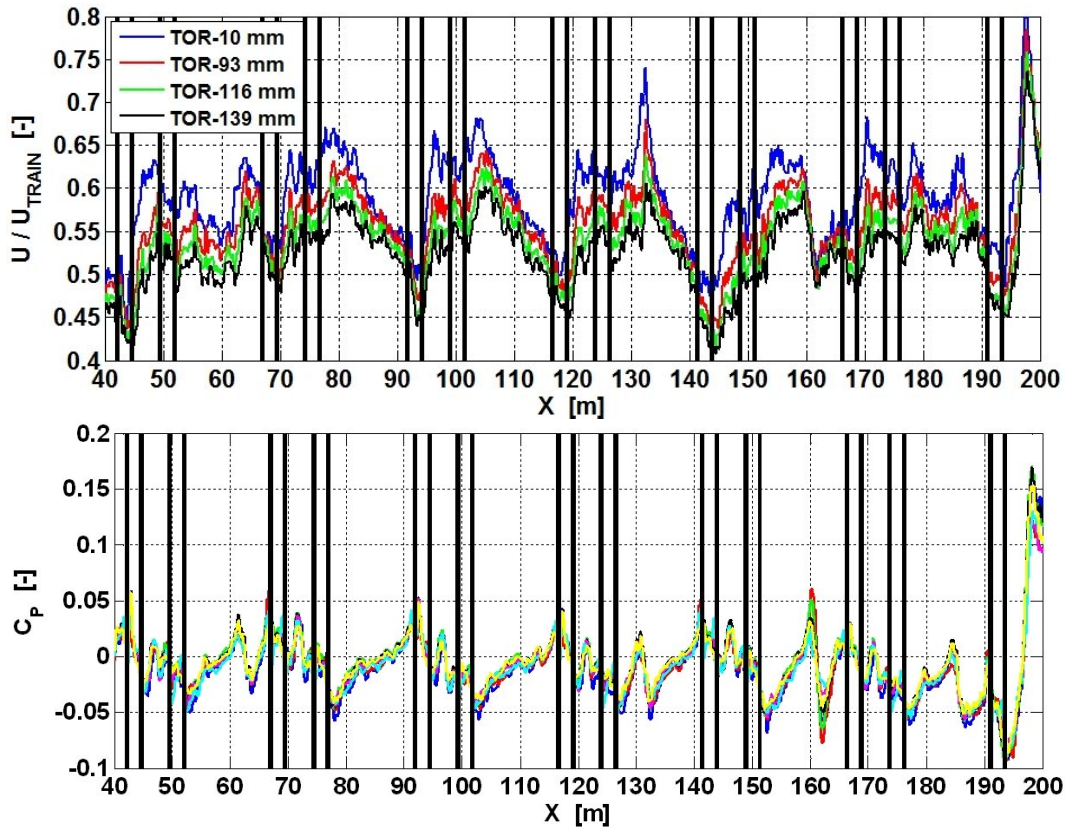


Figure 61: Close-up view of the normalised mean U velocity for the fully developed undercarriage flow between the fourth and the last bogie for the four Pitot-probes installed in the trackbed at the trackbed line of symmetry (upper plot) and the mean static surface pressure coefficient C_P on the trackbed plate for the pressure taps: P1($X = 500$ mm, $Y = 0$ mm) (blue), P2(1000 mm, 550 mm) (red), P3(1000 mm, 250 mm) (green), P4(1000 mm, 0 mm) (black), P5(1000 mm, -250 mm) (magenta), P6(1000 mm, -550 mm) (cyan) and P7(1500 mm, 0 mm) (yellow). The vertical black lines indicate the positions of the train axes.

car between $X = 90$ - 103 m in Figure 61. More precisely, the complex geometry of the bogies and of course the size and shape of the cavities (i.e. bogie housings and inter-car gaps), like the total depth (Z direction) and length (X direction), define the flow around the inter-car regions and therefore influence the undercarriage flow characteristics along the entire train length. Regarding the general undercarriage flow features around the decisive inter-car regions, the results obtained between the fourth and the fifth train cars in Figure 61 are used to describe the flow in a way generally applicable to all non-articulated high-speed trains. The first bogie of the inter-car region at $X \sim 92$ m demonstrates that the undercarriage flow speed is reduced at the beginning of the bogie housing by the sudden increase of the ground clearance. The undercarriage flow and the lateral flow exterior to the tracks at the sides of the train enters the bogie

housing (see the numerical simulations of Sima [39]), resulting in positive C_P values and the local minimum value of the mean U velocity. At the end of the same bogie region the flow is accelerated out of the bogie housing towards the trackbed as well as the in the lateral directions, strongly increasing the mean U velocities at $X = 95$ m in Figure 61. The following inter-car gap and bogie region accelerates the undercarriage flow further and displaces fluid in the lateral directions [39]. This results in the underpressure region found directly after the bogie region at $X = 103$ m and the local maximum mean U velocity. The pressure equalisation found along the smooth train car for $X > 103$ m enhances the momentum mixing between the undercarriage flow and the slower lateral flow exterior to the sides of the train. This is considered to be the main cause of the undercarriage flow deceleration along the smooth undercarriage of the train car. The undercarriage flow along the smooth train car is decelerated until the next inter-car region, from which the course of the flow repeats itself.

7.2 Comparison of the downscaled water-towing tank experiments to full-scale measurements

The PIV results of the water-towing tank experiments were compared to full-scale measurements to verify the relevance of the presented scale model experiments to full-scale high-speed trains under realistic conditions. The comparison also aims to identify similarities and differences between full-scale and scale model measurements. The reference train model on the smooth ground PIV results from the water-towing tank were compared to the DLR full-scale test campaign of the German high-speed train ICE3 as well as the full-scale measurements by Deeg et al. [47] of the Italian high-speed train ETR 500, both of which are non-articulated trains in commercial operation that cruised over concrete slab tracks. The comparisons of the measured horizontal and vertical mean U velocity profiles and of the streamwise velocity fluctuations U_{SD} are presented below in Figures 62 - 66.

In Figure 62, the vertical profiles from section 6.3.4 at the middle of each train car of the reference train model on the smooth ground are compared to the corresponding data of the four Pitot-probes in the trackbed line of symmetry from the full-scale measurement campaign. The results reveal that the water-towing tank experiments with downscaled train models generally underpredict the magnitude of the mean U velocity and of the streamwise turbulence level (U_{SD}). However, the large differences found for the leading end-car are also associated with the flow disturbances from

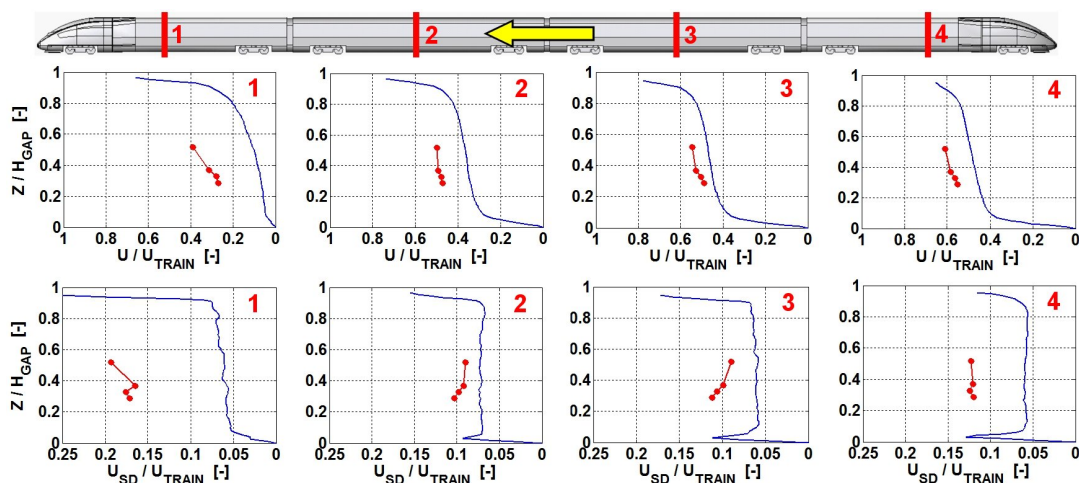


Figure 62: Comparison of the vertical profiles of the normalised mean U velocity (upper row) and of the velocity fluctuations U_{SD} (lower row) at the middle of the train cars for the 1:50 reference train model (T.C. 1) on the smooth ground (G.C. A) in the water-towing tank (blue lines) with vertical rake of Pitot-probes in the trackedbed line of symmetry for the presented full-scale measurements (red lines).

the auxiliary undercarriage equipment and/or the air ventilation outlets, as observed in Figure 56. The comparison of the trailing end-car of the water-towing tank train model with the fourth train car of the full-scale high-speed train, with no visible flow disturbances for the mean U velocity or U_{SD} (see Figure 56), confirms that the water-towing tank experiments predict lower mean U velocity and U_{SD} values. The lower values in the water-towing tank experiments are also linked to the simplified undercarriage geometry of the downscaled train model. This applies especially for the complex shape of the bogies. The simplified bogies used in the water-towing tank, shown in Figure 7, with smooth, solid and ground-parallel lower surfaces prevent the undercarriage flow from entering the bogie housings. The simplified bogies suppress the strong flow acceleration found for the full-scale measurements with similar bogies to the one shown in Figure 9, or to the extreme case of the rough train model with completely open bogie housings in section 6.3.2. Nevertheless, the roughly linear mean U velocity gradient and the nearly constant streamwise turbulence level were predicted correctly for the core of the undercarriage flow.

The streamwise variation of the mean U velocity and the standard deviation U_{SD} from the water-towing tank experiments were also compared with the second nearest Pitot-probe to the trackbed ($Z/H_{GAP} = 0.3289$ or 116 mm below the TOR) in the trackedbed line of symmetry of the conducted full-scale measurements. The comparison of the mean U velocity and U_{SD} are presented in Figure 63 and in Figure 64, respectively.

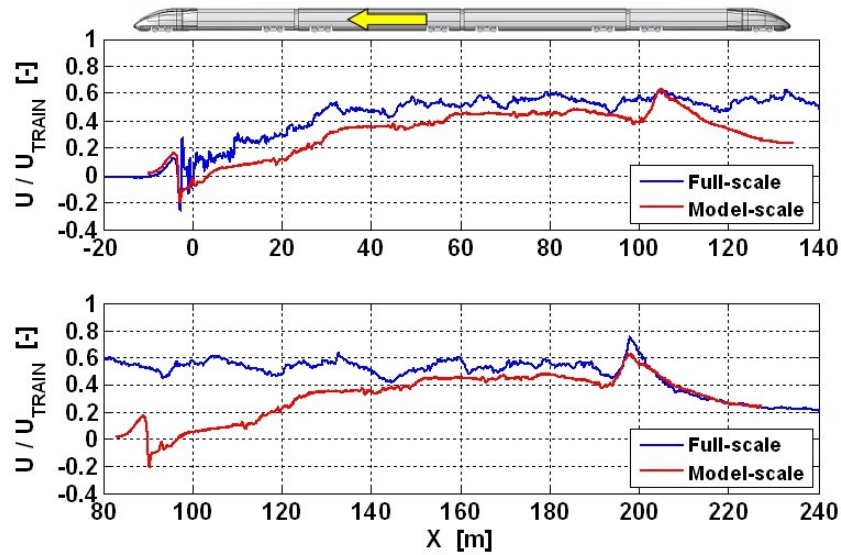


Figure 63: Comparison of the normalised mean U velocity at $Z / H_{GAP} = 0.3289$ of the 1:50 reference train model (T.C. 1) on the smooth ground (G.C. A) in the water-towing tank with the conducted full-scale measurements on the ICE3 high-speed train on a concrete slab track. The first axles of the trains are aligned in the upper plot and the last axles of the trains are aligned in the lower plot.

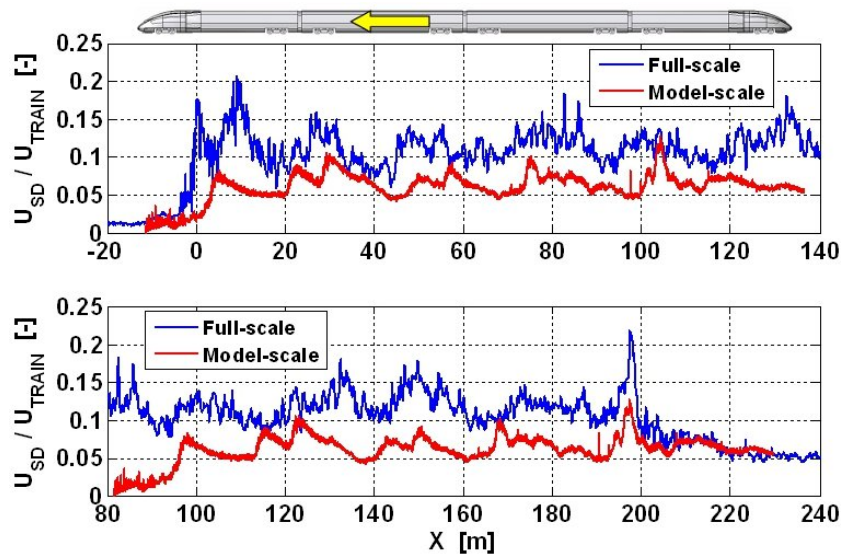


Figure 64: Comparison of the normalised streamwise turbulence (U_{SD}) at $Z / H_{GAP} = 0.3289$ of the 1:50 reference train model (T.C. 1) on the smooth ground (G.C. A) in the water-towing tank with the conducted full-scale measurements on the ICE3 high-speed train on a concrete slab track. The first axles of the trains are aligned in the upper plot and the last axles of the trains are aligned in the lower plot.

The X-coordinates for the horizontal profiles obtained in the water-towing tank were

multiplied by the train model-scale (i.e. 50) for the comparison to the full-scale measurements. Since the water-towing tank facility only allows train sets with a total length of four train cars in 1:50 scale, two comparisons were conducted. One with the first axles aligned (upper plots in Figure 63 and in Figure 64) and one with the last axles aligned (lower plots in Figure 63 and in Figure 64). The comparison of the horizontal profiles in Figure 63 and in Figure 64 confirms the overall difference found for the vertical profiles in Figure 62, with lower values of U and the U_{SD} in the undercarriage flow for the water-towing tank experiments. Nevertheless, the mean U velocity reveals that the flow characteristics around the head and the tail are captured in the water-towing tank, particularly for the accelerated flow around the head. The undercarriage flow became more or less fully developed after the third train car for both the water-towing tank experiments and the full-scale measurements, which also agrees with other full-scale measurements [29, 31, 32, 36, 47]. The comparison of the streamwise turbulence U_{SD} demonstrated a clear difference of the turbulence level, almost by a factor of two, with the only similar U_{SD} characteristic found in the near-wake flow around the tail of the train.

The ensemble average of the normalised U velocity and its standard deviation at the rail height for the reference train model on the smooth ground were also compared to those measured by Deeg et al. [47] for the ETR 500 cruising over a concrete slab track. The ensemble average of the U velocity and of U_{SD} for the ETR 500 were calculated from 30 train passages measured by an ultrasonic anemometer at the trackbed line of symmetry. The raw data from the ultrasonic anemometer were filtered with a two-pass (to avoid data shift), sixth-order Butterworth low-pass filter with a cut-off frequency of 75 Hz. Comparisons of the mean U velocity in Figure 65 and of U_{SD} in Figure 66 were done analogously to the previously presented comparison. Due to the different lengths of the train sets (4 units for the water-towing tank experiments and the 14 unit ETR 500), the first axles of the trains are aligned in the upper plots of Figure 65 and Figure 66 and the last axles of the trains are aligned in the lower plots of Figure 65 and Figure 66. It was not unanticipated that the horizontal profiles of the mean U velocity and U_{SD} would reflect a divergence, since the geometric shape of the end-cars of the trains and of the bogie pivot distance are different. Although the shape of the head and tail are different for the compared trains, the characteristic flow around the head and the tail in Figure 65 is still similar and captured by the downscaled water-towing tank experiments. The results in Figure 65 also reveal lower values of the mean U velocity along the train obtained for the downscaled mea-

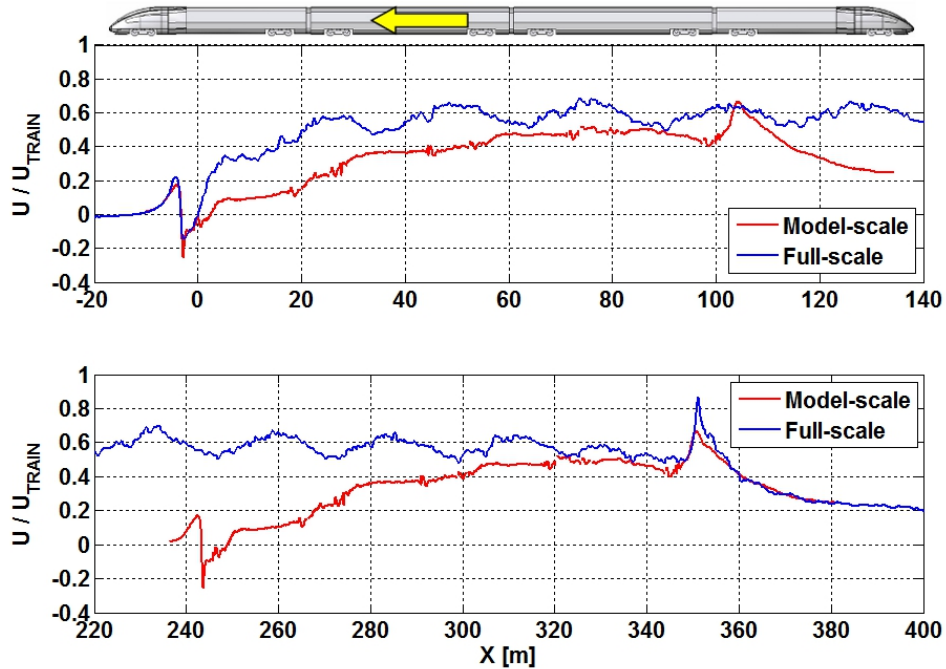


Figure 65: Comparison of the normalised mean U velocity for the reference train model (T.C. 1) on the smooth ground (G.C. A) in the water-towing tank with that of the full-scale measurements for the ETR 500 [47] at the height of the top of the rail ($Z / H_{GAP} = 0.476$). The first axes of the trains are aligned in the upper plot and the last axes of the trains are aligned in the lower plot.

measurements in the water-towing tank, as compared to the full-scale measurements of the ETR 500. This is also attributed to the smoother undercarriage of the reference train model in the water-towing tank, i.e. primarily due to the simplified bogies. The simplified bogies of the downscaled train model (see Figure 7) are much smoother than the actual bogies of the ETR 500, which feature disc brakes, gearboxes, electric motors, cables and other protruding objects. The geometric differences of the bogies are also considered to be one of the reasons for the wavy-pattern in the horizontal profiles of the mean U velocity found for the ETR 500 that is not reflected to the same extent for the reference train model in the water-towing tank.

The comparison of the standard deviation U_{SD} in Figure 66 reveals, however, that the turbulence in the undercarriage flow is reflected well in the downscaled experiments, as the magnitude and the pattern are similar. The X -locations of the local maxima of U_{SD} are assigned to the different bogie pivot distances for the two considered trains. Nevertheless, the strong generation of turbulence found around the region of the first bogie for the ETR 500 is associated with greater momentum transfer in the undercarriage flow and is therefore considered to be the reason for the faster U velocity

development around the first bogie and the leading end-car than that found for the downscaled model.

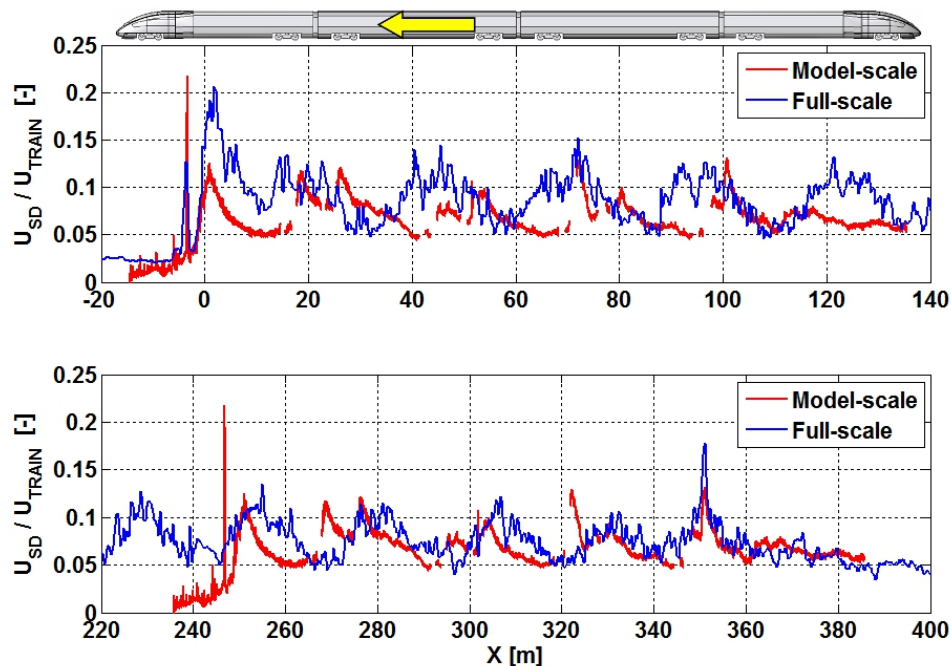


Figure 66: Comparison of the normalised standard deviation U_{SD} for the reference train model (T.C. 1) on the smooth ground (G.C. A) in the water-towing tank with that of the full-scale measurements on the ETR 500 [47] at the height of the top of the rail ($Z / H_{GAP} = 0.476$). The first axles of the trains are aligned in the upper plot and the last axles of the trains are aligned in the lower plot.

The comparison to the full-scale measurements demonstrated that the normalised mean U velocity along the train for the reference train model on the smooth ground in the water-towing tank qualitatively agrees with full-scale high-speed trains cruising at around 250 km/h over a concrete slab track. However, the mean U velocity values in the water-towing tank experiments were lower, which was linked to the smoother undercarriage of the 1:50 simplified high-speed train model. The mean U velocity of the water-towing tank experiments agree slightly better with the measurements of the ETR 500 than for the DLR full-scale test campaign. The streamwise velocity fluctuations (U_{SD}), however, differed strongly from each other, while the water-towing tank U_{SD} results agreed well with values obtained for the ETR 500 whereas those for the other high-speed train were almost a factor of two larger. The mean U velocities of both high-speed trains were still in the same range. The different applied measurement techniques can be ruled out as the reason for the large difference in the

streamwise fluctuations between the two measurement campaigns. Deeg et al. [47] showed that the difference of the measured velocities of the undercarriage flow using ultrasonic anemometers and Pitot-probes was below <2%. Additionally, both high-speed trains were measured on concrete slab tracks for similar train speeds (250 km/h for the ETR 500 and 260 km/h for the DLR test campaign), meaning that the velocity fluctuation difference should not be due to the different measurement techniques, Reynolds numbers or trackbed conditions. Furthermore, the undercarriage flow data treatment were consistent, with a sixth-order Butterworth low-pass filter being applied to the raw signals with a cut-off frequency of 75 Hz before the calculation of the statistical quantities (ensemble average and the standard deviation) from data sample of similar size (30 runs for the ETR 500 and 41 runs for the earlier presented full-scale measurements). This indicates that the difference in the streamwise turbulence (U_{SD}), measured for the two full-scale test-campaigns, is predominantly caused by the undercarriage differences of the two considered high-speed trains. Another indication of differences in the undercarriage geometry is the different traction concepts of the considered high-speed trains. The ETR 500 (first and second generation) uses a traditional power-car concept with two power-cars (the leading and the trailing end-cars), whereas the other ICE3 has a distributed traction concept (EMU). Nevertheless, the pronounced flow disturbances found along the smooth train car associated with auxiliary equipment and/or air ventilation outlets for the DLR test-campaign could not be identified for the ETR 500, strengthening the conclusions regarding the differences in the undercarriage geometry.

The difference between the undercarriage flow of a full-scale high-speed train (e.g. ETR 500) and the reference train model in the water-towing tank were thus far linked to the simplified bogies. The slower flow development (mean U velocity and U_{SD}) after the first bogie and along the leading end-car as well as the lower mean U velocity values for the fully developed undercarriage flow could however also be or partially be caused by differences in the Reynolds number. The presented Reynolds number effects in section 6.1 for the reference train model on the smooth ground confirm the slower undercarriage flow development after the first bogie for both the mean U velocity and for the velocity fluctuations for lower Reynolds number. Furthermore, lower U velocity values were also found for the two lowest Reynolds numbers ($U_{TRAIN} = 1$ and 2 m/s) for the more or less fully developed flow. This suggests that the difference between the full-scale case and the water-towing tank in Figure 63 and in Figure 65 could be or partially be a Reynolds number effect. The periodic structure

found for the horizontal profiles of the mean U velocity in Figure 65 for the ETR 500, with flow accelerations at the bogie regions and flow decelerations along the train car, was however also found for the rough train model with open bogie housings (in an extreme way). It is therefore thought that the wavy-characteristics of the mean U velocity are predominately caused by the flow acceleration around the inter-car regions and not by any difference in the Reynolds numbers.

8 Evaluation of ballast flight

The entire ballast flight sequence presented in Figure 1 is a complex problem involving different physical phenomena. The ballast flight process is therefore commonly divided into sub-processes like the ballast particle initiation, the ballast particle transport over the trackbed, the ballast particle flight, the ballast particle impact with the train and the re-impact with the trackbed. The role of the turbulent undercarriage flow in inducing aerodynamic forces, as shown in Figure 17 in section 6.1, as well as of the ballast particle properties like size, shape and initial position, reveal the stochastic nature of the ballast flight problem. Evaluating the entire ballast flight sequence including each of the many influencing parameters is a very time-consuming and difficult task. Consequently, the majority of the ballast flight calculations rely on simplifications of the physics of the different sub-processes as well as of the stochastic nature of the ballast properties. In the following sections the crucial sub-processes of the ballast flight problem will be evaluated using simplified physical approaches to assess the risk of ballast flight for the configurations measured in the water-towing tank.

8.1 Particle dislodgement

The initiation of particle movement by wind has been studied by numerous researchers, primarily as a geophysical topic referred to as particle erosion, particle sedimentation or as an aeolian process. However, the most known and currently used method is described in Bagnold's work on particle movement for sand dunes [30]. Bagnold proposed a now famous expression for the critical friction velocity close to the ground that is required to initiate particle movement, i.e. Equation (16).

$$U_{\tau_{critical}} = A \cdot \sqrt{\frac{\rho_p - \rho_f}{\rho_f} \cdot d_p \cdot g} \quad (16)$$

The critical friction velocity is calculated using the densities of the fluid (ρ_f) and the particle (ρ_p), the acceleration due to gravity (g), the particle diameter (d_p) and an empirical constant A . Bagnold suggested two different thresholds for the initiation of particle movement based on different values of the empirical constant A . The static threshold of $A = 0.1$ for the initial particle movement and the dynamic also known as the impact or fluid threshold of $A = 0.08$ that account for impacting (saltating) parti-

cles reducing the friction velocity threshold. The Bagnold expression holds for a large range of particle size and flows as long as the particle friction Reynolds number ($Re_\tau = (U_\tau \cdot d_p) / \nu$) exceeds 3.5. The experimental work of Kind [66] demonstrated that the formulation and the threshold values proposed by Bagnold were valid for particle sizes up to 19 mm. Although the main ballast size distribution for full-scale trackbeds (28-50 mm [112]) are mainly not in the proven validity range of Equation (16), the expression by Bagnold was still used to estimate the critical train speeds for the initiation of the ballast particle movement. The train-induced friction velocity for the considered train and ground configurations in the water-towing tank were calculated using the nearly fully developed undercarriage flow and assuming the validity of the law of the wall by applying the standard slope method analogously to the calculations in section 6.4.3. Thereafter, the maximum calculated friction velocity was used to calculate the skin friction coefficient for each measured configuration ($C_f = 2 \cdot (U_\tau / U_\infty)^2$) using the rig speed (U_{TRAIN}) instead of the free stream velocity (U_∞). In section 6.4.3, the difference of the skin friction coefficient due to the Reynolds number difference between the water-towing tank experiments and that of a full-scale train cruising at 300 km/h was estimated using the $1/7^{th}$ power law for a fully turbulent boundary layer over a smooth plate. The estimated skin friction coefficient in the water-towing tank was estimated to be larger by a factor of 2.3. The extracted skin friction coefficients from the water-towing tank experiments were therefore first corrected (divided) with the factor of 2.3. The corrected skin friction coefficient for the fully developed undercarriage flow for the reference train model on the smooth ground showed reasonably good agreement with the full-scale trackbed installed Preston-probe measurements on a high-speed train cruising at 300 km/h over a concrete slab track. This agreement justified the usage of the rough correction factor in order to obtain realistic values for the skin friction coefficient. The critical train speed was calculated using the corrected skin friction coefficients from the water-towing tank experiments together with the critical friction velocity for the particle dislodgement from Equation (16) with the static threshold value of $A = 0.1$, ballast particle density of $\rho_p = \rho_B = 2600 \text{ kg/m}^3$ and air density $\rho_f = 1.2041 \text{ kg/m}^3$. The critical train speeds for the three ballast particle sizes of $d_p = d_B = 28 \text{ mm}$, 40 mm and 50 mm , which represent most ballast particle sizes, are presented below in Table 6. The results in Table 6 generally reflect the outcome of the equivalent sand grain roughness calculations for the different ground configurations in section 6.4.3, i.e. that the increased ground roughness (larger k_s) is associated with larger values of the friction velocity, i.e. larger shear stresses. Regard-

T.C.	G.C.	$d_B = 28$ mm	$d_B = 40$ mm	$d_B = 50$ mm
1 (Reference)	A (Smooth)	440 km/h	526 km/h	588 km/h
2 (Smooth)	A	600 km/h	717 km/h	801 km/h
3 (Rough)	A	354 km/h	423 km/h	473 km/h
1	B (Rough)	284 km/h	339 km/h	379 km/h
2	B	529 km/h	632 km/h	707 km/h
3	B	289 km/h	345 km/h	386 km/h
1	C1 (Between sleepers)	237 km/h	283 km/h	317 km/h
2	C1	319 km/h	381 km/h	426 km/h
3	C1	177 km/h	211 km/h	236 km/h
1	C2 (Above sleeper)	438 km/h	524 km/h	585 km/h
2	C2	634 km/h	758 km/h	847 km/h
3	C2	357 km/h	427 km/h	478 km/h

Table 6: Critical train speeds according to the friction velocity threshold proposed by Bagnold in Equation (16) for the measured train and ground configurations in the water-towing tank for the ballast particle sizes of $d_B = 28, 40$ and 50 mm. The two characteristic flow regions are included, i.e. above and in the middle of a sleeper (C2) and $\Delta X = 8$ mm downstream of a sleeper in the inter-sleeper region (C1).

ing the risk of ballast flight, the results for the smooth ground and the ground with sleepers also indicate some limitations of the use of the friction velocity as a threshold for the dislodgement of ballast particles from a trackbed. It is not believed the risk of ballast flight is less for ballast lying on a smooth ground (slab track) or on top of a sleeper than ballast lying on a rough ground or between the sleepers as Table 6 indicates. It is more likely that the aerodynamic forces are dominated by pressure induced forces than by the shear stresses for exposed ballast particles (or foreign objects) lying on top of the concrete slab track or on top of a sleeper. According to CFD simulations by Garcia et al. [60] of a 2-D fully developed Couette-flow over a ballast trackbed with monoblock sleepers and a lowered ballast level, the total drag of the trackbed was clearly dominated by the pressure drag of the protruding sleepers. It is therefore concluded that the aerodynamic forces on exposed ballast particles on sleepers are dominated by the pressure induced drag and lift forces. Furthermore, since the protruding sleepers dominate the total drag of the trackbed, it is not very likely that the shear stress in the inter-sleeper regions is of sufficient magnitude to dislodge ballast particles at the low train speeds presented in Table 6. The shear stress in the inter-sleeper region calculated from the mean velocity gradient ($\partial U / \partial Z$) close to the ground, using the law of the wall, is not caused by the roughness of the ballast in the inter-sleeper region, but rather by the pressure drag of the protruding sleep-

ers. The train-induced aerodynamic forces thus act on the sleepers and not as a shear stress on the ballast in the inter-sleeper regions. This reveals that applying the law of the wall assuming a fully developed boundary layer over a flat wall is more suitable for surfaces with more homogeneous roughnesses than for the strongly localised effects around the sleepers. Calculating the shear stress assuming the law of the wall together with the friction velocity threshold suggested by Bagnold is only applicable for bi-block ballast trackbed designs (rough ground). Nevertheless, this approach was developed for sand dunes.

The outcome of the wind tunnel experiments by Nickling [122], based on different types of sediment revealed that the number of dislodge particles has a hyperbolic dependence on the friction velocity. Thus, starting slow and transforming into a rapid cascade of dislodging particles. The rather low particle dislodgement rate with increasing friction velocity at the beginning suggests that the initial particles are entrained by the drag and the lift forces concerning smaller particle sizes and particles in exposed positions on the surface. The increase in the rate of dislodgement is the dynamic effect of the re-impacts of initial particles dislodging larger and additional particles, forming a cascade for which flying particles rapidly dislodges new particles similarly to an avalanche effect. Furthermore, that the initial particles (smaller particle sizes and in susceptible positions on the surface) are set into motion by the drag and lift forces was also indicated from the experiments conducted within the AOA-project and presented by Kaltenbach et al. [41] on different downscaled trackbed designs. The hyperbolic dependence of the number of dislodged particles with increasing friction velocity was also found for the bi-block ballast trackbed design. The particle dislodgement first began, however, at a level twice as large as the classical threshold according to Bagnold (Equation (16)). The larger critical friction velocity threshold is associated with the trackbed preparation, i.e., removing the exposed and smaller ballast particles by "solidifying" the trackbed using a mechanical shaker and thereby levelling the ballast but also blowing out the exposed ballast particles on top of the trackbed surface prior to the tests started. It has been shown [41, 122] that the initiation of ballast particle motion is caused by drag and lift forces on small ballast particles and those in exposed positions on the trackbed. This motivates the evaluation in the following section.

8.2 Ballast particle initiation

8.2.1 Physical approach for the ballast particle initiation

Regarding aeolian processes in the literature as well as for ballast flight, different scenarios of the initiation of particle movement have been described based on experimental observations. The classical, well-known and commonly assumed particle movement, also considered as the most probable for ballast flight, is the one proposed by Bagnold [30] and sketched in Figure 1. According to Bagnold, particles slide or roll-over the surface, gain speed and begin to bounce or trip over the surface and are eventually entrained into the airstream. Bisal and Nielsen [123], however, suggested a different initiation of the particle movement based on their wind tunnel experiments. Their particles did not move over the surface as suggested by Bagnold. Instead, the particles vibrated in positions and ejected (lifted) into the airstream when the airstream velocity increased. The various described scenarios of the initiation of particle motion (slide, lift or take-off and roll-over) will be evaluated here to unveil the most likely scenario for ballast flight based on the obtained PIV flow field data in the water-towing tank experiments. The three different scenarios are evaluated for a simplified virtual ballast particle, positioned either on top of the other ballast in the trackbed as shown in Figure 67 or on top of a sleeper fully exposed to the undercarriage flow. The exposed ballast particle positions were based on the wind tunnel measurements by Nickling [122], indicating that the initial initiation of particle motion is associated with smaller particles and particles on more exposed positions on the surface.

Ballast particle slide

Figure 67 shows the governing forces for particle slide and direct take-off for an exposed ballast particle on top of other ballast in the trackbed or on top of a sleeper. The ballast particle is thought to begin its sliding motion over the trackbed as soon as the aerodynamic drag (F_D) in the main direction of the undercarriage flow (i.e. X direction) overcomes the static friction force of the ballast particle (F_{fr}), as defined in Equation (17). The static friction also referred to as the static Coulomb friction is defined by an empirical property (μ_{static}) of the two surfaces in contact and the normal force of the contact surfaces, i.e. the force pressing the surfaces together.

$$F_D > F_{fr} \quad (17)$$

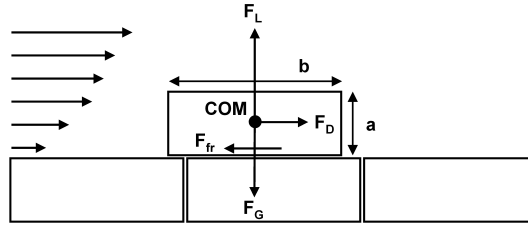


Figure 67: Governing forces for an exposed ballast particle in the evaluation for the initial particle movement scenarios denoted as ballast particle slide and ballast particle direct take-off.

The aerodynamic drag and lift on the ballast particle (F_D , F_L) in Equation (18) is calculated using the definition of the dimensionless ballast particle aerodynamic force coefficients (C_D , C_L) including shear stress and pressure induced forces.

$$F_D > \mu_{static} \cdot (F_G - F_L) \quad (18)$$

The weight of the ballast particle (F_G) is defined as the product of the mass (m_B) and gravity (g), as expressed in Equation (19).

$$\frac{1}{2} \cdot \rho_f \cdot U^2 \cdot A_B \cdot C_D > \mu_{static} \cdot (m_B \cdot g - \frac{1}{2} \cdot \rho_f \cdot U^2 \cdot A_B \cdot C_L) \quad (19)$$

The critical train speed necessary to initiate a sliding movement for an exposed ballast particle is calculated from Equation (19) with the mass of the ballast particle defined as the product of its volume ($V_B = a \cdot b \cdot c$) and density (ρ_B). The ballast particle surface perpendicular to the main flow is used as the aerodynamic reference area ($A_B = a \cdot c$) and the critical air velocity for the ballast particle slide reads as.

$$U_{crit-ballast-slide} = \sqrt{\frac{2 \cdot \mu_{static} \cdot V_B \cdot \rho_B \cdot g}{\rho_f \cdot A_B \cdot (C_D + \mu_{static} \cdot C_L)}} \quad (20)$$

Additionally, the train-induced trackbed vibration, which depends on the dynamic properties of the rolling stock and the response or stiffness of the trackbed, influences the resulting ballast weight as the trackbed accelerates up and down. The trackbed vibration measurements presented by Quinn et al. [32] indicated that strong vertical accelerations appeared for every passing bogie during train passages. The strong vertical trackbed accelerations around the bogies change the effective weight of the ballast. The effective weight is reduced when the trackbed accelerates away from the train and increases as the trackbed is accelerated towards the train. Regarding the

risk of ballast flight, the moment of interest is when the resulting weight of the ballast is lowered by the trackbed vibration. The effect of the trackbed vibration is taken into account in a simplified way by applying a vertical acceleration (a_z) away from the ground that reduces the resulting weight of the ballast particles. The critical air velocity regarding the train-induced trackbed vibration then reads as.

$$U_{crit-ballast-slide-vibration} = \sqrt{\frac{2 \cdot \mu_{static} \cdot V_B \cdot \rho_B \cdot (g - a_z)}{\rho_f \cdot A_B \cdot (C_D + \mu_{static} \cdot C_L)}} \quad (21)$$

Ballast particle direct take-off

The ballast particle direct take-off or ejection is possible when the aerodynamic lift is greater than the ballast particle weight, as specified in Equation (22). The critical air velocity for the direct take-off of ballast particles from the trackbed with and without trackbed vibration is calculated analogously to the ballast particle slide based on the dimensionless aerodynamic force coefficients of the ballast particle.

$$F_L > F_G \quad (22)$$

$$\frac{1}{2} \cdot \rho_f \cdot U^2 \cdot A_B \cdot C_L > m_B \cdot g \quad (23)$$

$$U_{crit-ballast-take-off} = \sqrt{\frac{2 \cdot V_B \cdot \rho_B \cdot g}{\rho_f \cdot A_B \cdot C_L}} \quad (24)$$

$$U_{crit-ballast-take-off-vibration} = \sqrt{\frac{2 \cdot V_B \cdot \rho_B \cdot (g - a_z)}{\rho_f \cdot A_B \cdot C_L}} \quad (25)$$

Ballast particle rolling

The third and last ballast particle initiation scenario is ballast particle rolling. To quantify the involved forces, it is assumed that the exposed ballast particle is blocked by other ballast in the trackbed and is thus forced to rotate around its own downstream lower edge, A, as shown in Figure 68. The ballast particle is considered to roll-over as the aerodynamic moment resulting around A caused by the aerodynamic drag (F_D),

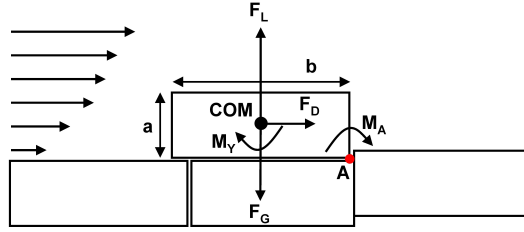


Figure 68: Governing forces and moments around the downstream edge, A, of an exposed ballast particle for the evaluation of the ballast particle rolling as the initial particle movement scenario.

lift (F_L) and moment around the Y-axis (M_Y) overcome the static counter moment of the ballast particle weight. In principle, the possibility of the ballast particle falling back to its initial position after the initiation should be considered. However, since the aerodynamic lift and roll-over moment of the ballast particle increases rapidly as soon as the ballast particle begins to rotate, the chance for the ballast particle to fall back to rest is low. Moreover, if the length of the ballast (b) decreases towards zero the chance that the ballast particle roll-over increases, e.g. a ballast with a large height (a) to length (b) ratio. The definition of the critical to ballast particle rolling air velocity with and without trackbed vibration are presented in Equation (28) and Equation (29), respectively.

$$F_D \cdot \frac{a}{2} + F_L \cdot \frac{b}{2} + M_Y > F_G \cdot \frac{b}{2} \quad (26)$$

$$\frac{1}{2} \cdot \rho_f \cdot U^2 \cdot A_B \cdot (C_D \cdot \frac{a}{2} + C_L \cdot \frac{b}{2} + C_{M_y} \cdot a) > m_B \cdot g \cdot \frac{b}{2} \quad (27)$$

$$U_{crit-ballast-rolling} = \sqrt{\frac{2 \cdot \rho_B \cdot g \cdot V_B \cdot b}{\rho_f \cdot A_B \cdot (C_D \cdot a + C_L \cdot b + 2 \cdot C_{M_y} \cdot b)}} \quad (28)$$

$$U_{crit-ballast-rolling-vibration} = \sqrt{\frac{2 \cdot \rho_B \cdot V_B \cdot b \cdot (g - a_z)}{\rho_f \cdot A_B \cdot (C_D \cdot a + C_L \cdot b + 2 \cdot C_{M_y} \cdot b)}} \quad (29)$$

8.2.2 Ballast particle initiation calculations: Influencing parameters

In order to calculate the critical air velocities for the three considered ballast particle

initiation scenarios, the ballast particle properties such as shape and size must be defined along with the corresponding aerodynamic force and moment coefficients (C_D , C_L , C_{My}). The shape of a cube was assumed instead of the shape of a realistic ballast particle for all ballast flight calculations in this work, simplifying the definition of the shape and the physical properties of the body. Assuming a cubic shape was also more practical since the aerodynamic force and moment coefficients are easier to obtain for simpler geometric shapes. The calculations were conducted assuming a drag coefficient of $C_D = 1.05$, as suggested by Hoerner [124]. Further, the lift coefficient $C_L = 1$ and the pitching moment coefficient $C_{My} = 0.25$ were applied in agreement with the values used in the AeroTRAIN-project [53] also for cubic shape particles. For the ballast particle slide calculations, the ballast-ballast static Coulomb friction coefficient was set to $\mu_{static} = 0.8$, corresponding to the value presented by Saussine et al. [125]. This value was also confirmed by Schroeder-Bodenstein [33], who suggested that the friction coefficient can be calculated from the angle (40° to the ground plane) of ballast downpour. This lead to a friction coefficient of $\mu_{static} = 0.8391$. The ballast particle density was set to $\rho_B = 2600 \text{ kg/m}^3$ in accordance with the value used in the AOA-project [41] and the density of air at 20°C to $\rho_f = 1.2041 \text{ kg/m}^3$. The calculated critical air velocities for the three considered ballast particle initiation scenarios are presented in Figure 69 as a function of the edge length of the simplified ballast particle (cube). The

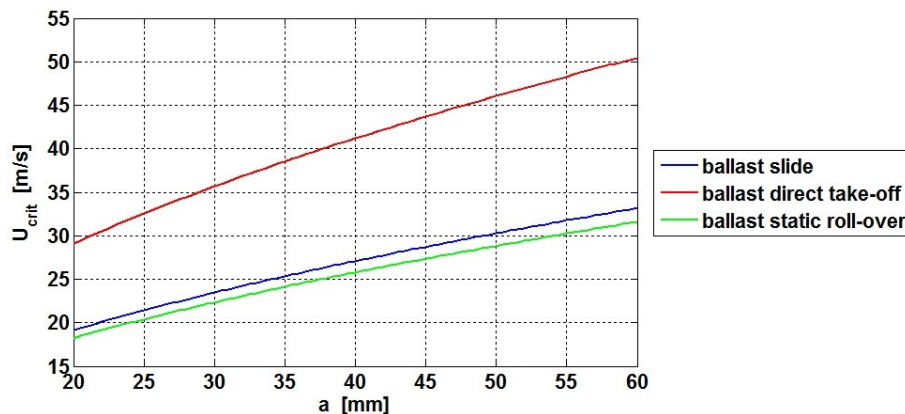


Figure 69: Critical air velocities as a function of the edge length of the simplified exposed cubical ballast particle for the three considered initiation scenarios.

results in Figure 69 clearly show that ballast particle slide and ballast particle rolling are more probable than the direct ejection from the trackbed. This underlines that the model for initial ballast particle movement is similar to the one described by Bagnold and shown in Figure 1. In addition, the results show that smaller ballast particles are

more susceptible to ballast flight since the aerodynamic forces increase quadratically with the projected surface towards the flow or reference area as the weight of the ballast particle (cube) increases with the third power of the edge length. The critical air velocity for the considered ballast particle initiation scenarios increased by 40% for the 40 mm and by 73% for the 60 mm ballast particle in comparison to the smallest considered ballast particle with a size of 20 mm.

The wind tunnel measurement conducted in the AOA-project with a full-scale trackbed [64] simulating the train-induced vibration in the sleeper with a vibrating pot concluded that the number of ballast particles set into motion increased with the strength of the vibration. The crucial influence of the trackbed vibration is reflected in Equations (21), (25) and (29). The influence of the trackbed vibration was simplified by assuming a constant trackbed acceleration away from the train that reduces the weight of the ballast (a_z). The data for the trackbed vibration (a_z) in Equations (21), (25) and (29) were extracted from the full-scale measurements by Quinn et al [32] for a Class 373 Eurostar train in commercial operation at speeds around 300 km/h. The train-induced vibration of the sleeper and the trackbed during train passages were measured by low-frequency geophones and a triaxial accelerometer. The presented mean maximum accelerations revealed horizontal accelerations of $a_z = 7 \text{ m/s}^2$ for the sleepers and $a_z = 3 \text{ m/s}^2$ for the ballast. The influence of the trackbed vibration were evaluated for the three considered ballast particle initiation scenarios assuming that an exposed simplified ballast particle lied on top of a sleeper ($a_z = 7 \text{ m/s}^2$) or in the trackbed on top of the other ballast ($a_z = 3 \text{ m/s}^2$). Additionally, the friction coefficient for the ballast particle on top of the smooth sleeper is lower than that for a ballast particle in the trackbed. The static friction coefficient for the ballast particle on top of the sleeper was therefore changed to $\mu_{static} = 0.6$ (instead of $\mu_{static} = 0.8$), which is the friction coefficient for a smooth concrete and a gravel rock surface [126]. The critical air velocities calculated assuming trackbed vibration for the exposed ballast particle lying in the trackbed and on top of a sleeper are presented in Figure 70 for the three considered ballast particle initiation scenarios. The obtained critical air velocity values in Figure 70 demonstrate the strong influence of the trackbed vibration. The vibration reduce the critical air velocity values for all three ballast particle initiation scenarios by almost 17% for $a_z = 3 \text{ m/s}^2$ and almost 46% for $a_z = 7 \text{ m/s}^2$ when compared to the values without trackbed vibration. The trackbed vibration did not change the fact that the ballast particle direct take-off was still considered as the most improbable ballast particle initiation scenario. In any case, direct ballast particle

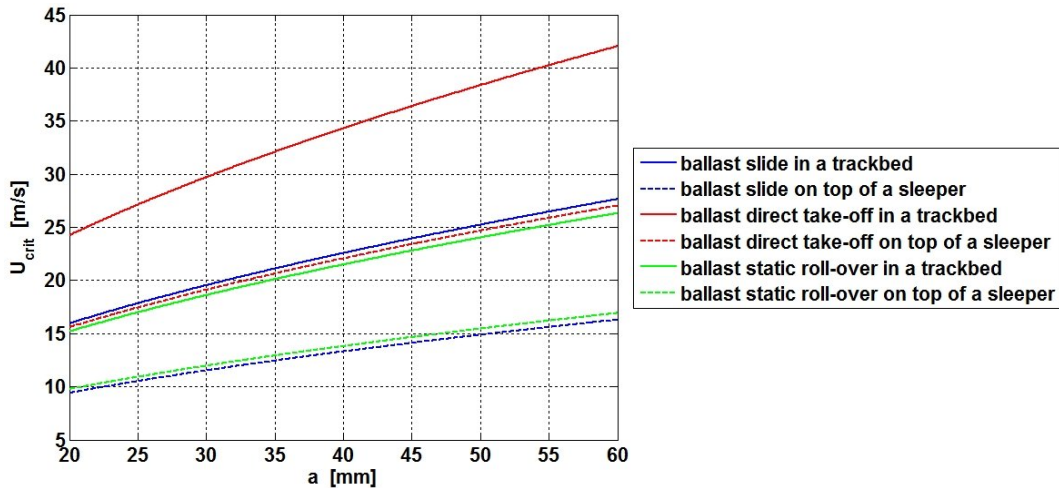


Figure 70: Critical air velocities as a function of the edge length for the simplified exposed ballast particle for the three considered ballast particle initiation scenarios under the influence of trackbed vibration in a trackbed ($a_z = 3 \text{ m/s}^2$) and on top of a sleeper ($a_z = 7 \text{ m/s}^2$).

take-off should not be completely ruled out since it was observed in wind tunnel experiments [29, 65, 123]. The small difference in the critical air velocity values in Figure 70 between ballast particle sliding and rolling reveal that both scenarios are possible for the exposed ballast particle in the trackbed as well as on top of a sleeper. Ballast particle rolling is, however, the most probable initiation scenario for ballast particles in the trackbed. Besides the slightly smaller values of the critical air velocity, the exposed ballast particle will most likely be blocked by the other ballast in the trackbed and thus preventing a sliding motion. Furthermore, the results show that the most susceptible position for a ballast particle is on top of a sleeper. The reasons are the strong sleeper vibration and the lowered value of the static friction coefficient.

The presented results conclude that the trackbed vibration should be included in the risk assessment of ballast flight. Further, it is considered to be sufficient to only consider the ballast particle slide and ballast particle rolling for the evaluation of the initiation of ballast particle motion. The only exception is for ballast particles with very strong lift coefficients.

8.2.3 Ballast particle initiation calculations: Critical train speeds

The PIV undercarriage flow fields for the considered train and ground configurations in the water-towing tank were used together with the results of the trackbed vibration measurements by Quinn et al. [32] to calculate the critical train speeds for the

initiation of ballast particle movement for the simplified ballast particles. Dependent on the ground configuration and the position of the simplified ballast particle on the trackbed, different boundary conditions were assumed based on the trackbed vibration measurements [32] and the calculations in the previous section. The boundary conditions applied for the considered cases or ballast particle trackbed positions are summarised in Table 7. For the ground with sleepers, both the central position on top

	Initiation scenario	Trackbed vibration
Smooth ground	Slide	$a_z = 7 \text{ m/s}^2$
Rough ground	Rolling	$a_z = 3 \text{ m/s}^2$
Above sleeper	Slide	$a_z = 7 \text{ m/s}^2$
Between sleepers	Rolling	$a_z = 3 \text{ m/s}^2$

Table 7: Applied boundary conditions for the considered ballast particle trackbed positions.

of a sleeper (above sleeper) and the inter-sleeper position at $\Delta X = 8 \text{ mm}$ downstream from the sleeper centre (between sleepers) were considered for the calculation of the critical train speed for the initiation of the ballast particle movement. The instantaneous u velocity data closest to the ground (i.e. $Z = 0.1 \text{ mm}$, 0.3 mm , 0.5 mm , 0.7 mm , 0.9 mm , 1.1 mm and 1.4 mm in scale 1:50) in the water-towing tank experiments were extracted along the entire train length (X direction) to determine the horizontal profiles of the mean U velocity and its corresponding standard deviation. The horizontal profiles of the mean U velocity and U_{SD} at the different vertical heights were then used to calculate the mean flow field over the vertical height of the simplified ballast particle (see Figure 71) for every X position along the train. The maximum value in

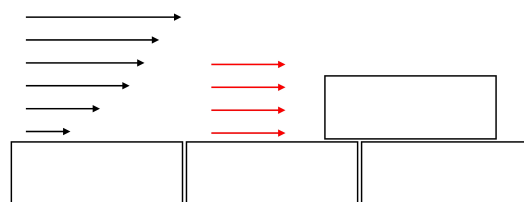


Figure 71: The actual flow field (black) and the mean flow field (red) over the ballast particle height.

the undercarriage flow of the normalised mean U velocity averaged over the ballast particle height, together with previously presented critical or threshold air velocity for the different ballast particle initiation scenarios, defines the lowest critical train speed capable of initiating ballast particle movement. The critical train speeds obtained using the mean U velocity data for the three considered train configurations are plotted

as a function of the edge length of the ballast particle in Figure 72 for the exposed simplified ballast particle lying in the trackbed on top of other ballast (rough ground and between sleepers), on top of a sleeper (above sleeper) and on top of a concrete slab track (smooth ground). The results in Figure 72 reflect the undercarriage flow re-

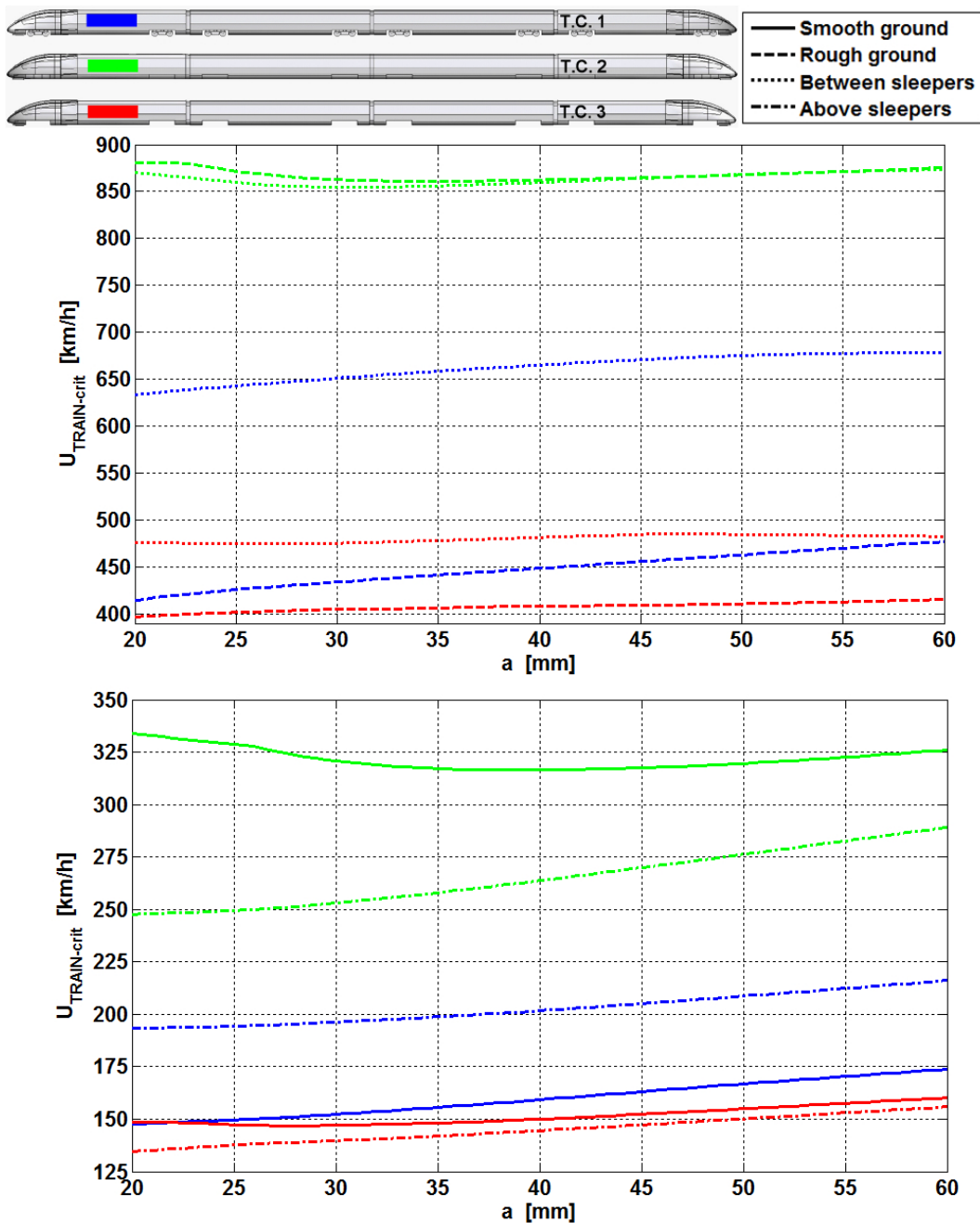


Figure 72: Critical train speeds for the initiation of ballast particle movement as a function of the edge length of the simplified exposed ballast particle for the three train models and the considered ballast particle trackbed positions using the mean U velocity flow field data.

sults presented in section 6, that a rougher undercarriage induces larger aerodynamic forces (larger U velocity values), whilst the increased drag of the trackbed (rough ground and sleepers) decreases the U velocity values especially near the trackbed. The critical train speeds in Figure 72 also reveal the strong, positive effect of lowering the ballast level for a trackbed with monoblock sleepers, which generally results in the largest critical train speeds for ballast particle initiation. The reason for this is that the protruding sleepers shield the ballast in the inter-sleeper regions from the undercarriage flow. The lowered ballast in the inter-sleeper region is therefore considered to have ballast particles with the lowest risk for ballast flight. However, the critical train speeds in Figure 72 reveal the strongly increased risk of ballast flight when ballast particles lie on top of sleepers. Ballast particles on the sleeper are seen to slide for the reference and the rough train models for the entire considered ballast size range (20-60 mm) at the conventional speed range of today's high-speed trains. Even more interesting is the fact that the smooth train model, which has the lowest mean U velocity values, velocity gradients close to the ground and streamwise turbulence, was capable of setting ballast particles on top of the sleepers into motion for realistic train speeds. This clearly highlights the danger of ballast particles on sleepers and the importance of the trackbed maintenance for ballast trackbeds with monoblock sleepers. For well-maintained ballast trackbeds (avoiding ballast particles on sleepers), the largest risk of ballast flight is found for ballast trackbeds with a ballast level flushed with the upper surface of the sleepers and for trackbeds with bi-block sleepers. A smooth ground reflecting a concrete slab track was included in the ballast particle initiation calculations, given the trackbed transition regions from ballast trackbed to concrete slab track. Ballast particles displaced from the ballast trackbed onto the concrete slab track are those susceptible to ballast flight due to the lower critical train speed for ballast particle initiation on a concrete slab track. The risk of ballast flight is therefore higher for rolling stock travelling from a concrete slab track to a ballast trackbed. This initiates ballast particles lying on the concrete slab track, which may eventually initiate more ballast particles further downstream on the ballast trackbed as shown in Figure 1. Taking the static and dynamic threshold of Bagnold in Equation (16) for particle dislodgement into account reveals the danger of the trackbed transitions with ballast particles lying on concrete slab tracks, since the dynamic threshold of impacting particles for particle dislodgement is 20% lower than the initial threshold (static). Besides the danger from ballast trackbed transitions, foreign objects similar to the simplified ballast particle, lying exposed on a concrete slab track, can damage

the train or injure trackside workers and passengers on railway station platforms as well as trackside objects.

The critical train speeds for initiating ballast particle motion is around 450 km/h for the reference train model and 400 km/h for the rough train model for the rough ground. These speeds are considered to be too large since ballast flight incidents were reported to occur for train speeds around 300 km/h. This indicates, once again, that the previously presented turbulence or streamwise velocity fluctuations (U_{SD}) in the undercarriage flow should be taken into account regarding the risk assessment of ballast flight. The critical train speeds for ballast particle initiation were estimated analogously to the previous presented results in Figure 72, but using the mean U velocity + U_{SD} and the expected maximum u velocity values (mean U velocity + $2 \cdot U_{SD}$) instead of the mean U velocity. The outcome is presented in Figure 73 for the mean U velocity + U_{SD} and in Figure 74 for the expected maximum u velocity values (mean U velocity + $2 \cdot U_{SD}$). Considering the velocity fluctuations by summing the standard deviation and the mean U velocity values decreases the critical train speeds necessary for the initiation of ballast particle motion. The critical train speeds based on the expected maximum u velocity (mean U velocity + $2 \cdot U_{SD}$) in Figure 74 were all reduced by a factor of two compared to the results in Figure 72, which uses only the mean U velocity. Including the velocity fluctuations results in more realistic critical train speeds for the reference and the rough train models for the rough ground these being 275-340 km/h and 250-290 km/h based on the mean U velocity + U_{SD} and being 200-270 km/h and 180-210 using the maximum expected u velocity (mean U velocity + $2 \cdot U_{SD}$). This signifies that the streamwise turbulence (U_{SD}) should be accounted for in the risk assessment of ballast flight. The estimated critical train speed is deduced from the maximum u velocity value (with and without U_{SD}) in the undercarriage flow, thus the lowest possible train speed able to initiate ballast particle movement. In order to realistically start the ballast particle movement and accelerate the ballast particle over the trackbed with the risk of initiating ballast flight impacting the train undercarriage, larger train speeds than the presented estimated critical train speeds in Figures 72 - 74 would therefore be required. This favours the usage of the expected maximum u velocity (mean U velocity + $2 \cdot U_{SD}$) for the definition of the critical train speed for ballast particle dislodgement. Using the streamwise turbulence (U_{SD}), as is for the expected maximum u velocity, to determine the critical train speeds for the assessment of ballast flight also reflects the reported full-scale observations of a stochastic or sporadic occurrence of ballast flight incidents that is difficult to predict.

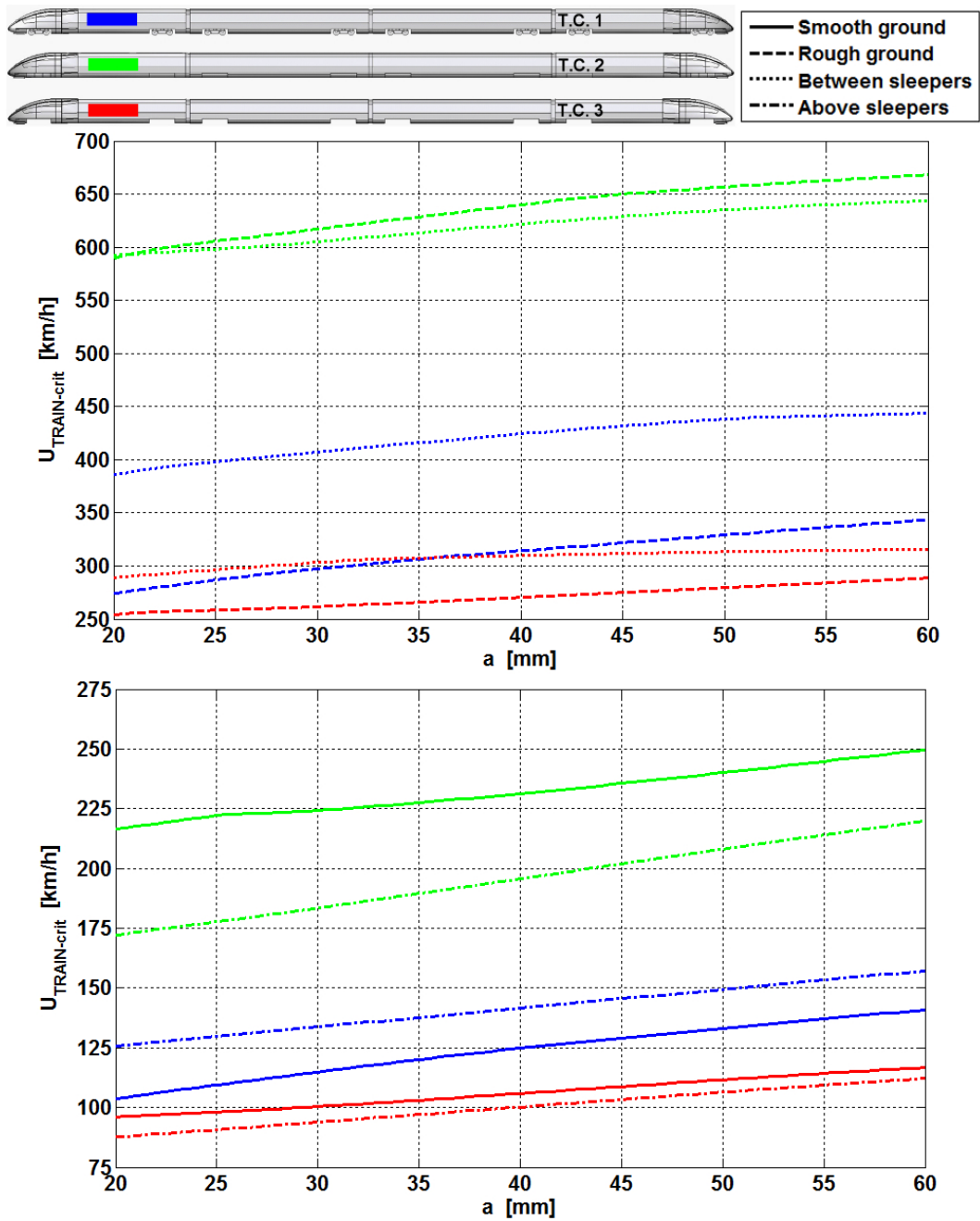


Figure 73: Critical train speeds for the initiation of ballast particle movement as a function of the edge length of the simplified exposed ballast particle for the three train models and the considered ballast particle trackedbed positions using the mean U velocity + U_{SD} flow field data.

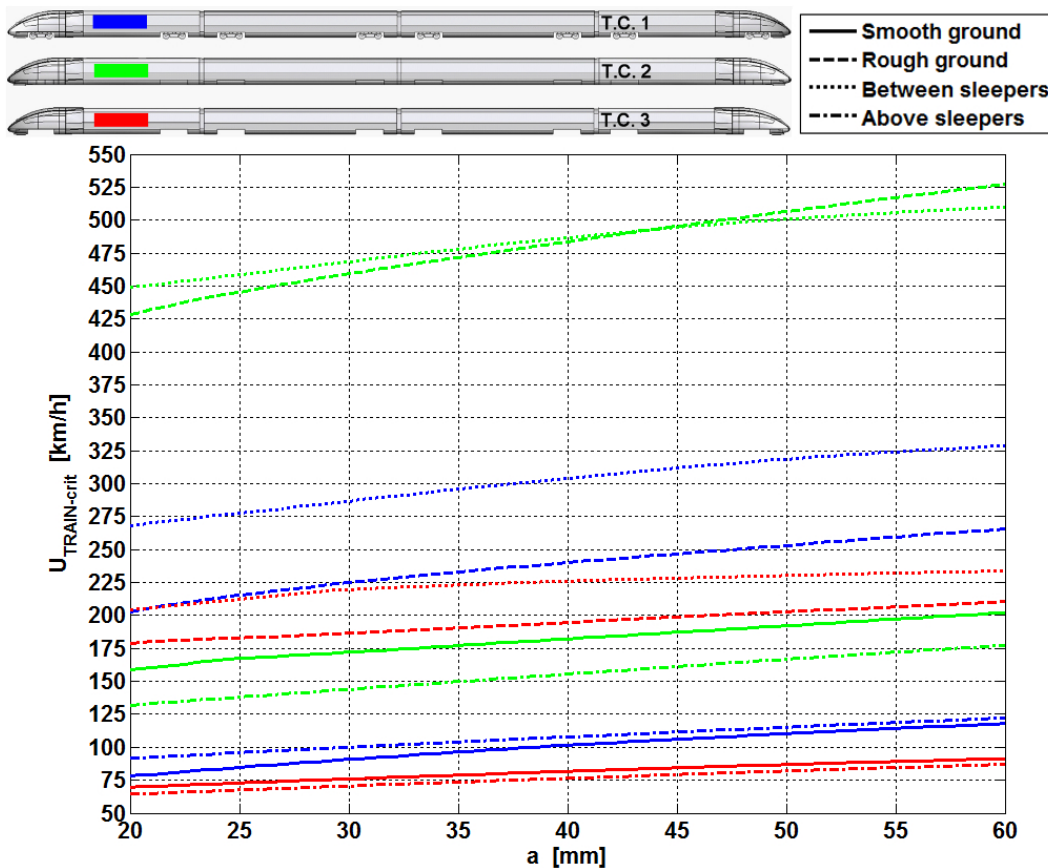


Figure 74: Critical train speeds for the initiation of ballast particle movement as a function of the edge length of the simplified exposed ballast particle for the three train models and the considered ballast particle trackbed positions using the mean U velocity + $2 \cdot U_{SD}$ data flow field data.

According to Guler and Mert [112], ballast particles used for railway trackbeds worldwide are in the size range of 1.2-63 mm, whereas the European standard EN-13450 [98] uses ballast in a size range of 22.4-63 mm. The majority of the ballast for all trackbeds is however between 28 mm and 50 mm [112]. The risk assessment of ballast flight should therefore concern the majority of the ballast in the trackbed (i.e. 28-50 mm). Critical train speed data were extracted from the results in Figures 72 - 74 and presented in Table 8 to provide a more detailed comparison between the measured configurations. The table shows the three ballast particle sizes of $a = 28, 40$ and 50 mm, corresponding to ballast particle masses of $m_B(28, 40, 50 \text{ mm}) = 57.1, 166.4$ and 325 g. The critical train speeds in Table 8 reflect the susceptibility of the different trackbed designs to ballast particle motion as well as the maximum u velocity value appearing in the undercarriage flows. The lowest critical train speeds are thus found for the rough train model, with the largest local mean U velocity and velocity fluctuation

T.C.	G.C.	mean U	mean U + U_{SD}	mean U + 2· U_{SD}
		a = 28, 40, 50 mm	a = 28, 40, 50 mm	a = 28, 40, 50 mm
1	A	151, 159, 167 km/h	113, 125, 133 km/h	88, 102, 110 km/h
2	A	324, 317, 320 km/h	223, 231, 240 km/h	170, 182, 192 km/h
3	A	147, 150, 155 km/h	99, 106, 112 km/h	75, 82, 87 km/h
1	B	431, 449, 463 km/h	294, 314, 329 km/h	221, 240, 253 km/h
2	B	865, 862, 868 km/h	612, 640, 657 km/h	454, 484, 507 km/h
3	B	404, 408, 411 km/h	260, 271, 280 km/h	185, 195, 203 km/h
1	C1	648, 665, 675 km/h	403, 424, 438 km/h	283, 304, 319 km/h
2	C1	856, 860, 868 km/h	602, 622, 635 km/h	464, 487, 501 km/h
3	C1	475, 482, 485 km/h	301, 310, 313 km/h	217, 226, 230 km/h
1	C2	195, 202, 209 km/h	132, 142, 149 km/h	98, 108, 115 km/h
2	C2	251, 264, 276 km/h	181, 196, 208 km/h	142, 156, 167 km/h
3	C2	139, 145, 150 km/h	93, 100, 106 km/h	69, 77, 82 km/h

Table 8: Critical train speeds for the initiation of motion for the exposed simplified ballast particle with an edge length of $a = 28, 40$ and 50 mm for the reference (T.C. 1), smooth (T.C. 2) and rough (T.C. 3) train models on the smooth ground (G.C. A), rough ground (G.C. B) and the two considered positions of the ground with sleepers, i.e. in a inter sleeper region (G.C. C1) and on top of a sleeper (G.C. C2).

(U_{SD}) values around the open bogie housings for ballast particles lying on top of a sleeper. Considering the values calculated using the expected maximum u velocity, the right column in Table 8, reveal that ballast particle motion can be expected for a high-speed train travelling at 300 km/h (based on the results for the reference and the rough train models), independent of the trackbed design. At 300 km/h, particle motion for exposed ballast particles on top of a sleeper or on the slab track (ballast to slab track transition) can also be expected for a highly aerodynamically optimised high-speed train (smooth train model), once again accentuating the importance of trackbed maintenance. The strong local flow acceleration around the open bogie housings of the rough train model initiate ballast particle motion at lower train speeds in comparison to the more steady undercarriage flows for the reference train model and of course the smooth train model. The calculated critical train speeds for the ballast particle initiation does not reflect if the more dynamic undercarriage flow of the rough train model, which has even lower mean U velocity values along the smooth train car than for the reference train model, causes more ballast flight incidents than the reference train model does. To assess the risk of ballast flight and the effect of the undercarriage flow characteristics of the different train configurations, especially for the reference and the rough train models, the ballast particle movement over the trackbed

after dislodgement from the trackbed must be evaluated. This was conducted and is presented in the next section. Regarding the different trackbed designs, the extracted critical train speeds in Table 8 clearly demonstrate that ballast particle motion is initiated at much lower train speeds for ballast particles lying on top of sleepers (ground configuration C2) or on concrete slab tracks (ground configuration A) than those lying on top of other ballast in the inter-sleeper region (ground configuration C1) or for a ballast trackbed with bi-block sleepers (ground configuration B). The large difference (more than a factor of two) of the critical train speeds necessary to initiate motion for ballast particles on top of sleepers compared to those lying on top of other ballast in a bi-block ballast trackbed is slightly misleading regarding the overall risk of ballast flight. The transition for the dislodged ballast particle to the transport phase over the trackbed must be treated differently considering the different trackbed designs (i.e. ground configurations). In other words, it depends on whether or not the trackbed has protruding sleepers. The transition to the transport phase for the rough ground (also valid for the smooth ground) is considered to be realised as soon as the critical train speed for ballast particle initiation is exceeded. Thereafter, the governing momentum equation in the travelling direction (X direction) defines the motion over the trackbed. This is, however, not the case for the ground with sleepers. The dislodged ballast particle initially on top of a sleeper as well as in the inter-sleeper region must at least have sufficient momentum to be transported over the first neighbouring sleeper before it could successfully enter the transport phase over the trackbed. Larger train speeds than those listed in Table 8 are therefore necessary for a true risk of ballast flight. This relates to the low susceptibility of ballast flight for a ballast trackbed with cross-going sleepers, lowered ballast level and a well-maintained trackbed quality (avoiding sleepers on top of the sleepers). There always remains, however, a risk that ballast particles may come to lie on top of sleepers, which is considered to be the worst-case scenario for ballast flight. Today's high-speed trains easily overcome the low critical train speeds in Table 8 for a ballast particle on top of a sleeper. The low critical train speeds for the ballast particle on top of a sleeper and its exposed position therefore indicate that a ballast particle might only slide off the sleeper and come to rest again in the inter-sleeper region as the undercarriage flow develops along the train length. This highlights the importance of the undercarriage flow at the beginning of the train, i.e. the flow around the head and the undercarriage flow developing along the leading end-car.

The impact of the flow around the head of the train on the exposed ballast in the

trackbed, especially for the one on top of a sleeper, was evaluated by calculating the critical train speeds using only the flow region around the head, i.e. $-0.06 < X / L_{TRAIN} < 0.07$ in Figure 37 in section 6.3.3. The calculations were conducted analogously to the previous ballast particle initiation calculations, but considering the direction of the flow ($U + U_{SD} \cdot \text{sign}(U)$). The calculations were only conducted on the reference train model since the geometry of the head was the same for the three train configurations and the undercarriage roughness mostly little influenced the characteristic flow around the head, as shown in Figure 37 in section 6.3.3. The results are presented in Table 9, revealing that the flow around the head of the train is strong enough to initiate motion for exposed ballast particles on top of sleepers or on slab tracks (smooth ground) for train speeds near 300 km/h. At those train speeds, exposed ballast par-

G.C.	U	$U + U_{SD} \cdot \text{sign}(U)$	$U + 2 \cdot U_{SD} \cdot \text{sign}(U)$
	a = 28, 40, 50 mm	a = 28, 40, 50 mm	a = 28, 40, 50 mm
Smooth ground	344, 370, 393 km/h	290, 323, 346 km/h	250, 286, 307 km/h
Rough ground	528, 592, 641 km/h	429, 500, 554 km/h	353, 433, 487 km/h
Between sleepers	601, 666, 716 km/h	504, 573, 625 km/h	434, 500, 547 km/h
Above sleeper	265, 291, 313 km/h	210, 240, 263 km/h	174, 203, 226 km/h

Table 9: Critical train speeds for the initiation of motion for the simplified exposed ballast particle with edge lengths of a = 28, 40 and 50 mm for the flow field around the head of the reference train model (T.C. 1) on the considered ground configurations.

ticles in the inter-sleeper region or in the bi-block trackbed (rough ground) can be considered to be at rest during the passage of the train's head. The obtained flow field around the head of the train model in the water-towing tank experiments revealed that the largest magnitude of u velocity values were found for the reverse flow region, independent of the ground condition. All critical train speeds in Table 9 were thus calculated from this local negative u velocity peak value, pushing the ballast particle opposite the direction the train is travelling. The critical train speeds for the positive u velocity peak had values around 10-65% larger than those for the negative u velocity peak. For larger train speeds or for other geometric shapes of the train's head, ballast particles can be initiated in both X directions, especially for ballast particles on top of sleepers.

The aerodynamic forces induced by passing trains on trackside objects and the trackbed ballast are not only linked to the train-induced air draft. The head pressure pulse [16, 17] is known to exert transient pressure loads on trackside objects as well as the ballast in the trackbed and should also be considered with regard to evaluating ballast

particle motion.

Influence of the static pressure:

The total instantaneous aerodynamic force on an exposed ballast particle in a trackbed is composed of the force induced by the air velocities and the transient pressure gradients appearing in the undercarriage flow. In the work of Odar and Hamilton [127], the total instantaneous force on a rectilinearly accelerating sphere was described by an equation with terms representing the force due to velocity, acceleration and history of the motion. The velocity-induced force term is the well-known steady-state viscous drag ($F_D = 0.5 \cdot \rho_f \cdot U_\infty^2 \cdot A_{ref} \cdot C_D$). The acceleration term does not include viscosity and corresponds to the force derived for an inviscid irrotational flow i.e. potential flow ($F_A = C_A \cdot V_{ref} \cdot \rho_f \cdot a_x$). The third, term representing the history of motion, diminishes rapidly with time but is still required, e.g. to represent the forces after a rapid stop caused by the residual velocities. The suggested definition of the total force by Odar and Hamilton [127] was applied, but without the history term, in order to evaluate the influence of the pressure gradients found in the undercarriage flow on the initiation of ballast particle motion. The evaluation of the aerodynamic forces caused by the steady-state flow (velocity term) were conducted analogously to the calculations in the beginning of this section. The acceleration term corresponding to the forces in an inviscid irrotational flow is also that typically applied calculating the unsteady forces of the transient head pressure pulse of high-speed trains [128]. Since only flow field measurements (PIV) were conducted in the water-towing tank experiments, the pressure data obtained from the full-scale measurements presented in section 7.1 was used to evaluate the influence of the aerodynamic forces induced by the static pressure gradients in the undercarriage flow. The static pressure coefficient data (C_P) from the static pressure probe installed in the trackbed line of symmetry at a height of 250 mm above the concrete slab track (see Figure 75) was applied together with the following equations and assumptions to calculate the critical train speeds for the initiation of ballast particle motion due solely to the static pressure gradients in the undercarriage flow. The previous results and assumptions regarding the initiation of ballast particle motion, dependent on the ground configuration or the ballast particle position in the trackbed (see Table 7), are applied for the evaluation of the static pressure gradients.

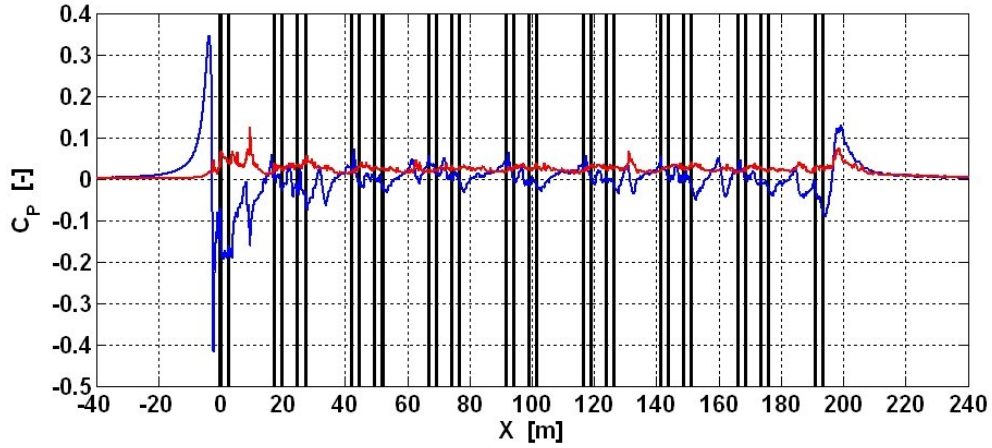


Figure 75: The mean static pressure coefficient C_P (blue line) and its corresponding standard deviation (red line) for the static pressure probe installed in the trackbed line of symmetry ($Y = 0$ mm) at a height 250 mm above the concrete slab track ($Z / H_{GAP} = 0.447$) of the conducted full-scale measurements. The black vertical lines indicate the train axle positions.

The governing forces on an exposed ballast particle due to the static pressure gradient and the governing equations are presented below for the ballast particle slide and ballast particle rolling in Figure 76 and Figure 77, respectively. The ballast particle

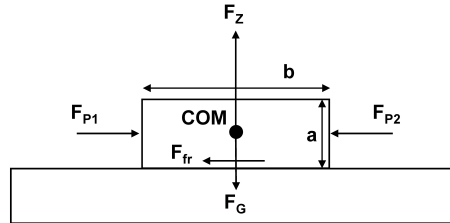


Figure 76: Governing forces on an exposed simplified ballast particle regarding the initial particle movement through ballast particle slide for the train-induced static pressure gradient.

slide criteria is defined in the same way as for the undercarriage flow, except that the acting force on the exposed ballast particle in the rail direction (F_X) is substituted for the force resulting from the static pressure gradient in the flow ($|F_{P1} - F_{P2}|$). Thus, the sliding motion starts as soon as the pressure gradient force overcomes the friction force (F_{fr}), as signified in Equation (30).

$$|F_{P1} - F_{P2}| > F_{fr} \quad (30)$$

Assuming a uniform distribution of the pressure on the upstream ($P1_{static}$) and downstream ($P2_{static}$) particle surfaces facing the flow, the resultant force from the pressure

gradient can be described as by the left hand side of Equation (31). The friction force (Coulomb friction) is defined by the empirical constant (μ_{static}) of the two surfaces in contact and the force pressing the two surfaces together, i.e. the normal force of the surface.

$$|P1_{static} - P2_{static}| \cdot A_B > \mu_{static} \cdot (F_G - F_Z) \quad (31)$$

The pressure difference on the left hand side in Equation (31) is caused by the pressure gradient along the train length acting on the exposed ballast particle. The resulting force of the pressure gradient on the ballast particle can be expressed in a simplified way as the product of the pressure gradient ($\partial P / \partial X$) at the centre of mass (COM) and the streamwise length of the ballast particle (ΔX), see Equation (32). Since the velocity component in the travelling direction of the train clearly dominates the undercarriage flow, the contribution of the pressure force resulting from the pressure gradient in the X direction is the one of interest. Once more, the way the trackbed vibration affect the ballast particle weight is very simplified and assumes a worst-case scenario for ballast flight with a constant acceleration of the ballast particle (a_z) away from the trackbed, thus reducing the weight of the ballast.

$$\left| \frac{\partial P_{static}}{\partial X} \right| \cdot \Delta X \cdot A_B > \mu_{static} \cdot (m_B \cdot g - m_B \cdot a_z) \quad (32)$$

Using the definition of the dimensionless static surface pressure coefficient ($C_P = P_{static} / 0.5 \cdot \rho_f \cdot U_{TRAIN}^2$) and the definition of the ballast particle mass ($m_B = \rho_B \cdot V_B$) the critical train speed for initiating the sliding motion of ballast particles can be calculated using the measured pressure gradient according to Equation (33).

$$U_{train-crit-slide-vibration} = \sqrt{\frac{2 \cdot \rho_B \cdot V_B \cdot \mu_{static} \cdot (g - a_z)}{\rho_f \cdot \left| \frac{\partial C_P}{\partial X} \right| \cdot b \cdot A_B}} \quad (33)$$

The governing forces on an exposed ballast particle are the same as for the ballast particle slide but for which the resulting moment of the pressure gradient must overcome the counter-moment of the ballast particle's own weight around the downstream lower edge (A), as shown in Figure 77 and expressed in Equation (34).

$$|F_{P1} - F_{P2}| \cdot \frac{a}{2} + F_Z \cdot \frac{b}{2} > F_G \cdot \frac{b}{2} \quad (34)$$

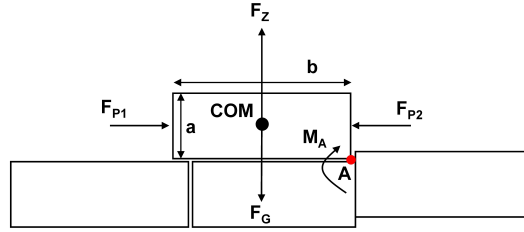


Figure 77: Governing forces on an exposed simplified ballast particle regarding the initial particle movement through ballast particle rolling for the train-induced static pressure gradient.

Using the same assumptions for the force caused by the static pressure gradient and the definition of the other variables (F_Z and F_G), the critical train velocity for the ballast particle rolling could be defined as in Equation (35).

$$U_{train-crit-rolling-vibration} = \sqrt{\frac{2 \cdot \rho_B \cdot V_B \cdot b \cdot (g - a_z)}{\rho_f \cdot \left| \frac{\partial C_P}{\partial X} \right| \cdot b \cdot A_B}} \quad (35)$$

The critical train speeds were calculated for the simplified ballast particle (cube) with Equation (33) dictating the initiation of the ballast particle slide using the static pressure coefficient data from the full-scale measurements presented in Figure 75 (from a high-speed train cruising over a concrete slab track around 300 km/h). The critical train speeds for the initiation of the ballast particle sliding motion were calculated for the flow around the head of the train, for the fully developed undercarriage flow and for the near-wake flow around the tail of the train. The data used for the undercarriage flow region were extracted from the undisturbed (no local flow disturbances from axillary equipment or cooling air outlets) region of the fourth and fifth train cars, $67 \text{ m} < X < 127 \text{ m}$ in Figure 75. This region is most representative of a generic high-speed train. Only the positive pressure gradients (i.e. pressure forces in the travelling direction) in the undercarriage flow and the near-wake flow regions were considered since they contribute to the overall aerodynamic forces on the ballast, given that the streamwise characteristics dominate the flow in these regions. The forces caused by the static pressure gradients in the undercarriage flow are represented by the term for the acceleration forces in the total force decomposition proposed by Odar and Hamilton [127]. This decomposition assumes an inviscid and irrotational flow (potential flow). Using the acceleration force term to represent the contribution of the aerodynamic forces on the ballast induced by the static pressure gradients for the fully devel-

oped undercarriage flow and near-wake flow does not imply that these flow regions are considered to be inviscid and irrotational, which they are clearly not. Nevertheless, the static pressure gradients from the full-scale measurements under realistic conditions (viscous flow) show that there are forces on the ballast particle induced by the static pressure gradients. The total force decomposition approach of Odar and Hamilton is still therefore applied and considered to be a realistic approximation for the total force on the ballast, even for the viscous undercarriage flow regions. The calculated critical train speeds for the initiation of the ballast particle sliding motion caused by the static pressure gradients in the flow around the head, the fully developed undercarriage flow and the near-wake flow are presented in Table 10. The

	$\left(\frac{\partial C_P}{\partial X}\right)_m$	$\left(\frac{\partial C_P}{\partial X}\right)_m + \left(\frac{\partial C_P}{\partial X}\right)_{SD}$	$\left(\frac{\partial C_P}{\partial X}\right)_m + 2 \cdot \left(\frac{\partial C_P}{\partial X}\right)_{SD}$
Cube edge length	a = 28, 40, 50 mm	a = 28, 40, 50 mm	a = 28, 40, 50 mm
Head flow	245, 245, 245 km/h	234, 234, 234 km/h	224, 224, 224 km/h
Undercarriage flow	878, 878, 879 km/h	640, 639, 640 km/h	486, 485, 486 km/h
Near-wake flow	922, 922, 922 km/h	497, 497, 498 km/h	370, 371, 371 km/h

Table 10: Critical train speeds in for the initiation of sliding motion for the simplified ballast particle on the smooth ground (G.C. A) using the static pressure coefficient, mean, mean + SD and mean + 2·SD data from the conducted full-scale measurements in section 7.

results in Table 10 reveal that the flow around the head of the train is the most interesting flow region regarding the influence of the static pressure gradients on the total force on the ballast. Comparing the critical train speeds in Table 10 to the corresponding values caused by the flow for the reference train model on the smooth ground in Tables 8 and 9 indicate that the force contribution of the static pressure gradients for the fully developed undercarriage flow and in the near-wake flow is of little interest regarding the risk of ballast flight. The results also confirm that using the total force decomposition was an adequate approximation, since the viscous forces clearly dominate the total force for the fully developed undercarriage flow. Based on the results presented in Table 10 and in order to assess the risk of ballast flight correctly the force contribution of the static pressure gradients around the head of the train should be incorporated. The critical train speeds presented for the flow around the train head in Table 10 were all calculated from the largest pressure gradient, all found around the underpressure region, with a negative pressure gradient. The ballast particles are therefore forced in the opposite train direction of travel, analogously to the flow induced forces in Table 9. Further, the estimated critical train speeds reveal that the forces caused by the static pressure gradients are independent of the ballast particle

size. This is also confirmed by Equation (32), where the pressure gradient force as well as the counter forces (friction force and counter-moment) retaining the ballast particle from sliding or turning-over are all proportional to the volume of the ballast particle. This shows that the influence of the static pressure gradient force on the total force on the ballast particle becomes more significant for larger ballast particles since the viscous- or flow-induced forces (F_D , F_L) are proportional to the exposed surface. Since it was argued that the static pressure gradients around the head of the train should be included in the risk assessment of ballast flight, calculations of the critical train speed for the initiation of ballast particle movement were undertaken incorporating both the induced flow and the static pressure gradients around the head of the train. Assuming that the flow around the head of the train is inviscid and irrotational, the corresponding head pressure pulse of the considered train and ground configurations could be calculated from the measured flow fields in the water-towing tank experiments using potential flow theory. This is a well-accepted approach according to Baker [129]. According to potential flow theory, the flow around the head of the train can be described by the Euler momentum conservation equation for the X direction (rail direction), i.e. Equation (36).

$$\frac{\partial u}{\partial t} + u \cdot \frac{\partial u}{\partial X} + \frac{1}{\rho_f} \cdot \frac{\partial P}{\partial X} = 0 \quad (36)$$

Using the potential flow theory for the head pressure pulse also assumes that the flow around the exposed ballast particle is symmetric (no flow separations) and thus that the aerodynamic forces on the exposed ballast particle are only caused by the linear effects, i.e. the transient static pressure gradients, according to Sanz-Andrés [128]. The Euler equation could therefore be linearised and expressed according to Equation (37).

$$\rho_f \cdot \frac{\partial u}{\partial t} = - \frac{\partial P}{\partial X} \quad (37)$$

The flow field data (instantaneous u velocity) around the head of the train and near the trackbed used for the previous evaluation of the ballast particle initiation were also used to calculate the corresponding static pressures around the head of the train. The mean U velocity data around the head of the train and closest to the trackbed (i.e. 0.1 mm and 0.3 mm in scale 1:50) reveal the thinness of the boundary layer on the trackbed, as the data for $Z = 0.5$ mm, 0.7 mm, 0.9 mm, 1.1 mm and 1.4 mm are outside

the boundary layer. In order to calculate the pressure around the head of the train, an irrotational and inviscid flow (no boundary layer) was assumed and the extracted u velocity data at $Z = 0.9$ mm (45 mm in full-scale) above the trackbed were used for the calculations. The time derivation of u needed to calculate the static pressure gradient (Equation (37)) was calculated using Taylor's frozen flow hypothesis from the available spatial u velocity distribution according to Equation (38) using the train model speed of $U_{TRAIN} = 4$ m/s.

$$U_{TRAIN} \cdot \frac{\partial u}{\partial X} = \frac{\partial u}{\partial t} \quad (38)$$

The mean static pressure coefficient (C_P) around the head for the reference train model on the smooth ground is compared to the results of the static pressure probe installed in the trackbed line of symmetry from the full-scale measurements in Figure 78. The

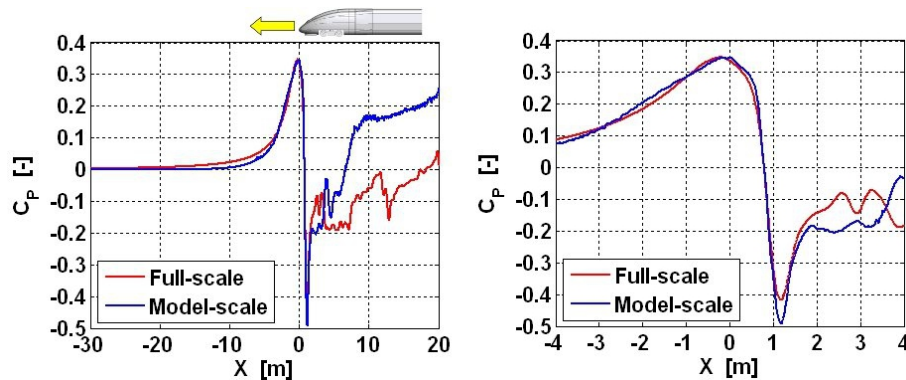


Figure 78: Comparison of the mean static pressure coefficient around the head of the train for the static pressure probe installed in the trackbed line of symmetry for the full-scale measurements in section 7 (red) with the calculated mean static pressure coefficient from the flow field data of the reference train model (T.C. 1) on the smooth ground (G.C. A) (blue).

good agreement of the calculated static pressure coefficient with the one from the full-scale measurements confirms the validity of the accepted approach for treating the flow around the head of the train as inviscid and irrotational [129]. The comparison in Figure 78 clearly reveals that viscous effects after the first bogie appear and begin to dominate the undercarriage flow along the train length as flow separations occur and boundary layers on the trackbed and the train's undercarriage form. The presented approach using the measured flow field data from the water-towing tank experiments and potential flow theory were applied to calculate the static pressure around the head of the train for all measured train and ground configurations in the water-towing tank. The critical train speeds evaluated from the calculated static

pressure gradients around the head of the train for the reference train model on the different ground conditions are presented in Table 11. The good agreement of the

	$\left(\frac{\partial C_P}{\partial X}\right)_m$	$\left(\frac{\partial C_P}{\partial X}\right)_m + \left(\frac{\partial C_P}{\partial X}\right)_{SD}$	$\left(\frac{\partial C_P}{\partial X}\right)_m + 2 \cdot \left(\frac{\partial C_P}{\partial X}\right)_{SD}$
Cube edge length	a = 28, 40, 50 mm	a = 28, 40, 50 mm	a = 28, 40, 50 mm
Smooth ground	250, 250, 250 km/h	243, 243, 243 km/h	236, 236, 236 km/h
Rough ground	601, 601, 601 km/h	594, 594, 594 km/h	583, 583, 583 km/h
Between sleepers	645, 645, 645 km/h	634, 634, 634 km/h	621, 621, 621 km/h
Above sleeper	270, 270, 270 km/h	262, 262, 262 km/h	255, 255, 255 km/h

Table 11: Critical train speeds for the initiation of ballast particle slide (smooth ground and above sleeper) and rolling (rough ground and between sleepers) for simplified exposed ballast particles with edge lengths of a = 28, 40 and 50 mm using the calculated mean, mean + SD and mean + 2·SD static pressure gradient data, taking positive and negative pressure gradients into account (mean + SD·sign(mean)) around the head for the reference train model (T.C. 1).

static pressure coefficient values (C_P) around the head for the reference train model on the smooth ground in the water-towing tank and those determined by the full-scale measurements in Figure 78 is reflected by the critical train speeds for the initiation of ballast particle slide seen in Tables 10 and 11. The critical train speeds calculated for the static pressure gradients around the head for the reference train model on the different ground conditions in Table 11 are all in the same range as the corresponding values estimated for the flow in Table 9. It is therefore again, concluded that the static pressure gradients around the head of the train should be included in the ballast flight risk assessment. The results in Table 11 reveal that the additional drag due to the ground roughness decreased not only the U velocity values around the head of the train, but also the static pressure gradients. Even for the accelerated flow over the sleepers, for which there are the largest u velocity values around the head of the train, the increased drag of the protruding sleepers lowered the static pressure gradients in comparison to those found for the smooth ground. This indicates that the increased drag from the ground roughness (rough ground and protruding sleepers) has a positive influence regarding ballast flight, decreasing the static pressure gradients around the head of the train and thus decreasing the load on the ballast. Of additional interest regarding ballast flight is the fact that both the flow and the static pressure gradients around the head of the train can single-handedly initiate ballast particle motion for exposed ballast particles on a concrete slab track or on top of a sleeper. The actual or resulting forces on the ballast particle however result from the interaction of the forces caused by the static pressure gradients and the flow. The interaction of the

static pressure and the flow around the head of the train is presented in Figure 79 for the calculated mean static pressure coefficient and the measured ensemble average U velocity for the reference train model on the smooth ground. Regarding the maxi-

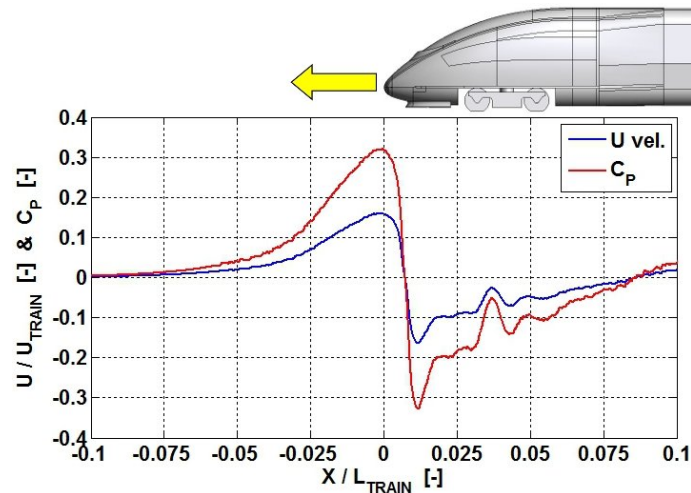


Figure 79: The normalised mean U velocity and its corresponding mean static pressure coefficient around the head of the train for the reference train model (T.C. 1) on the smooth ground (G.C. A) at the height $Z / H_{GAP} = 0.091$.

imum load on the ballast particle induced by the flow around the head of the train, it was earlier determined that the largest force on the ballast particle caused by the flow was found for the negative peak in the U velocity in the reverse flow region around $X / L_{TRAIN} = 0.01$ in Figure 79. The presented C_p distribution in Figure 79 clearly reveals that the largest pressure-induced forces on the ballast particles (i.e. largest static pressure gradients) are also found close to the local minimum U velocity, as the static pressure coefficient rapidly changes from positive to negative C_p -values for the region $0 < X / L_{TRAIN} < 0.01$.

The minimum value of the critical train speeds calculated using both the static pressure and the flow around the head for the reference train model are thus all found to occur just before the local minimum U velocity around $X / L_{TRAIN} = 0.01$, forcing the ballast particle in the opposite direction of the train travelling direction and presented in Table 12. The lower values of the critical train speed in Table 12, in comparison to those values found in Tables 9 and 11, reveal that the interaction of the static pressure and the flow increases the local maximum aerodynamic forces on the ballast around the head of the train. This accentuates the importance of considering the interaction of the flow and the static pressure around the head of the train. The calculations using both the flow and the static pressure revealed that most of the aerodynamic force on

Ground config.	mean	mean + SD	mean + 2·SD
	a = 28, 40, 50 mm	a = 28, 40, 50 mm	a = 28, 40, 50 mm
Smooth ground	232, 235, 237 km/h	212, 218, 222 km/h	193, 202, 206 km/h
Rough ground	494, 523, 540 km/h	402, 441, 465 km/h	338, 381, 407 km/h
Between sleepers	518, 555, 577 km/h	438, 472, 494 km/h	375, 405, 425 km/h
Above sleeper	238, 247, 252 km/h	193, 205, 212 km/h	161, 173, 182 km/h

Table 12: Critical train speeds for initiation of ballast particle sliding (smooth ground and above sleeper) and rolling (rough ground and between sleepers) for simplified exposed ballast particles using the mean, mean + SD and mean + 2·SD of the calculated static pressure gradients together with the flow field data around the head of the reference train model.

an exposed ballast particle around the head of the train is caused by the static pressure gradients. The fraction of the local maximum total force on an ballast particle around the head for the reference train model on the considered ground conditions that is the pressure force was calculated for a train speed of 300 km/h (U_{TRAIN}) and plotted for the considered ballast particle size range in Figure 80. The results in Figure 80 show

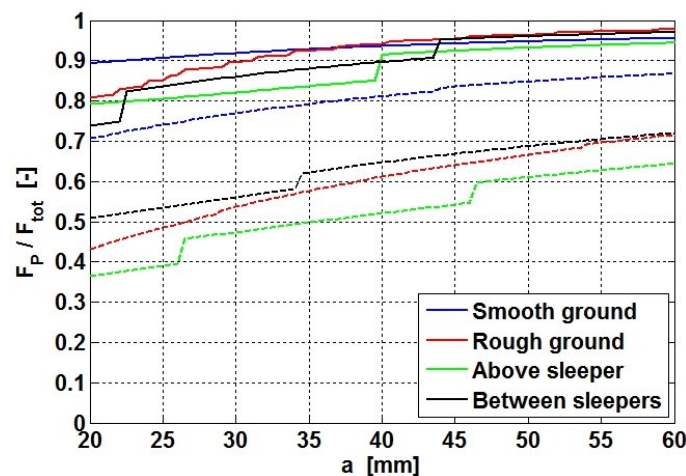


Figure 80: Pressure force (F_P) fraction of the maximum total force (F_{tot}) on a simplified ballast particle (cube) with an edge length of $a = 0.02 - 0.06$ m, induced by the mean (full lines) and the mean + $2 \cdot \sigma$ (dashed lines) flow and static pressure around the head of the reference train model (T.C. 1) for the considered ground configurations.

the importance and dominance of the pressure forces, especially for the case considering the ensemble average of the flow and the static pressure with a pressure force contribution of more than 80 % of the total force for the considered ballast particle size range. Taking the effect of the turbulence or fluctuations of the static pressure and the flow around the head of the train into account, in a simplified way by summing the standard deviation and mean value (mean + $2 \cdot \sigma \cdot \text{sign}(\text{mean})$) reveals the larger influ-

ence of the turbulence on the u velocity than for the static pressure gradient, increasing the contribution and importance of the flow-induced force on the ballast. The increasing influence of the pressure force with the increasing ballast particle size in Figure 80 confirms that the pressure force is proportional to the volume (a^3), as the flow-induced force is proportional to the flow-facing surface area (a^2) of the ballast particle. This indicates that the pressure forces dominate the total aerodynamic forces on larger ballast particles or objects (e.g. infrastructure) as the flow-induced forces dominate the movement of small particles like dust or sand.

The fact that the aerodynamic forces induced by the head of the train are capable of quickly initiating ballast particle motion on sleepers both with and against the direction of the train inhibits a continuous movement of ballast particles. This also poses questions about the worst-case scenario for ballast flight considered earlier, where aerodynamic forces around the head of the train could simply sweep ballast particles lying on top of sleepers into the inter-sleeper region where they may come to rest again. The presented results reveal that the critical train speed for the ballast particle initiation is not sufficient on its own as a global risk parameter for ballast flight. The decisive and important transport phase over the trackbed of the ballast flight problem movement should therefore also be evaluated to more accurately assess the risk of ballast flight. However, if the ballast dislodgement or movement increases hyperbolically after the threshold is exceeded, as for the wind tunnel measurements by Nickling [122] on different particles, the calculated critical train speeds should be treated with caution, especially when considering a ballast trackbed with bi-block sleepers.

The presented results of the critical train speed for ballast particle initiation confirm the observations and conclusions from the undercarriage flow field in section 6, that a smooth underbelly or achievement of the undercarriage aerodynamics of the smooth train model, together with a lowered ballast level with cross-going sleepers, reduces the risk of ballast flight. The ballast particle initiation calculations also revealed the strong influence of the trackbed vibration in reducing the critical train speed. This suggests that reducing the dynamics of the rolling stock as well as improving the dynamic response of the trackbed (damping) would reduce the chance of ballast flight. Other trackbed measures that can be applied to increase or maintain the resistance to ballast flight are the use of larger ballast particles and the maintenance of the ballast size range to avoid the creation of smaller, crushed or fouled ballast particles. Nevertheless, the ballast particle density could also be increased to resulting in larger

critical train speeds for the ballast particle dislodgement from the trackbed.

8.3 Ballast particle transport over the trackbed

8.3.1 Physical approach for the ballast particle transport over the trackbed

In the previous section it was shown that ballast particle motion can be initiated at the speeds of today's commercial high-speed rail operations through sliding motion or rolling motions, dependent upon the ballast particle position in the trackbed. The critical train speed for ballast particle initiation did not however reveal whether ballast particles commence a longer continuously motion over the trackbed or whether the ballast particle returns to rest again. This chiefly concerns problems regarding the influence of strong local flow accelerations addressed earlier, like those found around the head of the train and around the open bogie housing of the rough train model, but also regarding whether dislodged ballast particles gain enough momentum to pass the subsequent sleeper for the ground with sleepers. To be able to answer these open questions, e.g. the influence of local flow accelerations, and in order to assess the risk of ballast flight more accurately, the ballast particle movement over the trackbed also known as the ballast transport phase was evaluated. The ballast particle motion over the trackbed was evaluated with the momentum equation in the X direction (rail direction) presented below. As soon as the critical train speed for ballast particle initiation (force equilibrium) is exceeded, a ballast particle is considered to be dislodged and its acceleration in the rail direction is defined according to Equation (39).

$$\frac{dU_B}{dt} = \frac{\rho_f}{2 \cdot m_B} \cdot \left((U - U_B)^2 \cdot C_D \cdot A_B + (U_{TRAIN} - U_B)^2 \cdot V_B \cdot \frac{\partial C_P}{\partial X} \right) - \mu_{dynamic} \cdot \left(g - a_z - \frac{\rho_f \cdot A_B \cdot C_L}{2 \cdot m_B} \cdot (U - U_B)^2 \right) \quad (39)$$

The aerodynamic drag and the static pressure gradient (around the head of the train) contribute to the ballast particle acceleration over the trackbed with respect to the ballast particle's own velocity. The momentum loss due to repetitive contacts with the trackbed is described by the Coulomb friction force. Furthermore, when the ballast velocity (U_B) becomes zero without an dominating contribution of the train induced flow field, e.g. $U = 0$, the ballast particle is considered to be at rest again. The criteria for the ballast particle initiation must be achieved again before the ballast is considered to be in motion again. Equation (39) was applied to describe the ballast particle

motion over the trackbed for the three considered ground or trackbed configurations. Thus, it describes the ballast particle sliding motion on the concrete slab track or on top of a sleeper as well as the rolling motion over the other ballast in the trackbed. Different physical simplifications and assumptions are however applied for the different ground conditions, e.g. using different values of empirical constants like the dynamic friction coefficient ($\mu_{dynamic}$) and the aerodynamic lift coefficient (C_L). The ballast particle velocity (U_B) is calculated by integrating Equation (39) over time using an explicit scheme, as presented below in Equation (40) for the undercarriage flow field. The static pressure gradient for the undercarriage flow is negligible and therefore set to zero.

$$U_B(i) = U_B(i-1) + \frac{\rho_f \cdot A_B}{2 \cdot m_B} \cdot (C_D \cdot (U(i) - U_B(i-1))^2 \cdot \text{sign}(U(i) - U_B(i-1))) \cdot \Delta t(i) - \text{sign}(U_B(i-1)) \cdot \mu_{dynamic} \cdot \left(g - a_z - \frac{\rho_f \cdot A_B \cdot C_L}{2 \cdot m_B} \cdot (U(i) - U_B(i-1))^2 \right) \cdot \Delta t(i) \quad (40)$$

Since the aerodynamic forces (drag, lift and static pressure gradient) are calculated from the relative incoming undercarriage flow velocity ($U_f - U_B$), the time step or increment (Δt) used in Equation (40) should be as well. Thus, the time increment is defined according to Equation (41).

$$\Delta t(i) = \frac{\Delta X}{V_{TRAIN} - U_B(i-1)} \quad (41)$$

All calculations of the ballast particle transport phase over the trackbed (momentum calculations in the X direction) were conducted under the same conditions as the previously presented calculations of the ballast particle initiation, i.e. for an exposed simplified ballast particle (cube) with a density of $\rho_B = 2600 \text{ kg/m}^3$ and an air density of $\rho_{air} = 1.2041 \text{ kg/m}^3$. Analogous to the ballast particle initiation calculations, the horizontal profiles of the mean U velocity and of U_{SD} along the train length at different vertical heights close to the trackbed were used to calculate the vertical averages of the mean U velocity and U_{SD} for the correspondent height of the simplified ballast particle, see Figure 71. The vertically averaged U velocity and U_{SD} for the corresponding simplified ballast particle were used in Equation (39) to calculate the ballast particle velocity (U_B) over the trackbed. The static pressure around the head of the train calculated from the measured flow fields in the water-towing tank using the potential flow theory, as presented in the previous section, were incorporated into Equation (39) to account for the aerodynamic forces contributed by the static pressure

gradients. The two different ballast particle motions over the trackbed (i.e. sliding motion on the smooth ground (slab track) or on top of the sleeper and the rolling motion over the other ballast in the trackbed for the rough ground and in the intersleeper region for the ground with sleepers), were described by Equation (39) using different physical simplifications and assumptions. The physical simplifications and assumptions for the ballast particle sliding motion were identical for the previous calculations of the ballast particle slide ($C_D = 1.05$, $C_L = 1$ and a constant ballast particle acceleration of $a_z = 7 \text{ m/s}^2$, reflecting the trackbed vibration), except that the dynamic friction coefficient $\mu_{dynamic} = 0.4$ [126] was used instead of the static friction coefficient $\mu_{static} = 0.6$ [126]. The ballast particle rolling or bouncing motion over the other ballast in the trackbed is more complex and simplifications are required to use Equation (39) for the momentum calculations. The used simplifications and assumptions were deduced from the research and data for falling rocks or boulders on mountain slopes [130, 131, 132, 133]. The dynamics of rockfall are typically divided into different types of motion, i.e. free-fall or flight, bouncing, rolling and sliding, for which the latter three are of interest regarding the ballast particle transport over the trackbed. A pure sliding or rolling motion of falling rocks is rare. According to Petje et al. [133], a rolling-dominated motion over a mountain slope is found for spherical rocks and for rocks much larger than the roughness size of the slope. However, even for spherical rocks or smoother slopes, the falling rock will eventually begin to bounce at a critical speed or/and due to small irregularities of the slope. The typical motion of falling rocks down a mountain slope is consequently a combination of a rolling and a bouncing motion. This is also most likely for the ballast particle moving over the other ballast in the trackbed. According to Dorren [132], the rolling and bouncing motion is the most economical way of motion for the falling rock regarding the loss of energy. This motion is, however, complex to simulate and the ballast particle motion over the trackbed was therefore simplified to assume a pure rolling motion that can be described fairly accurate with the Coulomb friction law according to Statham [134]. Considering only the rolling motion of the ballast particle assumes a quickly rotating particle, close to the trackbed that is almost constantly in contact with the trackbed on its outer edges. The centre of mass is therefore moving more or less in a straight line [132, 133], as shown for the simplified ballast particle in Figure 81. The momentum loss caused by the contact with the trackbed is described by the rolling friction coefficient $\mu_{dynamic} = 0.6$, which according to Azzoni et al. [135] reflects the rolling friction coefficient of debris with moderate angularity on angular rock fragments. The

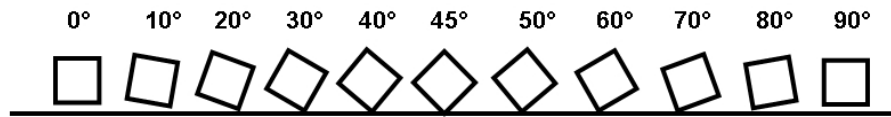


Figure 81: Ballast particle rolling over the trackbed.

rotation of a ballast particle continuously changes the angle of attack to the incoming undercarriage flow and thereby also the resulting aerodynamic drag and lift forces. The aerodynamic coefficients defining the drag and lift force (C_D and C_L) on the simplified ballast particle (cube) should therefore be defined for all angles of attack. Additionally, the rotation of the ballast particle also introduces Magnus effects increasing the drag and lift forces on the moving ballast particle. Since it is difficult to find appropriate published data of the aerodynamic coefficients at different angle of attack to the incoming flow for a cube close to a wall as well as suitable data of the Magnus effect, simplifications and assumptions were necessary for the conducted momentum calculations. The drag coefficients presented by Hoerner in [124] for a cube on a wind tunnel floor at 0 and 45 degree angles, as in Figure 81, reveal that the drag coefficient of the rolling simplified ballast over the trackbed attains values between $C_D(45^\circ) = 0.8$ and $C_D(0^\circ) = 1.05$. These drag coefficient values were however determined without the influence of the Magnus effect. The wind tunnel experiments by Kenserud [136] showed that the Magnus effect could noticeably increase the drag for quickly rotating spheres, e.g. the dimpled pitching machine ball. The Magnus effect of spheres was applied for the simplified ballast particle since suitable published data of the Magnus effect of rotating cubes could not be found. The effect of the constantly changing angle of attack as well as the overall increased drag coefficient due to the Magnus effect for the rotating ballast particle over the trackbed was simplified in a crude way by setting it to the constant value of $C_D = 1.05$. The calculation of the drag force on the simplified ballast particle during the transport phase over the trackbed was done using the flow field for the slightly elevated ballast particle position at an angle of attack of 0 degree, see Figure 81. In other words, the only change in comparison to the sliding motion of the ballast particle on the smooth ground and on top of the sleeper (also using $C_D = 1.05$) is that the undercarriage flow field used for the ballast particle rolling motion over the other ballast in the trackbed has a vertical offset from the trackbed. The influence on the lift force of the slightly elevated and quickly rotating ballast particle close to the trackbed is much stronger than the discussed influence on the drag force. The

lift force is strongly influenced by the proximity of the ground, the angle of attack to the incoming flow and the Magnus effect. Due to the vertical elevation of the ballast particle alone, the lift coefficient is lower than the previously assumed value of $C_L = 1$. Due to its proximity to the ground, however, it is not the case that $C_L = 0$, as for a cube at an angle of attack of 0 degree (see Figure 81) to a symmetrical flow. The experimentally determined characteristic lift coefficient changes due to ground proximity for a cylinder with a rectangular cross-section by Malavasi and Guadagnini [139] were adopted for the simplified ballast particle and are presented in Appendix D. The lift coefficient caused by the ground proximity for the slightly elevated simplified ballast particle during the transport phase over the trackbed was estimated at $C_L = 0.6$. Once more, the rotation of the ballast particle continuously changes the angle of attack to the incoming flow, which influences the lift force. For a rotating cube in a symmetrical flow without any influence of a nearby wall, the lift force will oscillate sinusoidally, but with a constant shift away from $C_L = 0$ due to the Magnus effect. This sinusoidal lift force characteristic will, however, be disturbed by the proximity of the ground. Considering the simplified ballast particle with an angle of attack of 10 degree, see Figure 81, a symmetrical flow (from left to right) would cause a lift force towards the ground. The narrow gap between the ground and the ballast particle's lower side however restrains the flow along the lower side of the ballast particle and increases the pressure, causing a lift force away from the ground [137, 138]. It is therefore assumed that a quickly rotating ballast particle close to the ground always has a lift force away from the ground at all angles of attack to the incoming flow. The resulting lift force on the ballast particle used for the momentum calculations within this work was simplified to considering only the lift effect of the ground proximity at an angle of attack of 0 degrees and the contribution of the Magnus effect. The applied Magnus effect was extracted from the previously mentioned experiments of rotating spheres by Kenserud [136]. The dimpled pitching machine balls were used for this work since they demonstrated nearly independence of the Reynolds number (as the simplified ballast particle) in comparison to the results for smooth spheres [136]. The assumed Magnus effect over the ballast particle rotating around its own axis and based on the experimental data of Kenserud [136] is presented in Appendix E. The rotation of the ballast particle, defining the Magnus effect contribution to the lift force, was defined according to Equation (42), assuming no slip or momentum loss for the contact of the outer edge of the ballast particle with the trackbed that causes the rotation.

$$\omega_B = \frac{U_B}{r_B}, \quad r_B = a \cdot \sin(45^\circ) \quad (42)$$

8.3.2 Ballast particle transport calculations

The first ballast particle transport calculations were conducted for the exposed simplified ballast particle on top of a sleeper to clarify whether the aerodynamic forces around the head of the train can slide ballast particles off a sleeper. The velocity and displacement calculated near the head for the reference train model for the simplified ballast particle on top of a sleeper with an edge length of $a = 28$ mm are presented in Figure 82 for different train speeds. The ballast particle velocity and displacement

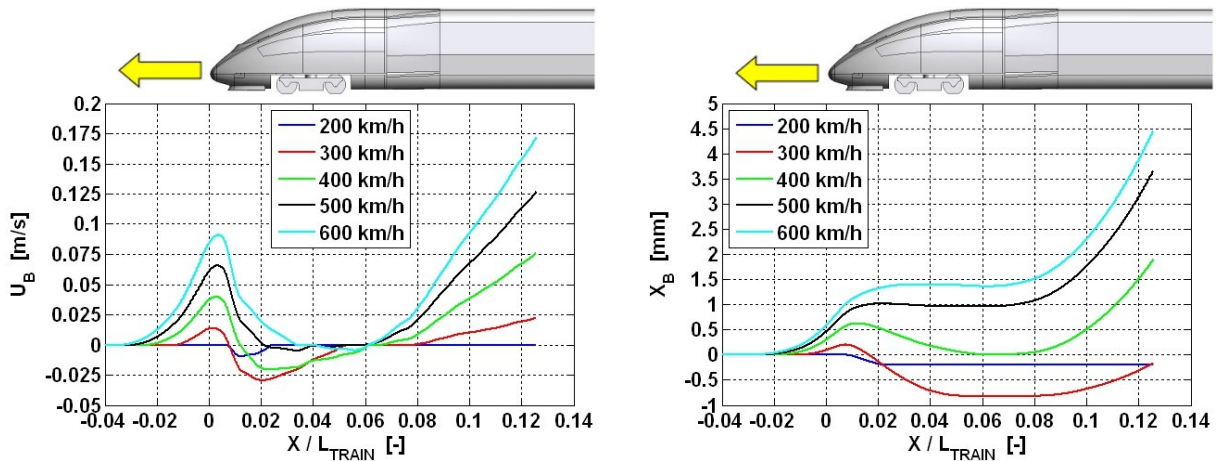


Figure 82: Velocity (left) and displacement (right) of the simplified ballast particle on top of a sleeper (initially the central position) with an edge length of 28 mm exposed to the expected maximum aerodynamic forces (mean + 2·SD·sign(mean)) around the head of the reference train model (T.C. 1) for different train speeds.

values presented in Figure 82 reveal that the aerodynamic forces induced around the head for the reference train model are not strong enough to swipe ballast particles off a sleeper. This is despite the low critical train speeds calculated for the ballast particle initiation in Table 12, all resulting from the aerodynamic forces around the reverse flow region. The momentum change of the ballast particle from this strong flow acceleration in the opposite direction from which the train is travelling (200 km/h in Figure 82) resulted only in very low values of the ballast particle velocity and displacement due to the short exposure time. With increasing train speed the ballast particle velocity and displacement is determined by the interaction of the two characteristic flow

accelerations around the head of the train, see Figure 79, which induce strong aerodynamic forces in both rail directions (X directions). Since the flow around the head of the train accelerates the ballast particle in both rail directions, restrains the ballast particle from reaching larger velocity and displacement values. Thus, the ballast particle consequently slides off the sleeper for the later and stronger incoming undercarriage flow.

Momentum calculations for the ballast particle velocity and displacement corresponding to those presented in Figure 82 were conducted for the exposed simplified ballast particle in the ballast trackbed (i.e. the rough ground and the inter-sleeper region for the ground with sleepers). The momentum calculations reflected the larger critical train speeds for the initiation of ballast particle motion in Table 12, as the ballast particle was first set into motion for a train speed of 400 km/h. The overall ballast particle velocity and displacement values were therefore also lower for the ballast particle in the ballast trackbed in comparison to those presented in Figure 82. The lower values of the ballast particle velocity and the displacement are associated with the increased drag of the trackbed roughness that decreases the mean U velocity and U_{SD} values close to the ground (see section 6.4) as well as the applied trackbed vibration based on the full-scale measurements of Quinn et al. [32]. The momentum calculations show further that the ballast particle in the ballast trackbed came back to rest again after the first bogie for all evaluated train speeds, while the corresponding ballast particle on top of the sleeper was set into motion again for train speeds over 300 km/h. The continuation of the ballast particle motion after the first bogie is, however, not only an effect of the trackbed roughness and vibration but also an effect of the aerodynamic properties of the first bogie region (bogie and bogie housing). This highlights not only the importance of the aerodynamic shape of the train head but also of the first bogie region. Since the different train configurations were realised by changing the undercarriage roughness around the bogie regions of the same train model (i.e. the same geometric shape of the head), the influence of the first bogie region could be evaluated. In Figure 83, the velocity and displacement for the simplified ballast particle ($a = 28$ mm) on top of the sleeper are compared to each other for the flow around the head of the three considered train configurations for a train speed of 400 km/h. The results in Figure 83 indicate the strong influence of the aerodynamic properties of the first bogie region (bogie and bogie housings) in changing the characteristics of the ballast particle motion around the head of the train. The comparison of the mean U velocity field (XZ-plane) along the leading end-car previ-

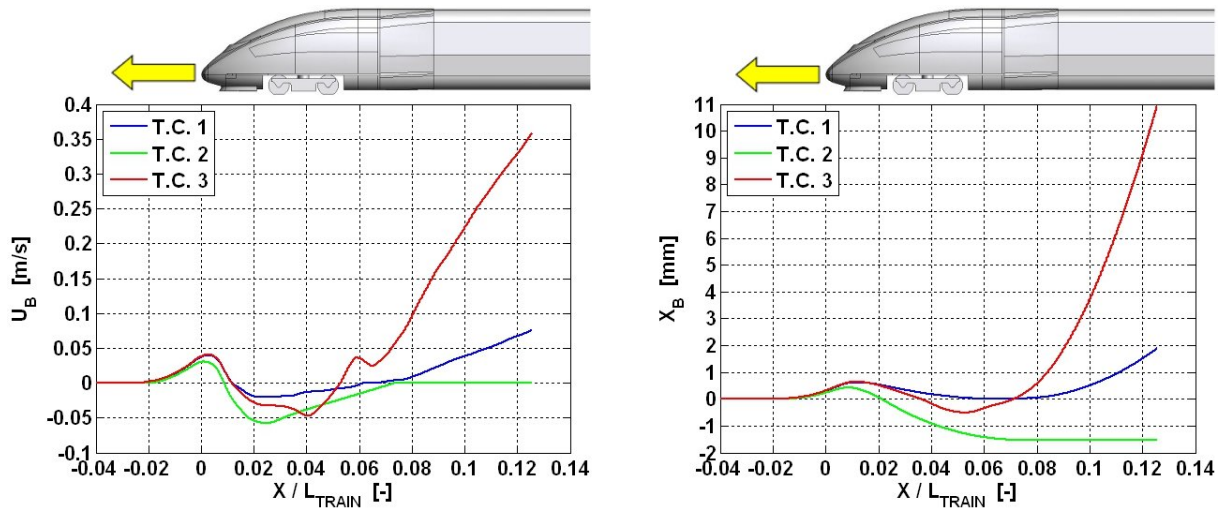


Figure 83: Velocity (left) and displacement (right) for the simplified ballast particle on top of a sleeper (initially the central position) with an edge length of 28 mm exposed to the expected maximum aerodynamic forces (mean + 2·SD·sign(mean)) around the head for the reference (T.C. 1), smooth (T.C. 2) and the rough (T.C. 3) train models for a train speed of 400 km/h.

ously presented in Figure 21 in section 6.3.1 revealed that the increased roughness of the first bogie region accelerated the development of the undercarriage flow, i.e. turning the flow back in the travelling direction after the reverse flow region around the head. The results in Figure 21 clearly reflect the effect of the increased roughness of the first bogie region with the largest ballast particle velocity and displacement values for the rough train model with the open bogie housings and the smallest values for the completely smooth undercarriage of the smooth train model. Despite the strong flow acceleration and increased turbulence intensity around the open bogie housing of the rough train model, the values of the ballast particle velocity and displacement are still modest. This strengthens the previous statement based on the ballast particle velocity and displacement for the reference train model in Figure 82, that the ballast particles on top of sleepers will first slide off the sleeper as they are exposed to the later and stronger undercarriage flow. The values of the ballast particle velocity and displacement around the head of the train also suggest that ballast flight impacts and even ballast pitting are highly unlikely for the leading end-car of the train set. Nevertheless, the aerodynamic shape of the head and the first bogie region are still important regarding ballast flight since the faster undercarriage flow development increases the effective length of the train set, i.e. the train length contributing to the acceleration of dislodged ballast particles as well as an increased undercarriage surface susceptible to ballast flight impacts.

The roughness effect of the leading end-car on the later or final ballast particle velocity is presented in Figure 85 for a simplified ballast particle with an edge length of 40 mm sliding over the smooth ground. Before discussing the results in Figure 85, the actual undercarriage flow inducing the aerodynamic forces on the simplified ballast particle is presented in Figure 84 for an better insight of the later results presented in Figure 85. The normalised mean U velocity and its corresponding velocity fluctuation (U_{SD}) val-

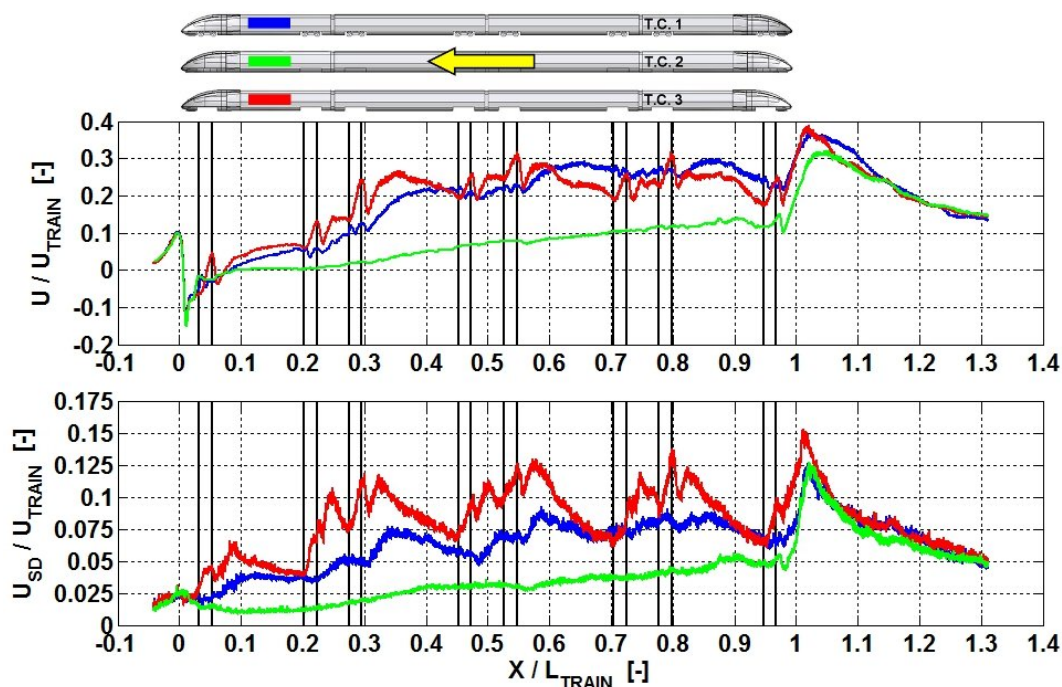


Figure 84: The normalised mean U velocity (upper) and its corresponding velocity fluctuations U_{SD} (lower) spatially-averaged over the vertical height of a simplified ballast particle with an edge length of $a = 40$ mm on the smooth ground (G.C. A) for the three considered train configurations.

ues, spatially-averaged over the vertical height of the simplified ballast particle with an edge length of 40 mm (mean U velocity and U_{SD} at the ballast particle COM), are presented in Figure 84 along the train length for the three considered train configurations on the smooth ground. The results in Figure 84 reflect the previously presented horizontal distributions of the normalised mean U velocity and U_{SD} at the rail height in Figure 37 in section 6.3.3. Furthermore, the larger undercarriage roughness of the rough train model that more strongly accelerates the flow also enhances the generation of turbulence along the first half of the train are associated to the larger values of the ballast particle velocity and displacement found for the rough train model in comparison to the two smoother train configurations in Figure 83. The faster undercarriage flow development for the rough train model along the first half of the train

set induces the earlier initiation of the ballast particle sliding motion presented in Figure 85. The later or final ballast particle velocity is, however, not only determined by

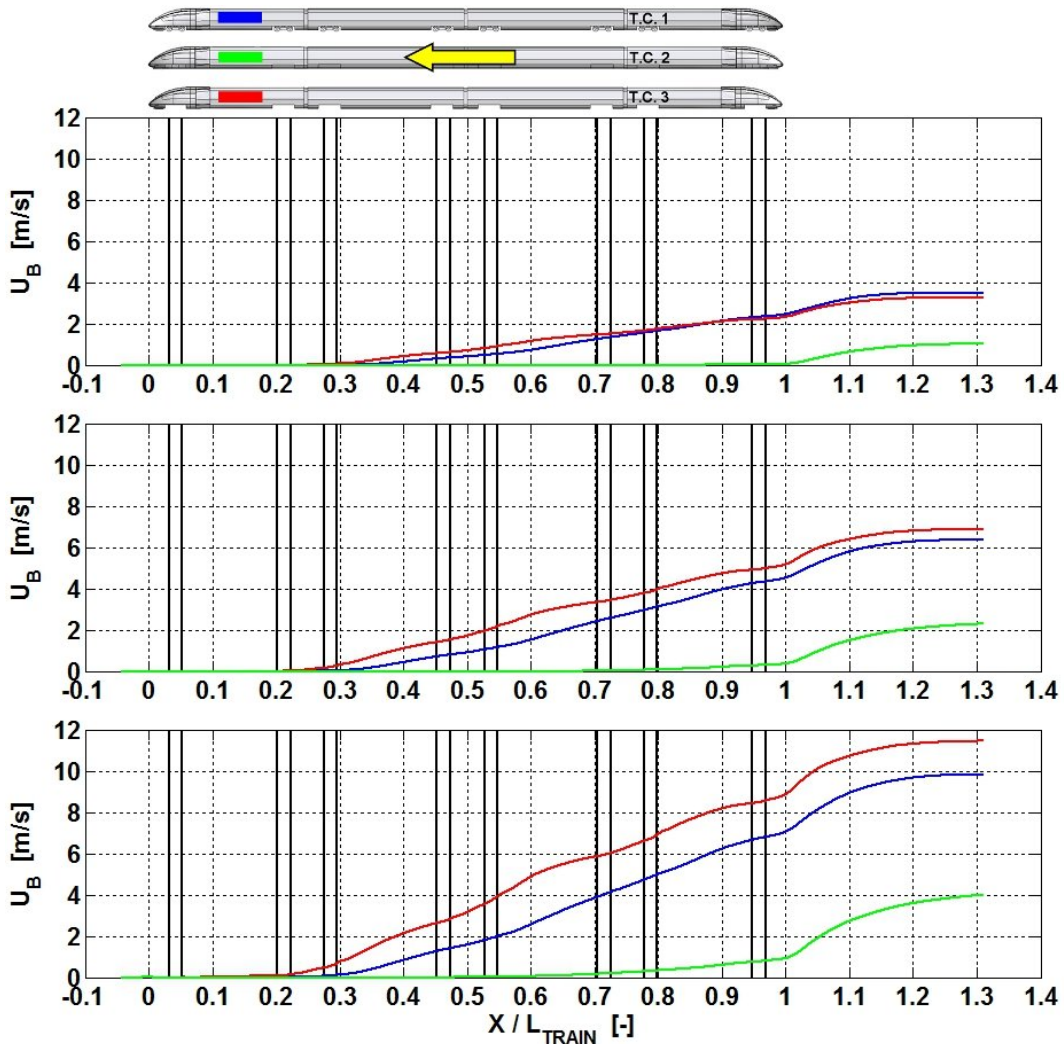


Figure 85: Comparison of the ballast particle velocity along the train length for the three considered train configurations on the smooth ground (sliding motion) for a simplified ballast particle with an edge length of 40 mm and a train speed of 350 km/h using the mean (upper), mean + SD (middle) and mean + 2·SD U velocity and C_p data taking the direction of the induced aerodynamic force into account, mean + SD·sign(mean).

the location of initiation but also of the development and characteristics of the entire undercarriage flow. This is clearly the case for the momentum calculations in the upper plot in Figure 85 for the reference and the rough train models using only the mean U velocity. Despite the larger undercarriage roughness of the rough train model and the earlier initiation of ballast particle motion, the final ballast particle velocity at the end of the train set is nearly the same (with slightly larger values for the reference

train model). The reason for this is that the mean U velocity values for the more or less fully developed undercarriage flow of the rough train model are lower overall compared to those for the reference train model, see Figure 84. Since the importance of including the velocity fluctuations (U_{SD}) for the ballast flight risk assessment was motivated by the previously presented calculations of the mean U velocity, mean U velocity + U_{SD} and mean U velocity + $2 \cdot U_{SD}$, the corresponding flow fields were used to calculate the ballast particle velocity as presented in Figure 85. Comparisons of the applied mean U velocity, mean U velocity + U_{SD} and mean U velocity + $2 \cdot U_{SD}$ along the train lengths of the three considered train configurations on the smooth ground as well as for the other two ground configurations are found in Appendix F. The results in Figure 85 reveal the strong influence of the velocity fluctuations in increasing the u velocity values along the entire train length and thus the ballast particle velocity values. The most distinctive influence of the velocity fluctuations are, however, found for the comparison of the reference and the rough train models. The strong velocity fluctuations for the rough train model enhance the u velocity difference for the first half of the train, with the largest values for the rough train model, while the difference between the reference and rough train models diminishes for the second half, resulting in larger final ballast particle velocity values for the rough train model. The presented undercarriage flow field and the ballast velocity results indicate that improving or partially covering the open bogie housings of the leading end-car of the rough train model retains the faster development of the undercarriage flow while realising ballast particle velocity values in the range of the reference train model. Consequently, the aerodynamic shape of the undercarriage of the entire train should be considered for the overall risk of ballast flight.

The strong influence of the undercarriage flow development at the beginning of the train is presented in Figure 85. The results for the mean U velocity in Figure 85 (upper graphic), however, indicate that the relevance of the nearly fully developed flow after first mid-car increases for longer trains-sets. Calculations were therefore also undertaken for longer train sets by extrapolating the fully developed undercarriage flow between the middle of the second mid-car and the trailing end-car to simulate 8- and 16-unit train sets. The ballast particle momentum calculations for the longer train sets revealed that the different characteristics of the fully developed undercarriage flow between the reference and the rough train models (see Figure 84) had no considerable effect on the final ballast particle velocity. The final ballast particle velocity was governed by the spatially-averaged U velocity of the nearly fully developed

undercarriage flow. Therefore, for the longer train sets (8- and 16-unit), it was only for the expected maximum u velocity (mean U velocity + $2 \cdot U_{SD}$) where the final ballast particle velocity value for the rough train model was larger than that of the reference train model. This agrees with the spatial averages of the mostly fully developed undercarriage flow in Table B8 of Appendix B. Nevertheless, the flow development at the beginning of the train can still be decisive for the occurrence of ballast flight impacts if the spatial U velocity averages of the fully developed undercarriage flow of two trains are similar. This indicates, once more, that the aerodynamic properties of the entire train set should be included in the risk assessment of ballast flight. Finally, the results in Figure 85 demonstrate the positive effect of the smooth undercarriage of the smooth train model in inducing lower velocity values for the dislodged ballast particle and therefore a lower risk of ballast flight.

8.4 Ballast particle flight

8.4.1 Physical approach to the ballast particle flight phase

To further improve the accuracy of the risk assessment of ballast flight incidents, which for this case was the calculation of the critical train speed, the flight phase of dislodged and moving ballast particles should be simulated. Since the ballast particle movement over the trackbed was simplified to the sliding motion only for the smooth ground and to the rolling motion over the other ballast in the trackbed, there is no natural development of bounces with increasing vertical heights of the moving ballast particle, as observed for in-situ rockfalls. The observed bouncing motion of a rockfall is highly dependent on the topology of the mountain slope or in this case, the orientation of the ballast particles in the trackbed, which is difficult to simulate. The crucial ballast particle bounce or upward deflection from the trackbed that initiates ballast flight was therefore triggered along the train length. Numerous angles and initial conditions for the ballast flight calculations depend on the orientation of the impacting and rotating dislodged ballast particle as well as on the orientation of the ballast particles in the trackbed. This was simplified for the ballast flight calculations within this work to the upward deflection being the worst-case scenario, i.e. the changing of the horizontal ballast particle motion over the trackbed completely into a vertical ballast particle motion after an impact with the trackbed. Considering the worst-case scenario for the upward deflection and assuming that the incoming angle

is equal to the reflected angle, an impacted ballast particle surface in the trackbed has an inclination of 45° angle to the horizontal plane. The ballast particle impact with the trackbed is described as a partially inelastic collision, according to Equation (43).

$$\bar{V}_{out} = e \cdot \bar{V}_{in} \quad (43)$$

The momentum loss at the impact is described by the restitution coefficient e . Two values of the restitution coefficient were used for the conducted calculations, dependent on whether the ballast particle rotated about its own axis or not. The restitution coefficient of $e = 0.4$ determined by the ballast gun experiments in the AOA-project [41] was used for the non-rotating ballast particle sliding off the sleeper. For the quickly rotating ballast particle rolling over the trackbed, an increased restitution coefficient value of 0.5 was applied to reflect the effect of the ballast particle rotation according to the experiments by Buzzi et al. [140] on falling rotating concrete blocks of different cross-sectional shapes. The flight phase of the ballast particle after an upward deflection is described for the measured XZ-plane in the trackbed line of symmetry by the debris flight equations according to Baker [72] and presented below in Equations (44) and (45). The rotation speed of the ballast particle caused by the repetitive contacts with the trackbed is considered to be constant as is the Magnus effect during the entire flight phase.

$$\frac{\partial U_B}{\partial t} = \left(\frac{A_B \cdot \rho_f}{2 \cdot \rho_B \cdot V_B} \right) \cdot (C_D \cdot (U - U_B) - C_L \cdot (W - W_B)) \cdot ((U - U_B)^2 + (W - W_B)^2)^{\frac{1}{2}} \quad (44)$$

$$\frac{\partial W_B}{\partial t} = \left(\frac{A_B \cdot \rho_f}{2 \cdot \rho_B \cdot V_B} \right) \cdot (C_D \cdot (W - W_B) + C_L \cdot (U - U_B)) \cdot ((U - U_B)^2 + (W - W_B)^2)^{\frac{1}{2}} - g \quad (45)$$

8.4.2 Ballast flight calculations for the rough ground

With the help of the aforementioned debris flight equations, the critical train speed for a ballast particle impact with the train could be calculated. The absolute height reached by the ballast particle along its flight path is primarily influenced by the initial vertical velocity of the ballast particle (W_B) after the upward deflection and by its in-flight lift force. The in-flight lift coefficient is defined by the ballast particle rotation, but the fact that the horizontal motion is also completely changed into a vertical motion through the upward deflection from the trackbed means that the maximum

height reached by the ballast particle is proportional to the horizontal velocity (U_B). If the ballast particle is dislodged from the trackbed and the aerodynamic forces are larger than the losses due to the repetitive contacts with the trackbed, the ballast particle velocity (U_B) will increase along the train length as shown in Figure 85 in the previous section. Hence, the risk of ballast flight incidents increases with the total length of the train. As it was only feasible to measure the undercarriage flow of a 4-unit train set ($L_{TRAIN} \sim 100$ m in full-scale) in the water-towing tank and that most European high-speed trains (e.g. ICE, Siemens Velaro and TGV) are around 200 m long, realistic train set lengths could not be measured. However, the water-towing tank data were extracted from the nearly fully developed flow for the second half of the train set (between the middle of the second mid-car and the middle of the trailing end-car) and extrapolated for the simulation of a full-length train for the ballast flight calculations. Because the nearly fully developed undercarriage flow of the smooth train model is first found at the beginning of the trailing end-car (see Figure 37 in section 6.3.3), the undercarriage flow along the trailing end-car was used for the extrapolation to simulate the longer train set of the smooth train model. The extrapolated undercarriage flow fields for the three considered train configurations on the rough ground condition simulating a full-size train set and used for the ballast flight calculations are presented in Figure 86. The transport of the ballast particle over the trackbed was simplified to a pure sliding or a rolling motion and therefore there is, once again, no natural initiation of ballast flight. For the presented ballast flight calculations, the initiation of ballast flight (i.e. the upward deflection from the trackbed) was triggered at every $\Delta X = 5$ m for the second half of the extrapolated train set (i.e. $X = 100$ -200 m in Figure 86). Ballast flight calculations triggering upward deflections for the entire train length (after ballast particle initiation) revealed that it was only the flight paths for the second half of the train ($X > 100$ m) that reached vertical heights of interest. This also agrees with the physical assumptions and simplifications applied for the simplified exposed ballast particle and strengthen the conclusion that the risk of ballast flight impacts is larger for the last cars of a train. Nevertheless, ballast flight impacts at the beginning of the nearly fully developed flow (i.e. after the fourth train car) are not considered to be impossible if the dislodged ballast particle has a strong in-flight lift force.

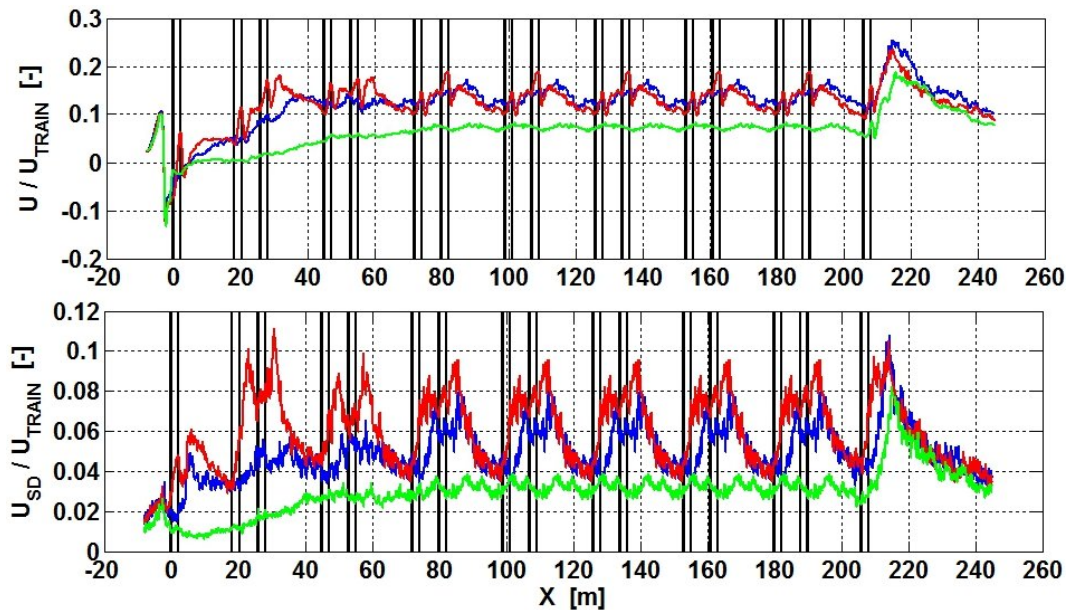


Figure 86: The normalised extrapolated mean U velocity (upper) and its corresponding velocity fluctuations U_{SD} (lower), spatially-averaged over the vertical height of the exposed simplified ballast particle with an edge length of $a = 40$ mm on the rough ground (G.C. B) for the reference train model (blue), rough train model (red) and smooth train model (green) as 8-unit train sets.

The calculated critical train speeds for a ballast particle impact with the train undercarriage using the mean, mean + SD and mean + 2·SD U and W velocity and C_p data taking the direction of the aerodynamic forces into account, mean + SD·sign(mean), are presented in Figure 87 for the three train configurations on the rough ground. The results in Figure 87 agree with the ballast particle initiation calculations in showing that smaller ballast particles are more susceptible to ballast flight. The physical approach for the initiation, transport and flight of the ballast particle confirms that smaller ballast particles are more likely to cause ballast flight incidents since the aerodynamic forces increase with their projected area perpendicular to the flow (a^2), while the countering forces in form of friction (initiation and transport) and gravity (flight) increase with the volume of the ballast particle (a^3). The flow velocity and pressure fluctuations of highly turbulent undercarriage flow increase the aerodynamic forces and therefore have a strong influence on the critical train speeds for ballast flight impacts. Since ballast flight incidents are commonly described as sporadic or stochastic and therefore difficult to predict, the undercarriage flow turbulence should be included in the ballast flight assessment. This is also argued because the calculated critical train speeds for ballast particle initiation using only the mean U velocity were considered to be unrealistically high (see Table 8 for T.C.1 and T.C. 2 on G.C. B), which

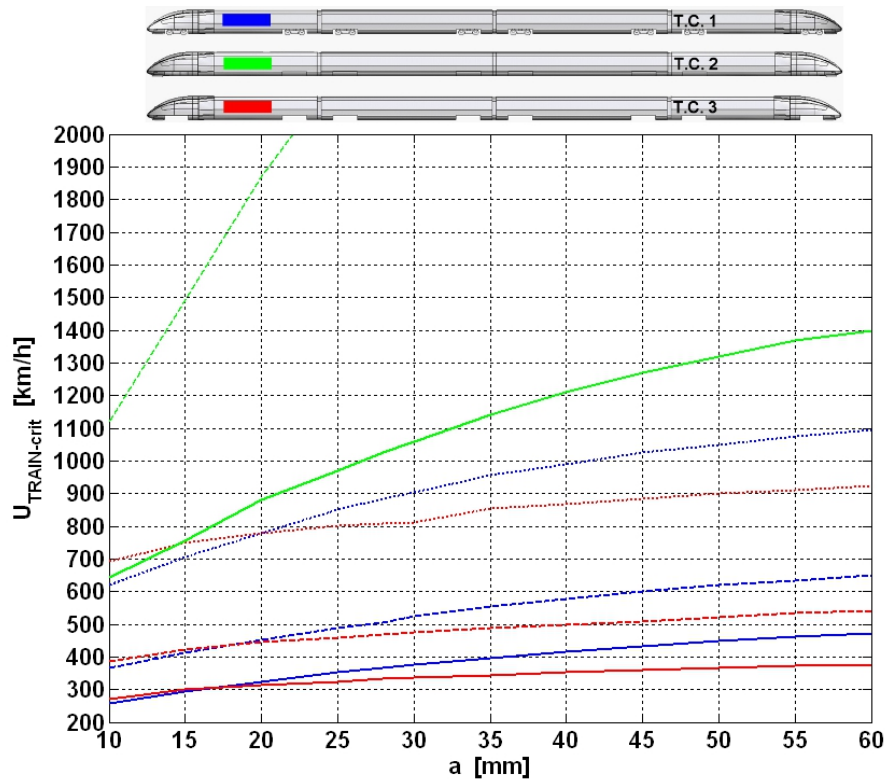


Figure 87: Critical train speeds for the ballast particle impact with the train undercarriage for the three considered train configurations on the rough ground (G.C. B) using the mean (dotted lines), mean + SD (dashed lines) and mean + 2·SD (full lines) U and W velocity and C_p data, taking the direction of the flow and pressure gradient into account (mean + SD·sign(mean)).

is also the case for the critical train speeds based on the mean undercarriage flow field in Figure 87 for the reference and rough train models. Regarding the risk of ballast flight incidents, the train passages with instantaneous u velocity values in the range between the mean U velocity and mean U velocity + $2 \cdot U_{SD}$ are of greatest interest since they induce larger aerodynamic forces. However, the assumption that the instantaneous u velocity attains the expected maximum values (U vel. + $2 \cdot U_{SD}$) along the entire train length is unlikely and was never the case for any of the single runs conducted in the water-towing tank. The undercarriage flow field data of the single runs conducted in the water-towing tank revealed that the instantaneous u velocity values for the train passages of interest regarding ballast flight fluctuated between the mean U velocity and mean U velocity + $2 \cdot U_{SD}$ for nearly the entire train length. Additionally, sequences with almost instantaneous u velocity values close to the expected maximum value (mean U velocity + $2 \cdot U_{SD}$) for $\Delta X = 5-10$ m (full-scale) were also found for the undercarriage flow measured in the water-towing tank. The under-

carriage flow results indicate that assigning a level or range of the u velocity values reflecting the realistic risk of ballast flight by adding the velocity fluctuation (by a factor between 0-2) to the mean U velocity is very difficult. Using the expected maximum aerodynamic force (mean + 2·SD) for the ballast particle initiation is still, as discussed and argued in section 8.2, considered to be realistic since a short instantaneous flow effect or fluctuation can be enough to surpass the static threshold and set the ballast particle into motion. Assuming that the realistic critical train speeds for ballast flight impacts are somewhere between the presented mean + SD and mean + 2·SD (probably closer to mean + SD) yields critical train speeds for the reference and rough train models in Figure 87 that are slightly larger than those values (~320 km/h) reported for full-scale ballast flight incidents. However, given the lower mean U velocity values (see section 7.2) and the thicker boundary layer at the ground obtained in the water-towing tank as well as that other ballast particle shapes (with stronger in-flight lift) are more susceptible to ballast particle motion and flight, the results in Figure 87 are still in a realistically range. Nevertheless, for this work the aim was to reveal the influence of different undercarriage flows and different ground conditions regarding ballast flight, rather than presenting realistic critical train speeds. The largest theoretical aerodynamic forces (mean + 2· U_{SD}) were therefore used for the comparison of the considered train and ground configurations. The largest theoretical aerodynamic forces for the ballast flight calculations would also in theory generate the lowest critical train speeds, or in other words, critical train speeds with factor of safety.

Comparing the results for the three considered train configurations in Figure 87 clearly reveal the advantage of the completely smooth undercarriage of the smooth train model. Even for the largest theoretical aerodynamic forces, i.e. mean + 2·SD·sign(mean), on the exposed simplified ballast particle, ballast flight impacts with the train undercarriage are only possible for train speeds outside the range of today's high-speed trains. Additionally, as presented in Figure 87 for the smooth train model, ballast flight calculations were only conducted on the smallest ballast particle sizes for the mean + SD and no calculations were undertaken for the mean values of the undercarriage flow field since the critical train speeds clearly exceeded the realistic range for the wheel-rail system. The results for the smooth train model in Figure 87 are expected when one considers the results of undercarriage flow field and the ballast particle initiation calculations. The more interesting comparison, in the sense of the difficulty of predicting the outcome regarding the risk of ballast flight, is the one between the more stable undercarriage flow for the reference train model and the

more dynamic undercarriage flow of the rough train model. The lowest critical train speeds for ballast flight impacts with the train undercarriage were found for the reference train model, see Figure 87, despite the fact that the rough train model has the roughest undercarriage, which initiates ballast particle motion at lower train speeds. The reason that the reference train model has the lowest critical train speeds is that the strong flow effects from the open bogie housings of the rough train model decrease with the distance from the train undercarriage, as the influence of the ground roughness strongly increases. The mean U velocity and U_{SD} values around the bogie regions closest to the ground for the reference and the rough train models are in the same range, see Figure 52 and Figure 53 in section 6.5. The strongly accelerated flow around the open bogie housings of the rough train model is therefore not strong enough to compensate for the later flow deceleration along the smooth undercarriage of the train car between both bogies that induces an overall lower aerodynamic force on the smallest ballast particle sizes in comparison to the reference train model. However, for ballast particle sizes above 20 mm, the effect of the accelerated flow around the open bogie housings becomes significant and thus the lowest critical train speeds for ballast flight impacts are found for the rough train model. Regarding the overall risk of ballast flight, the rough train model is considered to be the most conducive to ballast flight impacts since the mean critical train speed for the entire ballast particle size range is lower than that for the reference and of course the smooth train models. Furthermore, taking a well-maintained European trackbed with a ballast particle size ranging between 22.4 and 63 mm [98] into account, strengthens the conclusion according to the results in Figure 87 that the rough train model is the most conducive train configuration to ballast flight. Analogously to the presented momentum calculations for the ballast particle slide on the smooth ground, local flow effects (e.g. the accelerated flow around the open bogie housings of the rough train model) demonstrated only a secondary influence on the risk for ballast flight impacts in comparison to the overall level of the u velocity (aerodynamic force) along the entire train length. It was also found that the spatial average between the first and the last axle of the undercarriage for the flow at the height of an exposed ballast particle reflected the outcome of the critical train speeds for ballast flight impacts with the train undercarriage presented in Figure 87. Thus, the spatial average of the undercarriage flow between the first and the last axle of the train at the height of an exposed ballast particle (i.e. close to the trackbed) is sufficient as a ballast flight risk parameter for the comparison of different high-speed trains.

Besides the ballast particle impact with the train undercarriage, the ballast particle can also be crushed between the wheel-rail running surface, referred to as ballast pitting, damaging both the rail and the wheel-running surface. The damages caused by ballast pitting lead to poor travel comfort and changed track dynamics, which form hollow areas between sleepers (track voiding) that reduce the track stability and is a major maintenance cost [141]. Assuming the undercarriage flow to be homogeneous for the lateral positions between both rails makes it possible to use the measured undercarriage flow field in the trackbed line of symmetry to calculate the risk of ballast flight for any position in the trackbed. It was additionally assumed that the most susceptible ballast for ballast pitting was that closest to the rail, minimizing the influence of the lateral component of the ballast flight path (V_B), which was neglected for the calculations. The calculated critical train speeds for ballast pitting are presented in Table 13 together with the corresponding results from Figure 87. Interestingly, the

Ballast particle size	T.C. 1	T.C. 2	T.C. 3
a = 10 mm	250, 257 km/h	602, 642 km/h	263, 271 km/h
a = 20 mm	309, 325 km/h	760, 880 km/h	302, 314 km/h
a = 28 mm	343, 368 km/h	835, 1025 km/h	315, 333 km/h
a = 40 mm	385, 416 km/h	920, 1210 km/h	331, 353 km/h
a = 50 mm	409, 449 km/h	965, 1320 km/h	341, 367 km/h
a = 60 mm	427, 473 km/h	1000, 1400 km/h	350, 378 km/h

Table 13: Critical train speeds for ballast pitting (left, $Z_B = 235$ mm (1:1)) and ballast impact with the train undercarriage (right, $Z_B = 500$ mm (1:1)) for the reference (T.C. 1), the smooth (T.C. 2) and the rough train model (T.C. 3) on the rough ground (G.C. B) using the mean + 2·SD·sign(mean) data of the U and W velocity and C_p field for different sizes of the exposed simplified ballast particle.

results in Table 13 for the reference and the rough train models show that only a small train speed increase is sufficient to elevate a ballast particle from the height of the top of the rail ($Z = 235$ mm) to the undercarriage of the train ($Z = 500$ mm). However, an increase in the train speed influences the entire chain of events from the ballast particle initiation to the ballast flight. The train speed increase dislodges the ballast particle from the trackbed earlier, extending the transport phase and thus the momentum transfer time from the undercarriage flow to the moving ballast particle, resulting in increased ballast particle velocities. The increased transport phase is also accompanied by a strong increase in the resulting force, $(F_D - F_{fr})$, accelerating the ballast particle over the trackbed, since both the drag force F_D and the lift force F_L (F_L reduces the friction force according to Equation (39) increase quadratically with

the train speed. Furthermore, the rotation of the ballast particle caused by repetitive contacts with the trackbed induces an additional lift force directly proportional to the ballast particle velocity, referred to as the Magnus effect (transport phase: $C_L = 0.6 + \text{Magnus effect according to Appendix E}$), promoting the ballast particle acceleration over the trackbed by decreasing the friction force. By now it is clear that a train speed increase strongly influences the ballast particle velocity over the trackbed (U_B). The increased ballast particle velocity will, by upward deflection from the trackbed, result in a larger initial vertical ballast particle velocity (W_B), as the faster ballast particle rotation is associated with a larger lift force (Magnus effect), enabling greater vertical heights to be reached by the ballast particle. Last but not least, the ballast particle will be exposed to the stronger undercarriage flow with the increasing distance to the trackbed and the aerodynamic forces will increase further. This highlights that a small increase of the train speed can drastically change the risk of ballast flight incidents. The results in Table 13 also show that the relative train speed increase needed to change the risk from only ballast pitting to the additional risk of a ballast flight impact with the train undercarriage increases with the ballast particle size. This is however in agreement with the governing equations for the ballast particle initiation, transport and flight, which are all proportional to the ballast particle size. Thus, in order to reach the vertical height of the train undercarriage, a bigger ballast particle requires a larger relative increase of the train speed. The larger relative train speed increase for the smooth train model in comparison to the two other train configurations is associated with the lower normalised flow velocity (U / U_{TRAIN} and W / U_{TRAIN}) and velocity fluctuation (U_{SD} / U_{TRAIN} and W_{SD} / U_{TRAIN}) values over the entire gap of the undercarriage flow. The contribution of the simulated train speed increase is weighted by the measured and normalised flow velocity values (e.g. $\Delta U_{sim} = (U_{Meas} / U_{TRAIN}) \cdot \Delta U_{TRAIN-sim}$), resulting in larger relative train speed increases for the smooth train model in order to increase the risk from ballast pitting to ballast impact with the train undercarriage. Critical train speeds for the intermediate ballast particle sizes of the results shown in Table 13, as well as for ballast flight impacts with the bogie gearboxes or disc brakes ($Z = 363$ mm) and bogie frames ($Z = 435$ mm) using the mean, mean + SD and mean + 2·SD, are found in Appendix G.

The presented governing equations and applied physical assumptions and simplifications show that there are a large set of influencing parameters regarding the risk assessment of ballast flight. Some of these parameters, like the restitution coefficient and the train set length, were varied to evaluate their influence on the risk of ballast

flight. The results of the calculations with an increased restitution coefficient value of 0.75 (instead of 0.5) are presented in Table 14 for the extrapolated undercarriage flow (8 cars) of the three considered train configurations on the rough ground. The

Z_B	Reference train model	Rough train model	Smooth train model
235 mm	323 (343) km/h	292 (315) km/h	713 (835) km/h
500 mm	336 (368) km/h	306 (333) km/h	833 (1025) km/h

Table 14: Critical train speeds for ballast pitting ($Z = 235$ mm (1:1)) and impact with the train undercarriage ($Z = 500$ mm (1:1)) for the three considered train configurations on the rough ground (G.C. B) using the mean + 2-SD-sign(mean) data of the U and W velocity and C_p field for the exposed simplified ballast particle with an edge length of $a = 28$ mm and a restitution coefficient of $e = 0.75$ and $e = 0.5$ (in brackets).

increased restitution coefficient value of 0.75 [135] assumes the worst-case scenario, with a ballast particle deflecting upward against the concrete sleeper located at the rail for the bi-block ballast trackbed design (without cross-going sleepers). The ballast flight calculations were conducted for the smallest and most susceptible ballast particle of the main ballast size distribution, i.e. the simplified ballast particle with an edge length of $a = 28$ mm [112]. The results in Table 14 reflect the lower ballast particle momentum impact loss of the ballast particles from the upward deflection with the sleeper (higher restitution coefficient), resulting in decreased critical train speeds for ballast pitting and ballast flight impact with the train undercarriage. Additionally, the relative train speed increase needed to increase the vertical height of the flying ballast particle from $Z = 235$ mm (ballast pitting) to $Z = 500$ mm (impact with the train undercarriage) decreased as well with the higher restitution coefficient, thereby increasing the risk of ballast flight incidents. Full-scale measurement results showed the lateral dependency (across rail direction) of the undercarriage flow to be clearly dependent of the undercarriage topology of the measured high-speed train. The risk of ballast flight is therefore higher for the ballast at the rail (assuming an upward deflection with a sleeper), if the lateral dependency of the undercarriage flow is roughly homogeneous (as assumed for the presented results in Table 14) or asymmetric as for the full-scale measurements within this work (see section 7). For high-speed trains with the largest U velocity values in the trackbed line of symmetry [29, 32, 47], the risk of ballast flight can be considered to be more or less equal for different lateral positions across the trackbed.

One of the most decisive parameters regarding ballast flight is the total train length, which defines the duration of the momentum transfer phase from the undercarriage

flow to the moving ballast particle (transport phase) and thereby the ballast particle velocity and thus the critical train speed for ballast flight incidents as well. The train length is a realistic and highly interesting parameter, since various train lengths exist and two high-speed trains may even be coupled together (commonly for the German high-speed train ICE). The critical train speeds for ballast flight impact with the train undercarriage were calculated for the three considered train configurations on the rough ground using the measured undercarriage flow field (4 cars) and based on the water-towing tank data extrapolated for the undercarriage flow fields of 8 and 16 cars. The outcome of the ballast flight calculations are presented below in Table 15 for an upward deflection with a sleeper ($e = 0.75$) and the other ballast in the trackbed ($e = 0.5$). The results in Table 15 show that the critical train speed decreases with the train

Train length	Reference train model	Rough train model	Smooth train model
4 cars	852 (631) km/h	510 (421) km/h	- (-)
8 cars	368 (336) km/h	333 (306) km/h	1025 (833) km/h
16 cars	318 (302) km/h	297 (283) km/h	625 (588) km/h

Table 15: Critical train speeds for the ballast particle impact with the train undercarriage ($Z = 500$ mm (1:1)) for different train lengths of the three considered train configurations on the rough ground (G.C. B) using the mean + 2·SD-sign(mean) data of the U and W velocity and C_p field for the exposed simplified ballast particle with an edge length of $a = 28$ mm. Two values of the restitution coefficient were considered, $e = 0.5$ and $e = 0.75$ (brackets), representing the upward deflection off the other ballast in the trackbed and a sleeper.

length since the transport phase is extended (i.e. the ballast particle acceleration phase over the trackbed), allowing dislodged moving ballast particles to reach the critical velocity needed for a ballast flight incident at a lower train speed. Furthermore, with an increasing train length, the critical train speed for ballast flight impacts approaches its minimum value just above the critical train speed for ballast particle initiation (Table 8). For shorter train lengths on the other hand, larger train speeds are required to accelerate dislodged moving ballast particles to the crucial velocity for ballast flight over a shorter time frame. The ballast particle must also reach the train undercarriage during the train passage of the short train set, which additionally increases the critical train speed for ballast flight impacts, which is also reflected by the results in Table 15. Comparing the results for the considered train configurations in Table 15 reveals the importance of the undercarriage flow development at the beginning of the train regarding the risk of ballast flight, especially for the shortest train length in Table 15. The rough train model with the fastest undercarriage flow development realises critical train speeds in a realistic range regarding today's high-speed trains, while ballast

flight impact is considered to be impossible for the simplified ballast particle with the smooth train model. The slow undercarriage flow development of the smooth train model (nearly fully developed at the last train car) requires extreme train speeds to even accelerate the ballast particle to the critical velocity values associated with a ballast flight impact with the train undercarriage. At these train speeds, the total time of the train passage is very short and the flying simplified ballast particle is not able to reach the train undercarriage during the train passage and thus no critical train speed could be calculated for the smooth train model with a total of 4 train cars, see Table 15. The influence of the flow development at the beginning of the train decreases with the increasing length of the train, as the mostly fully developed undercarriage flow takes over. This is also the reason that the critical train speeds for the reference and the rough train models have similar values as the train length increases, since the difference in the overall u velocity values for the nearly fully developed undercarriage flow is small. Last but not least, the increased restitution coefficient value reduced the critical train speeds, analogously to the results in Table 14. Furthermore, the increased restitution coefficient value also reduced the relative difference of the critical train speed between the train lengths.

8.4.3 Ballast flight calculations for the ground with sleepers

The transport and flight calculations for the exposed simplified ballast particle on the rough ground without cross-going sleepers and assuming a homogeneous roughness of the ballast trackbed are influenced solely by the train location. The initial ballast particle position in the trackbed (X position) may be arbitrary chosen. This is clearly not the case for the simplified ballast particle on the ground with protruding sleepers, which is strongly influenced by both the train and trackbed positions. Regardless of the initial position of a ballast particle, in an inter-sleeper region or on top of a sleeper, it must at least pass the subsequent protruding sleeper to be regarded as a risk for ballast flight incidents. The ballast particle transport and flight calculations for the ground with sleepers were therefore primarily reduced to considering only an inter-sleeper region and its upstream and downstream sleepers in order to evaluate at which critical train speed a dislodged ballast particle is able to be transported over the subsequent sleeper. Another reason for constricting the ballast particle transport and flight calculations to this small part of the trackbed was the fact that a dislodged ballast particle in the inter-sleeper region must gain sufficient momentum to

be transported over the first downstream sleeper in a short distance. A strong acceleration of the ballast particle is thus required from the undercarriage flow close to the ground that induces the lowest aerodynamic forces (see Table 8), therefore requiring very large values of the train speed for ballast flight. The ballast particle transport and flight calculations applied the same physical simplifications and assumptions as those for the rough ground. The upward deflection was triggered at 11 different positions with equidistant spacing from the ballast particle initial position in the inter-sleeper region to the downstream sleeper. The ballast particle transport and flight calculations revealed that the critical train speed for initiating ballast particle motion is considerably lower than that with which the ballast particle may jump over the subsequent sleeper. The ballast particle is therefore set into motion during the development of the undercarriage flow at the beginning of the train for the train speeds associated with the ballast particle overcoming the subsequent sleeper. There was therefore no reason to extrapolate the measured undercarriage flow in the water-towing tank to a full-size high-speed train set (8 cars), as for the calculations for the rough ground condition. Additionally, for a dislodged ballast particle to even be considered as a risk for ballast flight, it must at least pass the first sleeper for the first half of the train (first 100 m in full-scale) to be able to gain enough momentum during the transport phase to have a ballast flight impact with the train undercarriage for the second half of the train. The critical train speeds needed for the exposed simplified ballast particle to be transported over the first downstream sleeper were calculated for nine different initial positions in the inter-sleeper region, i.e. $\Delta X = 25, 75, 125, 175, 225, 275, 325, 375$ and 425 mm in full-scale from the upstream sleeper, as presented in Figure 88.

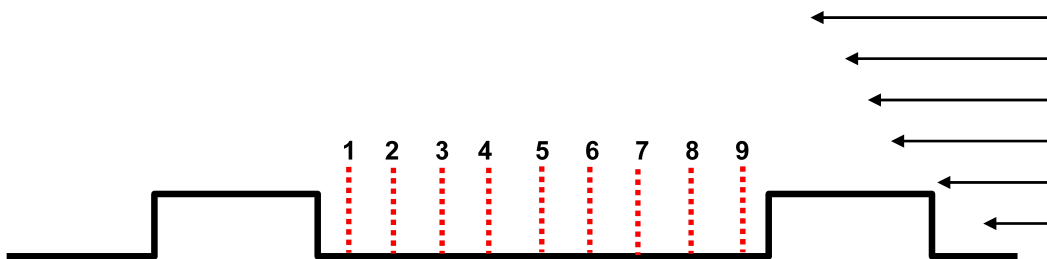


Figure 88: The considered initial positions for the calculation of the critical train speed needed for the simplified exposed ballast particle in the inter-sleeper region to be transported over the first downstream sleeper.

The calculated critical train speeds for simplified ballast particles of different sizes are presented in Table 16 for the reference train model and the nine considered inter-

sleeper positions. The train speed required to be transported over the downstream sleeper for some ballast particle sizes and initial inter-sleeper positions increased rapidly to unrealistic values for the wheel-rail system. Calculations exceeding 2000 km/h were therefore ignored. The results in Table 16 clearly show the difficulty (i.e.

Pos.	10 mm	20 mm	28 mm	40 mm	50 mm	60 mm
1	-	-	-	-	-	-
2	1550 km/h	830 km/h	820 km/h	790 km/h	780 km/h	760 km/h
3	560 km/h	620 km/h	630 km/h	610 km/h	600 km/h	590 km/h
4	490 km/h	520 km/h	540 km/h	550 km/h	550 km/h	535 km/h
5	430 km/h	490 km/h	500 km/h	500 km/h	500 km/h	495 km/h
6	490 km/h	555 km/h	570 km/h	555 km/h	535 km/h	515 km/h
7	1450 km/h	1430 km/h	1130 km/h	770 km/h	630 km/h	565 km/h
8	-	-	-	-	1215 km/h	875 km/h
9	-	-	-	-	1520 km/h	900 km/h

Table 16: Critical train speed to pass the downstream sleeper for simplified ballast particles of different sizes and for different inter-sleeper positions for the reference train model (T.C. 1) using the mean + 2·SD-sign(mean) data of the U and W velocity and C_p field.

large critical train speed values) as well as the impossibility of the ballast closest to the two sleepers (position 1, 8 and 9) gaining sufficient momentum to be transported over the first downstream sleeper. The ballast closest to the downstream sleeper (position 1 in Figure 88) is simply too close for even the largest train speeds to be sufficient to create the momentum needed for the ballast particles to pass the downstream sleeper. The dislodged ballast particle on the other side of the inter-sleeper region (position 8 and 9) with the largest distance to the downstream sleeper lie instead in the wake of the upstream sleeper, see Figure 45 in section 6.4.2. For the ballast particle sizes below the sleeper height ($a < 50$ mm), the entire or the main part of the ballast particle remains emerged in the wake flow of the upstream sleeper. Even if the aerodynamic forces are strong enough to dislodge a ballast particle (large train speed values), they may still not be strong enough to move the ballast particle outside of the wake of the upstream sleeper during the train passage. The critical train speed in this case could not be calculated. Risk of ballast flight is only found for the two largest ballast particle sizes ($a = 50$ and 60 mm) at positions 8 and 9, for which the upper end of the ballast particles protrude into the stronger undercarriage flow in the train travelling direction, though only for extreme or more or less unrealistic train speeds. The results in Table 16 also reveal that the most susceptible ballast particles regarding ballast flight incidents are those around the central position between both sleepers. The under-

carriage flow reattaches after the upstream sleeper for the central positions inducing larger aerodynamic forces and the distance to the downstream sleeper is sufficient for the ballast particle to gain the momentum needed to jump over the sleeper. Though the largest aerodynamic forces (largest U velocity values closest to the ground, see Figure 46 in section 6.4.2) were found around position 3 in the inter-sleeper region, the ballast particle acceleration necessary to pass the downstream sleeper was only realised for larger train speeds also capable of dislodging ballast particles further upstream. Due to the longer acceleration phase for ballast particles dislodged further upstream, the ballast particle momentum needed to jump over the subsequent sleeper is achieved at lower train speeds. Nevertheless, the upstream dislodged ballast particles are also accelerated by the largest aerodynamic forces (position 3) in the inter-sleeper region. The combination of critical train speed for ballast particle initiation and length of the acceleration phase most likely to be transported over the downstream sleeper and thus create the largest risk of ballast flight incidents for the reference train model is found for the ballast around position 5.

Comparing the critical train speeds in Table 16 for the different ballast particle sizes for each position reveals an effect inconsistent with the results of the rough ground presented earlier (see Figure 87). The critical train speed is hardly influenced or is even decreased for larger (position 2 and 7 in Table 16) and for the largest (position 3-6) ballast particle sizes. The ballast particle initiation, transport over the trackbed and flight are influenced by a large set of parameters. The main reasons for the decreasing or stabilised values of the critical train speed for the larger ballast particle sizes are, however, associated with the assumed rolling motion of the ballast particle over the trackbed. The quickly rotating motion only allowing the outer edges of the ballast particle to be in contact with the trackbed, presented in Figure 81, elevates the ballast particle into the stronger undercarriage flow, but also away from the shielding effect of the protruding sleepers, increasing the aerodynamic forces on dislodged ballast particles. Furthermore, the vertical elevation of a ballast particle rotating over the trackbed increases with the ballast particle size ($\Delta Z_{COM} = a \cdot (\sin(45^\circ) - 0.5)$) and thus decreases the height (ΔZ) of the vertical jump over the sleeper. The just mentioned effects of the ballast particle rolling motion and the increased surface area (a^2) for larger ballast particles, increase the aerodynamic forces enough to equalise or overcome the influence of the countering, gravitational force that increase with the third power (a^3). The critical train speeds can therefore be maintained or even reduced for larger ballast particle sizes in the inter-sleeper region.

The influence of the ballast particle size on the critical train speed in Table 16 needed to be transported over the downstream sleeper is also influenced by a particle's initial position in the inter-sleeper region. Regarding the more interesting region for ballast flight (i.e. position 3-6), the results show that the effect of increasing ballast particle size for the rolling motion over the trackbed is first effective for ballast particle sizes larger than $a = 28$ mm. The lowest critical train speeds for positions 3-6 were still found for the smallest ballast particles. The extreme critical train speeds for the smallest ballast particle size ($a = 10$ mm) for position 2 and the smaller ballast particle sizes for position 7 ($a = 10, 20$ and 28 mm), followed by a strong critical train speed decrease for the larger ballast particle sizes in Table 16, are more associated with the small distance to the sleeper (short acceleration phase and wake) and less so with the ballast particle rolling motion over the trackbed. Analogously to position 1, the dislodged ballast particles at position 2 must gain the momentum necessary to passing the downstream sleeper through a very short distance, thereby requiring large train speeds. The large train speeds associated with the strong acceleration needed to pass the downstream sleeper dislodge ballast particles from the trackbed at the beginning of the train, i.e. during the development of the undercarriage flow, additionally increasing the required train speed. The very early dislodgement of the smallest ballast particle ($a = 10$ mm) reveals that the ballast particle acceleration required to pass the downstream sleeper must be realised underneath the leading end-car, which is associated with very low U velocity and U_{SD} values close to the ground. This rapidly increases the train speed required to move ballast particles over the downstream sleeper, see Table 16. The delayed dislodgement of the larger ballast particles realised ballast particle acceleration by the later incoming and stronger undercarriage flow reducing the critical train speeds. Nevertheless, with increasing ballast particle size, the effects of the ballast particle rolling motion over the trackbed discussed above also contribute to reduce critical train speeds. The critical train speeds at position 7 are, like the upstream positions 8 and 9, strongly influenced by the wake of the upstream sleeper. However, since position 7 is located at the end of the wake of the upstream sleeper for the mostly fully developed undercarriage flow (see Figure 46 in section 6.4.2), the influence of the wake is stronger for the smaller ballast particles. The smallest ballast particle ($a = 10$ mm) is completely emerged in the reverse flow region of the upstream sleeper wake, as the second smallest ballast particle ($a = 20$ mm) just reaches the flow in the travelling direction of the train for the nearly fully developed undercarriage flow. Since the wake flow of the upstream sleeper develops

with the train length (downstream extension in the X direction), the only possibility for the two smallest ballast particles to be accelerated in the travelling direction of the train (instead of towards the upstream sleeper by the reverse flow) is an early ballast particle dislodgement and transport downstream before the wake flow becomes developed. The ballast particles can thereafter be accelerated by the stronger and incoming undercarriage flow outside the wake of the upstream sleeper. For the early dislodgement and transport of ballast particles to downstream positions in the inter-sleeper region for the low values of the U velocity and U_{SD} close to the trackbed at the beginning of the train, large train speeds are required, as reflected by the results in Table 16. Furthermore, with increasing ballast particle size the ballast particle protrudes further into the stronger undercarriage flow, increasing the aerodynamic forces on the ballast particle and thereby decreasing the critical train speed. The corresponding results in Table 16 for the smooth and rough train models are found in Appendix H. The critical train speeds for the most susceptible initial positions in the inter-sleeper region for the three considered train configurations are compared in Table 17 for different ballast particle sizes. The comparison of the critical train speeds for the different

	Reference train model	Smooth train model	Rough train model
a = 10 mm	430 km/h ⁽⁵⁾	900 km/h ⁽⁴⁾	380 km/h ^(5,6)
a = 20 mm	490 km/h ⁽⁵⁾	980 km/h ⁽³⁾	410 km/h ⁽⁵⁾
a = 28 mm	500 km/h ⁽⁵⁾	990 km/h ⁽³⁾	410 km/h ⁽⁵⁾
a = 40 mm	500 km/h ⁽⁵⁾	1000 km/h ⁽³⁾	420 km/h ⁽⁵⁾
a = 50 mm	500 km/h ⁽⁵⁾	1000 km/h ⁽³⁾	410 km/h ⁽⁷⁾
a = 60 mm	495 km/h ⁽⁵⁾	995 km/h ⁽³⁾	400 km/h ⁽⁷⁾

Table 17: Lowest critical train speed necessary for the simplified exposed ballast particle of different sizes in the inter-sleeper region to pass the downstream sleeper for the three considered train configurations using the mean + 2-SD-sign(mean) data of the U and W velocity and C_p field. The bracketed upper case numbers indicate the initial inter-sleeper positions of the ballast particles.

train configurations in Appendix H and those in Table 17 reveal that the previously presented and discussed effect of the ballast particle rolling motion over the trackbed for the reference train model is also found for the rough and the smooth train models. Thus, the critical train speed stabilises or even decreases for the larger ballast particle sizes. The different characteristics of the undercarriage flow for the considered train configurations changed the critical train speed values as well as the positions in the inter-sleeper region most susceptible to ballast flight. In contradiction to the reference train model, the inter-sleeper position most susceptible to ballast flight was

also influenced by the ballast particle size for the smooth and the rough train models. The discussion of the previously presented results for the reference train model concluded that the most susceptible position in the trackbed is primarily determined by the ballast particle initiation threshold, the distance to the sleeper (acceleration phase) and of course the incoming undercarriage flow after the ballast particle dislodgement. In other words, the timing of the ballast particle dislodgement and the development of the undercarriage flow is crucial. The lowest critical train speeds for the reference train model in Table 17 were therefore found for the delayed ballast particle dislodgement at position 5, causing aside from the longer acceleration phase, the ballast particle to be accelerated (transport and flight phase) by the stronger undercarriage flow for the second half of the four-car train set. The lowest critical train speeds presented in Table 17 for the smooth train model with a ballast particle dislodgement at position 3 (and position 4 for $a = 10$ mm) were, like for the reference train model, accelerated by the stronger undercarriage flow at the end of the train. The ballast was dislodged for position 3 in the inter-sleeper region by the largest U velocity and U_{SD} values and still accelerated by the stronger undercarriage flow at the end of the train due to the extreme train speeds needed for the ballast particle to pass the downstream sleeper. There is therefore no advantage of a delayed ballast particle dislodgement with a longer acceleration phase (besides for $a = 10$ mm) as for the reference train model (see results in Appendix H). The results for the fast undercarriage flow development and the strong flow accelerations around the open bogie housings of the rough train model revealed that two different scenarios of the crucial timing for the particle dislodgement from the trackbed and the undercarriage flow could result in the lowest critical train speed. In the first scenario, the ballast flight calculations reveal that the ballast particle becomes dislodged (position 5) just before the first inter-car region, at $X / L_{TRAIN} = 0.22$ in Figure F3 in Appendix F, being accelerated by the strong flow from the open bogie housings to jump over the downstream sleeper for the accelerated flow of the next inter-car region ($X / L_{TRAIN} = 0.52$ in Figure F3). In the second case, the ballast particle is initiated (position 7) later for the strong flow at the end of the first inter-car region ($X / L_{TRAIN} = 0.29$ in Figure F3) and uses the larger distance to the downstream sleeper to gain enough momentum to jump over the sleeper at the third inter-car region at $X / L_{TRAIN} = 0.83$ in Figure F3. The timing between the ballast particle dislodgement from the trackbed and the strong flow around the bogie regions thus defines the critical train speed for the rough train model. The lowest critical train speeds for the rough train model in Table 17 are

confirmed by the local and overall larger values of the expected maximum u velocity (mean U velocity + $2 \cdot U_{SD}$) along the train length in the inter-sleeper region in Appendix F. The lower critical train speeds for the rough train model in Table 17 are associated with the strong flow accelerations induced by the open bogie housings. The strong, accelerated flow leaving the open bogie housings towards the trackbed pushes the flow into the protected inter-sleeper region, thereby increasing the aerodynamic forces on the ballast for the entire inter-sleeper region (see Appendix H). It is therefore concluded that bogie regions or other undercarriage geometries inducing flow accelerations similar to those of the open bogie housings of the rough train model should be avoided, since they increase the aerodynamic forces on the more protected ballast in the inter-sleeper region, thereby increasing the risk of ballast flight. Regarding the risk of ballast flight incidents, i.e. ballast pitting or even impacts with the train undercarriage, larger vertical heights than the first sleeper must be reached by the flying ballast particles. In other words, greater ballast particle momentum is required. Comparing the critical train speeds in Table 17 with those of the rough ground (without cross-going sleepers) in Table 13 shows that the train speeds needed to force the ballast particle out of the inter-sleeper region are strong enough to accelerate the ballast particle over the trackbed for a later upward deflection reaching the height of the top of the rail or even the train undercarriage. However, the dislodged ballast particle must be transported over the following sleepers to avoid being captured in the inter-sleeper regions during the transport phase over the trackbed. The timing with the train undercarriage flow is thus a crucial requirement. The protruding sleepers alone as an obstacle for the moving ballast particle also reduce the risk of ballast flight incidents. The results in Table 17 indicate the effectiveness of a well maintained trackbed by assuring a lowered ballast level and avoiding fouled or crushed ballast ($a = 10\text{-}20$ mm), lowering the risk of ballast flight or even preventing ballast particles from escaping the inter-sleeper region. Further, combining a well-maintained ballast trackbed with cross-going sleepers and a high-speed train with an aerodynamically optimised undercarriage (undercarriage flow approaching that of the smooth train model), the risk of ballast flight can be minimised or considered as diminished even for very high-speed trains.

Ballast particles on top of sleepers are often considered as the worst-case scenario for ballast flight due to their exposed position in the strongly accelerated flow over sleepers. The low critical train speeds for the initiation of ballast particle motion previously presented in Table 8 are however misleading regarding the risk of ballast flight, since

a ballast particle must at least be transported over the downstream sleeper for which larger train speeds are required. To assess the risk of ballast flight for the considered worst-case scenario, ballast particle transport and flight calculations were conducted for the simplified ballast particle of different sizes, with an initial position on top of a sleeper. The conditions or simplifications previously argued and applied, i.e. the use of only one inter-sleeper region and its up- and downstream sleepers and the under-carriage flow of the measured 4-unit train set, were also applied for the evaluation of the critical train speed for ballast particles initially positioned on top of sleepers. Two different ballast particle trajectories were considered for the conducted calculations and are presented in Figure 89. The only difference between the two considered trajec-

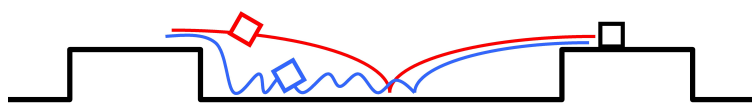


Figure 89: The two considered trajectories over the downstream sleeper for the simplified ballast particle with an initial position on top of a sleeper.

tories was the continuation of the ballast particle motion after the first impact with the trackbed in the inter-sleeper region. Thus, the ballast particle slides off the sleeper for both considered paths of motion. After the first impact with the trackbed the momentum of the ballast particle is completely transformed into a horizontal motion over the trackbed for a later upward deflection and flight over the downstream sleeper (see blue line in Figure 89). Alternatively, the momentum is changed completely into a vertical motion, directly initiating the flight over the downstream sleeper after the contact with the trackbed, i.e. a direct bounce of the trackbed as the red line in Figure 89. The ballast particle slide on top of the sleeper, rolling motion over the other ballast in the inter-sleeper region and the flight phase are simulated according to the previously presented calculations. For the flight phase or the drop off the sleeper, however, it is assumed that the ballast particle does not rotate, i.e. there is no Magnus effect, and therefore the restitution coefficient value at the first impact with the trackbed is also set to $e = 0.4$ [41] instead $e = 0.5$. The ballast particle rotation is initiated at the first impact with the trackbed and is thereafter defined as for the previously presented calculations according to Equation (42).

Three different initial positions on top of a sleeper, see Figure 90, were considered for the presented calculations. The lowest critical train speeds for a ballast particle initially positioned on top of a sleeper needed to be transported over the downstream

sleeper are presented in Table 18 of different sizes and for the three considered train configurations. The results of all conducted calculations are presented in Appendix H. The results in Table 18, like those of Table 17, reveal that the different undercar-

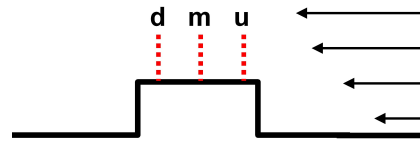


Figure 90: Three considered initial positions for the simplified ballast particle: downstream (d), middle (m) and upstream (u) at the corresponding distances of 125, 75 and 25 mm (1:1) from the upstream edge of the sleeper.

	Reference train model	Smooth train model	Rough train model
a = 10 mm	375 km/h ^(u)	-	340 km/h ^(m*)
a = 20 mm	425 km/h ^(u)	650 km/h ^(m*)	320 km/h ^(u*)
a = 28 mm	450 km/h ^(u)	685 km/h ^(m*)	350 km/h ^(u*)
a = 40 mm	460 km/h ^(u)	595 km/h ^(u*)	365 km/h ^(u)
a = 50 mm	460 km/h ^(u)	690 km/h ^(m*)	365 km/h ^(u)
a = 60 mm	455 km/h ^(u)	810 km/h ^(d*)	365 km/h ^(u)

Table 18: Lowest critical train speed necessary for the simplified exposed ballast particle of different sizes in the inter-sleeper region to pass the downstream sleeper for the three considered train configurations using the mean + 2·SD·sign(mean) data of the U and W velocity and C_p field. The bracketed upper case numbers indicate the initial inter-sleeper positions of the ballast particles.

riage flow characteristics of the considered train configurations not only change the value of the critical train speed, but also the initial position on the sleeper and the path of motion of greatest susceptibility. In general, the most susceptible initial position for ballast particles on top of a sleeper is the upstream position (see Figure 90), since the strong flow acceleration over sleepers is associated with large aerodynamic forces which accelerate the ballast particle over a longer time. However, with increasing train speeds that create enough momentum for the ballast particles to jump over the downstream sleepers, the influence of the flow around the head of the train becomes stronger, as does the reverse flow region in particular. Thus, for the upstream sleeper position the reverse flow around the head of the train swept the smallest ballast particle for the rough train model (a = 10 mm) and for a = 10, 20 and 28 mm for the smooth train model into the upstream inter-sleeper region before critical train speeds were reached. The most susceptible initial position on top of a sleeper for the

corresponding ballast sizes of the rough and smooth train models is therefore the central position instead of the upstream position (see Table 18). The longer reverse flow region for the smooth train model (see Figure 21 in section 6.3.1) pushes the smallest ballast particle into the upstream inter-sleeper region for all initial sleeper positions and the critical train speed could therefore not be determined. The ballast particle displacement on top of a sleeper caused by the flow around the head decreases with the ballast particle size, since the ballast particle acceleration is proportional to A_B / V_B according to Equation (39) in section 8.3.1. The larger ballast particles can thereby be accelerated by the stronger and later incoming undercarriage flow.

Further analysis of the results in Table H2 in Appendix H shows that the undercarriage flow development along the train length and the ballast particle size are decisive regarding which of the two considered trajectories in Figure 89 is taken, resulting in the lowest critical train speeds causing the ballast particle to pass the downstream sleeper. The most distinctive difference between the two paths over the downstream sleeper for a ballast particle initially on top of a sleeper is its contact with the trackbed, i.e. the ballast particle momentum loss. The direct upward deflection with only one contact or impact with the trackbed is clearly associated with a lower ballast particle momentum loss. However, for the ballast particle to pass the downstream sleeper by direct upward deflection it must first be accelerated to the sufficient velocity (U_B) before the first and only impact with the trackbed. U_B defines the initial vertical velocity W_B as well as the in-flight lift (i.e. Magnus effect caused by the ballast rotation) and thus the maximum height of the ballast particle flight path. Furthermore, due to the low critical train speed initiating the ballast particle motion on top of a sleeper, the needed ballast particle velocity to pass the downstream sleeper by direct upward deflection must be induced by the undercarriage flow along the beginning of the train. It is therefore only for the fast development and the larger aerodynamic forces of the undercarriage flow at the beginning of the train for the rough train model and for the smaller ballast particles more prone to ballast flight (ballast flight is proportional to $\sim A_B / V_B$ according to Equations (44) and (45)) for which the direct upward deflection resulted in the lowest critical train speeds. The fact that the smaller ballast particles were exposed to the stronger undercarriage flow at larger vertical heights during the flight instead of moving over the trackbed deep in the inter-sleeper region with lower aerodynamic forces also contributed to the lowest critical train speeds for the direct upward deflection. However, for the larger ballast particles ($a = 40, 50$ and 60 mm in Table 18) for the rough train model, the train speed required to realise the bal-

last particle velocity (U_B) necessary to pass the downstream sleeper by direct upward deflection surpassed the values for the ballast particle transport and later upward deflection from the trackbed. This is despite the increased ballast particle momentum loss due to the trackbed friction during the ballast particle transport phase and the strong loss (50%) for the second upward deflection from the trackbed. The lower critical train speeds for the ballast particle transport and the later upward deflection from the trackbed for the larger ballast particles of the rough train model are associated with the strong influence of the ballast particle rolling motion over the trackbed that was previously presented. The elevated position of the rolling, larger ballast particles that protrude more into the stronger undercarriage flow, the decreased vertical leap ($\Delta Z_{COM} = a \cdot (\sin(45^\circ) - 0.5)$) and the direct flight path over the downstream sleeper are considered as the primary reasons for the lower critical train speeds for the later upward deflection from the trackbed. The ballast flight calculations for the reference train model showed that the train speeds needed for ballast particles to be transported over the downstream sleeper by direct upward deflection were always larger than those values for a later upward deflection from the trackbed. Comparing the undercarriage flow for the reference and the rough train models shows that the consistently lower critical train speeds for the later upward deflection for the reference train model are linked to its lower aerodynamic forces for the first two train cars due to the slower undercarriage flow development. This contradicts the results for the smooth train model in Table 18 with the lowest aerodynamic forces for the entire undercarriage flow. The direct upward deflection for the smooth train model is an effect of the short four-car train set used for the conducted ballast particle transport and flight calculations. Conducting the calculations with only the four-car train set was justified by the fact that dislodged ballast particles must pass the downstream sleeper for the first half of the train length of a realistic train set of 8 cars to even be considered as a risk of ballast flight. The slow development and the low normalised U velocity and U_{SD} values of the undercarriage flow for the smooth train model only began initiating ballast particles (even those on top of sleepers) for the second half of the train for the large train speeds presented in Table 18. Besides the late initiation, the ballast particle motion over the trackbed is much slower in relation to the train speed and therefore the direct upward deflection was the only possible path of motion to pass the downstream sleeper during the short train passage of the considered train set of four-cars. The reasons the most susceptible initial position on top of a sleeper changes from the upstream position for $a = 40$ mm to the downstream position for a

= 60 mm in Table 18 are the late initiation of ballast particle motion, the large train speed and the consideration of only the 4-unit train set for the smooth train model. The train passage is simply too short and thus it was only possible to calculate the critical train speed for the shorter distances to the downstream sleeper as the ballast particle size increased.

The lowest critical train speeds for the rough train model in Table 18 highlight the strong influence of the undercarriage flow development at the beginning of the train set on the risk of ballast flight for ballast particles with initial positions on top of sleepers. Independent of the path of motion over the first downstream sleeper (direct upward deflection or later upward deflection from the trackbed), the acceleration of the ballast particle by the train-induced undercarriage flow at the beginning of the train set (approximately within the first two train cars) defines the critical train speeds for the later ballast flight incidents. Ballast particle acceleration over consecutive sleepers (after passing the first one) is further enhanced for the rough train model (see Figure 52 and Figure 52 in section 6.5) due to its largest aerodynamic forces in the entire inter-sleeper region and the strongest flow acceleration over sleepers for the mostly fully developed undercarriage flow. The critical ballast particle velocity (U_B) needed to reach the vertical heights of the rolling stock after upward deflection from the trackbed is therefore achieved more quickly for the rough train model. This increases the proportion of the train length susceptible to ballast flight impacts, which is rapidly increasing the overall risk of ballast flight incidents. It is therefore concluded that bogie regions (bogie and bogie housing) or any other geometric shape on the train undercarriage that generates flow effects similar to those found for the open bogie housings of the rough train model should be avoided in light of the risk of ballast flight.

8.5 Overall comparison of the risk of ballast flight incidents

The lowest calculated critical train speeds for ballast pitting (smooth and rough grounds) and for ballast particles to be transported over the first downstream sleeper (ground with sleepers) are compared to each other in Figure 91 for the considered train configurations and sizes of the simplified and exposed ballast particle. The critical train speeds needed to pass the first downstream sleeper calculated for a ballast particle with an initial position on top of a sleeper and in an inter-sleeper region using the four-car train set were considered as the threshold test for ballast flight. Once again,

it was assumed that a dislodged ballast particle should be transported over the first downstream sleeper within the first half of the train set of a conventional eight-car train set, e.g. the German high-speed train ICE, to even be regarded as a risk for ballast flight. If a ballast particle passes the following sleepers, the large train speed and the accelerated flow over the sleepers should at least transfer enough momentum to the moving ballast particle by the end of the train for the vertical height of the top of the rail to be within reach by upward deflection from the trackbed. The critical train speed results for ballast pitting for the smooth and rough grounds were therefore used in the overall comparison. The critical train speeds for ballast pitting for the smooth ground configuration (not previously presented) were included in the overall comparison to show the effect of the most susceptible scenario of a ballast particle laying on a concrete slab track close to a trackbed transition to a ballast trackbed. The ballast particle transport and flight calculations for a ballast particle on the smooth ground were conducted as those for the rough ground, but with the boundary conditions previously presented for the smooth ground, e.g. assuming that the ballast particle is initiated by a sliding motion. The ballast particle on the concrete slab track is initiated by a sliding motion, though after $\Delta X = 0.5$ m the sliding motion transitions to the rolling motion previously presented in Figure 81. This is in accordance to rock fall dynamics [133], that a falling rock, in this case a ballast particle, begins to rotate at a critical velocity or due to surface imperfections such as at the edges of the pre-cast segments commonly used for concrete slab tracks. The applied rolling friction coefficient value used for the smooth ground was the same as for the sliding motion, i.e. $\mu_{dynamic} = 0.4$. Additionally, the later ballast particle upward deflection is considered to occur when the ballast particle arrives at the ballast trackbed and the previously applied restitution coefficient of $e = 0.5$ was therefore also applied in the calculations for the smooth ground configuration.

The results in Figure 91 clearly show that the smooth ground does not influence or decelerate the train-induced undercarriage flow as much as for the rough ground or for the ground with sleepers. The thereby larger aerodynamic forces on the ballast particle, lower friction coefficients (static and dynamic) and the stronger trackbed vibration clearly decrease the critical train speeds for ballast pitting for all three train configurations. The results for the smooth ground clearly highlight the risk of ballast flight incidents around concrete slab track and ballast trackbed transitions. The transitions are however fairly uncommon or at least represent only a small portion of the total track length, strongly decreases the occurrence of ballast flight incidents caused

by ballast particles laying on the slab track. Besides the locations of the trackbed transitions being known, countermeasures against ballast particles being transported onto the slab track where they are more susceptible to flight for later train passages are fairly easy to realise by gluing or covering the ballast with nets [44] for the susceptible trackbed regions. Since trackbed transitions are quite rare and countermeasures are quite easily constructed, the risk of ballast flight incidents around trackbed transitions is easily avoided. The results for the more interesting ground conditions

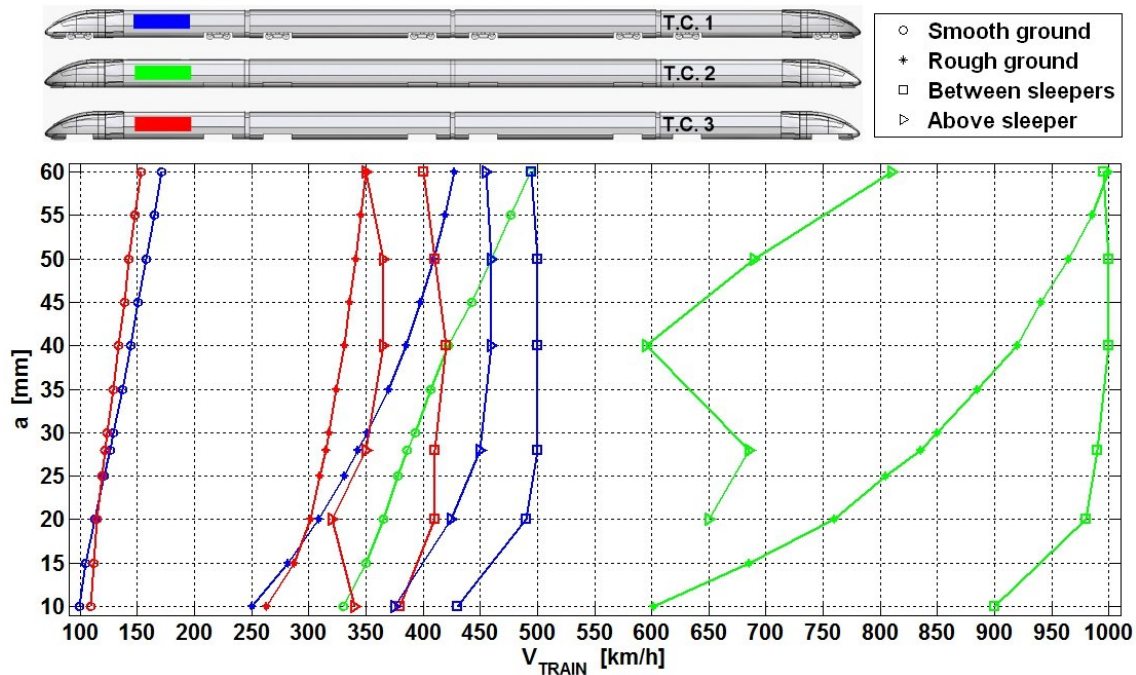


Figure 91: Comparison of the lowest critical train speeds for ballast pitting (smooth and rough grounds) and for a ballast particle to be transported over the downstream sleeper with an initial position on top of a sleeper and in an inter-sleeper region for the considered train configurations and sizes of the simplified exposed ballast particle using the mean + 2·SD·sign(mean) data of the U and W velocity and C_p field.

regarding ballast flight (i.e. the rough ground and ground with sleepers) in Figure 91 show that the exposed ballast particle in the trackbed without cross-going sleepers (rough ground) are more susceptible to ballast flight than those in an inter-sleeper region and even those for the "worst-case" scenario of ballast particles on top of a sleeper. The only exception is for the smooth train model, which clearly has lower critical train speeds for ballast particles initially on top of sleepers. The required train speeds needed for ballast particles to pass the first downstream sleeper are however in fairly unrealistic train speed ranges for the wheel-rail system and are therefore of less interest regarding the risk of ballast flight. Even though the overall aerodynamic

forces induced by the smooth train model on a moving ballast particle are larger for the ground with sleepers than they are for the rough ground (see vertical profiles of the U velocity and U_{SD} in section 6.4.4), the critical train speeds presented in Figure 91 for the ballast particles initially on top of a sleeper are still considered to be insufficient to cause ballast pitting. The reason for this is the strong train speed increase required for flying ballast particles to increase their maximum vertical height from the top of the rail to the height of the train undercarriage for the smooth train model on the rough ground (see Table 14). The great train speed increase is therefore also needed for ballast particles initially on top of sleepers to cause ballast pitting, due to the generally lower aerodynamic forces for the smooth train model and the short train passage at the large train speeds. This is however not the case for the reference and the rough train models, which have larger critical train speeds for the ground with sleepers, assuring the possibility that dislodged ballast particles may gain the needed momentum for ballast pitting. Regarding the risk of ballast flight incidents for the more interesting train configurations (i.e. reference and rough train models), the relatively low critical train speed difference for ballast particles initially on top of sleepers and in inter-sleeper regions was not directly expected. However, considering that ballast particles on top of sleepers become dislodged at the beginning of a train passage while the undercarriage flow develops, and that the ballast particles enter the inter-sleeper region before jumping over the first downstream sleeper, the small difference may be understood. The large critical train speed values for the ground with sleepers implies that the trackbed with cross-going sleepers and a lowered ballast level can be considered to be resistant to ballast flight events for larger train speeds, even though there is a chance that ballast particles lie on top of sleepers. This is, however, based on the calculations for the simplified ballast particle (i.e. a cube) and there is therefore a possibility that the outcome of the presented results in Figure 91 might change for other ballast particle shapes (e.g. with stronger lift coefficients) or for increased ballast levels (ΔZ between the trackbed and TOS decreases). Comparing the critical train speeds for the different train configurations in Figure 91, show that a rougher undercarriage generally increases the risk of ballast flight. Additionally, the results in Figure 91 reveal that the effect of the undercarriage roughness regarding the risk of ballast flight was also changed by the roughness and topology of the trackbed. The influence of the trackbed roughness on the critical train speeds is especially distinctive for the reference and the rough train models, where the critical train speeds for ballast flight change from nearly the same values for the smooth ground to clearly

different values for the ground with sleepers. Based on the presented results in Figure 91 for the reference and the rough train models, it is strongly advised to consider ground effects for the risk assessment of ballast flight. Furthermore, the critical train speeds in Figure 91 show the strong effect of the cavity-driven undercarriage flow for the rough train model, where even ballast particles in inter-sleeper regions are more susceptible to ballast flight than those on top of sleepers for the reference train model. This clearly highlights that cavities, bogie regions (bogie and bogie housing) or any other geometric objects inducing flow accelerations similar to those of the open bogie housings of the rough train model should be avoided. Furthermore, the smooth train model clearly demonstrates that covering the inter-car gaps and closing the bogie regions makes critical train speeds for ballast flight incidents more or less unrealistic for today's high-speed trains. Even if a completely smooth train undercarriage is unrealistic, striving for the undercarriage aerodynamics of the smooth train model by covering all gaps and by aligning all details of the undercarriages of high-speed trains as much as possible will allow increasing train speeds without increasing the risk of ballast flight incidents.

9 Conclusions and outlook

9.1 Conclusions

Particle image velocimetry (two-component 10 Hz and high-speed PIV) was applied to measure in a vertical plane (XZ) the horizontal and vertical velocities of the undercarriage flow in the line of symmetry of a trackbed. Three different 1:50 scale generic high-speed train configurations with a total length of four train cars were hauled at a train speed of 4 m/s (corresponding to a Reynolds number of $0.25 \cdot 10^6$) through a water-towing tank over a) smooth ground, b) rough ground and c) a ground with sleepers.

The applied non-intrusive high-speed PIV technique achieved a high spatial and temporal resolution for the entire (optically accessible) undercarriage gap, including the velocity gradients at the ground and the train undercarriage. Moreover, the high-speed PIV technique allowed close-up analysis and evaluation of the instantaneous undercarriage flow around such interesting features as bogie regions. It was difficult and extremely time consuming to gather flow field data samples sufficient to generate highly converged statistical measurements due to the low repetition rates, resulting from water settlement times in water-towing tanks following moving-model runs. The data, however, showed that high-speed PIV in a water-towing tank is an excellent method for scale train model experiments of the undercarriage flow when compared to the advantages and disadvantages of other test facilities and measurement techniques (see section 1.4). Even though the results obtained using the high-speed PIV in the water-towing tank were both temporally and spatially highly resolved, the undercarriage flow recorded still needed to be validated in order to verify the relevance of the scale model experiments. The data obtained for the reference model on the smooth ground was, therefore, compared to measurements done on commercially operating full-scale high-speed trains, an Italian ETR 500 and a German ICE, both cruising over concrete slab track. Comparisons to these full-scale measurements revealed that the main characteristics around the head and tail of the train as well as those with respect to the undercarriage flow were recreated by the 1:50 scale train model experiments in the water-towing tank. In addition, the undercarriage flow after the fifth bogie, which, for the most part, was fully developed in the water-towing tank, was also confirmed by the full-scale measurements. Even though the mean U velocity values for the fully developed undercarriage flow in the water-towing tank

were always lower than those observed for real high-speed trains, the velocity fluctuation values (U_{SD}) were still well reflected. The differences in the mean U velocity values are ascribed to the different geometries of the trains: the smoother undercarriage of the train model due to the lower degree of detail (especially with regard to the bogies) and the lower Reynolds numbers. Overall comparisons to the full-scale measurements showed the PIV in the water-towing tank on downscaled train models to be suitable for the study of the main characteristics of undercarriage flows of high-speed trains.

The horizontal and vertical profiles of the U and W velocities extracted along the length of the train revealed that the U velocity component clearly dominated the undercarriage flow for all measured train and ground configurations. It can, therefore, be concluded that the aerodynamic forces on the ballast in the trackbed are mainly induced by the horizontal velocity component in the travelling direction of the train, making it the most interesting factor with regard to assessing the risk of ballast flight. The undercarriage flow (U velocity) of the three train configurations can be divided into four characteristic flow regions: 1) head, 2) Couette-like undercarriage flow, 3) near-wake and 4) far-wake. Directly before the head of the train (head region), the flow is strongly accelerated in the train's travelling direction. This is an event immediately followed by a strong flow deceleration that reverses the flow direction just below the head of the train. After the first bogie, the flow reverses again to the train's travelling direction along the length of the train, developing into a nearly fully developed Couette-like undercarriage flow. In the near-wake region, the undercarriage flow is strongly accelerated and reaches its largest U velocity values, which then recede in the far-wake region. Comparing the results for the three different train configurations revealed that bogies, bogie housings, inter-car gaps, cavities and geometric obstacles or irregularities on a train's undercarriage increase the local and overall flow speeds, velocity gradients and turbulence levels in the undercarriage flow. The greater velocities, steeper velocity gradients and higher turbulence intensities increase the aerodynamic forces on the ballast in the trackbed and thus the risk of ballast flight. The results for the various train configurations also demonstrated that by changing the roughness in the decisive inter-car regions (bogie - inter-car gap - bogie) on the reference train model, three different characteristic undercarriage flows are possible. In comparison to the reference train model, the U velocity and U_{SD} values for the completely smooth undercarriage of the smooth train model were lower by nearly a factor of two and could be treated as the lower limit for the undercarriage

velocity values and turbulence levels achievable for high-speed trains with extremely optimised aerodynamics. Conversely, the rough train model revealed that the strong flow accelerations around the open bogie housings, simulating aerodynamically disadvantageous bogie regions, only locally increased the velocities and the velocity gradients at the ground. The open bogie housings of the rough train model strongly increased the turbulence intensity not only locally, but also along the entire length of the train. Increased turbulence intensities are associated with larger shear forces and, more importantly, with larger velocity fluctuations, creating the possibility of increased flow speeds and consequently greater form drag forces affecting exposed ballast particles in the trackbed. In addition, the instantaneous undercarriage flow around the open bogie housings on the rough train model revealed unsteady effects from flow expelled from the bogie housings toward the ground, strongly increasing the instantaneous flow velocities at the ground to almost train speed. This clearly emphasises the importance of considering the contributions of the velocity fluctuations and the highly turbulent nature of the undercarriage flow. Since the u and w velocity distributions were similar to Gaussian distributions, it was possible to estimate the expected maximum flow velocity of interest with respect to ballast flight by applying the 2σ -rule. Taking the velocity fluctuations into account (mean U velocity + $2 \cdot U_{SD}$), suggested that the rough train model is the train configuration most susceptible to creating ballast flight events due to its strong local flow accelerations and to the greater overall turbulence levels.

In general, the increased drag of the rough ground and the ground with sleepers slows the entire Couette-like undercarriage flow, decreasing, in particular, the flow speeds, velocity gradients and turbulence intensities near to the ground. The aerodynamic forces on exposed ballast particles in the trackbed are thus lower and the chance of ballast flight is reduced. The undercarriage flow over the ground with sleepers showed two different characteristic flow regions. One was the inter-sleeper flow region (between two sleepers) with low velocities, velocity gradients and turbulence intensities close to the trackbed, stemming from protruding sleepers that shield the inter-sleeper region from the undercarriage flow. The second was the accelerated flow region over the sleeper caused by the undercarriage gap contraction; in this case larger flow speeds, velocity gradients and turbulence intensities close to the upper surface of the sleeper were exhibited. The influence of the ground roughness on these three different characteristic undercarriage flows of the train models produced both similarities and differences, implying that the roughness of the train's undercarriage

as well as that of the trackbed should be considered in order to make a reliable assessment of the ballast flight risk. The more interesting effect with regard to ballast flight is that the expected maximum u velocity of the fully developed undercarriage flow for the rough train model is less influenced by the ground roughness than is the case with the other two train configurations. This especially applies for the ground with sleepers, where the accelerated flow around the open bogie housings together with the gap contraction from the protruding sleepers induced the largest values of the expected maximum u velocity (mean U velocity + $2 \cdot U_{SD}$).

The undercarriage flow fields obtained from the scale train model experiments in the water-towing tank were used to simulate the ballast particle dislodgement, transport and flight for an exposed simplified ballast particle (i.e. a cube). The calculations revealed that the ballast particle dislodgement from the trackbed is strongly influenced by the ground acceleration simulating the trackbed vibration. It can, therefore, be concluded that the initiation of ballast particle motion is caused by the combined effect of the aerodynamic forces and trackbed vibration induced by a particular train. The results also show that the initial motion of an exposed ballast particle on top of a sleeper or in a concrete slab track would most likely begin as a sliding motion, while a ballast particle in a trackbed would initiate as a rolling motion. A direct take-off for the simplified ballast particle is thus considered to be improbable. The ballast flight calculations for different train set lengths (extrapolated) of the three train configurations show that the risk of ballast flight increases with the length of the train set. The results for the smooth train model demonstrate, however, that even for the longest train set (16 units), extreme train speeds are possible without the risk of ballast flight, thus emphasising the importance of the undercarriage aerodynamics on ballast flight. Among the parameters evaluated with regard to the risk of ballast flight, the undercarriage aerodynamics and the total length of the train set are the two most decisive parameters of the rolling stock. The combination of both is crucial with respect to the risk of ballast flight occurring. The ballast flight calculations for ballast particles ranging in size from 10-60 mm (the size range in a European trackbed and including crushed and fouled ballast) revealed that smaller particle sizes are more susceptible to ballast flight as they are more prone to flight (the flight path is proportional to A_B / V_B). The smaller train speed increase needed to increase the risk of ballast pitting ($Z = 235$ mm) to that of ballast particle impact with the train undercarriage ($Z = 500$ mm) confirmed that smaller ballast particles are more prone to flight. The fact that the smaller ballast particles are more susceptible to ballast flight incidents and that the ballast flight

impact risk quickly increases once the threshold train speed is exceeded highlights the importance of trackbed maintenance. Small (thus problematic) as well as crushed or fouled ballast particles need to be cleaned away. When the critical train speeds for the various ground configurations are compared, the constellation most susceptible to ballast flight is, by far, the exposed ballast particles on top of a concrete slab track close to the transition to a ballast trackbed. Since the trackbed transitions, however, only occur in limited numbers and since effective countermeasures can be easily applied to prevent ballast from being transported onto the slab track, this specific problem area is of no great concern. The data for the two more interesting ground configurations with respect to ballast flight, demonstrates that trackbeds without cross-going sleepers are more susceptible to ballast flight incidents than are trackbeds with cross-going sleepers and lowered ballast levels, despite the fact that ballast particles may initially be lying on top of sleepers. The reason for the rather unexpectedly high critical train speed values for ballast particles initially lying on top of sleepers (considered as the worst-case scenario) can be ascribed a) to the large momentum loss(es) from impact(s) with the trackbed and b) to the path of motion through the inter-sleeper region shielded from the stronger undercarriage flow by the protruding sleepers. Thus, even for ballast particles initially located on top of sleepers, higher train speeds are necessary for ballast particles to gain sufficient momentum to be transported over the first downstream sleeper. Based on undercarriage flow analysis, the critical train speeds calculated for the various train configurations confirmed the previous statements, namely, that the rough train model is the most susceptible train configuration to ballast flight incidents for all ground conditions. The conclusion can, therefore, be drawn that all cavities, bogies, bogie regions or any other geometric irregularities inducing local flow accelerations similar to those of the open bogie housings of the rough train model should be avoided 1) to thereby preclude faster undercarriage flow development, 2) to prevent early ballast particle dislodgement and 3) finally and most importantly, to reduce the overall aerodynamic forces on the trackbed ballast. The attempt should be made to reproduce the undercarriage flow of the smooth train model by aligning all elements of a train undercarriage, covering all cavities and gaps and, of course, avoiding all protrusions as far as technically possible. For, if this can be transformed into a technical reality, this will reduce the aerodynamic forces on the trackbed and at the same time facilitate higher train speeds without increasing the risk of ballast flight.

In conclusion, the varied level of influence of the ground roughness on the under-

carriage flow is strongly reflected when the critical train speeds for the reference and the rough train models are compared. Even though the risk of ballast flight is nearly the same for both models with respect to the smooth ground, in the case of the rough train model the results reveal that exposed ballast particles in inter-sleeper regions are more susceptible to ballast flight than are those initially located on top of sleepers for the reference train model. It, therefore, follows that the effects of ground roughness must be taken into account to guarantee more accurate risk assessment of ballast flight incidents.

9.2 Outlook

The results of the high-speed PIV of the undercarriage flow for the scale train models in the water-towing tank and the corresponding simplified ballast flight calculations revealed the potential and necessity for further studies of the ballast flight problem. Conducting a large number of runs in the water-towing tank would improve the uncertainty of the statistical measures presented, like the ensemble average and the standard deviation of the horizontal (u) and vertical (w) velocities. The extended undercarriage flow field data bank, however, allows more comprehensive statistical analysis as well as the identification of flow patterns and flow behaviour along an entire train length. The extended data bank of undercarriage flow field data could therefore be used to analyse and evaluate a method for describing instantaneous flow phenomena of a turbulent undercarriage flow field with the help of statistical quantities, e.g. the mean U velocity $\pm C \cdot U_{SD}$ with C as a weighted parameter. A description of the undercarriage flow using statistically quantities would be very practical and simplify accurate ballast flight risk assessment calculations. Additionally, greater accuracy of the statistical quantities would also be very useful for the validation of numerical calculations on highly turbulent undercarriage flows. Conducting a large number of runs in the water-towing tank is nonetheless a very time-consuming effort.

Aside from conducting more runs in the water-towing tank, additional train and ground configurations would also provide useful information regarding the ballast flight problem and the potential of scale train model experiments. One of the more interesting configurations that could be measured in the water-towing tank would be a train model with more detailed bogies that could reveal whether the differences to the results of full-scale measurements are due in large part to simplified geometries if not simply to Reynolds number differences. Additional measurements with rails

would also clarify whether the canalising effect of the rails has any considerable influence on the undercarriage flow field in the trackbed line of symmetry or whether the more practical ground configuration without rails is sufficient. Further measurements in the water-towing tank that could be of interest might address the ballast roughness effect in the inter-sleeper region for the ground with sleepers as well as the influence of different sleeper heights (or ballast levels) with respect to the overall drag of the trackbed.

The many physical simplifications and assumptions for the conducted calculations of the ballast flight problem (particle dislodgement, motion over the trackbed and flight) highlight the great need for further research regarding the risk assessment of ballast flight incidents. Determining empirical coefficients like the aerodynamic force and moment coefficients for different realistic ballast particle shapes as well as for the sliding and rolling friction coefficients for the different trackbed designs would improve the accuracy of the ballast flight risk assessment calculations. The aerodynamic force and moment coefficients should not only be determined for different ballast particle shapes, but for different angles of attack to the train-induced undercarriage flow as well in order to account for the influence of the ballast particle rotation during the transport over the trackbed. This clearly implies that the realistic influence of the Magnus effect should also be defined for different ballast particle shapes. The influence of the ground proximity on the aerodynamic force and moment coefficients as well as of the Magnus effect for the different ballast particle shapes should also be determined for different distances to the trackbed. Applying a friction coefficient describing the overall ballast particle momentum loss for the rolling motion and for the more realistic mixed rolling and bouncing motion is very practical for the calculation of the ballast particle motion over the trackbed. It is therefore of great interest to determine the dynamic friction coefficients or validate those used in this work to describe the overall ballast particle momentum loss during transport over different trackbed designs. Nevertheless, the static friction coefficients for ballast particles should also be validated or determined. An extension of the numerical simulations and ballast gun experiments conducted in the AOA-project would also be a reasonable approach to the evaluation of the influence of ballast particle rotation on ballast impacts with the trackbed, i.e. of the restitution coefficient, as the experiments of Buzzi et al. [140] showed increased values of the restitution coefficient for rotating objects. Furthermore, trackbed vibration induced by trains should be modelled more realistically than by the application of constant values as for the presented calcula-

tions, e.g. by simulating the full-scale observations of Quinn et al. [32] with both strong upward and downward accelerations around the train axles. The strong influence of the trackbed vibration, especially for the ballast particle dislodgement, clearly suggests that the trackbed vibration should be measured simultaneously to the flow for the high-speed train of interest.

Determining, correcting or validating the aforementioned empirical constants would result in more accurate calculations of critical train speeds for ballast flight incidents. It is informative to estimate the lowest critical train speeds that may create a danger of ballast flight incidents by assuming worst-case scenarios for all physical subprocesses of the ballast flight problem. Still, the calculation of event probabilities for ballast flight incidents is still needed to assess the true risk and for the definition of maximum allowable train speeds. The probability of a ballast flight incident is best found by comprehensive stochastic calculations (e.g. Monte Carlo techniques) that model ballast particle shape, size and position as well as possible angles and directions of the ballast particle after upward deflection from the trackbed. With realistic empirical coefficients and constants as well as results from comprehensive stochastic ballast flight calculations, it may likely be possible to deduce simple methods well-suited for railway operators and train manufactures wishing to realistically assess the risk of ballast flight incidents given different damage tolerances.

References

- [1] Lee, T., Park, C., Kim, S., C., A study of the train performance simulation for Korean next generation high-speed train, In Proceedings of the 9th World Congress on Railway Research, Lille, France, 22-26 May, 2011.
 - [2] Davis W.J., The tractive resistance of electric locomotives and cars, *General Electric Review*, vol. 29, October 1926.
 - [3] Schetz, J.A., Aerodynamics of high-speed trains, *Annu. Rev. Fluid Mech.*, 33:371-414, 2001.
 - [4] Givoni, M., Development and impact of the modern high-speed train: a review, *Transport Reviews*, Vol. 26, No. 5, p. 593-611, September, 2006.
 - [5] Wennberg, D., Light-weighting methodology in rail vehicle design through introduction of load carrying sandwich problems, Licentiate thesis, TRITA AVE 2011:36, ISSN 1651-7660, ISBN 978-91-7501-002-1, Royal Institute of Technology (KTH), 2011.
 - [6] Winter, J., Novel rail vehicle concepts for a high speed train: the next generation train. Paper 22 in the Proceedings of the First International Conference on Railway Technology: Research, Development and Maintenance, Las Palmas de Gran Canaria, Spain, April 18-20, 2012.
 - [7] Kurzeck, B. and Valente, L., A novel mechatronic running gear: concept, simulation and scaled roller rig testing, In the proceedings of the EU FP7 AeroTRAIN project and first results. In Proceedings of the 9th World Congress on Railway Research, Lille, France, 22-26 May, 2011.
 - [8] Sandor, J., Wiebe, E., Bergendorff, M., Recagne, V., Nolte, R., Smart and efficient energy solutions for railways. The "Railenergy" results ,In the proceedings of the EU FP7 AeroTRAIN project and first results. In Proceedings of the 9th World Congress on Railway Research, Lille, France, 22-26 May, 2011.
 - [9] China introduces first light-rail train with new-energy fuel cells. *People's Daily* ,November 29, 2010.
 - [10] Cornic, D., Efficient recovery of braking energy through a reversible dc substation, In the proceedings of the EU FP7 AeroTRAIN project and first results. In Proceedings of the 9th World Congress on Railway Research, Lille, France, 22-26 May, 2011.
-

- [11] Liudvinavicius, L. and Lingaitis, L.P., Electrodynamic braking in high-speed rail transport, *TRANSPORT*, Vol. 22, No. 3, p.178-186, 2007.
- [12] Mair, W.A., and Stewart, A.J., The flow past yawed slender bodies with and without ground effect, *Journal of Wind Engineering and Industrial Aerodynamics*, Vol. 18, No. 301, 1985.
- [13] Copley, J.M., The 3-D flow around railways trains, *Journal of Wind Engineering and Industrial Aerodynamics*, Vol. 26, No. 21, 1987.
- [14] Chiu, T., An experimental study of the flow over a train in a crosswind at large yaw angles up to 90° , *Journal of Wind Engineering Industrial Aerodynamics*, Vol. 45, p. 47-74, 1992.
- [15] Diedrichs, B., Computational methods for crosswind stability of railway trains. Sciences report TRITA-AVE report 2005:27, Department of Aeronautical and Vehicle Engineering, Royal Institute of Technology (KTH), Stockholm, Sweden, 2005.
- [16] MacNeill, R.A., Holmes, S., Lee, H.S., MEASUREMENT OF THE AERODYNAMIC PRESSURES PRODUCED BY PASSING TRAINS, In the Proceedings of the 2002 ASME/IEEE Joint Rail Conference Washington, DC, April 23-25, 2002.
- [17] Kikuchi, K., Tanaka, Y., Iida, M., Yamauchi, N., Yoshida, Y., Nakanishsi, M., Takahashi, R.I., Countermeasures for Reducing Pressure Variation due to Train Passage in Open Sections, *Quarterly Reports of RTRI*, Vol. 42, No. 2, p. 77-82, May, 2001.
- [18] Baker, C.J., Dalley, S.J., Johnson, T., Quinn, A., Wright, N.G., The slipstream and wake of a high-speed train, *Proc. IMechE, Part F: J. Rail and Rapid Transit*, Vol. 215, p. 83-99, 2001. doi: 10.1243/0954409011531422.
- [19] Sterling, m., Baker, C.J., Jordan, S.C., Johnson, T., A study of the slipstreams of high-speed passenger trains and freight trains, *Proc. IMechE, Part F: J. Rail and Rapid Transit*, Vol. 222, p. 177-193, 2008. doi: 10.1243/09544097JRRT133.
- [20] Muld, T.W., Slipstream and flow structures in the near wake of high-speed trains, PhD Thesis, TRITA-AVE report 2012:28, Department of Aeronautical and Vehicle Engineering, Royal Institute of Technology (KTH), Stockholm, Sweden, 2012.
- [21] Endoh, H., Omino, K., Shiroto, H., Sawa, M., Tanemoto, K., Takei, Y., Tolerance Estimation of Human Postural Stability against Train Drafts, *Quarterly Reports of RTRI*, Vol. 50, No. 1, p. 49-55, February, 2009.
-

-
- [22] Raghunathan, R.S., Kim, H.D., Setoguchi, T., Aerodynamics of high-speed railway train, *Progress in Aerospace Sciences* 38, p. 469-514, 2002.
- [23] Howe, M.S., Iida, M., Fukuda T., Maeda, T., Theoretical and experimental investigation of the compression wave generated by a train entering a tunnel with flared portal, *Journal of Fluid Mechanics*, Vol. 425, p. 111-132, 2000.
- [24] Suzuki, M., Unsteady Aerodynamic Force Acting on High Speed Trains in Tunnel, *Quarterly Reports of RTRI*, Vol. 42, No. 2, p. 89-93, May, 2001.
- [25] Loose, S., Lauterbach, A., Algermissen, S., Heckmann, A., Next Generation Train - Activities in Acoustics, *RTR Rail Technology Review*, p. 51-60, ISBN: 978-3-7771-0435-5, 2011.
- [26] Giusti, A., Bianchini, C., Facchini, B., Andreini, A., Grazzini, F., Bellini, D., Chiti, F., Large Eddy Simulation for Train Aerodynamic Noise Predictions, In *Proceedings of the 9th World Congress on Railway Research*, Lille, France, 22-26 May, 2011.
- [27] Sueki, T., Ikeda, M., Takaishi, T., Aerodynamic Noise Reduction using Porous Materials and their Application to High-speed Pantographs, *Quarterly Reports of RTRI*, Vol. 50, No. 1, p. 26-31, February, 2009.
- [28] Ikeda, M., Mitsumoji, T., Sueki, T., Takaishi, T., Aerodynamic Noise Reduction in Pantographs by Shape-smoothing of the Panhead and Its Support and by Use of Porous Material in Surface Coverings, *Quarterly Reports of RTRI*, Vol. 51, No. 4, p. 220-226, November, 2010.
- [29] Kwon, H.B., and Park, C.S., An Experimental Study on the Relationship between Ballast-flying Phenomenon and Strong Wind under High-speed Train. In *Proceedings of the 7th World Congress on Railway Research*, Montreal, Canada, June 4-8, 2006.
- [30] Bagnold, R.A., *The physics of blown sand and desert dunes*. London: Methuen, 1941.
- [31] Lazaro, B.J., Gonzales, E., Rodriguez, Ma., Rodriguez, Mi., Osma, S. and Iglesias, J., Characterization and Modelling of Flying Ballast Phenomena in High-speed Train Lines. In *Proceedings of the 9th World Congress on Railway Research*, Lille, France, 22-26 May, 2011.
- [32] Quinn, A.D., Hayward, M., Baker, C.J., Schmid, F., Priest, J.A., Powrie, W., A full-scale experimental and modelling study of ballast flight under high-speed
-

- trains. Proc. IMechE, Part F: J. Rail and Rapid Transit, vol. 224, p. 61-74, 2009. doi: 0.1243/09544097JRRT294.
- [33] Schroeder-Bodenstein, K., Ballast Pick-Up, International Experiences with Highspeed-Trains: Observations, Physics and Counter-Measures. In Proceedings of the Bahntechnik Aktuell, Band 25, 2010, pp. 59 -74, Berlin, Germany, 24-25 Februar, 2010.
- [34] Wüst, C., Steinschlag von unten. DER SPIEGEL, Nr. 36, 2005.
- [35] Gautier, P.E., Poisson, F., Barcena, S. and Josse, F., TGV AT 360 KM/H: A RESEARCH PROGRAM FOLLOWING A TEST CAMPAIGN. In Proceedings of the 9th World Congress on Railway Research, Lille, France, 22-26 May, 2011.
- [36] Ido, A., Saitou, S., Nakade, K. and Iikura, S., Study on under-floor flow to reduce ballast flying phenomena. In Proceedings of the 8th World Congress on Rail research, Seoul, South Korea, 18-22 May, 2008.
- [37] Claus, P., Prestudy of Ballast Projection Incidents, Internal project report WP 1.2, DeuFraKo Project Aerodynamics in Open Air (AOA), 2007.
- [38] Weise, M. Schotterflugthematik: Einflussgrößen und Modellansätze. Proceedings of the Bahntechnik Aktuell, Band 25, 2010, pp. 47 - 57, Berlin, Germany, 24-25 Februar, 2010.
- [39] Sima, M., CFD investigation (RANS) of the ICE 3 mid-coach, Internal project report, WP 1.1 General flow field (CFD), DeuFraKo project Aerodynamics in Open Air (AOA), 2008.
- [40] Rüter, A., ICE 3 First Bogie CFD Results, Internal project report, WP 1.1 General flow field (CFD), DeuFraKo project Aerodynamics in Open Air (AOA), 2007.
- [41] Kaltenbach H. J., Gautier P.E., Agirre G., Orellano A., Schreoder-Bodenstein K., Testa M., Tielkes Th., Assessment of the aerodynamic loads on the trackbed causing ballast projection: results from the DEUFRAKO project Aerodynamics in Open Air (AOA). In the proceedings of the 8th World Congress on Railway Research (WCRR), paper 0738, Seoul, South Korea, May 18-22, 2008.
- [42] Rießberger, K., Schottergleise für hohe Geschwindigkeiten, Eisenbahntechnische Rundschau, October, 2007.
- [43] Knothe, K. Systemdynamik und Langzeitverhalten von Schienenfahrzeugen, Gleis und Untergrund, ZEVrail-Glasers Annalen 131, April, 2007.
-

-
- [44] Shinojima, K., Study on the Phenomena of Snow Adhering to and Dropping from Shinkansen Train, and the Countermeasures. Quarterly Reports of Railway Technical Research Institute, Vol. 25, No. 2, p. 41-44, 1984.
- [45] Felsing, A., Aufwirbeln von Schottersteinen durch herabfallende Eisbrocken von schnellen Reisezügen - Auswirkungen und Schutzmassnahmen. In ORE Kolloquium: Eisenbahnbetrieb bei Winterbedingungen, Basel, Switzerland. November 2 - 3, 1982.
- [46] Sima, M., Grappein, E., Weise, M., Paradot, N., Hieke, M., Baker, C., Licciardello, R., and Couturier, M., Presentation of the EU FP7 AeroTRAIN project and first results. In Proceedings of the 9th World Congress on Railway Research, Lille, France, 22-26 May, 2011.
- [47] Deeg, P., Jönsson, M., Kaltenbach, H.J., Schober, M., Weise, M., Cross-Comparison of Measurement Techniques for the determination of train induced Aerodynamic Loads on the trackbed. In Proceedings of the BBAA VI Conference, Milan, Italy, July 20 - 24, 2008.
- [48] Sorribes, F., Navarro-Medina, F., Sanz-Andrés, A., Perez-Grande, I., Martinez, A., Vega, E., Mascaraque, A., Rodriguez-Plaza, M., Iglesias-Dia, I.J., Andres-Alguacil, A. and Alonso-Gimeno, D., Criteria for Ballast Flight Initiation Induced by High Speed Trains. Paper 103 in the Proceedings of the First International Conference on Railway Technology: Research, Development and Maintenance, Las Palmas de Gran Canaria, Spain, April 18-20, 2012.
- [49] Saussine, G., Allain, E., Paradot, N., and Gaillot, V., Ballast Flying Risk Assessment Method for High Speed Line. In Proceedings of the 9th World Congress on Railway Research, Lille, France, 22-26 May, 2011.
- [50] Saussine, G., Masson, E., Thomas-Jean, J., Paradot, N., Allain, E. and Josse, F., Railway ballast flying phenomena: from numerical computations toward risk assessment. In Euromech Proceedings EUROMECH COLLOQUIUM 509: Vehicle Aerodynamics - External Aerodynamics of Railway Vehicles, Trucks, Buses and Cars, Berlin, Germany, pp. 269-280, 24-25 March, 2009.
- [51] Deeg, P., Kaltenbach, H.J., Schuster, P., Weise, M. and Jönsson, M., Trackside Measurements on the Line Rome - Florence, Internal project report WP 1.4, DeuFraKo Project Aerodynamics in Open Air (AOA), 2008.
-

- [52] Jacobs, W., Umformung eines turbulenten Geschwindigkeitsprofil, *Z. angew. Math. Mech.*, Bd. 19, Nr. 2 April, p. 87-100, 1939.
- [53] Weise, M., Licciardello, R., Output Document - TSI and CEN norm text proposal for evaluation method and limit for aerodynamic loads on track, AeroTRAIN project report, WP2 - Aerodynamic Loads on Tracks, AeroTRAIN project part of TrioTRAIN project, 2012.
- [54] Ido, A., Yoshihiko, K., Matsumara, T., Suzuki, M., Maeda T., Wind Tunnel Tests to Reduce Aerodynamic Drag of Trains by Smoothing the Under-floor Construction. *Quarterly Reports RTRI*, vol. 42, No. 2, p. 94-97, May, 2001.
- [55] Ido, A. and Yoshioka, S., Development of a Model Running Facility for a Study on under-floor Flow. *Journal of Mechanical Systems for Transportation and Logistics*, Vol.3, No. 1, pp 294-304, 2010.
- [56] Schlichting, H., *Boundary-Layer Theory*, Seventh Edition, McGraw-Hill Book Company, 1979.
- [57] Schitthelm, A., Analysis and Optimization of the Flow underneath a High Speed Train in relation to Ballast Projection. Thesis work 854 at the Chair of Fluid Dynamics, Institute of Fluid Dynamics and Technical Acoustics, Technical University of Berlin, 2008.
- [58] Kaltenbach H.J., Alonso-Portillo, I. and Schober, M., A generic train-underfloor experiment for CFD validation. In *Proceedings of the BBAA VI Conference*, Milan, Italy, July 20 - 24, 2008.
- [59] Sima, M., Gurr, A., Orellano A., VALIDATION OF CFD FOR THE FLOW UNDER A TRAIN WITH 1:7 SCALE WIND TUNNEL MEASUREMENTS. In *Proceedings of the BBAA VI Conference*, Milan, Italy, July 20 - 24, 2008. <http://bbaa6.mecc.polimi.it/uploads/treni/bpr03.pdf>
- [60] Garcia, J., Crespo, A., Alonso, I., Gimenez, G., Estimation of the flow characteristics between the train underbody and the ballast track. In *Proceedings of the BBAA VI Conference*, Milan, Italy, July 20 - 24, 2008.
- [61] Rocchi, D., Results of RANS simulation on the ETR500 train, Internal project report, WP 1.1 General flow field (CFD), DeuFraKo project Aerodynamics in Open Air (AOA), 2008.
- [62] Masson, E., Allain, E., Paradot, N., CFD ANALYSIS OF THE UNDERFLOOR AERODYNAMICS OF A COMPLETE "TGV" HIGH SPEED TRAIN SET AT FULL
-

-
- SCALE. In *Euromech Proceedings EUROMECH COLLOQUIUM 509: Vehicle Aerodynamics - External Aerodynamics of Railway Vehicles, Trucks, Buses and Cars*, Berlin, Germany, pp. 188-203, 24-25 March, 2009.
- [63] Jönsson, M., Numerical Investigation of the Flow Underneath a Train and the Effect of Design Changes. Master thesis work at the Division of Fluid Mechanics, Department of Applied Physics and Mechanical Engineering, Luleå University of Technology, Sweden, 2007. <http://pure.ltu.se/portal/files/31032814/LTU-EX-07079-SE.pdf>.
- [64] Saussine, G. and Paradot, N., Full scale tests on ballast track in wind tunnel, Internal project report, WP 1.2 Ballast Projection, DeuFraKo project Aerodynamics in Open Air (AOA), 2007.
- [65] Kaltenbach, H.J., Eisenlauer, M., Deeg, P., Investigation of particle dislodgement from a ballasted trackbed in scale 1:10, Internal project report, WP 1.2 Ballast Projection, DeuFraKo project Aerodynamics in Open Air (AOA), 2007.
- [66] Kind, R.J., Measurement in small wind tunnels of wind speeds for gravel scour and blowoff from rooftops. *Journal of Wind Engineering and Industrial Aerodynamics*, vol. 23, p. 223-235, 1986.
- [67] Sanz-Andrés, A. and Navarro-Medina, F., The initiation of rotational motion of a lying object caused by wind gusts. *Journal of Wind Engineering and Industrial Aerodynamics*, vol. 98, Nr. 12, p. 772-783, 2010.
- [68] Schroeder-Bodenstein, K., Ballast Gun Experiments, Internal project report, WP 1.2 Ballast projection, DeuFraKo project Aerodynamics in Open Air (AOA), 2007.
- [69] Saussine, G. and Paradot, N., Numerical analysis of the collision process between ballast grains and ballast bed, Internal project report, WP 1.2 Ballast projection, DeuFraKo project Aerodynamics in Open Air (AOA), 2007.
- [70] Kawashima, K., Iikura, S., Endo, T., Fujii, T., Experimental study on ballast-flying phenomenon caused by dropping of accreted snow/ice from high-speed trains, *Quarterly Reports of Railway Technical Research Institute (in Japanese)*, 2003.
- [71] Sanz-Andrés, A. and Navarro-Medina, F., The ballast pick-up problem in high speed trains, In the proceedings of the 5th International Scientific Conference "Theoretical and Practical Issues in Transport", Pardubice, Czech Republic, February 11-12, 2010.
-

- [72] Baker, C.J., The debris flight equations, *Journal of Wind Engineering and Industrial Aerodynamics*, vol. 95, No. 5, p. 329-353, 2007.
- [73] Holmes, J.D., Baker, C.J. and Tamura, Y., Tachikawa number: a proposal, *Journal of Wind Engineering and Industrial Aerodynamics*, vol. 94, No. 1, p. 41-47, 2006.
- [74] Hayward, M., Investigating the phenomena of ballast pitting on HS1, *Railway Gazette International*, p. 43-46, June, 2009.
- [75] Rüter, A., Modelling of ballast projection, Internal project report, WP 1.2 Ballast Projection, DeuFraKo Project Aerodynamics in Open Air (AOA), 2007.
- [76] Papenfuss, H.D. and Kronast, M., Moving-model technique used in automobile aerodynamics for measurement of ground effects, *Experiments in Fluids* 11, p. 161-166, 1991.
- [77] Eckelmann, H. (1997) *Einführung in die Strömungsmeßtechnik*, B.G. Teubner, Stuttgart
- [78] Tropea, C., Yarin, A.L., Foss, J.F., *Springer Handbook of Experimental Fluid Mechanics*, Berlin: Springer-Verlag Berlin Heidelberg, 2006.
- [79] Nitsche, W. and Brunn, A., *Strömungsmesstechnik 2 Auflage*, Berlin: Springer-Verlag Berlin Heidelberg, 2006.
- [80] Raffel, M., Willert, C.E., Wereley, S.T., Kompenhans, J., *Particle Image Velocimetry*, 2nd ed. Berlin: Springer-Verlag Berlin Heidelberg, 2007.
- [81] Arroyo, M.P and Greated, C.A., Stereoscopic particle image velocimetry. *Meas. Sci. Tech.*, 2, pp. 1181-1186, 1991.
- [82] Raffel, M., Westerwel, J., Willert, C., Gharib, M., Kompenhans J., Analytical and experimental investigations of dual-plane particle image velocimetry, *Optical Engineering*, 35, pp. 2067-2074, 1996.
- [83] Meng, H., Pan, G., Pu, Y., Woodward, S.H., Holographic particle image velocimetry: from film to digital recording, *Measurement Science and Technology*, vol. 15, pp. 673-685, 2004.
- [84] Elsinga, G.E., Scarano, F., Wieneke, B., Oudheusden van, B.W., Tomographic particle image velocimetry, *Experiments in Fluids*, vol. 41, pp. 933-947, 2006.
- [85] Santiago, J.G., Wereley, S.T., Meinhart, C.D., Beebe, D.J., Adrian, R.J., A particle image velocimetry system for microfluidics, *Exp. Fluids*, 25, pp. 316-319, 1998.
-

-
- [86] Dierksheide, U., Meyer, P., Hovestadt, T., Hentschel, W., Endoscopic 2D particle image velocimetry (PIV) flow field measurements in IC engines, *Experiments in Fluids*, 33, Berlin: Springer-Verlag, 2002.
- [87] Prasad, A.K., Particle image velocimetry, *Current Science*, vol. 79, No. 1, 10 July 2000.
- [88] Melling, A., Tracer particles and seeding for particle image velocimetry, *Meas. Sci. Technol.* 8, pp. 1406-1416, 1997.
- [89] Echols W.H. and Young J.A., Studies of portable air-operated aerosol generators, NRL Report 5929, Naval Research Laboratory, Washington D.C., 1963.
- [90] Willert, C., Moessner, S., Klinner, L., Pulsed Operation of High Power Light Emitting Diodes for Flow Velocimetry, In proceedings of 8th International symposium on particle image velocimetry - PIV 09, Melbourne, Australia, 25-28 August, 2009.
- [91] Estevadeordal, J. and Goss, L., PIV with LED: Particle Shadow Velocimetry (PSV), In proceedings of 43rd AIAA Aerospace Sciences Meeting and Exhibit, p. 12355-12364, 10-13 January, 2005.
- [92] Hain, R., Kähler, C.J., Tropea, C., Comparison of CCD, CMOS and intensified cameras, *Experiments in Fluids* 42, p. 403-411, 2007.
- [93] Gad-el-Hak, M., The water towing tank as an experimental facility: An Overview, *Experiments in Fluids* 5, p. 289-297, 1987.
- [94] Technical Specification for Interoperability (TSI) relating to the rolling stock subsystem of the trans-European high-speed rail system (2008/232/CE), 2008.
- [95] Jönsson, M., Wagner, C., Loose, S., Particle image velocimetry of the under-floor flow of generic high-speed train models in a water towing tank, *Proc. IMechE, Part F: J. Rail and Rapid Transit*, Vol. 228, Issue 2, pp. 194-209, 2014. doi: 10.1177/0954409712470607.
- [96] Jönsson, M., Wagner, C., Loose, S., Underfloor flow measurements of 1:50 generic high-speed train configurations for different ground conditions in a water towing tank, *The International Journal of Railway Technology*, Vol. 1, Issue 4, pp. 85-113, 2014, doi: 10.4203/ijrt.1.4.5
- [97] Aerodynamic Influences Of Vehicle Design On Wheel/Rail Contamination, Research Brief T546, Rail Safety & Standard Board (RSSB), September, 2007.
- [98] DIN EN 13450:2002 Aggregates for railway ballast, 2002.
-

- [99] Knothe, K. and Stichel, S., *Schienenfahrzeugdynamik*, Berlin: Springer, 2003.
- [100] PIVview 2C/3C User Manual, Version 2.4, PIVTec, 2006.
- [101] Adrian, R.J. and Westerweel, J., *Particle Image Velocimetry*, vol. 1, New York, USA, Cambridge University Press, 2011.
- [102] Harris, J.R., Investigation of relative importance of some error sources in particle image velocitmetry, University report, Utah State University, 2012.
- [103] Westerweel, J., Dabiri, D., Gharib, M., The effect of a discrete window offset on the accuracy of cross-correlation analysis of digital PIV recordings, *Experiments in Fluids* 23, p. 20-28, 1997.
- [104] Nobach, H., Damaschke, N., Tropea, C., High-precision sub-pixel interpolation in PIV/PTV image processing, *Proceedings of the 12th International Symposium on Applications of Laser Techniques to Fluid Mechanics*, 12-15 July, Lisbon, Portugal, 2004.
- [105] Kundu, P.K and Cohen, I.M., *FLUID MECHANICS*, third edition, San Diego, USA: Elsevier Academic Press, 2004.
- [106] Quinn, A. and Hayward, M., Full-scale aerodynamic measurements underneath a high speed train. In *Proceedings of the BBAA VI Conference*, Milan, Italy, July 20 - 24, 2008.
- [107] Gloerfelt, X., *Cavity noise*, VKI Lectures: Aerodynamic noise from wall-bounded flows, Von Karman Institute, 2009.
- [108] Sigloch, H., *Technische Fluidmechanik*, 7 Auflage, Berlin: Springer, 2009.
- [109] Vännman, K., *Matematisk statistik 2 upplagan*, Lund: Studentlitteratur AB, 2002.
- [110] Hucho, W.H., *Aerodynamik der stumpfen Körper: Physikalische Grundlagen und Anwendungen in der Praxis*, 2 Auflage, Wiesbaden: Vieweg+Teubner, 2011.
- [111] Cui, J., Patel, V.C., Lin, C.L., Large-eddy simulation of turbulent flow in a channel with rib roughness, *International Journal of Heat and Fluid Flow* 24, p. 372-388, 2003.
- [112] Guler, H. and Mert, N., A Comparative Analysis of Railway Ballast. Paper 132 in the *Proceedings of the First International Conference on Railway Technology: Research, Development and Maintenance*, Las Palmas de Gran Canaria, Spain, April 18-20, 2012.
-

-
- [113] Rotta, J. C., 1950 Das in Wandnähe gültige Geschwindigkeitsgesetz turbulenter Strömungen, *Ing. -Arch.* 18, p. 277-280, 1950.
- [114] Mohrig, D., Conservation of Mass and Momentum, 12.110: *Sedimentary Geology*, 2004.
- [115] Schultz, M. P. and Flack, K. A., The rough-wall turbulent boundary layer from the hydraulically smooth to the fully rough regime, *Journal of Fluid Mechanics*, vol. 580, p. 381-405, 2007. doi: 10.1017/S0022112007005502
- [116] Jiménez, J., Turbulent Flows over Rough Walls, *Annu. Rev. Fluid Mech.* 36, p. 17396, 2004. doi: 10.1146/annurev.fluid.36.050802.122103
- [117] Clauser, F. H., Turbulent boundary layers in adverse pressure gradients, *Journal of Aeronautical Science* 21, p. 91-108, 1954.
- [118] Hama, F. R., Boundary-layer characteristics for rough and smooth surfaces, *Transactions SNAME* 62, p. 333-351, 1954.
- [119] Baron, A. and Quadrio, M., On the Accuracy of Wall Similarity methods in Determining Friction Velocity Over Smooth and Ribletted Surfaces, *Journal of Fluids Engineering: Technical Brief*, Vol. 119, p. 1009-1011, 1997.
- [120] Nikuradse, J., Strömungsgesetze in Rauhen Rohren, *VDI-Forschung* 361, 1933.
- [121] Colebrook, C. F., Turbulent flow in pipes with particular reference to the transition region between the smooth- and the rough-pipe laws, *J. Inst. Civil Eng.* 11, p. 133-156, 1939.
- [122] Nickling, W. G., The initiation of particle movement by wind, *Sedimentology*, Vol. 35, Issue 3, p. 499-511, 1988.
- [123] Bisal, F. and Nielsen, K.C., Movement of soil particles in saltation, *Canadian Journal of Soil Science* 42, pp. 81-86, 1962.
- [124] Hoerner, S.F., *Fluid-dynamic drag: Practical information on aerodynamic drag and hydrodynamic resistance*, 1958.
- [125] Saussine, G., Allain, E., Vaillant, A., Ribourg, M., Néel, O., High speed in extreme conditions: ballast projection phenomenon, In proceedings of International Workshop on Railway Aerodynamics, University of Birmingham, Great Britain, April 8-10, 2013.
- [126] Stein, D., Möllers, K., Bielecki, R., *Microtunneling, Installation and renewal of*
-

- non man - size supply and sewage lines by the trenchless construction method, Ernst Sohn, Berlin, Germany, 1989.
- [127] Odar, F. and Hamilton, W.S., Forces on a sphere accelerating in a viscous fluid, *Journal of Fluid Mechanics*, vol. 18, issue 2, 1964.
- [128] Sanz-Andrés, A., Laverón, A., Cuerva, A., Baker, C., Vehicle-induced force on pedestrians, *Journal of Wind Engineering and Industrial Aerodynamics*, Vol. 92, Issue 2, p. 185-198, 2004.
- [129] Baker, C., The flow around high speed trains, *Journal of Wind Engineering and Industrial Aerodynamics*, Vol. 98, Issue 6, p. 277-298, 2010.
- [130] Bozzolo, D and Pamini, R., Simulation of rock falls down a valley side, *Acta Mechanica* 63, p. 113-130, 1986.
- [131] Azzoni, A. and Freitas, M. H., Experimentally gained parameters, decisive for rock fall analysis, *Rock Mechanics and Rock Engineering*, Vol. 28, Issue 2, p. 111-124, 1995.
- [132] Dorren, L. K. A., A review of rockfall mechanics and modelling approaches, *Progress in Physical Geography* 27, Vol. 1, p. 69-87, 2003.
- [133] Petje, U., Mikos, M., Majes, B., Motion of rock masses on slopes, *GEOLOGIJA*, Vol. 49, Issue 2, p. 393-408, 2006. doi: 10.5474/geologija.2006.028
- [134] Statham, I., A simple dynamic model of rockfall: some theoretical principles and model and field experiments, *International Colloquium on physical and geomechanical Models*, ISMES, Bergamo, Italy, 1979.
- [135] Azzoni, A. La Barbera, G., Zaninetti, A., Analysis and prediction of rock falls using a mathematical model, *International Journal of Rock Mechanics and Mining Science*, Vol. 32, No. 7, p. 709-724, 1995.
- [136] Kenserud, J. R., Determining aerodynamic properties of sports balls in situ, Master thesis work at Washington State University, USA, 2010.
- [137] Abramowski, T., Numerical investigation of airfoil in ground proximity, *Journal of Theoretical and Applied Mechanics*, Vol. 45, Issue 2, p. 425-436, 2007.
- [138] Halloran, M. and O'Meara, S., Wing in ground effect craft review, Contract report DSTO-GD-0201 for the Department of Defence Science & Technology Organisation (DSTO) of Australia, The Sir Lawrence Wackett Centre for Aerospace Design Technology, Royal Melbourne Institute of Technology, 1999.
-

-
- [139] Malavasi, S. and Guadagnini, A., Interactions between a rectangular cylinder and a free-surface flow, *Journal of Fluids and Structures*, Vol. 23, p. 1137-1148, 2007.
- [140] Buzzi, O., Giacomini, A., Spadari, M., Laboratory investigations on high values of restitution coefficients, *Rock Mechanics and Rock Engineering*, Vol. 45, Issue 1, p. 35-43, 2011, DOI: 10.1007/s00603-011-0183-0.
- [141] Cannon, D. F., Edel, K. O., Grassie, S. L., Sawley, K., Rail defects: an overview, *Fatigue & Fracture of Engineering Materials & Structures*, Vol. 26, Issue 10, p. 865-886, 2003.
-

Appendix

Appendix A: The reference train model

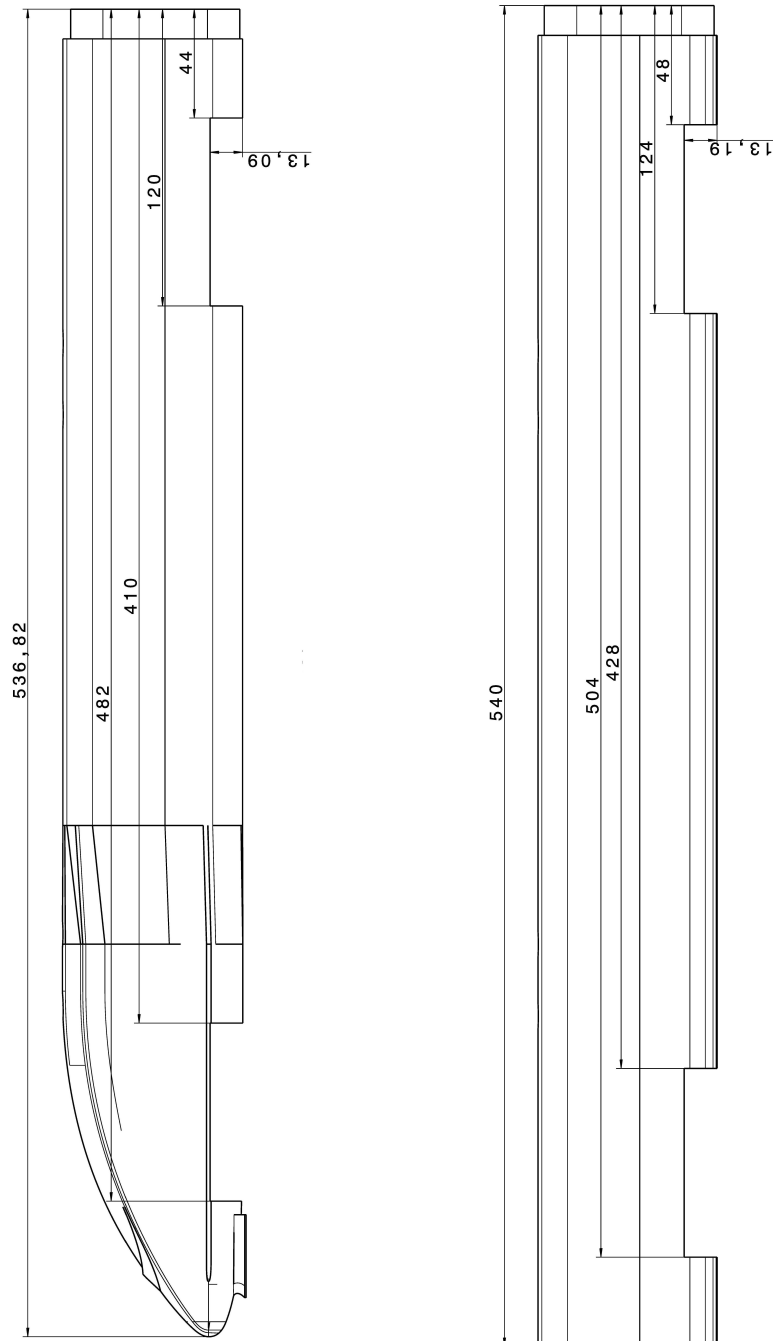


Figure A1: Dimensions of the end-car (left) and the mid-car (right) for the 1:50 reference train model (T.C. 1) for the water-towing tank experiments [mm].

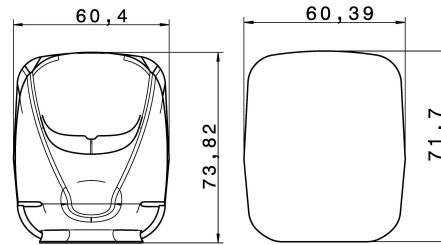


Figure A2: Dimensions of the end-car (left) and the mid-car (right) for the 1:50 reference train model (T.C. 1) [mm].

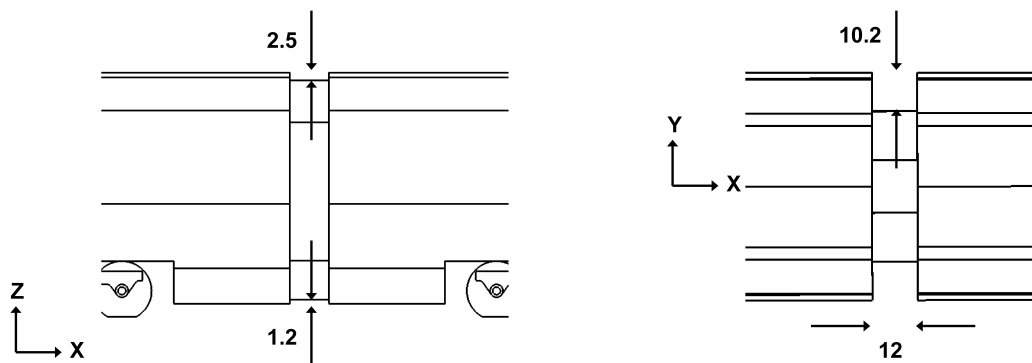


Figure A3: Dimensions of the inter-car gap region for the 1:50 reference train model (T.C. 1) [mm].

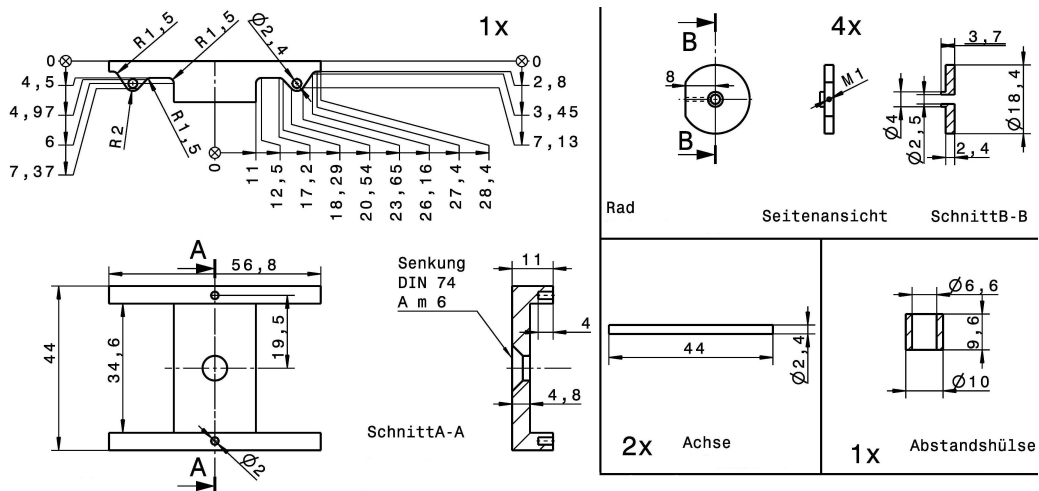


Figure A4: Drawings of the 1:50 simplified bogie for the reference train model (T.C. 1) [mm].

Appendix B: Spatial horizontal averages of the undercarriage flow field

Spatial horizontal averages between the first and last train axles.

T.C.	G.C.	U / U_{TRAIN}	W / U_{TRAIN}	U_{SD} / U_{TRAIN}	W_{SD} / U_{TRAIN}
1	A	0.2381	0.0020	0.0583	0.0170
2	A	0.0871	0.0015	0.0314	0.0094
3	A	0.2519	0.0019	0.0880	0.0202
1	B	0.1817	0.0036	0.0593	0.0224
2	B	0.0768	0.0014	0.0320	0.0121
3	B	0.2170	0.0015	0.0868	0.0268
1	C1	0.0981	0.0020	0.0493	0.0203
2	C1	0.0553	0.0002	0.0277	0.0118
3	C1	0.1281	0.0028	0.0666	0.0255
1	C2	-	-	-	-
2	C2	-	-	-	-
3	C2	-	-	-	-

Table B1: Spatial averages between the first and last train axles for the normalised mean U and W velocities and their corresponding velocity fluctuations U_{SD} and W_{SD} at the height of $TOR \times 0.125$ ($Z / H_{GAP} = 0.059$) for the reference (T.C. 1), smooth (T.C. 2) and the rough train model (T.C. 3) on the smooth ground (G.C. A), rough ground (G.C. B), between sleepers (G.C. C1) and above sleeper (G.C. C2). $U_{TRAIN} = 4$ m/s.

T.C.	G.C.	U / U_{TRAIN}	W / U_{TRAIN}	U_{SD} / U_{TRAIN}	W_{SD} / U_{TRAIN}
1	A	0.2718	0.0018	0.0583	0.0200
2	A	0.1072	0.0011	0.0337	0.0116
3	A	0.2883	0.0010	0.0918	0.0265
1	B	0.1979	0.0028	0.0610	0.0258
2	B	0.0854	0.0008	0.0335	0.0138
3	B	0.2342	0.0010	0.0898	0.0339
1	C1	0.1389	0.0033	0.0618	0.0257
2	C1	0.0799	-0.0006	0.0356	0.0143
3	C1	0.1792	0.0035	0.0830	0.0311
1	C2	0.1279	0.0017	0.0741	0.0267
2	C2	0.0679	0.0013	0.0399	0.0140
3	C2	0.1634	0.0011	0.0968	0.0292

Table B2: Spatial averages between the first and last train axles for the normalised mean U and W velocities and their corresponding velocity fluctuations U_{SD} and W_{SD} at the height of $TOR \times 0.25$ ($Z / H_{GAP} = 0.119$) for the reference (T.C. 1), smooth (T.C. 2) and the rough train model (T.C. 3) on the smooth ground (G.C. A), rough ground (G.C. B), between sleepers (G.C. C1) and above sleeper (G.C. C2). $U_{TRAIN} = 4$ m/s.

T.C.	G.C.	U / U_{TRAIN}	W / U_{TRAIN}	U_{SD} / U_{TRAIN}	W_{SD} / U_{TRAIN}
1	A	0.3013	0.0030	0.0609	0.0260
2	A	0.1277	0.0015	0.0377	0.0156
3	A	0.3176	0.0016	0.0951	0.0371
1	B	0.2267	0.0037	0.0658	0.0315
2	B	0.1030	0.0008	0.0383	0.0176
3	B	0.2607	0.0010	0.0952	0.0436
1	C1	0.2076	0.0078	0.0736	0.0284
2	C1	0.1187	0.0006	0.0440	0.0162
3	C1	0.2564	0.0054	0.0967	0.0375
1	C2	0.2432	0.0091	0.0715	0.0286
2	C2	0.1371	0.0034	0.0441	0.0164
3	C2	0.2951	0.0044	0.1000	0.0358

Table B3: Spatial averages between the first and last train axles for the normalised mean U and W velocities and their corresponding velocity fluctuations U_{SD} and W_{SD} at the height of $TOR \times 0.5$ ($Z / H_{GAP} = 0.238$) for the reference (T.C. 1), smooth (T.C. 2) and the rough train model (T.C. 3) on the smooth ground (G.C. A), rough ground (G.C. B), between sleepers (G.C. C1) and above sleeper (G.C. C2). $U_{TRAIN} = 4$ m/s.

T.C.	G.C.	U / U_{TRAIN}	W / U_{TRAIN}	U_{SD} / U_{TRAIN}	W_{SD} / U_{TRAIN}
1	A	0.3225	0.0041	0.0646	0.0313
2	A	0.1476	0.0017	0.0430	0.0194
3	A	0.3365	0.0027	0.0972	0.0452
1	B	0.2529	0.0050	0.0697	0.0358
2	B	0.1228	0.0011	0.0438	0.0212
3	B	0.2817	0.0017	0.0992	0.0513
1	C1	0.2463	0.0097	0.0767	0.0329
2	C1	0.1449	0.0012	0.0480	0.0188
3	C1	0.2966	0.0052	0.0992	0.0444
1	C2	0.2648	0.0109	0.0752	0.0337
2	C2	0.1529	0.0030	0.0473	0.0192
3	C2	0.3162	0.0052	0.1012	0.0445

Table B4: Spatial averages between the first and last train axles for the normalised mean U and W velocities and their corresponding velocity fluctuations U_{SD} and W_{SD} at the height of $TOR \times 0.75$ ($Z / H_{GAP} = 0.356$) for the reference (T.C. 1), smooth (T.C. 2) and the rough train model (T.C. 3) on the smooth ground (G.C. A), rough ground (G.C. B), between sleepers (G.C. C1) and above sleeper (G.C. C2). $U_{TRAIN} = 4$ m/s.

T.C.	G.C.	U / U_{TRAIN}	W / U_{TRAIN}	U_{SD} / U_{TRAIN}	W_{SD} / U_{TRAIN}
1	A	0.3455	0.0046	0.0686	0.0353
2	A	0.1727	0.0018	0.0489	0.0228
3	A	0.3549	0.0036	0.0995	0.0507
1	B	0.2795	0.0061	0.0736	0.0392
2	B	0.1464	0.0015	0.0492	0.0241
3	B	0.3012	0.0026	0.1023	0.0562
1	C1	0.2791	0.0100	0.0815	0.0374
2	C1	0.1708	0.0013	0.0527	0.0215
3	C1	0.3246	0.0048	0.1021	0.0504
1	C2	0.2888	0.0103	0.0798	0.0378
2	C2	0.1735	0.0023	0.0519	0.0216
3	C2	0.3341	0.0046	0.1026	0.0506

Table B5: Spatial averages between the first and last train axles for the normalised mean U and W velocities and their corresponding velocity fluctuations U_{SD} and W_{SD} at the height of the top of the rail ($Z / H_{GAP} = 0.475$) for the reference (T.C. 1), smooth (T.C. 2) and the rough train model (T.C. 3) on the smooth ground (G.C. A), rough ground (G.C. B), between sleepers (G.C. C1) and above sleeper (G.C. C2). $U_{TRAIN} = 4$ m/s.

T.C.	G.C.	U / U_{TRAIN}	W / U_{TRAIN}	U_{SD} / U_{TRAIN}	W_{SD} / U_{TRAIN}
1	A	0.3759	0.0045	0.0730	0.0377
2	A	0.2058	0.0018	0.0553	0.0256
3	A	0.3770	0.0043	0.1022	0.0541
1	B	0.3091	0.0067	0.0778	0.0419
2	B	0.1755	0.0021	0.0547	0.0269
3	B	0.3230	0.0038	0.1057	0.0592
1	C1	0.3084	0.0077	0.0847	0.0387
2	C1	0.2029	0.0016	0.0587	0.0235
3	C1	0.3520	0.0044	0.1061	0.0538
1	C2	0.3126	0.0080	0.0833	0.0386
2	C2	0.2032	0.0020	0.0578	0.0237
3	C2	0.3566	0.0046	0.1063	0.0540

Table B6: Spatial averages between the first and last train axles for the normalised mean U and W velocities and their corresponding velocity fluctuations U_{SD} and W_{SD} at the height of $TOR \times 1.25$ ($Z / H_{GAP} = 0.594$) for the reference (T.C. 1), smooth (T.C. 2) and the rough train model (T.C. 3) on the smooth ground (G.C. A), rough ground (G.C. B), between sleepers (G.C. C1) and above sleeper (G.C. C2). $U_{TRAIN} = 4$ m/s.

T.C.	G.C.	U / U_{TRAIN}	W / U_{TRAIN}	U_{SD} / U_{TRAIN}	W_{SD} / U_{TRAIN}
1	A	0.4291	0.0031	0.0808	0.0400
2	A	0.2516	0.0016	0.0616	0.0282
3	A	0.4080	0.0046	0.1069	0.0559
1	B	0.3465	0.0063	0.0833	0.0439
2	B	0.2125	0.0025	0.0613	0.0296
3	B	0.3508	0.0047	0.1102	0.0613
1	C1	0.3600	0.0050	0.0901	0.0396
2	C1	0.2469	0.0017	0.0632	0.0243
3	C1	0.3868	0.0043	0.1104	0.0536
1	C2	0.3606	0.0050	0.0886	0.0386
2	C2	0.2460	0.0019	0.0626	0.0246
3	C2	0.3886	0.0042	0.1101	0.0540

Table B7: Spatial averages between the first and last train axles for the normalised mean U and W velocities and their corresponding velocity fluctuations U_{SD} and W_{SD} at the height of $TOR \times 1.5$ ($Z / H_{GAP} = 0.713$) for the reference (T.C. 1), smooth (T.C. 2) and the rough train model (T.C. 3) on the smooth ground (G.C. A), rough ground (G.C. B), between sleepers (G.C. C1) and above sleeper (G.C. C2). $U_{TRAIN} = 4$ m/s.

Spatial horizontal averages between the middle of the second mid-car and the trailing end-car.

T.C.	G.C.	U / U_{TRAIN}	W / U_{TRAIN}	U_{SD} / U_{TRAIN}	W_{SD} / U_{TRAIN}
1	A	0.3534	0.0017	0.0652	0.0187
2	A	0.1524	0.0011	0.0417	0.0111
3	A	0.3182	0.0013	0.0947	0.0217
1	B	0.2543	0.0030	0.0677	0.0243
2	B	0.1382	0.0013	0.0431	0.0141
3	B	0.2691	0.0005	0.0916	0.0284
1	C1	0.1287	0.0013	0.0559	0.0244
2	C1	0.0868	0.0010	0.0380	0.0162
3	C1	0.1453	0.0024	0.0707	0.0282
1	C2	-	-	-	-
2	C2	-	-	-	-
3	C2	-	-	-	-

Table B8: Spatial averages for the nearly fully developed undercarriage flow between the middle of the second mid-car and the trailing end-car for the normalised mean U and W velocities and their corresponding velocity fluctuations U_{SD} and W_{SD} at the height of $TOR \times 0.125$ ($Z / H_{GAP} = 0.059$) for the reference (T.C. 1), smooth (T.C. 2) and the rough train model (T.C. 3) on the smooth ground (G.C. A), rough ground (G.C. B), between sleepers (G.C. C1) and above sleeper (G.C. C2). $U_{TRAIN} = 4$ m/s.

T.C.	G.C.	U / U_{TRAIN}	W / U_{TRAIN}	U_{SD} / U_{TRAIN}	W_{SD} / U_{TRAIN}
1	A	0.3984	0.0011	0.0616	0.0203
2	A	0.1868	0.0008	0.0437	0.0135
3	A	0.3630	0.0001	0.0972	0.0279
1	B	0.2759	0.0020	0.0696	0.0284
2	B	0.1519	0.0006	0.0457	0.0169
3	B	0.2906	-0.0006	0.0952	0.0364
1	C1	0.1877	0.0019	0.0716	0.0295
2	C1	0.1267	0.0011	0.0511	0.0191
3	C1	0.2071	0.0029	0.0907	0.0321
1	C2	0.1726	0.0009	0.0923	0.0291
2	C2	0.1037	0.0013	0.0581	0.0160
3	C2	0.1866	0.0012	0.1092	0.0305

Table B9: Spatial averages for the nearly fully developed undercarriage flow between the middle of the second mid-car and the trailing end-car for the normalised mean U and W velocities and their corresponding velocity fluctuations U_{SD} and W_{SD} at the height of $TOR \times 0.25$ ($Z / H_{GAP} = 0.119$) for the reference (T.C. 1), smooth (T.C. 2) and the rough train model (T.C. 3) on the smooth ground (G.C. A), rough ground (G.C. B), between sleepers (G.C. C1) and above sleeper (G.C. C2). $U_{TRAIN} = 4$ m/s.

T.C.	G.C.	U / U_{TRAIN}	W / U_{TRAIN}	U_{SD} / U_{TRAIN}	W_{SD} / U_{TRAIN}
1	A	0.4364	0.0022	0.0632	0.0250
2	A	0.2146	0.0016	0.0461	0.0172
3	A	0.3982	0.0006	0.1002	0.0382
1	B	0.3153	0.0026	0.0740	0.0333
2	B	0.1758	0.0007	0.0503	0.0206
3	B	0.3244	-0.0010	0.1015	0.0459
1	C1	0.2818	0.0055	0.0847	0.0300
2	C1	0.1881	0.0025	0.0621	0.0202
3	C1	0.3006	0.0047	0.1063	0.0376
1	C2	0.3215	0.0069	0.0830	0.0314
2	C2	0.2141	0.0041	0.0615	0.0203
3	C2	0.3430	0.0036	0.1093	0.0362

Table B10: Spatial averages for the nearly fully developed undercarriage flow between the middle of the second mid-car and the trailing end-car for the normalised mean U and W velocities and their corresponding velocity fluctuations U_{SD} and W_{SD} at the height of $TOR \times 0.5$ ($Z / H_{GAP} = 0.238$) for the reference (T.C. 1), smooth (T.C. 2) and the rough train model (T.C. 3) on the smooth ground (G.C. A), rough ground (G.C. B), between sleepers (G.C. C1) and above sleeper (G.C. C2). $U_{TRAIN} = 4$ m/s.

T.C.	G.C.	U / U_{TRAIN}	W / U_{TRAIN}	U_{SD} / U_{TRAIN}	W_{SD} / U_{TRAIN}
1	A	0.4615	0.0036	0.0665	0.0291
2	A	0.2364	0.0020	0.0498	0.0206
3	A	0.4218	0.0013	0.1013	0.0458
1	B	0.3492	0.0037	0.0761	0.0362
2	B	0.1973	0.0015	0.0531	0.0235
3	B	0.3504	-0.0006	0.1053	0.0530
1	C	0.3302	0.0065	0.0856	0.0342
2	C	0.2208	0.0023	0.0645	0.0221
3	C	0.3490	0.0040	0.1068	0.0435
1	C	0.3517	0.0078	0.0848	0.0348
2	C	0.2348	0.0032	0.0640	0.0223
3	C	0.3706	0.0034	0.1098	0.0437

Table B11: Spatial averages for the nearly fully developed undercarriage flow between the middle of the second mid-car and the trailing end-car for the normalised mean U and W velocities and their corresponding velocity fluctuations U_{SD} and W_{SD} at the height of $TOR \times 0.75$ ($Z / H_{GAP} = 0.356$) for the reference (T.C. 1), smooth (T.C. 2) and the rough train model (T.C. 3) on the smooth ground (G.C. A), rough ground (G.C. B), between sleepers (G.C. C1) and above sleeper (G.C. C2). $U_{TRAIN} = 4$ m/s.

T.C.	G.C.	U / U_{TRAIN}	W / U_{TRAIN}	U_{SD} / U_{TRAIN}	W_{SD} / U_{TRAIN}
1	A	0.4856	0.0040	0.0696	0.0317
2	A	0.2616	0.0022	0.0545	0.0234
3	A	0.4442	0.0021	0.1020	0.0506
1	B	0.3790	0.0048	0.0776	0.0382
2	B	0.2186	0.0020	0.0551	0.0251
3	B	0.3728	0.0003	0.1068	0.0574
1	C1	0.3634	0.0062	0.0863	0.0373
2	C1	0.2447	0.0018	0.0672	0.0235
3	C1	0.3805	0.0030	0.1089	0.0491
1	C2	0.3752	0.0067	0.0847	0.0375
2	C2	0.2514	0.0025	0.0661	0.0236
3	C2	0.3912	0.0027	0.1099	0.0492

Table B12: Spatial averages for the nearly fully developed undercarriage flow between the middle of the second mid-car and the trailing end-car for the normalised mean U and W velocities and their corresponding velocity fluctuations U_{SD} and W_{SD} at the height of the top of the rail ($Z / H_{GAP} = 0.476$) for the reference (T.C. 1), smooth (T.C. 2) and the rough train model (T.C. 3) on the smooth ground (G.C. A), rough ground (G.C. B), between sleepers (G.C. C1) and above sleeper (G.C. C2). $U_{TRAIN} = 4$ m/s.

T.C.	G.C.	U / U_{TRAIN}	W / U_{TRAIN}	U_{SD} / U_{TRAIN}	W_{SD} / U_{TRAIN}
1	A	0.5138	0.0036	0.0718	0.0328
2	A	0.2939	0.0022	0.0601	0.0253
3	A	0.4693	0.0028	0.1035	0.0527
1	B	0.4074	0.0058	0.0793	0.0398
2	B	0.2432	0.0028	0.0571	0.0262
3	B	0.3957	0.0016	0.1084	0.0598
1	C1	0.3936	0.0045	0.0883	0.0378
2	C1	0.2703	0.0014	0.0707	0.0237
3	C1	0.4088	0.0021	0.1115	0.0514
1	C2	0.3987	0.0051	0.0866	0.0379
2	C2	0.2732	0.0020	0.0696	0.0241
3	C2	0.4144	0.0023	0.1119	0.0521

Table B13: Spatial averages for the nearly fully developed undercarriage flow between the middle of the second mid-car and the trailing end-car for the normalised mean U and W velocities and their corresponding velocity fluctuations U_{SD} and W_{SD} at the height of $TOR \times 1.25$ ($Z / H_{GAP} = 0.594$) for the reference (T.C. 1), smooth (T.C. 2) and the rough train model (T.C. 3) on the smooth ground (G.C. A), rough ground (G.C. B), between sleepers (G.C. C1) and above sleeper (G.C. C2). $U_{TRAIN} = 4$ m/s.

T.C.	G.C.	U / U_{TRAIN}	W / U_{TRAIN}	U_{SD} / U_{TRAIN}	W_{SD} / U_{TRAIN}
1	A	0.5638	0.0024	0.0766	0.0333
2	A	0.3410	0.0019	0.0655	0.0274
3	A	0.5020	0.0031	0.1064	0.0532
1	B	0.4386	0.0062	0.0826	0.0407
2	B	0.2728	0.0032	0.0614	0.0275
3	B	0.4222	0.0029	0.1112	0.0614
1	C1	0.4426	0.0027	0.0928	0.0379
2	C1	0.3065	0.0015	0.0733	0.0230
3	C1	0.4431	0.0022	0.1146	0.0511
1	C2	0.4430	0.0029	0.0906	0.0379
2	C2	0.3080	0.0017	0.0723	0.0236
3	C2	0.4459	0.0021	0.1142	0.0516

Table B14: Spatial averages for the nearly fully developed undercarriage flow between the middle of the second mid-car and the trailing end-car for the normalised mean U and W velocities and their corresponding velocity fluctuations U_{SD} and W_{SD} at the height of $TOR \times 1.5$ ($Z / H_{GAP} = 0.713$) for the reference (T.C. 1), smooth (T.C. 2) and the rough train model (T.C. 3) on the smooth ground (G.C. A), rough ground (G.C. B), between sleepers (G.C. C1) and above sleeper (G.C. C2). $U_{TRAIN} = 4$ m/s.

Appendix C: Convergence of the calculated mean velocity values and their standard deviations for the undercarriage flow field

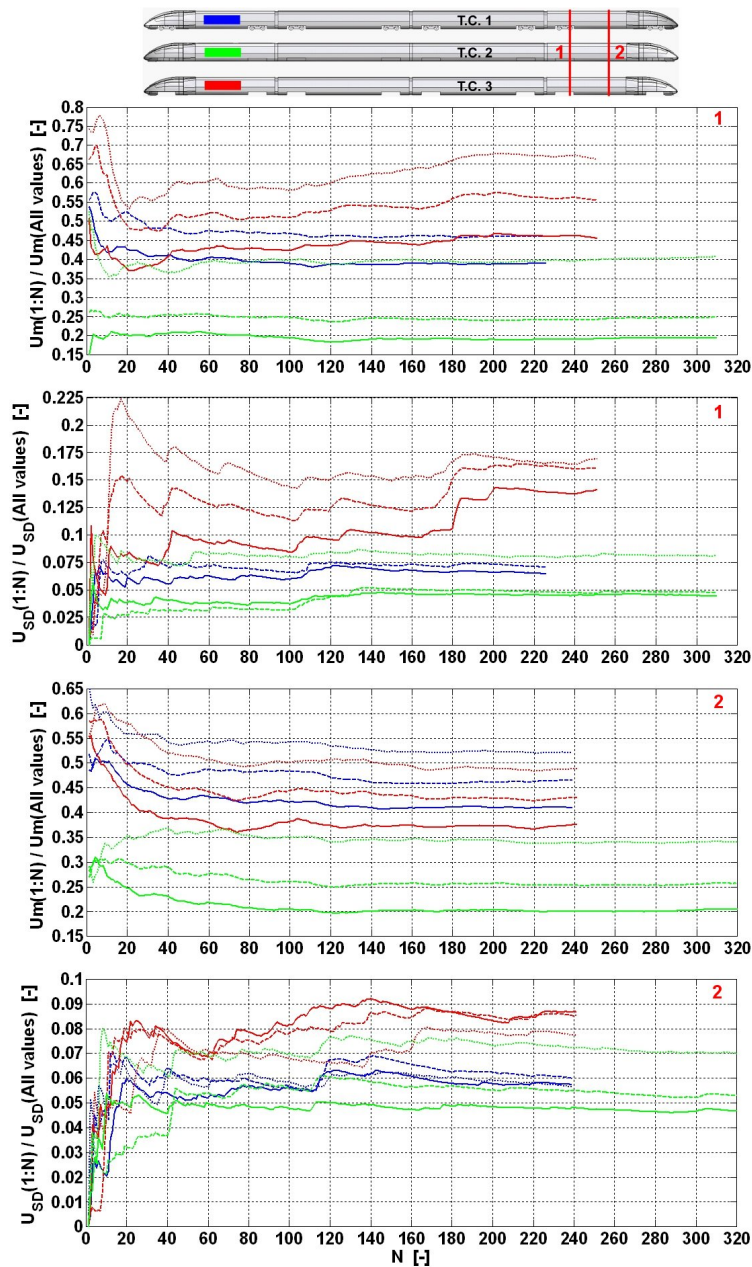


Figure C1: Convergence of the calculated mean U velocity and its corresponding standard deviation U_{SD} as a function of the number of data samples for the undercarriage flow field of the three considered train configurations on the smooth ground (G.C. A) at the end of the first bogie region (1) and between both bogie regions (2) of the trailing end-car and at heights of $Z / H_{GAP} = 0.119$ (solid lines), $Z / H_{GAP} = 0.356$ (dashed lines) and $Z / H_{GAP} = 0.713$ (dotted lines). $U_{TRAIN} = 4$ m/s.

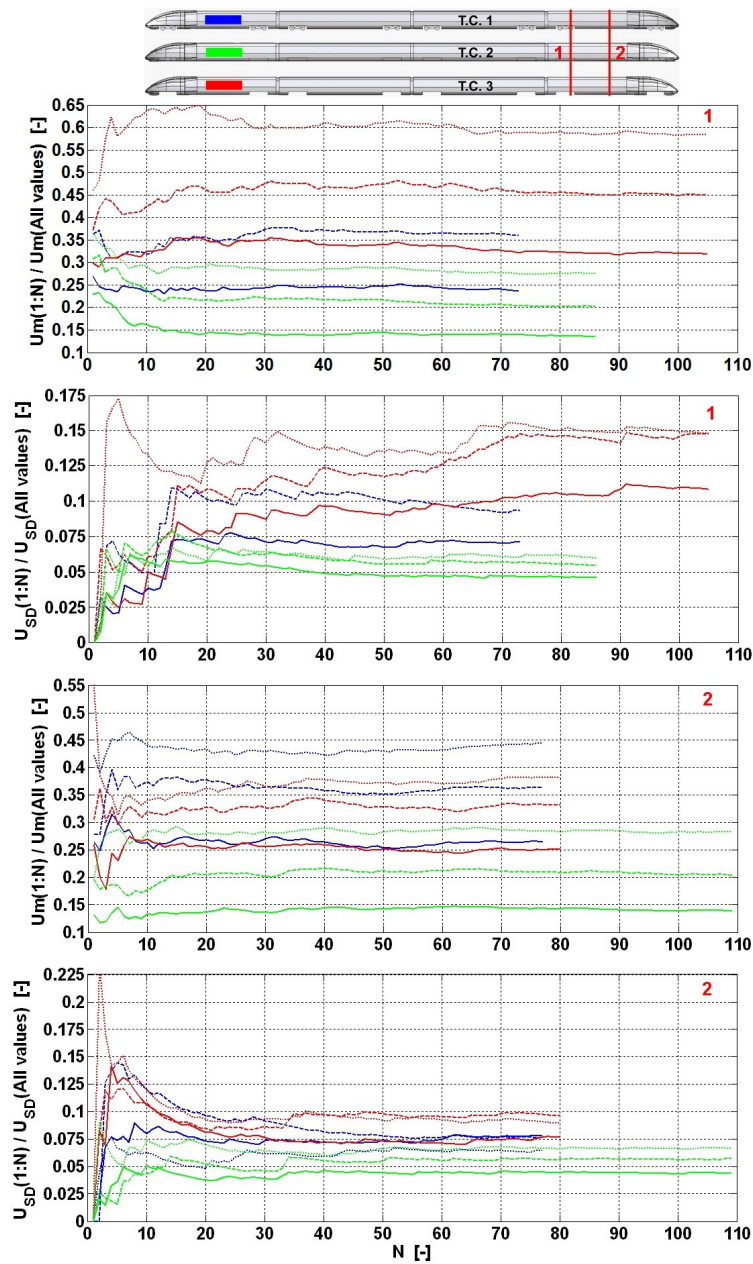


Figure C2: Convergence of the calculated mean U velocity and its corresponding standard deviation U_{SD} as a function of the number of data samples for the undercarriage flow field of the three considered train configurations on the rough ground (G.C. B) at the end of the first bogie region (1) and between both bogie regions (2) of the trailing end-car and at heights of $Z / H_{GAP} = 0.119$ (solid lines), $Z / H_{GAP} = 0.356$ (dashed lines) and $Z / H_{GAP} = 0.713$ (dotted lines). $U_{TRAIN} = 4$ m/s.

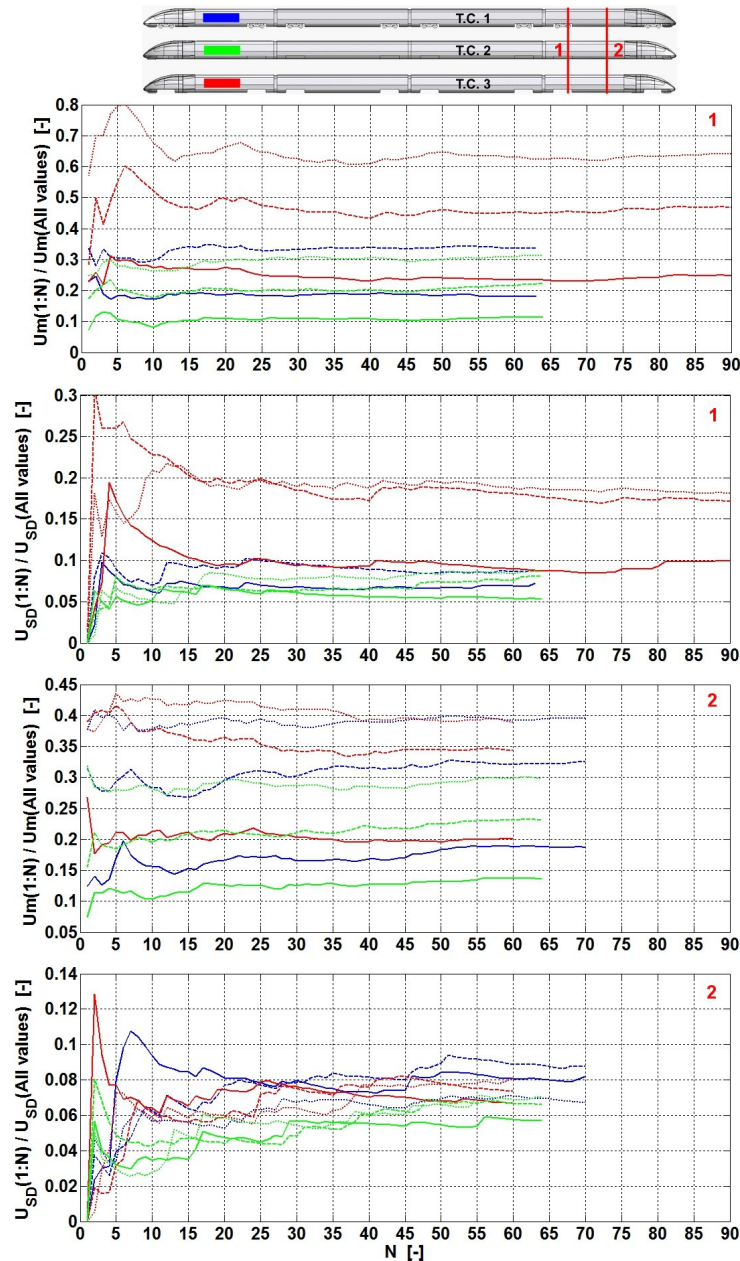


Figure C3: Convergence of the calculated mean U velocity and its corresponding standard deviation U_{SD} as a function of the number of data samples for the undercarriage flow field of the three considered train configurations on the ground with sleepers (G.C. C, between the sleepers: $\Delta X = 8$ mm downstream from a sleeper) at the end of the first bogie region (1) and between both bogie regions (2) of the trailing end-car and at heights of $Z / H_{GAP} = 0.119$ (solid lines), $Z / H_{GAP} = 0.356$ (dashed lines) and $Z / H_{GAP} = 0.713$ (dotted lines). $U_{TRAIN} = 4$ m/s.

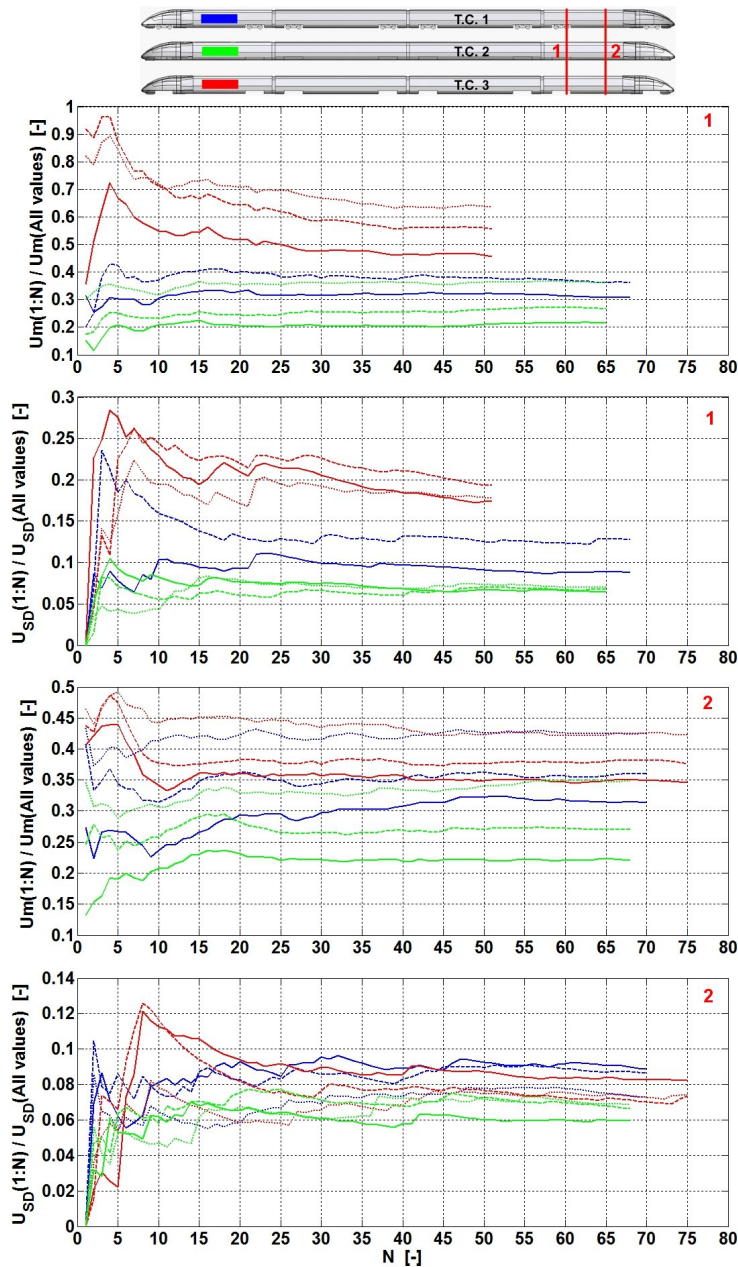


Figure C4: Convergence of the calculated mean U velocity and its corresponding standard deviation U_{SD} as a function of the number of data samples for the undercarriage flow field of the three considered train configurations on the ground with sleepers (G.C. C, above the sleeper) at the end of the first bogie region (1) and between both bogie regions (2) of the trailing end-car and at heights of $Z / H_{GAP} = 0.119$ (solid lines), $Z / H_{GAP} = 0.356$ (dashed lines) and $Z / H_{GAP} = 0.713$ (dotted lines). $U_{TRAIN} = 4$ m/s.

Appendix D: Influence of the ground proximity on the lift coefficient for the simplified ballast particle

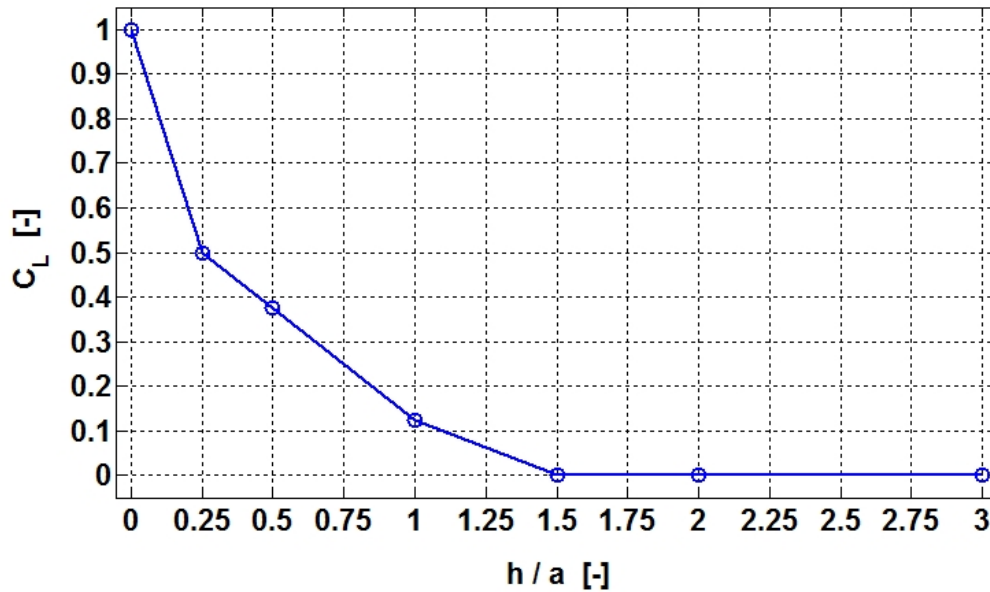


Figure D1: Influence of the ground clearance (h) on the lift coefficient for the simplified ballast particle (cube with an edge length a) based on the data of Malavasi and Guadagnini [139].

Appendix E: Magnus effect for the simplified ballast particle

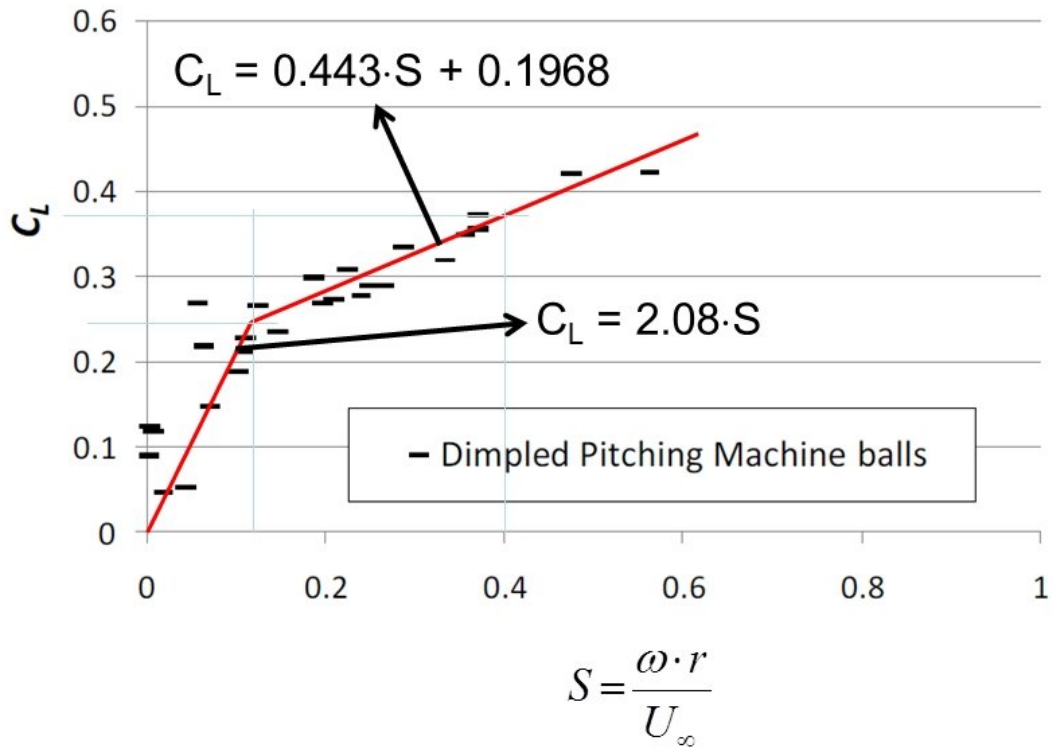


Figure E1: The Magnus effect (lift) for different spin factors (S) of dimpled pitching machine balls [136].



Figure E2: Dimpled pitching machine ball [136].

Appendix F: Vertically spatially-averaged U velocity along the train for the height of the exposed simplified ballast particle

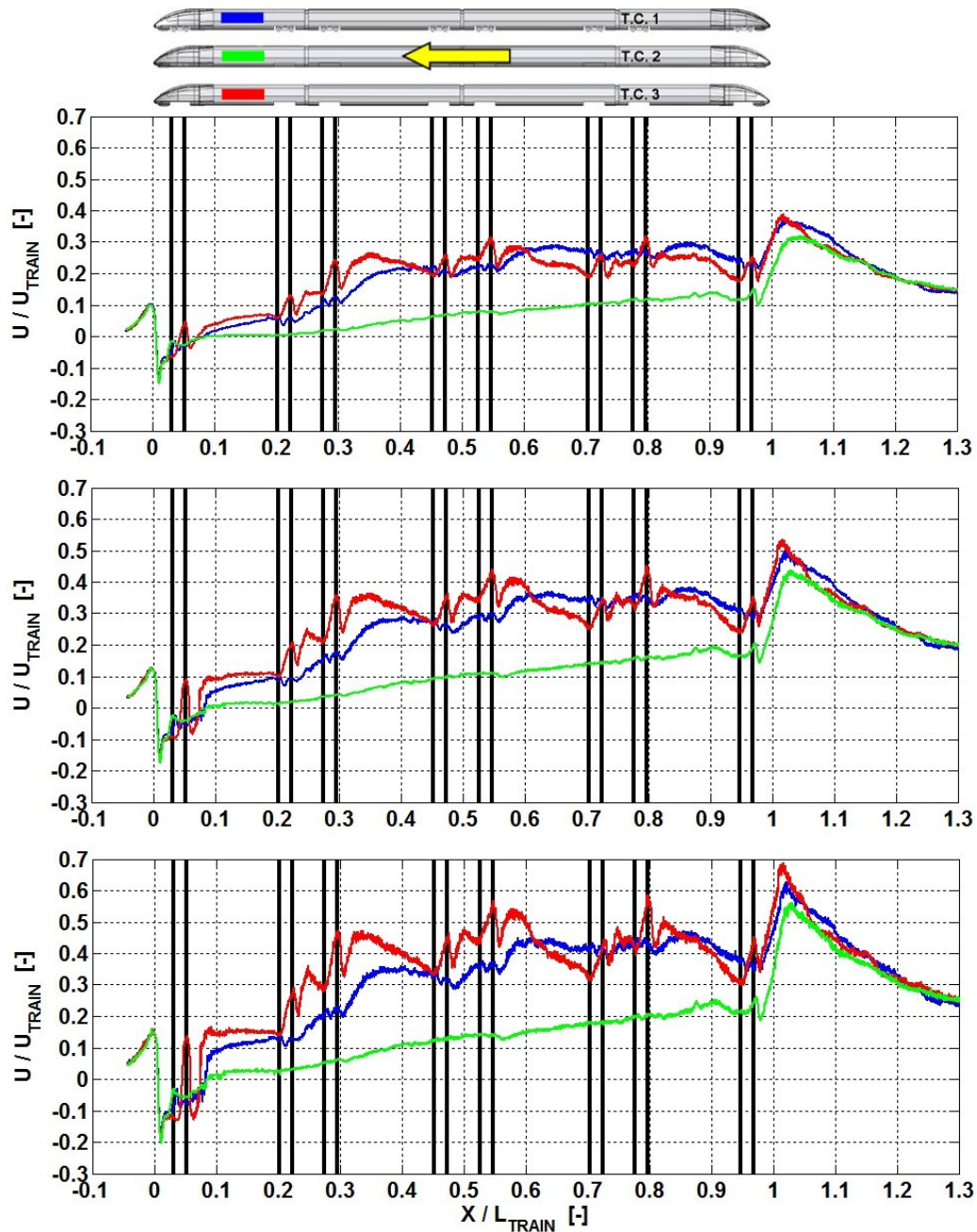


Figure F1: Normalised mean U velocity (upper), mean U velocity + U_{SD} (middle) and mean U velocity + $2 \cdot U_{SD}$ (lower) taking the flow direction into account (U vel. + $U_{SD} \cdot \text{sign}(U \text{ vel.})$) and spatially-averaged over the vertical height of the exposed simplified ballast particle (cube) with an edge length of $a = 0.04$ m for the smooth ground (G.C. A). $U_{TRAIN} = 4$ m/s.

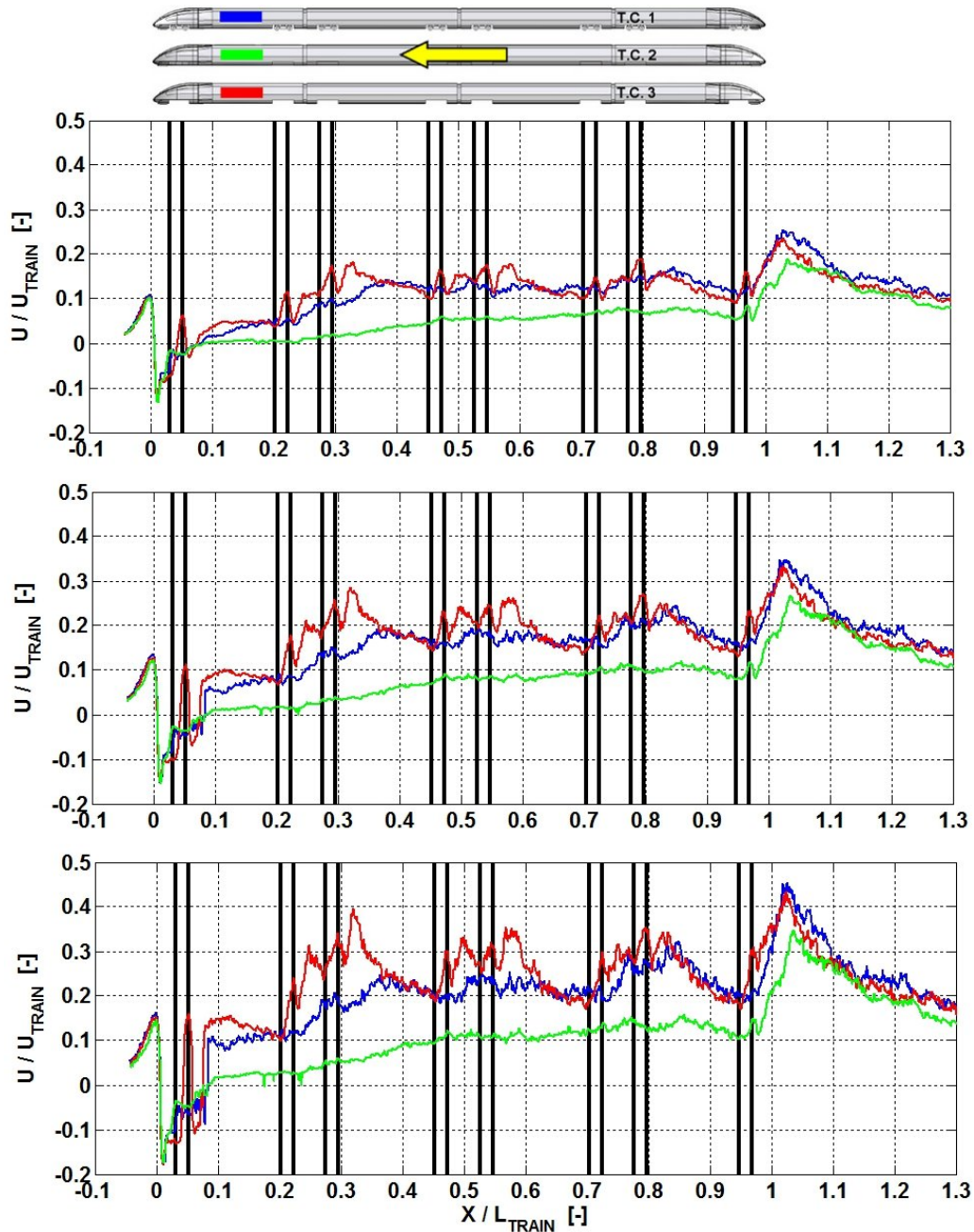


Figure F2: Normalised mean U velocity (upper), mean U velocity + U_{SD} (middle) and mean U velocity + $2 \cdot U_{SD}$ (lower) taking the flow direction into account (U vel. + $U_{SD} \cdot \text{sign}(U \text{ vel.})$) and spatially-averaged over the vertical height of the exposed simplified ballast particle (cube) with an edge length of a ≈ 0.04 m for the rough ground (G.C. B). $U_{TRAIN} = 4$ m/s.

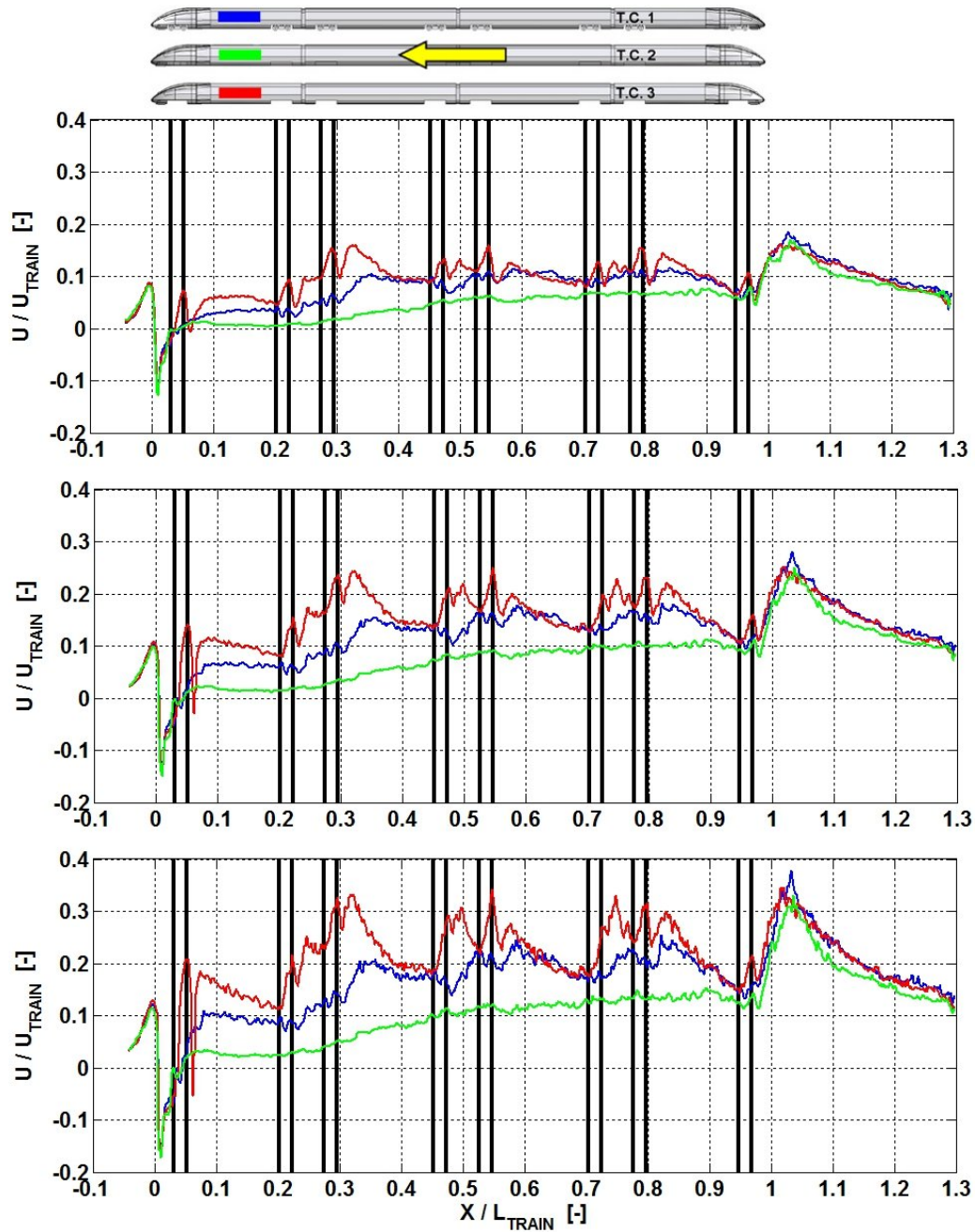


Figure F3: Normalised mean U velocity (upper), mean U velocity + U_{SD} (middle) and mean U velocity + $2 \cdot U_{SD}$ (lower) taking the flow direction into account (U vel. + $U_{SD} \cdot \text{sign}(U \text{ vel.})$) and spatially-averaged over the vertical height of the exposed simplified ballast particle (cube) with an edge length of $a = 0.04$ m for the inter-sleeper region (G.C. C1: $\Delta X = 8$ mm from the upstream sleeper). $U_{TRAIN} = 4$ m/s.

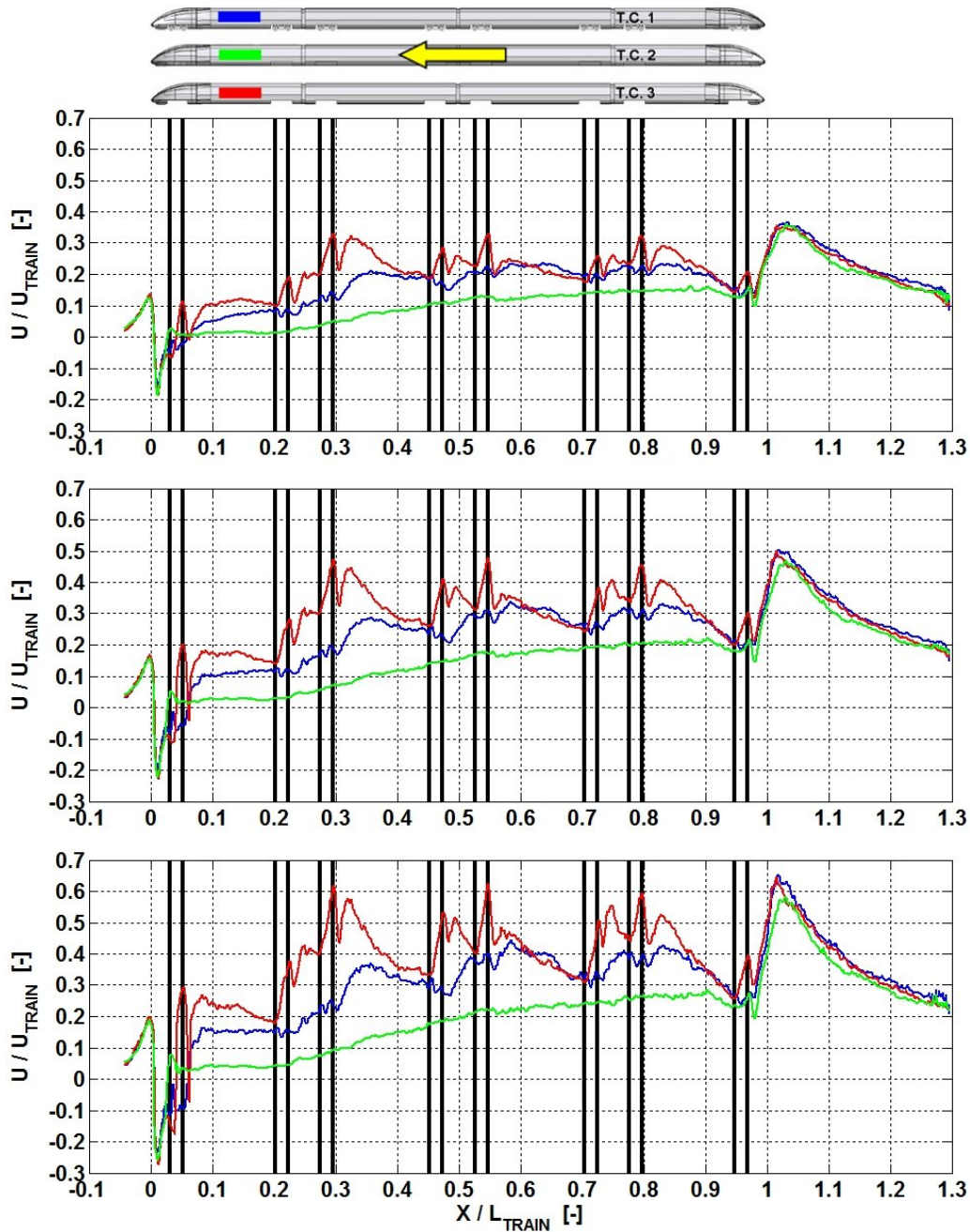


Figure F4: Normalised mean U velocity (upper), mean U velocity + U_{SD} (middle) and mean U velocity + $2 \cdot U_{SD}$ (lower) taking the flow direction into account (U vel. + $U_{SD} \cdot \text{sign}(U \text{ vel.})$) and spatially-averaged over the vertical height of the exposed simplified ballast particle (cube) with an edge length of $a = 0.04$ m for the central position on top of a sleeper (G.C. C2). $U_{TRAIN} = 4$ m/s.

Appendix G: Critical train speeds of ballast flight incidents for the rough ground condition

Size (a)	$H_Z = 235$ mm	$H_Z = 363$ mm	$H_Z = 435$ mm	$H_Z = 500$ mm
10 mm	250, 360, 595	254, 360, 610	256, 364, 615	257, 366, 620
15 mm	282, 400, 665	287, 405, 680	290, 410, 690	293, 412, 705
20 mm	309, 424, 704	316, 442, 745	321, 448, 770	325, 452, 780
25 mm	331, 451, 732	341, 473, 790	347, 480, 820	353, 487, 850
28 mm	343, 465, 760	354, 490, 815	361, 506, 850	368, 506, 885
30 mm	351, 478, 772	362, 500, 825	370, 518, 870	377, 524, 905
35 mm	370, 500, 796	380, 522, 855	389, 543, 905	397, 554, 955
40 mm	385, 518, 814	398, 548, 875	405, 566, 935	416, 579, 990
45 mm	398, 533, 830	412, 564, 895	424, 585, 965	431, 600, 1025
50 mm	409, 546, 842	424, 578, 910	437, 602, 985	449, 619, 1050
55 mm	419, 558, 852	434, 590, 925	448, 616, 1000	462, 635, 1075
60 mm	427, 568, 862	443, 599, 930	458, 629, 1015	473, 649, 1095

Table G1: Critical train speeds [km/h] for ballast pitting (235 mm) and ballast particle impact with the bogie gear boxes or disc brakes (363 mm), bogie frames (435 mm) or train car undercarriages (500 mm) using the mean + 2·SD, mean + SD and mean U and W velocity and C_p data taking the direction of the aerodynamic forces into account (mean + SD·sign(mean)) for the reference train model (T.C. 1).

Size (a)	$H_Z = 235$ mm	$H_Z = 363$ mm	$H_Z = 435$ mm	$H_Z = 500$ mm
10 mm	263, 378, 666	269, 384, 678	270, 385, 687	271, 386, 693
15 mm	287, 409, 703	294, 420, 727	297, 422, 742	299, 424, 748
20 mm	302, 423, 729	309, 439, 747	312, 442, 762	314, 445, 777
25 mm	310, 431, 733	319, 448, 760	323, 456, 772	325, 460, 802
28 mm	315, 436, 733	324, 454, 772	329, 464, 787	333, 469, 808
30 mm	318, 439, 730	328, 458, 775	333, 469, 805	337, 474, 811
35 mm	324, 446, 742	335, 467, 784	341, 481, 820	345, 487, 853
40 mm	331, 453, 746	342, 474, 794	348, 492, 833	353, 498, 869
45 mm	336, 459, 748	348, 480, 804	355, 500, 846	360, 509, 885
50 mm	341, 465, 753	353, 487, 813	360, 507, 855	367, 523, 900
55 mm	346, 474, 758	357, 496, 820	365, 512, 865	373, 534, 910
60 mm	350, 480, 763	362, 500, 823	370, 523, 871	378, 540, 922

Table G2: Critical train speeds [km/h] for ballast pitting (235 mm) and ballast particle impact with the bogie gear boxes or disc brakes (363 mm), bogie frames (435 mm) or train car undercarriages (500 mm) using the mean + 2·SD, mean + SD and mean U and W velocity and C_p data taking the direction of the aerodynamic forces into account (mean + SD·sign(mean)) for the rough train model (T.C. 3).

Size (a)	H _Z = 235 mm	H _Z = 363 mm	H _Z = 435 mm	H _Z = 500 mm
10 mm	602, 960, -	626, 1030, -	636, 1080, -	642, 1120, -
15 mm	685, 1150, -	724, 1310, -	738, 1360, -	756, 1490, -
20 mm	760, 1260, -	815, 1500, -	850, 1670, -	880, 1870, -
25 mm	805, 1330, -	885, 1620, -	925, 1870, -	970, -, -
28 mm	835, 1370, -	920, 1690, -	970, -, -	1025, -, -
30 mm	850, 1390, -	940, 1730, -	995, -, -	1060, -, -
35 mm	885, 1450, -	985, 1820, -	1055, -, -	1140, -, -
40 mm	920, 1490, -	1030, 1890, -	1110, -, -	1210, -, -
45 mm	940, 1530, -	1060, 1950, -	1160, -, -	1270, -, -
50 mm	965, 1560, -	1090, 1990, -	1190, -, -	1320, -, -
55 mm	985, 1590, -	1110, -, -	1220, -, -	1370, -, -
60 mm	1000, 1610, -	1120, -, -	1250, -, -	1400, -, -

Table G3: Critical train speeds [km/h] for ballast pitting (235 mm) and ballast particle impact with the bogie gear boxes or disc brakes (363 mm), bogie frames (435 mm) or train car undercarriages (500 mm) using the mean + 2·SD, mean + SD and mean U and W velocity and C_p data taking the direction of the aerodynamic forces into account (mean + SD·sign(mean)) for the smooth train model (T.C. 2). All critical train speeds over 2000 km/h are denoted with (-).

Appendix H: Critical train speeds for the simplified ballast particle to be transported past the consecutive sleeper

Position	a = 10 mm	a = 20 mm	a = 28 mm	a = 40 mm	a = 50 mm	a = 60 mm
1	-	-	-	-	-	-
2	1550	830	820	790	780	760
3	560	620	630	610	600	590
4	490	520	540	550	550	535
5	430	490	500	500	500	495
6	490	555	570	555	535	515
7	1450	1430	1130	770	630	565
8	-	-	-	-	1215	875
9	-	-	-	-	1520	900

Table H1: Critical train speeds [km/h] needed for simplified ballast particles (cubes) of different sizes and at different initial inter-sleeper positions to be transported over the consecutive sleeper for the reference train model (T.C. 1) using the mean + 2·SD·sign(mean) U and W velocity and C_p field data. All critical train speeds over 2000 km/h are denoted with (-).

Position	a = 10 mm	a = 20 mm	a = 28 mm	a = 40 mm	a = 50 mm	a = 60 mm
1	-	-	-	-	-	-
2	-	1920	1380	1250	1170	1120
3	1040	980	990	1000	1000	995
4	900	990	1020	1030	1020	1020
5	1110	1260	1250	1190	1130	1075
6	-	-	-	1830	1500	1305
7	-	-	-	-	-	1540
8	-	-	-	-	-	-
9	-	-	-	-	-	-

Table H2: Critical train speeds [km/h] needed for simplified ballast particles (cubes) of different sizes and at different initial inter-sleeper positions to be transported over the consecutive sleeper for the smooth train model (T.C. 2) using the mean + 2·SD·sign(mean) U and W velocity and C_p field data. All critical train speeds over 2000 km/h are denoted with (-).

Position	a = 10 mm	a = 20 mm	a = 28 mm	a = 40 mm	a = 50 mm	a = 60 mm
1	-	-	-	-	-	-
2	1400	1270	1070	890	610	570
3	810	500	510	510	500	495
4	390	430	450	450	450	445
5	380	410	410	420	420	415
6	380	420	430	430	420	420
7	680	620	540	450	410	400
8	-	-	-	830	560	460
9	-	-	-	890	620	495

Table H3: Critical train speeds [km/h] needed for simplified ballast particles (cubes) of different sizes and at different initial inter-sleeper positions to be transported over the consecutive sleeper for the rough train model (T.C. 3) train models using the mean + 2·SD·sign(mean) U and W velocity and C_p field data. All critical train speeds over 2000 km/h are denoted with (-).

T.C. 1			
Position	Upstream (u) m	Middle (m)	Downstream (d)
a = 10 mm	375 (405)	430 (440)	525 (575)
a = 20 mm	425 (465)	455 (535)	585 (710)
a = 28 mm	450 (505)	480 (580)	605 (760)
a = 40 mm	460 (515)	485 (585)	580 (725)
a = 50 mm	460 (515)	480 (585)	555 (690)
a = 60 mm	455 (510)	470 (580)	530 (655)
T.C. 2			
Position	Upstream (u) m	Middle (m)	Downstream (d)
a = 10 mm	160* (160*)	400* (400*)	875* (875*)
a = 20 mm	375* (375*)	- (650)	- (700)
a = 28 mm	665* (665*)	- (685)	- (755)
a = 40 mm	- (595)	- (680)	- (780)
a = 50 mm	- (-)	- (690)	- (790)
a = 60 mm	- (-)	- (-)	- (810)
T.C. 3			
Position	Upstream (u) m	Middle (m)	Downstream (d)
a = 10 mm	200* (200*)	345 (340)	470 (405)
a = 20 mm	340 (320)	375 (425)	450 (535)
a = 28 mm	360 (350)	380 (445)	450 (555)
a = 40 mm	365 (375)	385 (445)	440 (550)
a = 50 mm	365 (380)	385 (440)	430 (530)
a = 60 mm	365 (385)	380 (425)	425 (510)

Table H4: Critical train speeds [km/h] for simplified ballast particles (cubes) of different sizes and at different initial positions on top of a sleeper to be transported over the consecutive sleeper for the reference (T.C. 1), smooth (T.C. 2) and rough train models (T.C. 3) using the mean + 2·SD·sign(mean) U and W velocity and C_p field data. The critical train speeds in the brackets are calculated assuming the single direct bounce motion of the trackbed and the other train speeds consider the rolling motion over the trackbed. All critical train speeds over 2000 km/h are denoted with (-) and the (*) indicates where the reverse flow region around the head of the train is strong enough to slide the ballast particle into the upstream inter-sleeper region.

Curriculum Vitae

Family name: Jönsson
Given name: Mattias
Date of birth: May 24th, 1982 in Rebbelberga, Sweden

- 10.2014 - present:** Development engineer aerodynamics and aeroacoustics at AUDI AG, Ingolstadt, Germany.
- 04.2007 - 10.2014:** Research associate at the German Aerospace Center (DLR), Göttingen, Germany.
- 08.2006 - 03.2007:** Master thesis work at Bombardier Transportation, Department of Aerodynamics and Thermodynamics, Västerås, Sweden.
- 06.2006 - 08.2006:** Internship at Bombardier Transportation, Department of Aerodynamics and Thermodynamics, Hennigsdorf, Germany.
- 09.2004 - 08.2005:** ERASMUS exchange student at the Technical University of Hamburg-Harburg (TUHH), Germany.
- 08.2002 - 03.2007:** Master of Science (Civilingenjör) in Mechanical Engineering with specialisation in applied mechanics at the Luleå University of Technology (LTU), Sweden.
- 08.1998 - 06.2001:** Secondary school at Ängelholms gymnasieskola, Sweden.
- 08.1989 - 06.1998:** Primary school at Rebbelberga grundskola and Kungsgårdsskolan högstadie, Ängelholm, Sweden.
-